CHEMICAL REVIEWS

pubs.acs.org/CR

Review

Chemomechanics of Rechargeable Batteries: Status, Theories, and Perspectives

Luize Scalco de Vasconcelos,[⊥] Rong Xu,[⊥] Zhengrui Xu, Jin Zhang, Nikhil Sharma, Sameep Rajubhai Shah, Jiaxiu Han, Xiaomei He, Xianyang Wu, Hong Sun, Shan Hu, Madison Perrin, Xiaokang Wang, Yijin Liu,* Feng Lin,* Yi Cui,* and Kejie Zhao*

Cite This: *Chem. Rev.* 2022, 122, 13043−13107

Read Online

ACCESS | Metrics & More | Article Recommendations

ABSTRACT: Chemomechanics is an old subject, yet its importance has been revived in rechargeable batteries where the mechanical energy and damage associated with redox reactions can significantly affect both the thermodynamics and rates of key electrochemical processes. Thanks to the push for clean energy and advances in characterization capabilities, significant research efforts in the last two decades have brought about a leap forward in understanding the intricate chemomechanical interactions regulating battery performance. Going forward, it is necessary to consolidate scattered ideas in the literature into a structured framework for future efforts across multidisciplinary fields. This review sets out to distill and structure what the authors consider to be significant recent developments on the study of chemomechanics of rechargeable batteries in a concise and accessible format to the audiences of different backgrounds in electrochemistry, materials, and mechanics. Importantly, we review the significance of chemomechanics in the context of battery performance, as well as its mechanistic understanding by combining electrochemical, materials, and mechanical perspectives. We discuss the coupling between the elements of electrochemistry and mechanics, key experimental and modeling tools from the small to large scales, and design considerations. Lastly, we provide our perspective on ongoing challenges and opportunities ranging from quantifying mechanical degradation in batteries to manufacturing battery materials and developing cyclic protocols to improve the mechanical resilience.

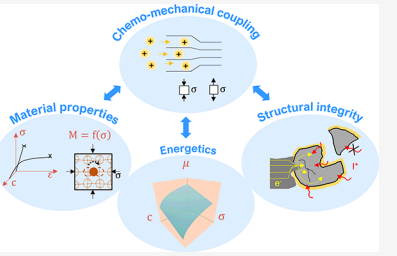

CONTENTS

Received: January 3, 2022
Published: July 15, 2022

https://doi.org/10.1021/acs.chemrev.2c00002
Chem. Rev. 2022, 122, 13043−13107

1. INTRODUCTION

From helping uncover the relationship between electricity and magnetism[1,2] to enabling the modern era of portable electronics,[3] batteries have shaped our society. Once more, opportunities for transformative changes, including the transition from hydrocarbon sources to clean energies,[4−6] and the expansion of digital health (Internet of Humans era),[7] rely on technological breakthroughs in energy storage. It has been increasingly evident that such breakthroughs are contingent on managing the interplay between mechanics and chemistry.

While achieving high energy and power densities are the key criteria for the electrification of transport,[8] mechanical degradation resulting from the large chemical strains inherent of high-capacity materials has restricted the operation window[9] and composition of electrodes.[10] For example, a pure silicon (Si) anode could significantly improve the specific capacity of Li-ion batteries (LIBs); however, to limit structural degradation, Si has only been added in trace amounts to commercial anodes.[11] All-solid-state batteries (ASSBs) can increase the energy efficiency and reduce the safety risk for large-scale applications; however, they suffer from added mechanical instabilities that have so far prevented their commercial use. The hampering costs of scarce raw materials with increasing global demand requires a paradigm shift toward sustainable batteries;[12] counteractively, chemomechanical degradation has interfered with the implementation of otherwise viable, earth-abundant, environmentally, and socially responsible chemistries.[13−15]

Moreover, revolutions in the power supply for next-generation devices add stringent mechanical requirements to the list of new demands faced by rechargeable batteries.[16] Recently, research has shown that soft electronics have the potential to transform healthcare from sporadic clinic visits to clinical-grade continuous tracking of biophysical and biochemical signals through wearable and biointegrated electronics.[17] In this field, power supply integration is a major obstacle, and the research into flexible, biocompatible electrochemical energy storage is still in its infancy.[7] A similar revolution of power supply integration occurs in the applications of lightweight satellites and aircraft, where maximizing the propulsion of power sources and their resistance to structural damage are two key criteria.[18] To combine energy storage and structural functionality together, the structural batteries, a kind of functional energy storage device that has robust mechanical properties to withstand mechanical stress, have been developed to adapt to various kinds of deformation (i.e., compression and stretch) while maintaining an stable electrochemical performance.[19,20]

Overall, mechanical issues impose limitations on the choice of materials and configurations, resulting in a final product with lower performance and higher cost. Although it has long been accepted that mechanical stability is a crucial aspect of the design of battery materials,[21] the incentive and ability to pursue a deeper understanding of its mechanisms and implications have only recently gained traction with the tightening of performance requirements, and with the development of advanced experimental and computational tools to probe and model these systems at small scales and in realistic configurations.[22,23]

Batteries are complex, dynamic systems with continuously evolving composition, microstructure, and properties. The chemical reactions generate deformation and structural degradation, and, conversely, the mechanical degradation regulates the chemical activity. We can categorize the chemomechanical interactions in rechargeable batteries into three major types (dashed circle, Figure 1). One broad category accounts for the coupling between material constitutive behaviors and the composition and stress states of the material (left blue circle, Figure 1). For instance, the mobility of an ion across a lattice may be affected by stress.[24] Also, it has been recognized that the mechanical properties of most active materials, if not all, are greatly dependent on their state of charge (SOC) and are continuously evolving during the (dis)charging of the battery.[25] A second category encompasses the intrinsic coupling between mechanics and chemistry through the thermodynamic relationship between the mechanical stress and the energy landscape (middle blue circle, Figure 1).[26,27] Through this coupling, stress alters the driving force and equilibrium condition for chemical processes such as mass transport, surface charge transfer, and interfacial reactions. Lastly, and perhaps the most tangible interaction, is the relationship between structural stability and the pathways for charge transport (right blue circle, Figure 1). Once the structural integrity of the battery components is disrupted, for instance, by a crack caused by either external or internal loads, the desired electrochemical reaction could be locally impeded and side reactions intensified. An external load could consist of a battery attached to the human body being bent during natural movement or a battery in an electric vehicle being punctured in a crash. In contrast, an internal load results from inherent strains associated with chemical reactions. Regardless of the source, the resulting structural change ultimately regulates the battery operation through a wide range of direct and indirect processes, such as electrical insulation of active materials,[28] solid electrolyte interphase (SEI) reconstruction,[29,30] Li consumption,[31] and short-circuiting.[32]

The intimate chemomechanical interplays are ubiquitous in various types of rechargeable batteries. In LIBs, the reversible

https://doi.org/10.1021/acs.chemrev.2c00002
Chem. Rev. 2022, 122, 13043−13107

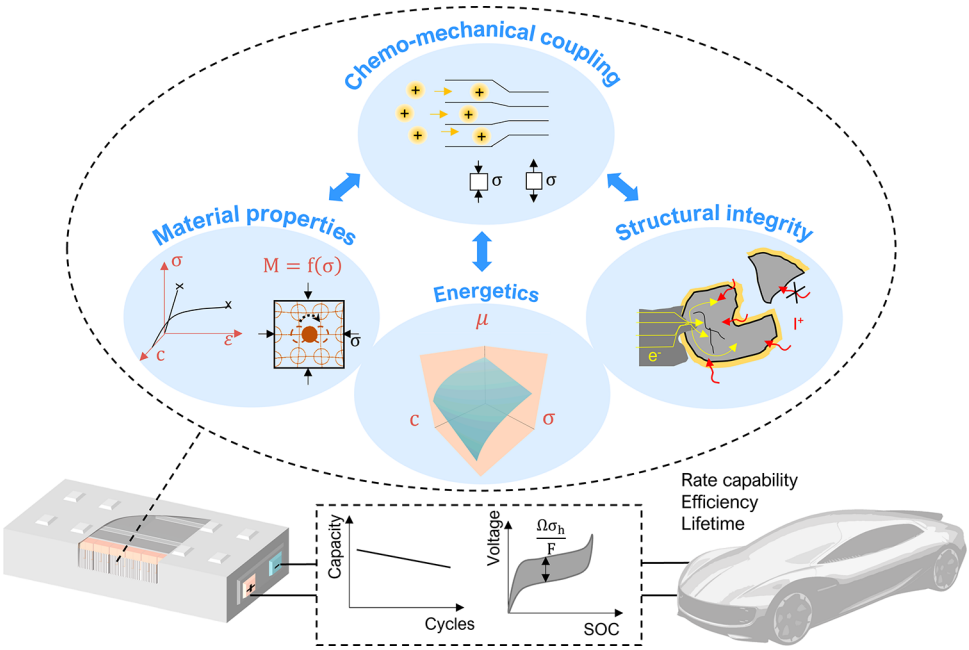

Figure 1. Chemomechanical processes taking place inside the battery regulate its performance. The schematic circled by the dashed line categorizes the chemomechanical coupling into three types: (i) material properties, the dependence of material constitutive behaviors on the chemical state and the stress state; (ii) energetics, stress regulation of the equilibrium conditions and kinetics for the chemical reactions; (iii) structural integrity, structural degradation resulting from the redox reactions, and conversely, its effect on the charge transport and side reactions. These processes regulate the battery pack's electrochemical output, including the rate performance, cyclic efficiency, and lifetime.

chemical reactions between a mobile ion (e.g., Li+) and the host materials in the electrodes result in a chemical strain that varies widely across different electrode chemistries.[33] Usually, increasing the specific capacity comes at the expense of larger chemical strains as more guest ions are introduced per unit lattice of the host, Figure 2. Traditional carbonaceous electrodes for LIBs store about one Li atom per six host atoms, which results in a lower specific capacity (372 mAh g^{-1}) and a smaller volume change (<10%) compared to high-capacity electrodes such as the Si anode, which offers 10 times the specific capacity (4200 mAh g^{-1}), but experiences much larger volume expansion as a consequence (>300%). This large strain drives mechanical stresses and degradation that lead to low cyclic stability of electrodes, limiting their practical adoption. Recently, the further pursuit of high-energy-density rechargeable batteries (>500 Wh kg^{-1}) has revived the research on the Li metal batteries (LMBs) that utilize the Li metal as the anode. The Li metal is considered the ideal anode material because it offers the highest specific energy density and lowest voltage potential ;[34,35] however, the volume change of Li metal during its plating and striping often incurs the mechanical degradation of the SEI, leading to the nonuniform Li deposition and despoliation, which is linked to the performance decay of LMBs.[36]

ASSBs promise to dramatically increase cell- and system-level energy density for electric vehicles by enabling the use of Li metal anodes and simplifying the balance-of-system as well as to bolster safety.[37,38] In recent years, the discovery of a variety of promising solid-state electrolyte (SSE) materials with high ionic conductivity (10^{-4}–10^{-2} S cm^{-1}), including NASICON-type,[39,40] garnet-type,[41,45] and sulfide-based SSEs,[42] paves the way to the realization of ASSBs operating under the current in practical applications. Nevertheless, the complex chemomechanical phenomena, particularly the electrochemical and mechanical incompatibilities between the SSE and the electrode materials, constitute scientific and engineering challenges that need to be addressed before ASSBs can realize their full potential in energy density and safety.[43−45] For example, in the absence of porous space in the electrodes of LIBs, mechanical stresses associated with the volume change of active materials can quickly build up and be effectively transmitted, thereby leading to the premature chemomechanical failure of ASSBs.[46] Moreover, different from the conformal liquid−solid contact between the electrolyte and the electrodes in LIBs, the poor solid−solid contact in ASSBs, originated either from the void formation at SSE/Li interface caused by Li plating/striping or from the repetitive strains between the SSE and the active material in the composite cathode upon ion insertion/extraction, can mechanically damage the SSE and electrochemically inhibit ion and electron transport.[47,48] Last, despite the presence of SSE, Li dendrites still nucleate at the Li/SSE interface and penetrate the SSE, leading to the fracture of SSE and associated short-circuiting of ASSBs.[49,50]

In addition to Li-battery chemistries, announcements of developing alternative, next-generation, beyond-Li battery chemistries, including Na-ion,[51,52] multivalent-ion,[53] and metal-air batteries,[54,55] are now a regular occurrence. It is postulated that these chemistries can open new doors toward either higher-capacity, higher-rate, or lower-cost rechargeable batteries, according to dramatically different electrochemical characteristics. However, in terms of chemomechanics, most alternative battery chemistries present similar phenomena to the Li-battery chemistries.[56,57] For example, the Na^+ intercalation can impose a considerable strain on the host materials.[58,59] Such a large strain inevitably creates mechanical stresses that impact the kinetics of mass transport, charge transfer, and interfacial reactions, and hence the potential and capacity of the battery.[60] The slight difference is that the Na and other multivalent ions usually have a larger ionic size, so the structural failure during battery cycling can be even more

https://doi.org/10.1021/acs.chemrev.2c00002
Chem. Rev. 2022, 122, 13043−13107

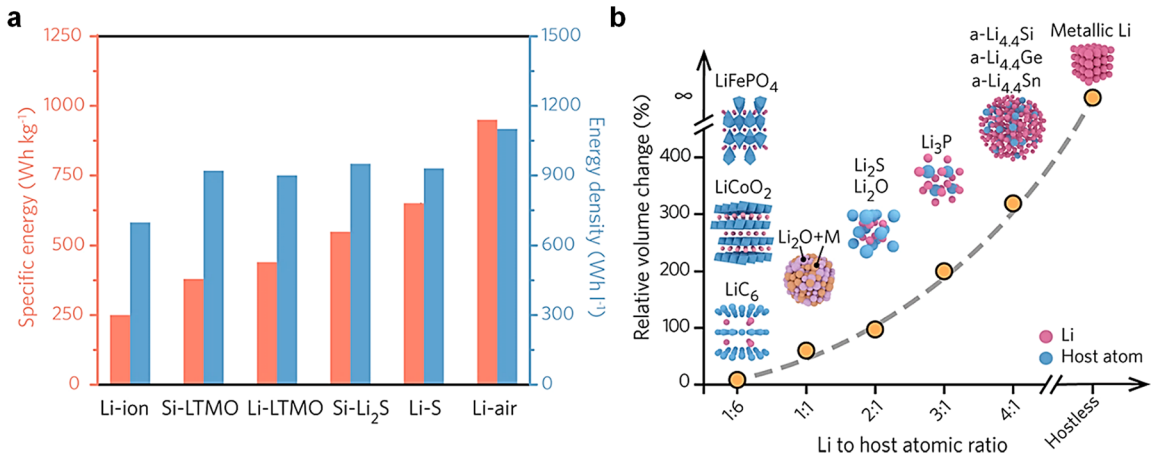

Figure 2. (a) Specific energy (left axis) and energy density (right axis) of the state-of-the-art Li-based battery chemistries. (b) Increased specific capacity leads to a more considerable volumetric change of the host. Reproduced from ref 33. Copyright 2017 American Chemical Society.

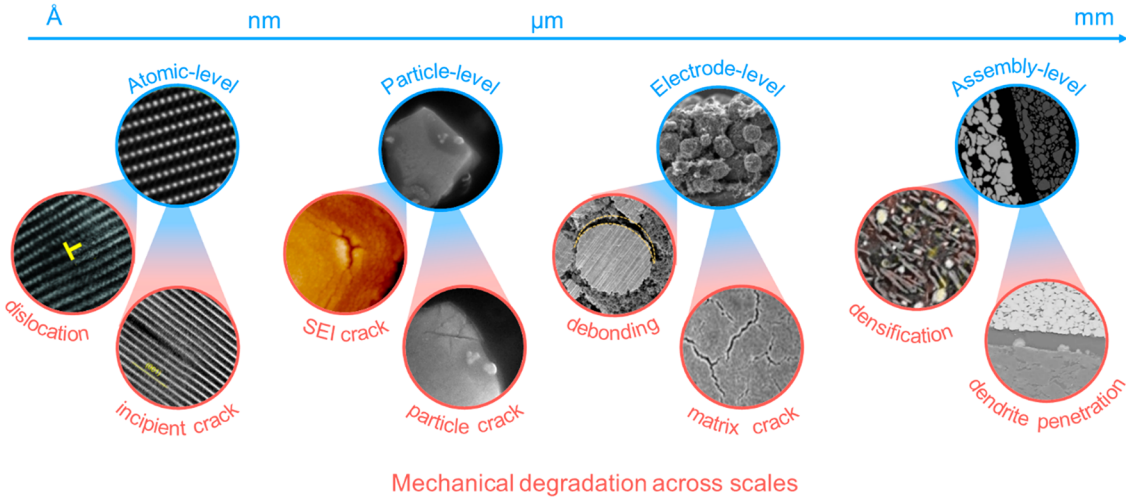

Figure 3. Examples of material degradation spanning multiple length scales, including dislocations and incipient cracks at the atomic level, SEI and particle fracture at the particle level, interfacial debonding, and matrix crack in the composite electrode, and densification and dendrite penetration at the cell level. Images reproduced from refs 9, 62−67. Copyright 2017 Springer Nature. Copyright 2019 Elsevier. Copyright 2016 American Chemical Society. Copyright 2014 Elsevier. Copyright 2016 Elsevier. Copyright 2016 Springer Nature.

severe because of the larger volume change of the host.[56,57,61] In this review, considering the similar underlying mechanisms of the chemomechanical coupling in different electrochemical systems, we will mainly review the references on LIBs and ASSBs, given the extensiveness of their literature pool. However, the concepts, theories, modeling, and experiments applied to the Li batteries are well suited for most alternative battery chemistries.

Overall, this review is intended to be accessible and serve as a bridge for readers from different communities to identify, understand, and address mechanical issues in electrochemical energy storage. It will cover the following aspects of the chemomechanics of rechargeable batteries: how mechanical problems arise at different scales as a result of redox reactions (Section 2), and how they, in turn, impact the electrochemical performance (Section 3); advanced experimental and computational methods to study the chemomechanical behaviors in batteries (Sections 4, 5, and 6); promising solution strategies (Section 7); and the authors' views on needed research efforts (Section 8).

2. ORIGIN OF CHEMOMECHANICAL DEGRADATION

Mechanical damage in batteries spans multiple length scales (Figure 3). At the atomic level, Å ∼ nm size defects such as dislocations and incipient cracks emerge as local stresses develop from the shuttling of guest ions. At the active particle level, mismatched strains can lead to crack growth from nm to μm size and particle disintegration. Finally, there are large structural changes (μm size and beyond) at the electrode and cell assembly level, including pore closing, particle−matrix debonding, and dendrite growth across the electrode and separator. The following subsections will cover the origin and evolution of the mechanical damage arising from chemical reactions in batteries, along with the current understanding of its relationship with design and operation parameters such as the charging protocol, material properties, and microstructure.

2.1. Atomic Scale

The interruption of periodic arrangements of atoms in crystalline materials creates different types of atomic-scale defects (Figure 4g). These defects can be categorized on the basis of their dimensions: zero-dimensional defects (0D defects, Figure 4a−c), one-dimensional defects (1D defects,

https://doi.org/10.1021/acs.chemrev.2c00002
Chem. Rev. 2022, 122, 13043−13107

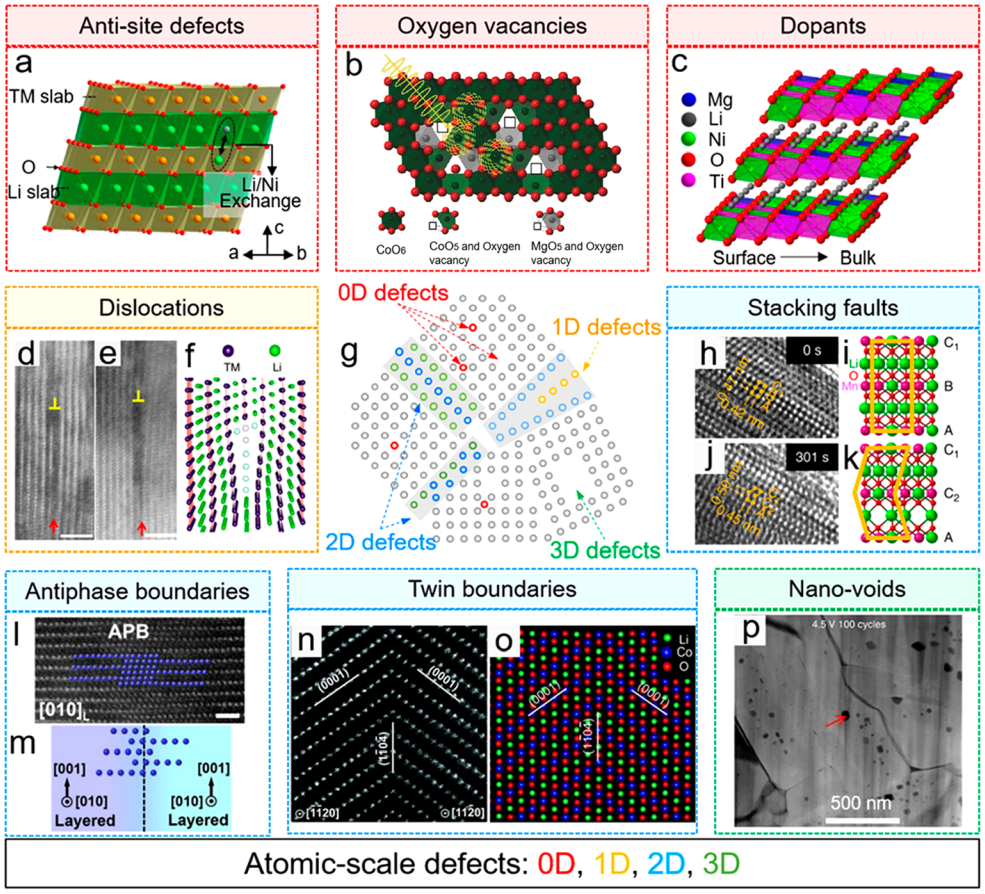

Figure 4. Material degradation at the atomic scale. The four sets of panels of different colors show the crystallographic defects. (a–c) Zero-dimensional (0D). Reproduced from refs 68–70. Copyright 2019 American Chemical Society. (d–f) One-dimensional (1D). Reproduced from ref 9. Copyright 2017 Springer Nature. (h–o) Two-dimensional (2D). Reproduced from refs 71–73. Copyright 2019 Springer Nature. Copyright 2020 American Chemical Society. (p) Three-dimensional (3D). Reproduced from ref 9. Copyright 2017 Springer Nature.

Figure 4d–f), two-dimensional defects (2D defects, Figure 4h–o), and three-dimensional defects (3D defects, Figure 4p). This section will focus on the formation of atomic-scale defects and how their presence regulates mechanical behaviors, whereas Section 3.1 is dedicated to their effect on the electrochemical performance of batteries.

The 0D defects, including antisite defects (Figure 4a), oxygen vacancies (OVs, Figure 4b), and dopants (Figure 4c), may induce nanoscale strain fields to battery materials in similar patterns: antisite defects involve the position exchange of various atoms, destroying the periodic arrangement of atoms; oxygen vacancies refer to the loss of oxygen atoms from the lattice; dopants are purposely incorporated into the lattice, substituting the original atoms and leading to a disrupted arrangement of atoms. These 0D defects are either generated in the material synthesis process because of thermodynamic and kinetic limitations or generated during the battery cycling process. During the material synthesis process, atoms of similar sizes can exchange their positions, e.g., Li and Ni position exchange has been widely observed in layered oxide materials.[74−76] In addition to the intrinsic antisite defects, various atoms can also exchange their sites during the electrochemical cycling process, e.g., Ni goes to the Li site under a high delithiation state, leading to more antisite defects in battery materials. Moreover, under a high state of charge or thermal abuse condition, the oxygen ions may not be stable and can escape from the lattice in the form of oxygen gas.[77] The resulting OVs directly contribute to the crack formation and growth in battery materials: the oxygen release induces local phase transformations, which leads to local stress mismatch and, subsequently, the initiation and propagation of cracks in battery materials.[78−80] Dopants are usually purposely introduced into a perfect lattice, which can cause lattice deformation and electronic structure change,[81] altering the mechanical and electronic properties of battery materials. The crack formation (so-called chemomechanical breakdown) can be effectively mitigated by optimizing the dopant species, contents, and distributions.

Dislocations are widely present in battery materials (Figure 4d–f) as 1D defects. They either form in the material synthesis process or during the battery cycling. Readers interested in the dislocation formation process under battery cycling can refer to these papers.[9,82,83] It is postulated that the influence of dislocations on the stability of battery materials can be 2-fold. On the one hand, dislocations facilitate crack formation. They result in a stress field near the dislocation core,[78] which leads to crack formation.[9,84,85] Dislocation gliding can also lead to oxygen release from the lattice,[71] which is another significant contributor to the crack formation in battery materials.[78] On the other hand, dislocations can decohere the various phases in battery materials and relieve the strain to limit chemo-mechanical breakdown.[86]

Common 2D defects in batteries are stacking faults (Figure 4h–k), antiphase boundaries (Figure 4l,m), and twin

https://doi.org/10.1021/acs.chemrev.2c00002
Chem. Rev. 2022, 122, 13043−13107

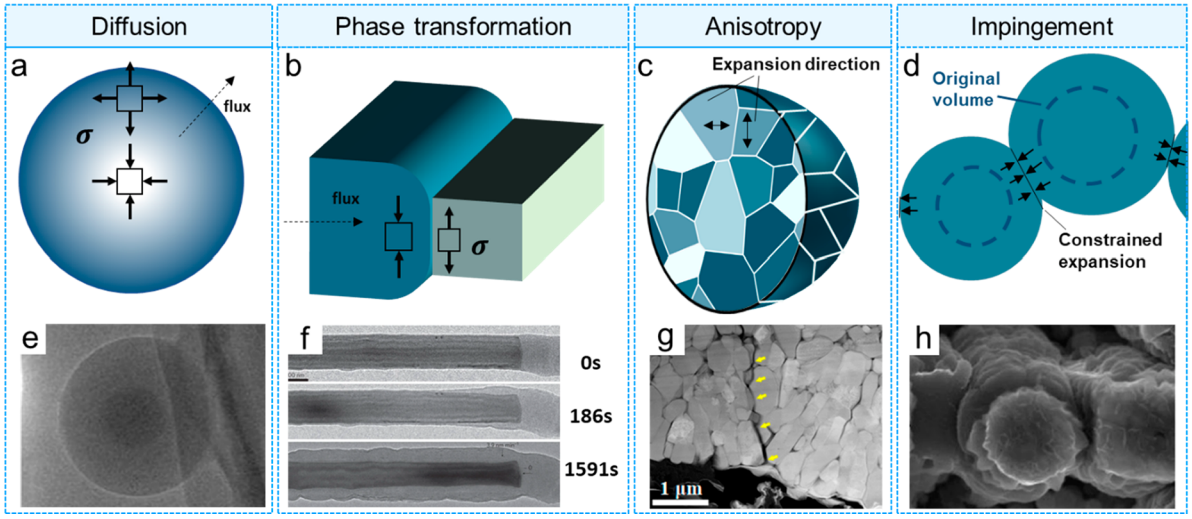

Figure 5. Chemomechanical degradation at the particle level. The upper (a–d) and lower (e–h) panels show the schematics and experimental observations of various mechanisms, respectively. (a, e) Diffusion-induced stress and fracture of active particles. Reproduced from ref 99. Copyright 2013 American Chemical Society. (b, f) Mismatch strain at the phase boundary. Reproduced from ref 104. Copyright 2012 Springer Nature. (c, g) Mismatch strain and anisotropic deformation at the grain boundaries. Reproduced from ref 105. Copyright 2013 IOP Publishing. (d, h) Impingement because of the material contact upon expansion. Reproduced from ref 106. Copyright 2015 Springer Nature.

boundaries (Figure 4n,o). Tarascon and co-workers found that stacking faults are related to oxygen release in $Li_2Ir_{1-y}Sn_yO_3$ layered oxide. Oxygen release can then lead to voltage fade and chemomechanical breakdown.[87] Yet, in a similar material system (Li_2MnO_3), Li et al. showed that the low mobility of stacking faults only minimally contributed to the oxygen release.[71] Some studies suggest that stacking faults may increase the energy state of the materials, which can lower the activation energy of Li diffusion.[88] To date, a detailed understanding of stacking fault in battery materials is still missing. Grain boundaries, including antiphase boundaries and twin boundaries, regulate the phase transformation process.[89] Although experimentally investigating the grain boundaries can be challenging, prior computational works suggest that grain boundaries can hinder diffusion.[90−92] The mismatched volume change in different grains leads to crack formation along grain boundaries.[93,94]

Nanovoids commonly occur as 3D defects in energy materials (Figure 4p).[9,95−97] They are likely generated by vacancy aggregation upon local rearrangement of atoms following ion extraction. They grow in size through the coalescence of small pores, which reduce the total surface area and minimize the surface energy in the system.[95] Researchers have conflicting ideas on the mechanical implications of nanopores. For Sb_2Se_3 nanowires in Na-ion batteries, a correlation was observed between nanopore growth and capacity fade over cycles that the authors claim attributed to mechanical degradation facilitated by the weakened porous structure.[97] In contrast, Liu et al.[95] observed that Ge nanowires become highly porous after the first delithiation and can be cycled reversibly without fracture. The authors point out that pore formation can be an effective stress relaxation mechanism because of the relatively fast short-range diffusion of vacancies.[95] The cycling condition, including charging rate[96] and cutoff voltage,[97] determines whether pores form and can be cycled reversibly. Zhou et al.[96] observed that Ge particles would only form pores under moderate to fast C-rates. Under moderate C-rate, the pores continually aggregate, eventually leading to particle pulverization. At a fast C-rate, however, kinetic limitations restrict the level of (de)lithiation, preserving the structure over the same number of cycles. Hence, holistically, it appears that (i) pore formation can be avoided under certain conditions and (ii) up to a certain extent, pores help relax stresses and prevent crack growth; however, excessive uncontrolled pore growth can itself become a failure mode, causing structure disintegration. There are still ongoing developments in understanding the mechanism and consequences of nanovoid formation. For example, a recent study revealed that nanovoids formed on the surface of silicon electrodes entrap SEI and migrate inward with cycling, continuously carrying new SEI with it.[98]

2.2. Particle Level

2.2.1. Damage of Active Particles. This section discusses the mechanisms leading to stress accumulation and damage of active particles at the continuum level, including diffusion limitation, phase transformation, anisotropy, and impingement.

The insertion of guest ions into a host is generally accomplished with some volume change. This volume change may induce stresses if the expansion or contraction is constrained. Constraints may be geometric (e.g., a thin film electrode bonded to a substrate) or result from an inhomogeneous distribution of the guest ions within the host (and hence strain mismatch). When guest ions (e.g., Li in Li-ion batteries) are inserted/extracted at a rate faster than they can homogenize inside the particle by diffusion, the guest atoms are crowded/sparse in the outer shell of the particle, creating a significant strain mismatch between the center and the surface of the particle and consequently large stresses. Conversely, if the (dis)charge rate is sufficiently slow such that guest atoms can homogenize, the mismatched strain inside the particles is small, and so is the stress. Figure 5a illustrates the scenario of outward Li flux where the shell region (Li poor) is under tension and the core region is under compression because the shell's volume decreases more than the core. The transmission electron microscopy (TEM) image Figure 5e shows an example of radial heterogeneity where the outer shell expands upon Li insertion under a large voltage bias (fast

https://doi.org/10.1021/acs.chemrev.2c00002
Chem. Rev. 2022, 122, 13043−13107

discharge).[99] A combination of high C-rates, large particle sizes, and low diffusivity leads to highly inhomogeneous Li distribution and significant stresses.[100,101] Zhao et al.[102] defined a dimensionless parameter χ to describe the inhomogeneity of Li distribution and found the critical particle size and corresponding charging rate to avoid crack propagation. In addition, a Li diffusivity that is strongly dependent on the Li concentration can lead to large concentration gradients that are easily misunderstood by the sharp interface characteristic of phase transformations.[103]

During ion insertion into the host lattice, instead of a gradual increase in volume caused by an incremental increase in the guest atom concentration, phase transforming materials, such as $LiFePO_4$, crystalline Si, Ge, and Sn, experience an abrupt change in Li content from one equilibrium state to another. This abrupt change in Li content leads to a drastic change in volume and a sharp interface between reacted and unreacted regions. The volume mismatch leads to stresses at the interface as the expansion of the transformed phase is constrained by the untransformed phase (Figure 5b). Figure 5f shows the sharp interface observed between crystalline Si (dark gray region) and amorphous Li_xSi (light gray region) upon Li insertion by in situ TEM.[107] Recently, Deng et al. developed an image-learning platform based on correlative 4D scanning TEM and X-ray spectro-ptychography images to investigate the composition-eigenstrain field and the associated strain heterogeneities at the nanoscale.[108] The analytical model by Hu et al. predefines the pristine region and transformed region with anisotropic deformation and estimates the maximal energy release rate among various cracks configurations to predict the critical particle size to avoid fracture in $LiFePO_4$.[109] Liu et al. developed a coevolving phase transformation and stress model, which shows that fracture initiates at the particle surface and that small particle size tends to avert fracture.[100] It is worth noting that the sharp reaction front in this work[100] was created by defining the diffusivity as a function of concentration, which is simply a numerical approximation. Zhao et al. proposed a model of concurrent reaction and plasticity, which described the velocity of the reaction front as a function of reaction rate instead of diffusivity and showed that cracks could be averted with small particle size and low yield strength.[110]

It is not uncommon that the chemical strain in batteries is anisotropic. For example, anisotropy is significant in layered structures (intercalation electrodes), where the change in the lattice parameter is generally more pronounced along the out-of-plane direction.[111] Anisotropy is especially problematic in polycrystalline particles, as illustrated in Figure 5c, where the different colors indicate the randomly oriented single-crystal domains. Any two misoriented neighboring single crystals will expand in different directions creating a mismatched strain at the boundary between these two grains. The mechanical stress induced by the anisotropic deformation leads to the intergranular fractures and disintegration of the polycrystalline particles.[112] Figure 5g shows these intergranular fractures in $LiNi_xMn_yCo_zO_2$ (NMC, $x + y + z = 1$) cathodes observed by scanning electron microscopy (SEM).[113] The role of the material composition and operating conditions such as cycling rate and depth of discharge on the degree of damage caused by anisotropic polycrystals have been investigated thoroughly.[112−114]

Impingement happens when the chemical strain is constrained by neighboring particles so that the constrained boundaries are under compression (Figure 5d). Lee et al.[106] experimentally observed the mechanical clamping (impingement) phenomenon of Si nanopillars and found that this mechanical interaction changes the reaction kinetics and fracture location (Figure 5h). It also indicated that the clamping might improve the fracture resistance by lessening the tensile stresses.[106] The role of impingement on the stress distribution has been studied for different electrode microstructures and mechanical properties via numerical modeling.[115−117] These studies indicate that the stress states and Li profiles in particle assemblies are different from those in a free-standing configuration. The constraint from neighboring particles leads to nonaxisymmetric stresses which can be significant even in layered oxide cathodes that undergo relatively moderate chemical strains.[117] The magnitude of the effect depends on the electrode characteristics (e.g., volume fraction of active materials, porosity, and elastic modulus of the binders).

2.2.2. SEI Breakdown. Understanding the electrochemistry at the interface between the electrode and the electrolyte is essential for improving the performance of Li-ion and Li metal batteries.[118] However, interfacial electrochemistry is usually complicated and challenging to explore owing to the presence of the SEI, a nanoscale passivation layer formed on the electrode surface from the electrochemical/chemical decomposition of electrolytes.[119,120] After the first observation of SEI on Li metal soaked in nonaqueous electrolyte by Dey and Sullivan,[120] exploration on SEI, particularly on the mechanisms of its formation, growth, and degradation, as well as the characterization of its structure and composition, has been going on for decades and is yet far from the end today.[121−125] The current well-acknowledged SEI model was originally proposed by Peled et al.[124,126] and further enriched by Aurbach et al.[122] In their pioneering studies, SEI is considered an ionically conducting and electronically insulating solid electrolyte that provides the ionic channel for Li-ions to flow into and out of the electrode material while blocking electrons to prevent further electrolyte decomposition. According to this model, the ideal SEI should be an intact layer of solid electrolyte with a homogeneous structural and compositional distribution that promotes the uniform lithiation/delithiation of host materials in Li-ion batteries and uniform Li plating/stripping in Li metal batteries. However, SEI formed during the practical battery operation usually exhibits structural and compositional heterogeneity. Organic (e.g., $LiCH_3$, $LiOCO_2CH_3$, Li_2CO_3) and inorganic (e.g., LiF, Li_2O) decomposition products from the electrolyte are precipitated and distributed heterogeneously within the SEI.[122,127,128] This so-called mosaic SEI structure was first proposed by Peled et al.[126] and experimentally confirmed by a series of studies using atomic force microscopy (AFM), Fourier-transform infrared spectroscopy (FTIR), X-ray photoelectron spectroscopy (XPS), secondary ion mass spectrometry (SIMS), and cryogenic electron microscopy (Cryo-EM).[128−132] The heterogeneous distribution of organic and inorganic components deteriorates the uniformity of ionic conductivity of SEI, which further disturbs the distribution of Li-ion flux into and out of the electrode. Consequently, Li intercalation (deintercalation), alloying (dealloying), or plating (stripping) can be localized in some regions, imposing excessive local strains on the SEI and thus causing mechanical degradation such as a fracture or delamination.[66,133,134]

https://doi.org/10.1021/acs.chemrev.2c00002
Chem. Rev. 2022, 122, 13043−13107

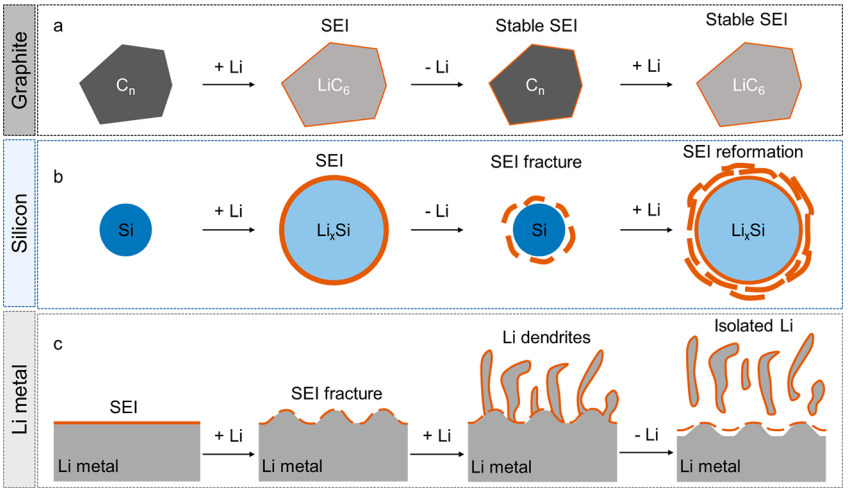

Figure 6. SEI failure mechanisms for different anode materials. The SEI is relatively stable on (a) graphite electrodes because of the limited volume expansion and contraction during cycling; More SEI mechanical failure is expected on high-capacity anode materials, such as (b) Si or (c) Li, because of the larger volume change.

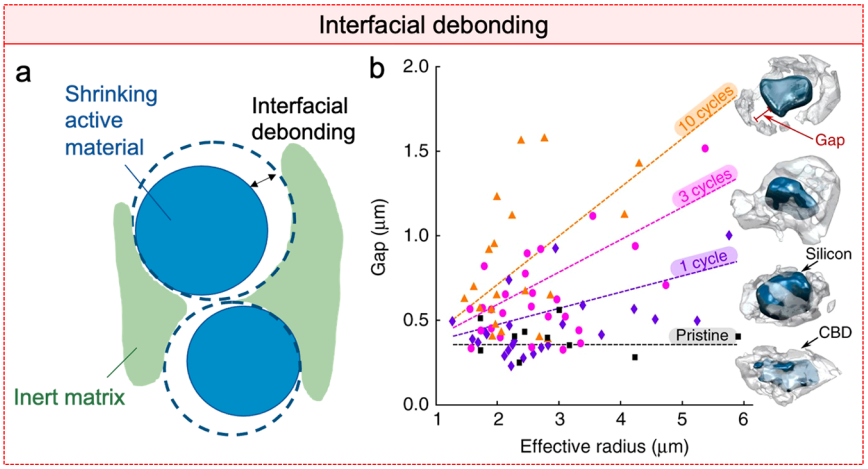

Figure 7. (a) Schematic of the debonding between the active material and the carbon binder matrix because of mismatched deformation. (b) Average gap between the surface of a Si particle and the carbon black-binder domain over cycles as a function of the effective particle radius. Reproduced from ref 160. Copyright 2018 Springer Nature.

It is increasingly evident that the mechanical reliability of SEI plays an essential role in determining the protectivity of SEI and thus the performance of Li-ion and Li metal batteries.[124,135,136] SEI is mechanically stable on graphite electrodes because of graphite's limited volume expansion and contraction during cycling.[137] The intact SEI film prevents the continuous side reactions at the electrolyte/electrode interface, contributing to the excellent cycling performance of graphite electrodes (Figure 6a). The mechanical integrity of SEI faces more challenges when the high-capacity anode materials such as Si, Sn, and Li metal are introduced. For example, the SEI is hardly mechanically stable when forming on the Si anode because the large volume change (~300%) of Si during cycling imposes a considerable strain/stress on the SEI.[138−141] Particularly, extensive cracking might occur during Si lithiation as the SEI film is subjected to large tensile strains/stresses because of the lithiation-induced expansion (Figure 6b). The failure mechanism of SEI on Si has been clearly articulated by Kumar et al.[66] and Guo et al.[134] using in situ AFM, ex situ focused ion beam (FIB) measurements, and finite element modeling. The SEI on the Li metal anode is postulated to crack easily as the nonuniform Li plating can impose large local strains on the SEI film (Figure 6c). Different from the Si anode, the cracking of SEI film on the Li metal anode can act as hot spots to intensify the nonuniform Li plating and stripping, which promotes the formation of Li dendrites, "dead" Li (isolated Li), and "mossy" Li (porous Li).[35,135,142] Nevertheless, the direct observation of SEI rupture on Li metal is relatively challenging as the high reactivity between Li and the electrolyte can quickly reform a new SEI at the cracked regions. Several studies on the in situ observation of Li dendrite nucleation and growth using a liquid cell-based TEM suggest that the dendrites seem to grow as extrusions through some weak points on the SEI, which potentially indicates the SEI breakdown because of the morphological change of the Li metal electrode.[143,144] Thus, to prevent the performance decay of high-capacity batteries, the SEI film must possess excellent mechanical reliability that enables the SEI to survive from the considerable morphological variation of electrodes.

Despite recognition of the importance of SEI robustness in stabilizing the electrode/electrolyte interface, the composition−structure−property relationship of SEI remains largely

https://doi.org/10.1021/acs.chemrev.2c00002
Chem. Rev. 2022, 122, 13043−13107

unknown so far, which hinders the improvement of battery performance through designing better electrolytes or artificial SEI. As previously mentioned, the mechanical properties of the SEI are primarily determined by its compositional distributions, which can be significantly altered by the selection of electrolyte systems. For example, the SEI formed in the ethylene carbonate (EC)-based electrolyte (e.g., 1 M $LiPF_6$ in EC/dimethyl carbonate (DMC)) is mainly composed of porous organic species from electrolyte decomposition. It thus exhibits a low mechanical strength and poor fracture resistance.[123,145] In contrast, the SEI formed in fluoroethylene-rich (e.g., 1 M $LiPF_6$ in fluoroethylene carbonate (FEC)/DMC) or high concentrated electrolytes (e.g., 4 M LiFSI in dimethoxyethane (DME)) exhibits high-modulus and fracture resistance because of the presence of inorganic species such as LiF and Li_2O.[131,146−148] To understand the composition−structure−property relationships of the SEI and associated protectivity for the electrode/electrolyte interface, several advanced characterization techniques such as AFM-based nanoindentation,[149,150] thin-film buckling measurement,[151] and acoustic wave measurement,[152,153] have been developed to either in situ or ex situ quantify the mechanical strength of SEIs formed in different electrode/electrolyte systems. We will review all these characterization techniques in Section 5.1.2.

2.3. Composite Electrode

2.3.1. Interfacial Debonding. The electrode microstructure and mechanical properties are designed to balance rate-capability, energy density, and cycle life. A porous network serves as a fast ion transport channel across the electrode thickness, while a conductive matrix (mixture of polymer binders and conductive additives) maintains the electrical contact between active particles and the current collector. This microstructure needs to reversibly accommodate the mismatch strains between active particles experiencing chemical strain and the inert matrix. If the bonding strength of the binder-particle interface is insufficient to sustain the interfacial stresses, debonding takes place, as illustrated in Figure 7a. The debonding of the interface causes an increase in local electrical impedance,[62] leading to reaction heterogeneity within the electrode, which affects the capacity retention. These cascading effects of debonding will be discussed in-depth in Section 3. Here, we will instead focus on the parameters influencing the stress levels that develop at the interface during operation and the interfacial strength across electrode materials.

In general, active and inactive materials have highly contrasting mechanical properties, with the elastic modulus differing by orders of magnitude.[25,154−157] The binder's mechanical properties and its fraction in the electrode affect the debonding at the interface with the active material.[158] Using numerical calculation, Iqbal et al.[159] demonstrated the effect of binder confinement around active particles in regulating the debonding behavior. A uniform distribution of binder around the active material helps reduce the asymmetry of stress development at high C-rates and reduces mechanical failure.

Active materials that undergo a larger volumetric change are more prone to debonding. Müller et al.[160] used transmission X-ray tomography to track the progression of the gap between active Si particles (volume expansion up to 300% upon lithiation) and the surrounding carbon binder domain (CBD). The data (Figure 7b) indicates that the gap increases with cycles until the particle completely detaches from the CBD and becomes electrochemically inactive for further cycles. Figure 7b shows that the shape and size of the active material also influence local debonding, with larger particles experiencing a higher degree of debonding. It is worth noting that a particle may fracture internally before it debonds from the binder, preserving the interface between the binder and cracked particle in the process. In this scenario, a theoretical study[161] found that large graphite particles have a higher probability of fracture for the same C-rate and binder contact area than smaller graphite particles. Conversely, smaller particles are more likely to debond from the matrix than to crack internally. Lee et al.[162] calculated the strength of the interface between polyvinylidene fluoride (PVDF) binder and graphite particle to assess the traction separation response of the interface. Despite interfacial debonding being a common and consequential degradation mechanism in batteries, we find that the literature on the interfacial properties necessary to model these behaviors is scarce. Hence, there is a pressing need for new experimental methods to characterize the interfacial properties of electrodes, especially in situ, given the high sensitivity of the mechanical properties of traditional binders to the electrolyte solution.[154,163]

Similar to interfacial debonding of the active materials from the binder, the volume expansion/contraction of the composite electrode as a whole during electrochemical cycles can cause separation from the current collector.[164] The separation (often termed delamination) at the binder/current collector interface is a significant degradation mechanism occurring during the electrochemical cycles.[165] The delamination from the current collector increases the contact resistance and generates electronic limitations within the electrode. The characteristics of the electrode fabrication process dictate the electrode-collector interfacial properties. During the drying process, the capillary force-driven binder gradient can evolve across the electrode thickness. This generates less binder concentration near the current collector[166] in the dried electrode, thus increasing the possibility of delamination at the binder/current collector interface. Baunach et al.[167] showed that reducing the drying temperature helps maintain a uniform carbon binder composition and increases the adhesion force. With the increase of surface roughness of the current collector, Jeon et al.[168] demonstrated an improvement in the adhesion strength of a Si electrode with a Cu current collector. The higher interfacial area and the enhanced mechanical interlocking of the roughened surface suppress delamination under cyclic loading. Peeling tests showed that this interfacial strength decreases dramatically over cycles for common anode and cathode configurations (by a factor of 6 for $LiCoO_2$/aluminum and 5 for graphite/copper after 200 cycles).[169] Depending on the mechanical properties of the binder, active material-induced volumetric changes can create considerable stress accumulation in the electrode during cycling. While a stiff binder can make it difficult to fully accommodate the reversible volumetric expansion and contraction of active materials,[170] a highly elastic binder can help minimize the delamination.[171]

2.3.2. Heterogeneous Degradation. The uniformity of the electrode's microstructure relies on the characteristics of its ingredients and the fabrication process parameters. The presence of nonuniformity in the microstructure leads to reaction heterogeneity and the spatial variation of mechanical

https://doi.org/10.1021/acs.chemrev.2c00002
Chem. Rev. 2022, 122, 13043−13107

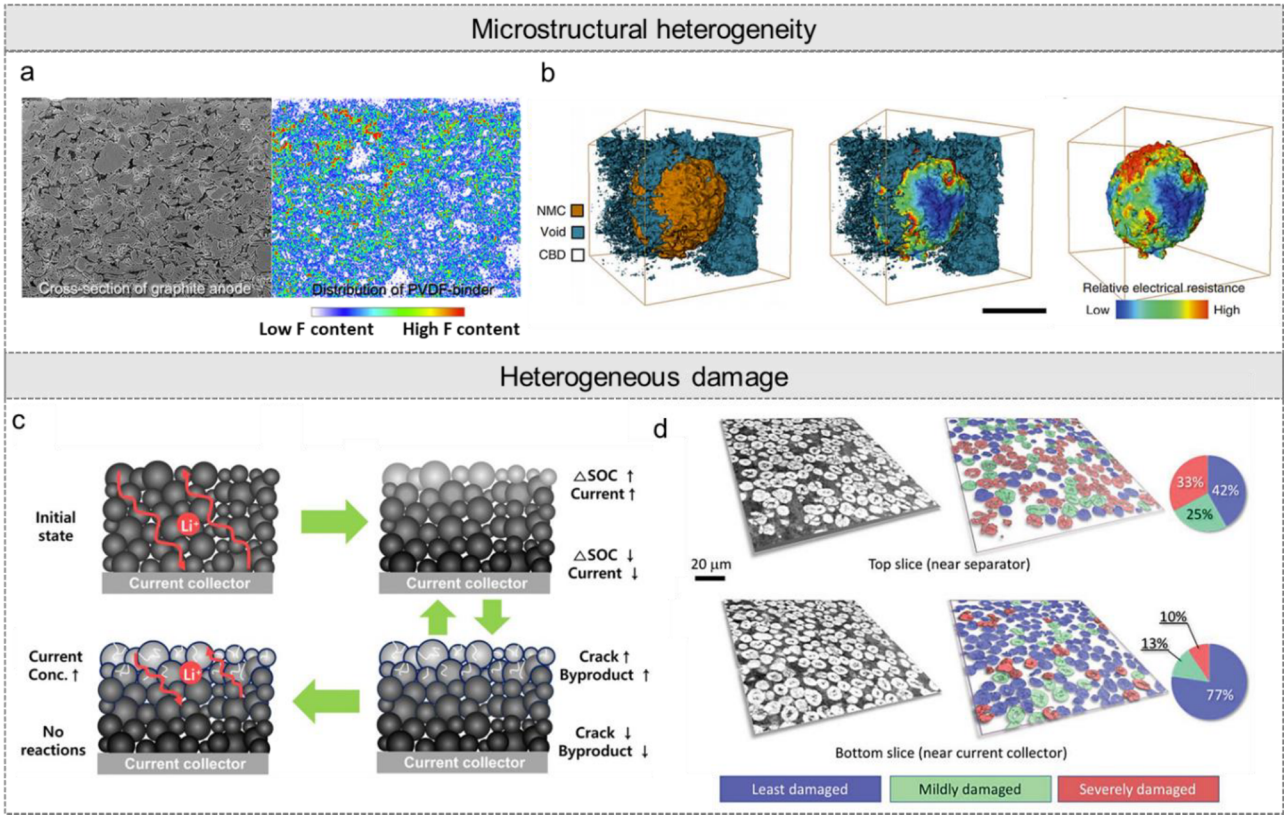

Figure 8. Microstructural heterogeneity (upper panel) and heterogeneous damage (lower panel) in the composite electrodes of Li-ion batteries. Heterogeneous features include the spatial variation of the (a) binder distribution[175] and (b) particle−matrix contact.[176] Reproduced from refs 175 and 176. Copyright 2017 Elsevier. Copyright 2020 Springer Nature. (c) In thick electrodes, the rate limitation of ionic transport through the electrolyte leads to the higher states of charge/discharge of the particles close to the separator. Reproduced from ref 177. Copyright 2020 Elsevier. (d) Classification of particle damage in an NMC electrode from the nanotomography analysis. Reproduced from ref 178. Copyright 2019 Wiley-VCH GmbH.

deformation. Li et al.[172] demonstrated the effect of the particle size on the electrochemical behavior of the $LiFePO_4$ cathode. As per observation, for a good electronically conductive network across the electrode, smaller-sized particles (higher surface area to contact ratio) react faster than large particles. Controlling the size of particles requires tighter control of fabrication process parameters which is commercially challenging.[173] A nonuniform distribution of multisized electrode particles thus can lead to heterogeneous reactions throughout the electrode. The nonspherical shape of active particles can generate tortuosity anisotropy within the electrode.[174] The slenderness ratio of particles and their local orientation influence the local tortuosity, hence limiting ion transport during electrochemical cycling.

The typical electrode fabrication process includes making a slurry suspension in a solvent, followed by casting, drying, and calendaring. The outcome of each intermediate step highly influences the characteristics of the end product of the whole fabrication process. A uniform slurry is essential for homogeneous microstructure distribution throughout the electrode. The rheological properties of the slurry, such as low shear viscosity, yield stress, and storage modulus, are important factors controlling the uniformity[179] in the electrode before the drying step. Colloidal stability of the slurry controls the consistency of the carbon binder domain around the active material[180] throughout the electrode. In Figure 8b, the NMC secondary particle is coated nonuniformly with the carbon binder.[176] The plot of relative electric resistance demonstrates the local impedance variation on the surface, potentially leading to heterogeneous electrochemical reactions and damage. The correlation between electrochemical activity and the connection with the conducting network was investigated by Zielke et al.[181] for Si microparticles embedded PVDF/CB matrix using in situ synchrotron X-ray tomography. They found that if the conductive matrix covered less than 40% of the Si particle surface, the particle remained inactive (and did not fracture). Beyond 40%, the degree of cracking increased monotonically with the coverage amount. Regardless of the cracking extent, these findings suggest that chemical activity and particle coverage by the conductive matrix are strongly coupled, and full particle coverage is essential to increase the accessible capacity.

The drying time is another parameter in electrode fabrication that can cause the segregation of inactive materials across the electrode because of rapid solvent evaporation at the surface. Hawley et al.[179] used elemental spectroscopy analysis and found that drying process parameters such as higher temperature and higher mass loading led to the inhomogeneous distribution of both conductive additive and binder in the electrodes. As shown in Figure 8a, the binder distribution determined by Energy dispersive X-ray spectroscopy (EDS) varies throughout the cross-section of the graphite anode.[175] Such drying process-induced inhomogeneous distribution is more likely to occur as the electrode thickness or areal loading increases. The calendaring process can either positively or negatively impact the microstructure heterogeneity within the

https://doi.org/10.1021/acs.chemrev.2c00002
Chem. Rev. 2022, 122, 13043−13107

Table 1. Mechanical Properties of SSEs and Electrode Materials in ASSBs

	materials	Young's modulus, GPa	hardness, GPa	fracture toughness, MPa·m$^{1/2}$	ref
SSE	$Li_{10}GeP_2S_{12}$	37.19	N/A	N/A	191
	Li_3PO_4	77	3.9	N/A	192
	$Li_{1.5}Al_{0.5}Ge_{1.5}(PO_4)_3$	90.2 ± 10.5	4.5 ± 0.8	N/A	193
	$Li_{1.3}Al_{0.3}Ti_{1.7}(PO_4)_3$	102.5	8.0	1.1 ± 0.3	194
	$Li_7La_3Zr_2O_{12}$	140	8.1 ± 0.8	0.97 ± 0.1	195
	$Li_{6.91}Al_{0.13}La_3Zr_2O_3$	140 ± 9	7.6 ± 0.8	1.19 ± 0.13	196
	$Li_{6.5}La_3Zr_{1.5}Ta_{0.5}O_{12}$	153.8 ± 2.7	5.1	1.28	197, 198
	$Li_{0.33}La_{0.57}TiO_3$	186 ± 4	9.7 ± 0.7	0.91 ± 0.06	199
anode	Li (bulk)	1.9−8.5	0.57−244 (yield stress, MPa)	N/A	200−203

electrode.[182] While it helps create long-range electronic conductive paths, the local porosity reduction and active material breakdown[183] can lead to nonuniform microstructure throughout the electrode.

Microstructural heterogeneity and the kinetic limitation of ionic/electronic conduction in the electrode create nonuniform reactions. Spatial variation of electrochemical reactions generates heterogeneous damage throughout the electrode. From numerical calculations on a 3D reconstructed electrode, Roberts et al.[184] demonstrated the effects of anisotropic swelling. The local inhomogeneous compositional distribution led to additional stresses at the particle−particle contacts. In thick electrodes, ionic limitation (Figure 8c)[177] causes local reaction heterogeneity and, thus, nonuniform material degradation. Only the particles near the separator where the electrolyte is readily accessible can participate fully in the electrochemical cycle. As cycles proceed, particles near the current collector are obstructed from taking part in the reaction, which leads to unusable capacity. The numerical study by Chen et al.[185] demonstrated the competition between the ionic and electronic conductivities in porous electrodes. The ionic limitation promotes reaction activity near the separator, while electronic limitation leads to more reaction activity toward the current collector. Such restrictions are amplified at high C-rates, and the composite electrode might experience spatially varying damage. In thick electrodes, Li concentration and reaction heterogeneity can be diminished by incorporating a particle size gradient across the thickness.[186] Stacking smaller particles toward the current collector can make them more efficiently utilized because of their longer Li^+ diffusion length. Hence, although microstructure heterogeneity can be destructive, there are ways in which it can be intentionally introduced to enhance battery performance.[187]

2.4. Added Challenges from ASSBs

Li metal batteries are considered as the most promising next-generation high-energy-density batteries.[34,35] However, their commercialization is hampered because of the high reactivity between the Li metal and organic liquid electrolytes, as well as the safety issues raised from the dendrite-induced shorting.[37] The recent development of ASSBs is postulated to revive the Li metal anode because the SSEs can inhibit the consumptive side reactions at the Li/electrolyte interface and meanwhile suppress the uncontrollable growth of Li dendrites.[188] Nevertheless, when ASSBs operate at a practical current density, they still face numerous issues such as impedance increase, poor rate performance, low capacity retention, and premature short-circuit.[38,189] These technical challenges are in large part derived from the all-solid nature of the system, where the electrochemical processes in different components and at their interface (e.g., Li plating/striping, Li-ion transport, and intercalation/deintercalation) prompt a wide variety of local mechanical degradation (e.g., void formation, crack propagation, and interfacial debonding).[44] It has been increasingly evident that the practical adoption of ASSBs will not be realized without elucidating the fundamental interplays between the electrochemistry and mechanics in the SSEs and electrodes, and at their interfaces.

We will start this section at a basic level by providing a survey of the mechanical properties of SSEs and Li metal, followed by illustrating the considerable influence of their mechanical properties on the fabrication, integration, and operation of ASSBs. We then elucidate, from a chemo-mechanical perspective, how the electrochemical processes incur different types of mechanical degradations and how these mechanical degradations, in turn, accelerate the performance decay and premature failure of ASSBs. We hope this review can shed some light on the understanding of complex and coupled electrochemistry and mechanics in the ASSBs and potentially guide the rational design of the ASSBs with optimum mechanical stability and electrochemical performance.

2.4.1. Solid-State Electrolytes. It has been well acknowledged that the mechanical properties of SSEs and electrode materials are critical regarding the fabrication and performance of ASSBs. Table 1 summarizes Young's modulus, hardness, and fracture toughness of the SSEs and electrode materials commonly adopted in ASSBs. Specifically, Young's modulus (E) is a measure of the stiffness of materials deformed in the linear elastic region, while the hardness (H) is a measure of their resistance to plastic deformation. As presented in Table 1, the modulus and hardness of inorganic SSEs are mostly determined by their phase structures. For example, the Young's modulus and hardness are in an descending order from perovskite (e.g., $Li_{0.33}La_{0.57}TiO_3$ (LLTO)), garnet (e.g., $Li_7La_3Zr_2O_{12}$ (LLZO)), NASICON (e.g., $Li_{1.5}Al_{0.5}Ge_{1.5}(PO_4)_3$ (LAGP), and $Li_{1.3}Al_{0.3}Ti_{1.7}(PO_4)_3$ (LATP)), phosphate (e.g., Li_3PO_4 (LiPON)), to thiophosphate (e.g., $Li_2S-P_2S_5$ (LPS) and $Li_{10}GeP_2S_{12}$ (LGPS)) structured SSEs, with the magnitude from 200 to 20 GPa and 10 to 2 GPa, respectively. Despite the modulus variation, most SSEs have a shear modulus (G) high enough to suppress the Li dendrite growth, i.e., at least twice higher than that of Li metal (~4 GPa) according to the Monroe−Newman model. However, experiments show that typical SSEs such as LLZO and LGPS fail to suppress dendrite growth as predicted; in contrast, dendrites grow even more easily in these SSEs than in liquid electrolytes.[190] This contradiction might be attributed to the enhanced mechanical strength of microsize Li filament and the softening in the SSE modulus because of grain boundaries (GBs) and defects. We will further discuss this in the later section.

https://doi.org/10.1021/acs.chemrev.2c00002
Chem. Rev. 2022, 122, 13043−13107

The modulus and hardness are closely correlated with the formability of SSEs themselves and their compatibility to the electrode materials, particularly for cathode materials. Most oxide-based SSEs with high modulus and hardness are exceedingly resistant to mechanical deformation and thus need high-temperature sintering to form the dense structure. This high-temperature sintering is usually uneconomical and may cause undesirable side reactions with electrode materials, which places significant challenges for cell fabrication and performance. In contrast, the compliant sulfide-based SSEs can be densified using room-temperature cold-pressing, making them more practically promising. Mechanical compatibility of SSEs with the cathode materials is another essential aspect that needs to be considered when assembling the ASSBs. Generally, the composite cathode in ASSBs consists of the SSEs, carbon black, and cathode materials. Co-sintering fabrication techniques can be used in principle to achieve high-density composite cathode but have not been practically adopted yet because they might cause side reactions or elemental diffusion between SSEs and cathode materials. The relatively conformable solid−solid contact between SSE and cathode materials is usually achieved by the high stack pressure at room temperature. Most currently used cathode materials have a high modulus and hardness,[204] meaning the deformation during the cold pressing is small. Therefore, the major deformation needed for the conformable solid−solid contact should be compensated by the SSEs. Those compliant sulfide-based SSEs such as LPS and LGPS can plastically deform during the pressing to form a relatively conformable contact around the cathode materials. In contrast, although oxide-based SSEs such as LLZO are more electrochemically stable with cathode materials, they are seldomly used as the ion-conducting medium in the composite cathode because of their poor formability.

The fracture toughness, representing the capability of a material to resist fracture, is another important mechanical property of SSEs determining the battery performance. SSEs with higher fracture toughness will be more resistant to the fracture caused by Li dendrite penetration, thereby presenting a better capability to prevent the dendrite-induced shorting of ASSBs. As shown in Table 1, the fracture toughness of most SSEs is within the range from 0.2 to 1.2 MPa·m$^{1/2}$, near the low end of the fracture toughness range for ceramic materials (0.5 to 5 MPa·m$^{1/2}$), suggesting the highly brittle nature of the SSEs. Moreover, the fracture toughness of the GBs in polycrystalline SSEs can be significantly lower than the bulk grain owing to the local defects aggregated. As a result, many polycrystalline SSEs such as LLZO often show low resistance to the Li dendrite penetration, although their modulus is one order higher than that of Li metal. Therefore, we suggest more attention be paid to toughening the brittle SSEs to prevent SSE cracking and dendrite growth. The toughening strategies frequently used in the traditional ceramic industry, such as fiber reinforcement and transformation toughening, could be possible solutions for SSE toughening.[194]

In addition to the fracture resistance of SSEs, the driving force for crack propagation also needs to be revisited to address the issue of dendrite growth in ASSBs. As reported by Porz et al.,[205] Li will preferentially deposit in the surface cracks and voids in SSEs during the plating, which inevitably causes a field of tensile stress at the crack tip to drive crack propagation. Based on linear elastic fracture mechanics, this crack driving force, i.e., energy release rate, is directly related to the mechanical properties of Li metal, particularly to its yield strength. Therefore, in order to understand the Li plating-induced cracking in SSEs, it is beneficial to provide a retrospect of the mechanical properties of Li metal.

The early exploration of the mechanical behavior of Li metal can be traced back to the 1950s, at which Hull and Rosenberg investigated the deformation of Li metal using tensile experiments.[206] Soon after, a series of works on the plastic and creep behavior of Li metal, along with other alkali metals, were reported by Gorgas et al. and Pichl et al.[207,208] The first systematically measurement of mechanical properties, including Young's modulus and yield strength of Li metal was reported by Schultz et al.[209] Owing to the reviving of Li metal anode for high-energy batteries, several groups start revisiting the mechanical behavior of the Li metal using either conventional tensile/compressive test or advanced nano-indentation test.[200,201,210] As shown in Table 1, the Young's modulus of bulk Li metal can range from 1.9 to 7.8 GPa at room temperature, depending on the grain size and crystal plane orientation.[207,210] The temperature-dependent elastic and visco-plastic properties of Li metal were also extensively reported but not listed here.[200,206,207] It is generally accepted that at high temperatures, the creep of Li metal would dominate its visco-plastic response, while at low temperatures, Li metal shows a significant strain hardening.

Different from Young's modulus, the yield strength of Li metal shows a large discrepancy ranging across two orders from 1.6 to 244 MPa, which mainly arises from the strong dependence of Li strength on the tested length scale and time scale. Specifically, the yield strength of Li metal increases significantly with decreasing length scale from bulk to nanoscale, following the well-adopted notion that "'smaller is stronger"' in conventional metals.[211] Fincher et al. utilized a combination of bulk tensile testing and nanoindentation to characterize the yield strength of Li metal across different length scales.[201] They found that the yield strength of Li metal can decrease from about 15 to 2.5 MPa when the characteristic size for the nanoindentation measurement increases from 250 nm to 10 μm. Their bulk tensile testing further indicates that the bulk yield strength of Li metal can be even lower (0.57 MPa for the strain rate of 5×10^{-4} s^{-1}). It should be emphasized here that the yield strength of nanoscale Li whiskers seems to be much higher than expected. He et al. and Zhang et al. utilized a similar setup (AFM with an environmental TEM, AFM-ETEM) to in situ grow individual Li whiskers and then measure their yield strength.[202,203] They both found the yield strength of Li whiskers can reach above 100 MPa (as high as 244 MPa), 1−2 orders higher than the widely used values for predicting the propagation of cracks and Li dendrites in SSEs. Therefore, many previous chemo-mechanical analyses on the crack and dendrite propagation through SSEs might need to be revisited.

2.4.2. ASSBs Degradation. ASSBs have attracted tremendous attention as the most promising solution for enabling safe and high-energy batteries. Currently, the bottleneck for the practical adoption of ASSBs is no longer the slow kinetics of Li-ion diffusion in the electrolyte, but the low capacity retention, poor rate capability, and short lifetime caused by the complex chemomechanical degradations in ASSBs.[38,188,189] In this section, we will present the distinctive features of typical degradations in ASSBs and summarize the recent work on identifying, understanding, and mediating these degradations. We primarily focus on the ASSBs with inorganic

https://doi.org/10.1021/acs.chemrev.2c00002
Chem. Rev. 2022, 122, 13043−13107

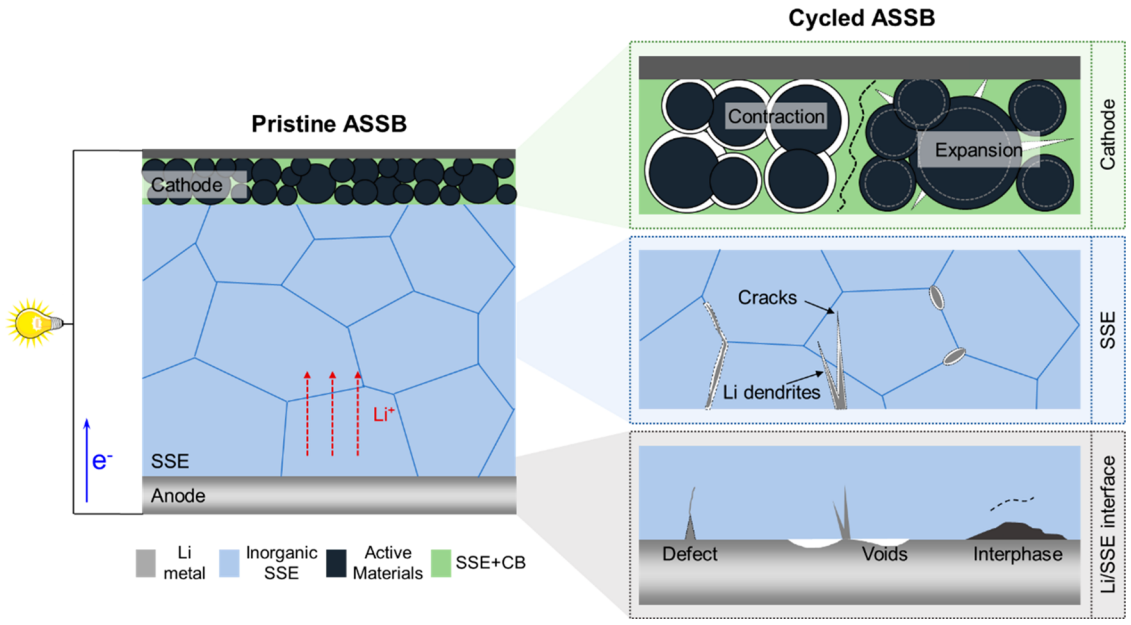

Figure 9. Schematic of ASSLBs with a composite cathode, inorganic SSE and Li metal anode. During cycling, chemomechanical failure can occur at the Li/SSE interface, in the bulk SSE, and the composite cathode.

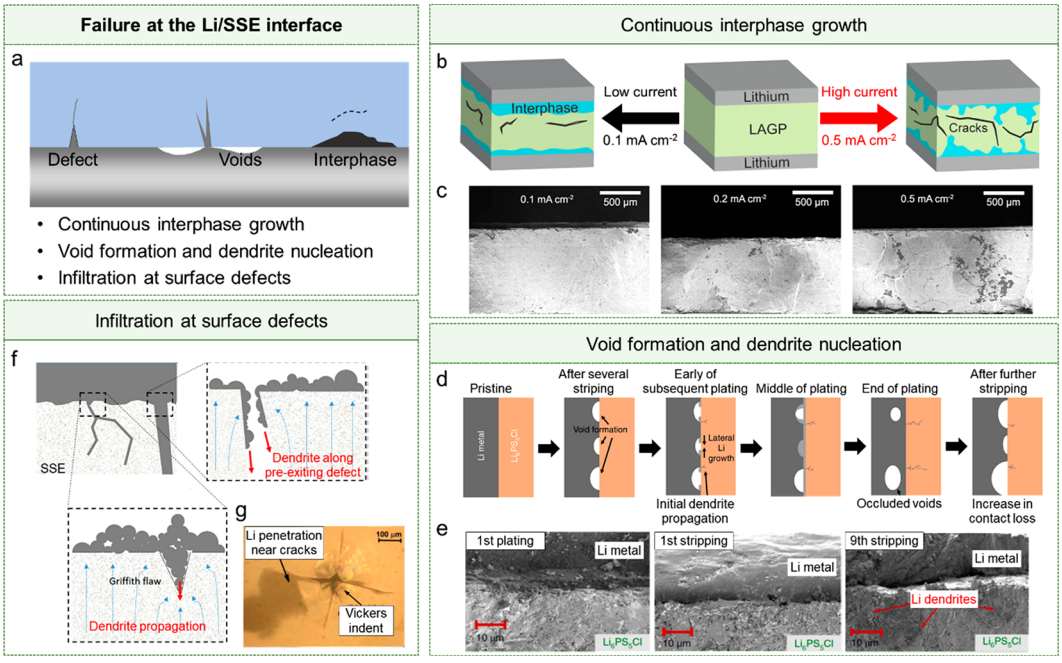

Figure 10. (a) Schematic of the failure mechanisms at the Li/SSE interface. (b) Schematic and (c) cross-sectional SEM images of continuous interphase growth at the Li/LAGP interface. Reproduced from ref 214. Copyright 2019 American Chemical Society. (d) Schematic and (e) cross-sectional SEM images of the void formation and dendrite nucleation at Li/Li_6PS_5Cl interface cycled at a high current density. Reproduced from ref 47. Copyright 2019 Springer Nature. (f) Schematic of Li infiltration into the preexisting surficial defects in SSEs and propagation across the defects. Reproduced from ref 189. Copyright 2017 IOP Publishing. (g) Li nucleates and grows into single-crystal garnet from the corner-cracks produced by Vickers indents. Reproduced from ref 216. Copyright 2018 IOP Publishing.

SSEs not only because of their state-of-the-art ionic conductivity and excellent electrochemical stability but also because of their stiff nature that promotes various types of chemomechanical degradations, including but not limited to the contact loss, void formation, and fracture. The major degradations in ASSBs (Figure 9) can be classified into three categories based on the locations where they occur, i.e., at the Li/SSE interface, in the SSEs, and in the composite cathode.

2.4.2.1. At the Li/SSE Interface. One of the reasons behind the growing interest in ASSBs is the potential adoption of the high-capacity Li metal anode. However, several recent works demonstrate that directly pairing the Li metal anode with SSEs might generate various morphological degradations at their interfaces, such as interphase growth, void formation, and dendrite nucleation (Figure 10a).[47,212−216] These degradations are considered to be the origin of the eventually short-circuit of

https://doi.org/10.1021/acs.chemrev.2c00002
Chem. Rev. 2022, 122, 13043−13107

ASSBs, and thus need to be investigated and understood before practical and stable ASSBs can be realized.

The interphase growth between Li metal and SSEs is one of the major chemomechanical degradations in ASSBs. Because many SSEs such as NASICON-type SSEs (e.g., LAGP and LATP) are thermodynamically unstable to Li metal, directly contacting them with Li metal will reduce their surface to a layer of a mixed conductor, called "interphase". As this newly formed interphase is partially electronically conductive, the reaction can further propagate into the bulk SSE and gradually reduce it, leading to continual interphase growth. Once the SSE is completely reduced to become a mixed electron and ion conductor, short-circuit of ASSBs happens. Even worse, in situ TEM observations revealed that the transformation from a pristine SSE to the reacted interphase is accompanied by a large volume expansion (~38% for the interphase formed at the Li/LAGP interface), which can drive the cracks to initiate from the Li/SSE interface and propagate toward the bulk SSE, eventually leading to the catastrophic fracture of the SSE.[47] This reaction-growth-crack degradation process usually shows a current-dependent nature where high current density causes more nonuniform growth of the interphase and thus a more severe SSE fracture (Figure 10b,c). Similar to the NASICON-type SSEs, the sulfide-based SSEs such as Li_6PS_5Cl can also be reduced by Li metal to form the interphase. However, their reduced products are electronically insulative or have an electronic conductivity low enough to limit the continual growth of the interphase. Therefore, even though the SSE itself is not thermodynamically stable to Li metal, a stable interphase with a thickness of a few nanometers, sometimes called metastable interphase, could still form at the Li/SSE interface, which is beneficial for the mechanical integrity of SSE and the stability of ASSBs.[217]

Unlike NASICON-type and sulfide-based SSEs, some SSEs such as garnet-type SSEs (i.e., LLZO) have been proved to be chemically stable with Li metal, but their interface to the Li metal anode could still deteriorate because of the continual Li plating/stripping.[45,218] More specifically, during Li striping, Li atoms at the Li/SSE interface dissolve into the SSE, and meanwhile, the Li atom diffusion in Li metal replenishes the Li loss from the interface. Usually, the rate of Li striping exceeds the kinetic limit of Li atom diffusion, causing the nucleation and growth of Kirkendall voids at the interface.[215] The morphological degradation becomes even worse during the subsequent plating. Li prefers to deposit at the regions still in contact with the SSE instead of the detached areas, thereby developing a nonuniform Li deposition that further promotes the Li dendrite nucleation and the short-circuit of ASSBs (Figure 10d,e). This interfacial morphological degradation dominated by the void formation and subsequently Li dendrite nucleation occurs not only in garnet-type SSE but also in different SSE systems such as sulfide-based SSEs, as recently observed by advanced X-ray computed tomography techniques.[47,217]

The stack pressure applied on ASSBs is revealed to effectively mediate the void formation at the Li/SSE interface. Li metal near the interface can mechanically deform by the pressure, offering another route to replenish the Li loss and thus preventing the void formation. In fact, this void suppression strategy has been reported for both oxide-based and sulfide-based ASSBs where the "critical stack pressure" needs to be particularly considered. Specifically, the applied pressure on ASSBs cycled at a certain current density must be higher than the "critical stack pressure" in order to effectively suppress the void formation at the interface. Otherwise, the mechanical deformation will be slower than the electrochemical deformation caused by Li stripping, leading to an insufficient Li replenishment to the interface. In this case, the voids still form at the interface, followed by the nucleation and growth of Li dendrites. It should be noticed that the "critical stack pressure" can reach several MPa for the ASSBs cycled under relatively low current density (e.g., 7.5 MPa for the Li/garnet/Li cell cycled under 0.2 mA cm^{-2}),[215] which might place new challenges for the application of ASSBs in the electric vehicles. In this context, developing sophisticated strategies of cell integration that enable the ASSBs to operate at the low stack pressures and high current densities will be urgently needed for the practical applications of ASSBs.[219,220]

The defects on the surface of SSEs such as pre-existing microcracks or compositional heterogeneities also play a critical role in determining the Li dendrite nucleation at the Li/SSE interface. As theoretically predicted and experimentally confirmed,[216,221] a pre-existing crack on the SSE surface can be easily filled by Li deposition because of the electric field amplification (as indicated by the blue arrows in Figure 10f). Further insertion of deposited Li into the crack will induce a high hydrostatic pressure at the crack tip, promoting crack propagation toward the bulk SSEs. To demonstrate the underlying correlation between preexisting cracks and Li dendrite propagation, Swamy et al. performed an operando optical observation of Li electrodeposition on a single-crystal LLZO.[216] The absence of GB excludes the side effects from the GBs, so the preference of Li dendrite nucleation and growth is solely regulated by the artificially introduced surface cracks with known size. They confirmed that electric field amplification can drive Li dendrite penetration into the surface cracks on the SSE surface (i.e., corner-cracks of Vickers indent, Figure 10g) and cause brittle cracking in the SSE.

The impurity precipitates on the SSE surface also cause the nonuniform Li deposition and thus trigger the Li dendrite nucleation.[222] Take the widely studied garnet-type LLZO as an example: LLZO can be easily contaminated by the moisture and CO_2 in the air to form the surface impurities such as LiOH and Li_2CO_3. They are considered Li-ion insulators that impede the local Li deposition at the Li/SSE interface. Therefore, other regions without surface impurities will experience higher local current density, and therefore Li nucleation will be promoted there. Meanwhile, the lithiophobic nature of these surface impurities often instigates the formation of residual voids between Li metal and SSE, leading to the huge interfacial resistance and nonuniform Li deposition as aforementioned.[223]

2.4.2.2. In the SSEs. Compared with liquid electrolytes or polymer SSEs, inorganics SSEs own the advantage of high shear modulus (i.e., at least twice that of Li metal), which can theoretically suppress the uncontrollable Li dendrite growth from the Li metal anode.[224] However, Li dendrites have been found to grow through most oxide- and sulfide-based SSEs at a current density and capacity even lower than in liquid electrolytes or polymer SSEs. This discrepancy is mainly originated from the fact that the widely cited Monroe–Newman criterion is intended for polymer SSEs without any inhomogeneities or defects, but not applicable to polycrystalline materials like most inorganic SSEs. The polycrystalline SSEs usually contain extensive inhomogeneities or defects, such as GBs, voids, and microcracks, making them more vulnerable to Li dendrite penetration.[50,224−226] Currently, the

https://doi.org/10.1021/acs.chemrev.2c00002
Chem. Rev. 2022, 122, 13043−13107

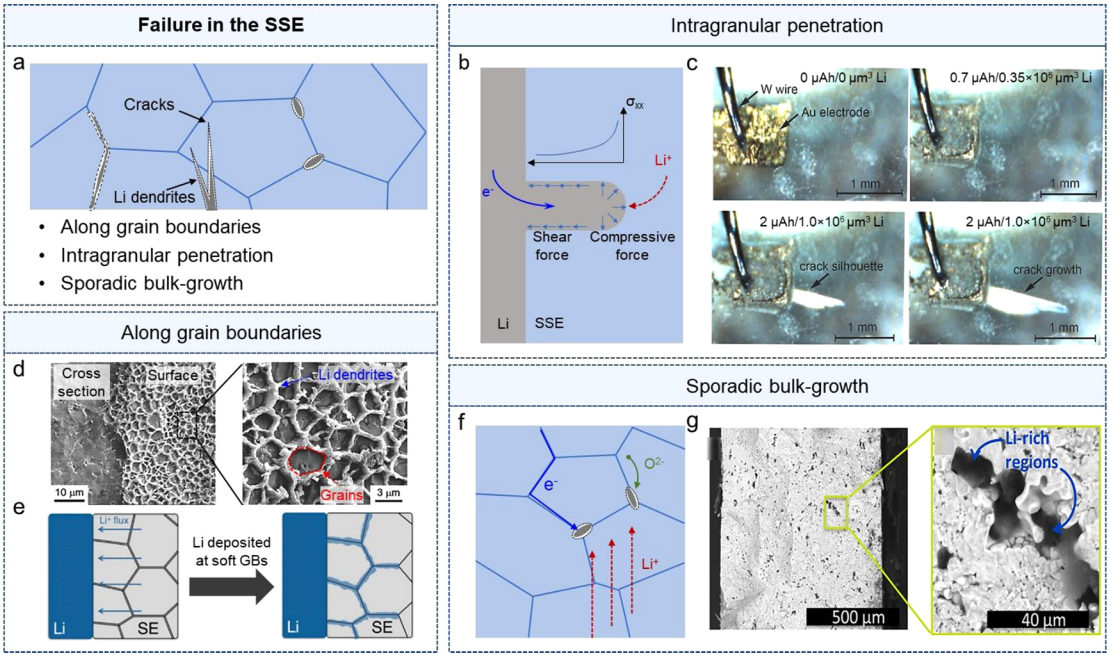

Figure 11. (a) Schematic of the failure mechanisms in the SSE. (b) Schematic of the penetration of Li filament into the SSE. The arrows at the rounded end of the filament depict the applied pressure from the Li metal and the arrows along the side show shear tractions because of friction along this interface. (c) Optical microscopy images of the Li electrodeposition on a single-crystal LLZO. Reproduced from ref 205. Copyright 2017 Wiley-VCH GmbH. (d) SEM image showing web-structure Li-metal plating along the GBs in the bulk LLZO. Reproduced from ref 50. Copyright 2017 Elsevier. (e) Li preferentially accumulates in the softer grain boundaries of SSEs. Reproduced from ref 227. Copyright 2018 American Chemical Society. (f) Schematic of sporadic bulk-plating mechanism in the SSE. Li-ions in SSE are reduced by recombination with an electron from the oxygen network or the residual electronic conductivity, forming Li dendrites and clusters in the bulk SSE. (g) SEM images showing the presence of Li metal in the pores of LLZO. Reproduced from ref 228. Copyright 2017 American Chemical Society.

dominating mechanism for the Li dendrite propagation through polycrystalline SSEs is still under debate, and elucidating this mechanism seems to be more complicated than that in the polymer SSEs because of the exitance of GBs, random voids, and cracks in SSEs. Several hypotheses have been proposed to illustrate the possible mechanisms for counterintuitive dendrite propagation in inorganic SSEs (Figure 11a).

The prevailing dendrite propagation mechanism in inorganic SSEs is related to the Griffith-like crack extension through brittle materials (Figure 11b). As suggested by the prior work of Porz et al., Li-plating in pre-existing cracks and voids in the SSEs or near the Li/SSE interface builds up the hydrostatic stress that can easily reach the GPa level at the crack tip, depending on the amount of overpotential applied and the crack size.[205] According to the Griffith theory,[229] once the crack driving force at the crack tip exceeds the fracture toughness of SSEs, the crack starts to propagate, opening a channel for further Li infiltration into the SSEs. This process will repeat until the crack reaches the cathode, and subsequent Li infiltration along the crack will cause the eventual short-circuit of the battery. Related chemomechanical model and experimental evidence for this mechanism can be found in a series of works by Chiang's group (Figure 11c).[188,205,216] Recently, Klinsmann et al. proposed a more comprehensive model by considering the counterbalance of the compressive stress developed in the crack on the Li infiltration.[221] They postulated that the high compressive stress could potentially block the reaction for Li deposition and thus suppress the Li infiltration into the crack, making the crack non-propagating. This situation only occurs for cracks shorter than a critical length. Therefore, to avoid the propagation of cracks and Li dendrites in SSEs, it is wise to minimize the size of pre-existing cracks either via delicate polishing or artificial coating.

Compared with the single-crystal SSEs, polycrystalline SSEs are far more practical in terms of their easy processability (i.e., simply through powder sintering).[226,230] However, the GBs in polycrystalline SSEs have been reported to enormously facilitate the Li dendrite propagation in SSEs, leading to the web-structure Li plating along the GBs in the SSE (Figure 11d).[50,225] The significant reduction in elastic modulus of the GBs was proposed as a potential mechanism for dendrite propagation along GBs (Figure 11e). The variations in atomic structure and vicinity density of the GB plane led to a lower local elastic modulus. For example, molecular dynamics (MD) simulations have revealed that the modulus of GBs in polycrystalline LLZO can be as much as 50% smaller than that in the bulk grain.[227,223] In this scenario, metallic Li is more likely to nucleate at the softer regions near GBs. Nevertheless, the lower ionic conductivity of the GBs, compared with the bulk grain, is considered another main reason for the Li dendrite propagation. Both MD simulations and experiments have confirmed that Li-ion migration activation energy for all GBs in the LLZO is consistently higher relative to its bulk grain, and therefore Li-ion mobility through the GBs can be largely reduced. This higher ionic resistance of the GBs near the Li/SSE interface can lower the local electrical potential to become negative, instigating the Li plating and dendrite nucleation at the GBs.[231] In addition to the described mechanisms, other inhomogeneities at the GBs, such as the segregation of doping elements and localized high electronic

https://doi.org/10.1021/acs.chemrev.2c00002
Chem. Rev. 2022, 122, 13043−13107

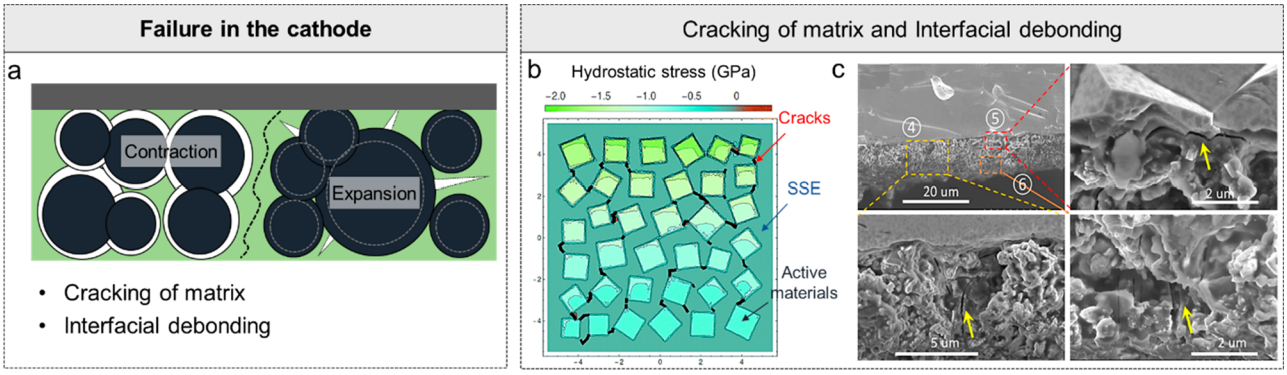

Figure 12. (a) Schematic of the failure mechanisms in the cathode. (b) Hydrostatic stress developed during the operation of a composite cathode containing SSE and active materials. The high stress caused by the mismatch strain between SSE and active materials can induce the interfacial debonding and the fracture of SSE. Reproduced from ref 46. Copyright 2017 Royal Society of Chemistry. (c) Cross-sectional SEM images of cathode/SSE composites showing the cracking occurs at the cathode/SSE interface and within the SSE. Reproduced from ref 48. Copyright 2019 American Chemical Society.

conductivity, have also been proven to facilitate the Li dendrite propagation along the GBs.[232,233]

The mentioned hypotheses for Li dendrite propagation are usually classified into the continuous root-growth mechanism, suggesting Li initially nucleates at the Li/SSE interface and then penetrates toward the cathode through the SSEs. An alternating mechanism reported recently is the sporadic bulk-plating mechanism. It shows that the initial Li plating can occur in the bulk SSE (i.e., sporadic Li filaments) instead of at the Li/SSE interface. As Li plating proceeds, the eventual interconnection of these filaments results in the short-circuit of ASSBs. The sporadic Li plating requires the SSEs with an electronic conductivity high enough to allow electrons to pass into the bulk SSE, and thus the reduction of Li ions could occur inside the bulk SSE (Figure 11f). This is particularly true for the polycrystalline SSEs such as LLZO and LPS, as their GBs usually exhibit a relatively high electronic conductivity.[232,234] Moreover, microstructure and composition heterogeneities in SSEs such as voids and impurities might trap excess electrons and negative charges (e.g., O^{2-}), further facilitating the sporadic Li plating.[235] Direct evidence for the sporadic Li plating can be found in the work of Aguesse et al., in which they performed a post-mortem analysis on the cycled LLZO and observed the existence of island-like metallic Li (indicated as the black spots in Figure 11g) inside the pore space of LLZO.[228] Liu et al. recently utilized an in situ TEM setup to further confirm that Li ions can be easily reduced in the void at the junction of GBs and forms local Li filaments.[225] All these discoveries suggest that the minimizing electronic conductivity of the GBs must be a primary concern for the SSE optimization.

2.4.2.3. In the Composite Cathode. Different from the Li metal anode, the cathode in ASSBs is usually a composite consisting of both SSE and cathode materials (e.g., NMC). Therefore, building a stable cathode/SSE interface will be essential for the realization of high-performance ASSBs, but it is also challenging because of the electrochemical and mechanical incompatibility between SSE and cathode materials. Side reactions at the cathode/SSE interface are a major type of electrochemical degradation. There are already plenty of review articles on understanding the electrochemical stability at the cathode/SSE interface,[218,236] thus we will not further specify it here. Instead, we will primarily focus on the mechanical degradation at the interface, which encompasses the poor initial contact and the subsequent contact loss during battery cycling.

Unlike the liquid electrolytes that can form conformable wetting on cathode materials, the SSEs usually form a poor solid−solid contact with the cathode materials because of their stiff nature. Therefore, a high stack pressure of tens to hundreds of MPas is required to assemble the composite cathode with relatively conformable particle contact and low porosity. However, this strategy can only be applied to those more compliant sulfide-based SSEs (e.g., LPS), but it is not applicable to the oxide-based SSEs (e.g., LLZO) mainly because of their poor formability, as discussed in Section 2.4.1. Indeed, the challenges for integrating LLZO with cathode materials have become a major stumbling block limiting the practical adoption of LLZO in ASSBs, although it shows the state-of-the-art ionic conductivity and electrochemical stability.[45] In addition, even though the relatively conformal interface can be initially built under a high stack pressure, interfacial degradation is still likely to occur upon battery cycling because of the mismatched volume strains between SSE and cathode materials. It is now well-known that most cathode materials undergo a volume change upon cycling that ranges from a few percent to tens of percent, while SSEs should not participate in the electrochemical reaction to undergo the volume change. This mismatch volume change between SSE and cathode materials will induce the complex stress state in the cathode material, in the SSE, and at the cathode/SSE interface, generating extensive microcracks in the composite cathode (Figure 12a). Bucci et al. numerically revealed that the crack propagation in the composite cathode highly depends on the material properties of SSEs (Figure 12b).[46] For example, the sulfide-based SSEs with local modulus and hardness can easily deform to accommodate the volume change of cathode materials, which effectively mediates the debonding at the cathode/SSE interface. However, the low fracture toughness of sulfide-based SSEs (e.g., 0.23 $MPa{\cdot}m^{1/2}$ for LPS, Table 1) determines that they will be more vulnerable to the bulk fracture, i.e., crack initiation and propagation within the SSEs, instead of at the interface. Experimental investigations on the mechanical degradation of the composite cathode can be found in the work of Koerver et al. and Wang et al. (Figure 12c).[48,237] They found that the formation of both interfacial and bulk cracks in composite cathode will lead to the increased cell impedance because of

https://doi.org/10.1021/acs.chemrev.2c00002
Chem. Rev. 2022, 122, 13043−13107

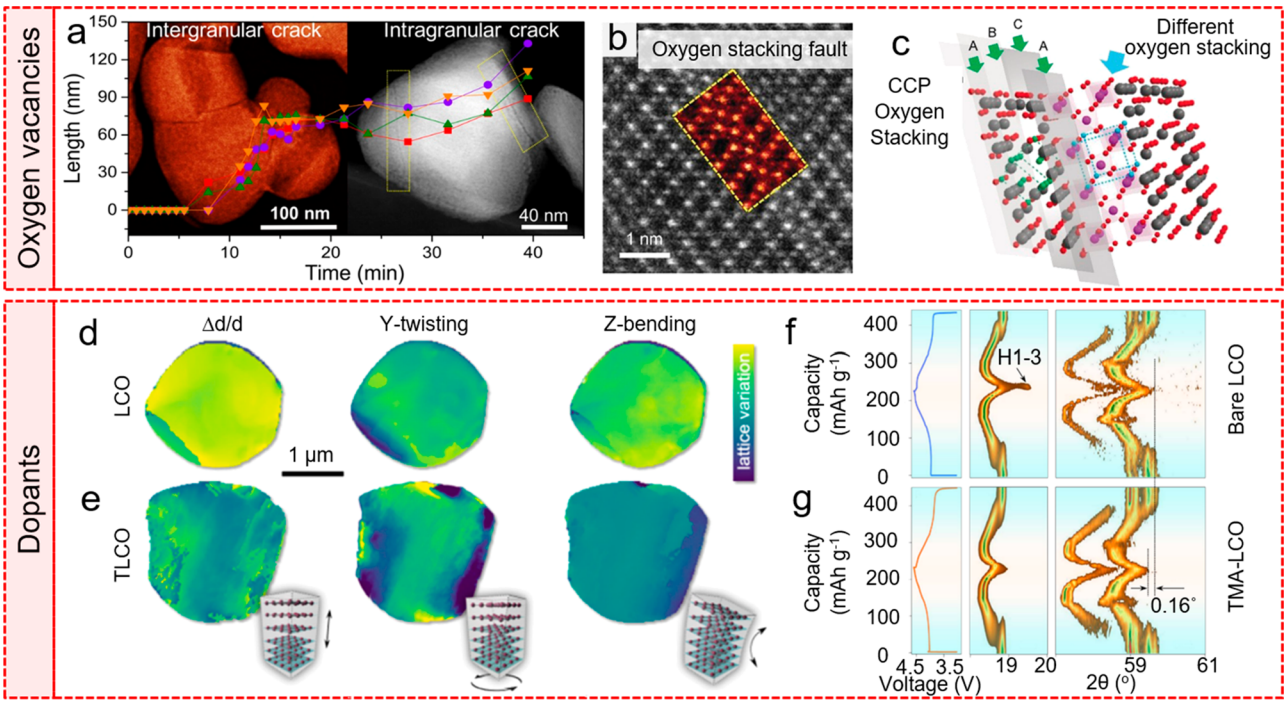

Figure 13. Role of one-dimensional atomic defects on the diffusivity and reactivity of the active materials. Oxygen vacancies in battery materials can induce (a) intragranular crack formation[78] and (b, c) phase transformations.[243] Reproduced from refs 78 and 243. Copyright 2018 American Chemical Society. Copyright 2019 Wiley-VCH GmbH. (d, e) Doping induced lattice deformation[94] can mitigate the detrimental phase transformation (f, g) in layered oxides battery materials at high voltages.[245] Reproduced from refs 94 and 245. Copyright 2020 Elsevier. Copyright 2019 Springer Nature.

the reduced contact area for Li-ion transport between the cathode materials and the electrolyte, which will further slow the reaction kinetics, lower the CE, and hinder rate performance of ASSBs.

3. IMPACT ON ELECTROCHEMICAL PERFORMANCE

In this section, we will focus on how mechanical stresses and degradation, including those arising from atomic-scale defects, macro-scale deformation and fracture of SEI, particle, and solid electrolytes, reflect on the electrochemical activity that regulates performance metrics (power fade, capacity fade, and Coulombic efficiency).

3.1. Atomic Defects

Antisite defects can directly change the chemical environment of the defective region, impeding ion diffusion and deteriorating battery performance in most cases.[68,238−240] The impeded ion diffusion can be attributed to two reasons: (1) antisite defects act as obstructions along the ion diffusion pathways;[241] (2) antisite defects cause lattice shrinkage and thus increase ionic diffusion energy barriers.[242] OVs are intrinsic defects in many battery materials, and their presence can dramatically alter the chemical and mechanical stability of battery materials. For example, the crack formations because of the OVs' condensation under high state-of-charge or thermal abuse conditions can cause side reactions between the newly generated electrode surface and the electrolyte, leading to resistance build-up, gas evolution, and irreversible capacity fading (Figure 13a).[78] Moreover, OVs also contribute to many undesired phase transformations (Figure 13b,c),[243] which generate redox-inactive phases and cause irreversible capacity loss. To avoid these unfavorable phase transformations, many researchers proposed foreign element doping solutions. For example, $LiCoO_2$, a widely used cathode material but of a low volumetric energy density, experiences a detrimental phase change (O3 to H1−3 phases, Figure 13f) at high voltages. Further pushing the performance of $LiCoO_2$ by increasing the upper cutoff voltage is difficult because of the poor structural stability at highly delithiated states. Hong et al. reported that trace amounts of Ti (∼0.1 wt %) doping leads to lattice deformations such as *d*-spacing change, Y-twisting, and Z-bending (Figure 13d,e).[94] These lattice deformations induce lattice strains in the doped $LiCoO_2$, which contribute to the lattice robustness and suppress the detrimental phase change (Figure 13g).[94,244] The improved structural stability enables stable cycling of $LiCoO_2$ with an upper cutoff voltage of 4.6 V, dramatically enhancing its volumetric density.

Dislocations are mostly detrimental to the electrochemical performance of batteries in two aspects. First, dislocations induce harmful phase transformations. The newly generated phases are usually redox inactive, which reduces the battery capacity substantially. Moreover, the new phases may decrease electronic and ionic conductivities, further impairing battery performance.[9,84,246] Second, dislocations-aided crack formations (Figure 14a,b) generate fresh surfaces for undesired reactions at the electrode−electrolyte interface, which considerably increases the resistance.[9,71,84,246] Although dislocations are primarily detrimental to the long-term cycling performance, a few studies showed that one could potentially use dislocations to guide or promote redox reactions in batteries. Dislocations likely act as nucleation points for redox reactions such as in spinel[82] and layered oxides.[83] It was also found that layered oxide single grains with high dislocation densities tend to have a deeper charging state than perfect grains with fewer lattice distortions (Figure 14c−f). Such findings suggest that engineering the dislocation density and

https://doi.org/10.1021/acs.chemrev.2c00002
Chem. Rev. 2022, 122, 13043−13107

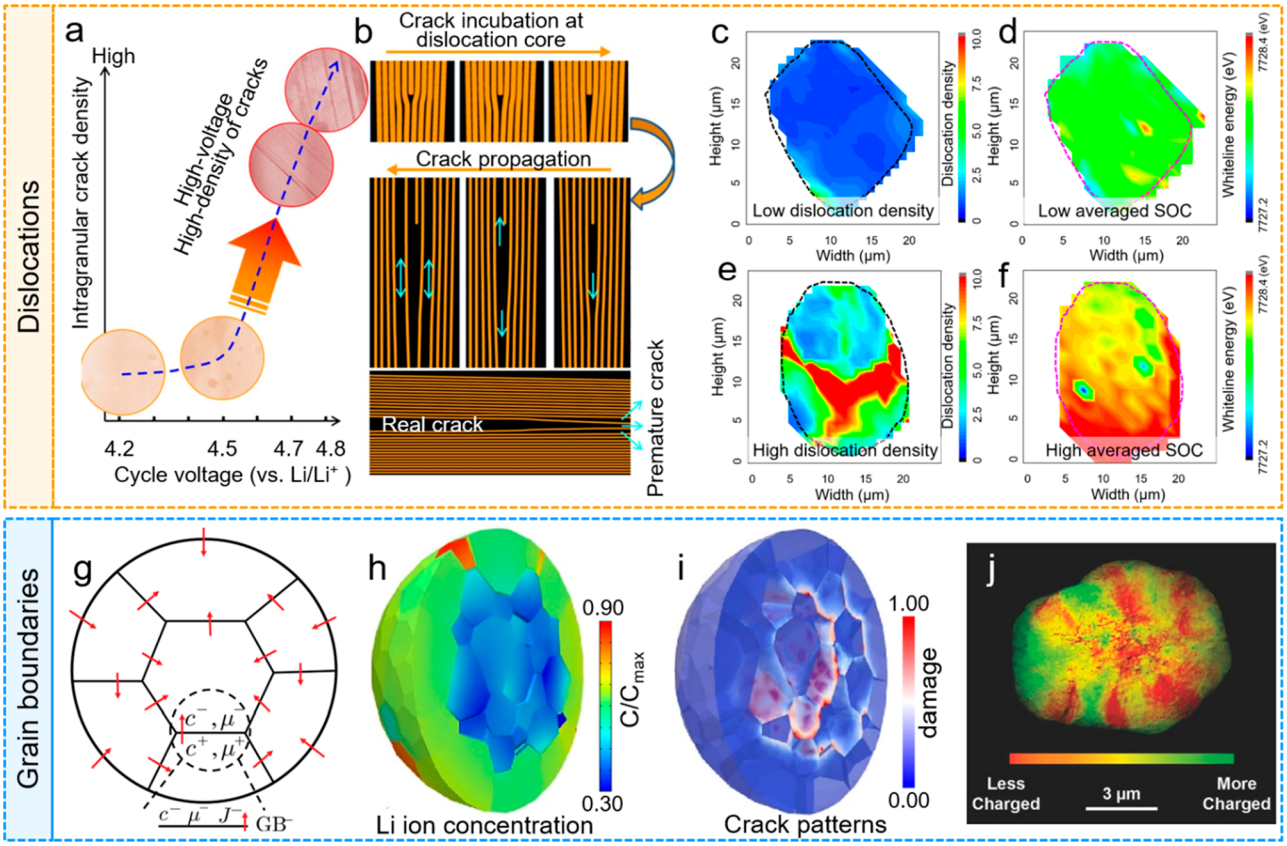

Figure 14. (a) Voltage-dependent intragranular crack formation in battery materials. (b) Schemes showing the dislocation-assisted crack incubation and propagation processes. Reproduced from ref 9. Copyright 2017 Springer Nature. (c–f) High geometrically necessary dislocation density facilitates redox reactions in battery materials at the early charging stage. Reproduced from ref 250. Copyright 2020 Wiley-VCH GmbH. (g) Illustration of ion diffusions along grain boundaries. (h) Li-ion concentration and (i) crack formations induced by the ion diffusion along grain boundaries. Reproduced from ref 251. Copyright 2020 Elsevier. (j) State-of-charge distributions of a cathode particle, where red represents less charged domains and green represents more charged domains. Reproduced from ref 252. Copyright 2016 Wiley-VCH GmbH.

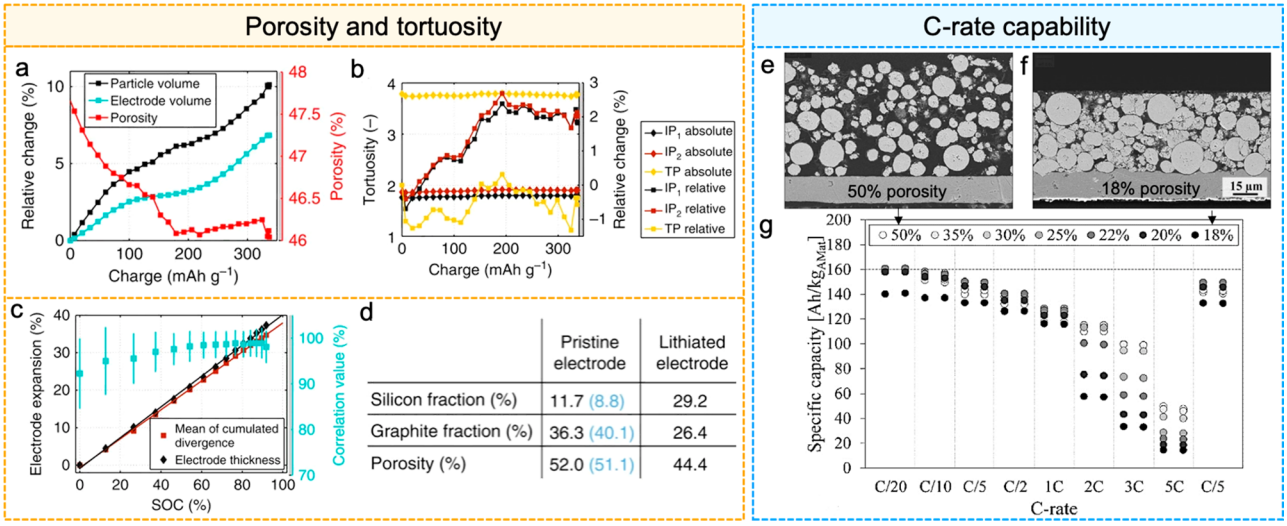

Figure 15. Effect of deformation and compaction on electrochemical performance. (a) The change in particle volume, electrode volume, and electrode porosity as a function of charge of a graphite electrode. (b) The absolute in-plane and transverse plane tortuosities and the respective relative change as a function of charge of graphite electrode. (c) The expansion of SiC composite electrode and the spatial average of correlation value at different SOC. (d) Volume fractions of Si, graphite, and pore in the pristine and lithiated state (a–d). Reproduced from ref 67. Copyright 2016 Springer Nature. (e, f) SEM cross section views of NMC cathode with 50% porosity (e) and 18% porosity (f). (g) Specific capacity at different porosities as a function of C-rate for NMC cathode (e–g). Reproduced from ref 256. Copyright 2018 Elsevier.

distributions may facilitate the redox reactions in batteries to enhance their performance.

Grain boundaries are widely dispersed in batteries and largely regulate ionic and electronic transport (Figure 14g), yet

https://doi.org/10.1021/acs.chemrev.2c00002
Chem. Rev. 2022, 122, 13043−13107

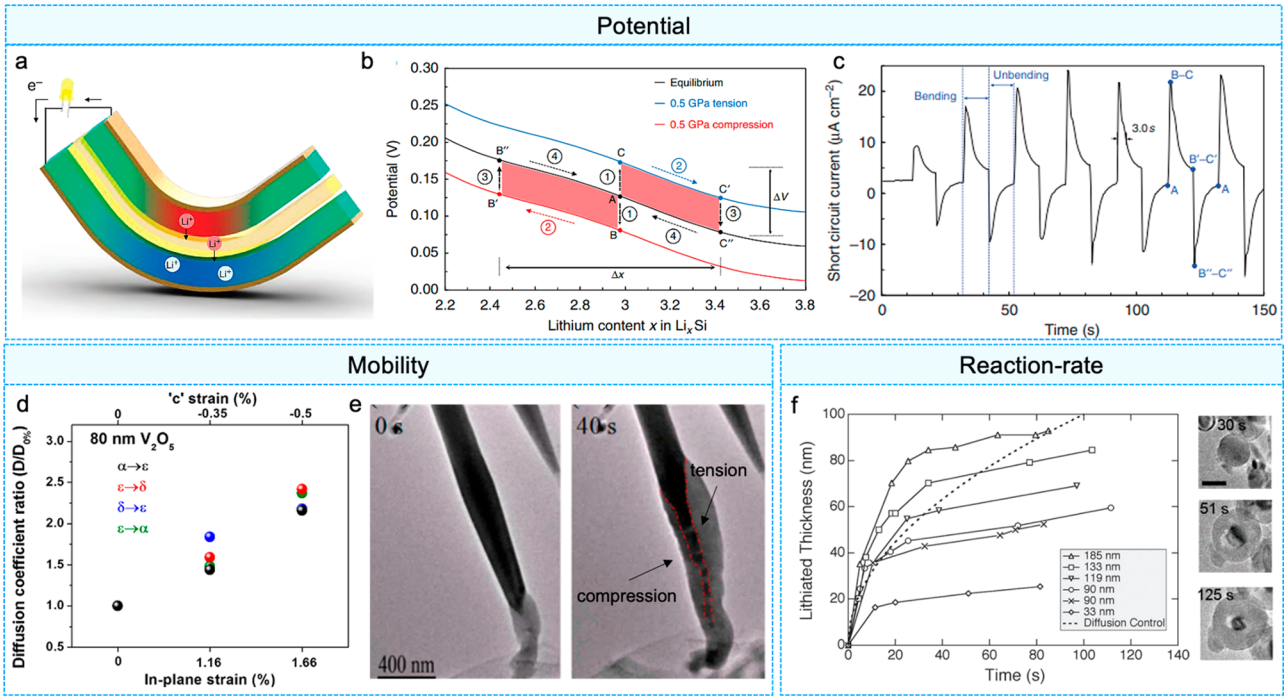

Figure 16. Examples of stress modulated electrochemistry. (a) Schematic of a symmetric thin film battery, and the corresponding (b) voltage shift and (c) electrical current driven by the stress gradient under bending. Reproduced from ref 257. Copyright 2016 Springer Nature. (d) Variation on the diffusion coefficient of Li in V_2O_5 because of the change in the activation energy under different applied strains. Reproduced from ref 260. Copyright 2017 American Chemical Society. (e) Breaking of the lithiation symmetry in Ge nanowires via bending as a result of faster diffusion under tensile stress and slower diffusion under compression. Reproduced from ref 261. Copyright 2014 American Chemical Society. (f) Retardation of the reaction front propagation because of the stress difference between the reacted and unreacted phases of crystalline Si. Reproduced from ref 262. Copyright 2012 Wiley-VCH GmbH.

the understanding of grain boundaries in redox-active materials is limited. Ion transport along grain boundaries can cause inhomogeneous state-of-charge distributions (Figure 14h), which was observed in experiments of many polycrystalline active materials (Figure 14j).[247,248] The inhomogeneous charge distribution results in significant mismatch strains and lead to crack formations as theoretically predicted (Figure 14i) and experimentally observed[249] in various systems.

3.2. Deformation

The deformation resulting from chemical reactions can lead to stresses and mechanical degradation, which are intertwined with electrochemical performance. Deformation, however, also has a direct effect on ion transport via the change in the electrode porosity. Many factors are involved in this regulation, including how much the electrode as a whole is allowed to expand given the physical constraint of the dense layered structure of multiple cells within the battery casing, and the mismatched volume change between cathode and anode layers.

Pietsch et al.[67] used digital volume correlation on tomography data to study the microstructural evolution in graphite anodes during lithiation. The cells were prepared using prelithiated graphite−graphite electrodes separated by a glass fiber separator and enclosed within a polyether ether ketone housing tube. During the first half of the first lithiation (up to ∼160 mAh g^{-1}, Figure 15a), the particles (black curve) expand at a greater rate (greater slope) than the overall electrode (cyan curve), causing a decrease in porosity (red curve). That is, a portion of the volume expansion of the particles is accommodated by the pores (inward expansion). The porosity then remains constant over the second half of lithiation as the particles and the electrode expand at the same rate. They also found that because of the predominant expansion of the graphite platelets along their *c*-axis (aligned parallel to the current collector), the in-plane (IP) tortuosity increased in the first half of lithiation and remained about constant during the latter half, while the transverse plane (normal to the current collector, TP) tortuosity remained virtually constant throughout (Figure 15b). The effect of deformation is more pronounced in the case of high-capacity electrode materials such as Si. Pietsch et al.[67] also tested a composite electrode composed of 1:3 weight ratio of Si to graphite and found that the composite electrode expansion (close to 35%) is much larger than that of the pure graphite electrode and varies linearly with the state of charge (Figure 15c), which suggests that the large electrode expansion is predominantly because of the expansion of Si. The volumetric expansion of Si reduces the porosity of the electrode by 8% (Figure 15d). Volume expansion driven porosity reduction is more significant in nano Si electrodes, as reported by Radvanyi et al.[253] They used several characterization techniques to show that, because of the drastic reduction of the micrometric porosity over 100 cycles, large portions of the electrode were blocked from the Li^+ access, leading to rapid capacity loss. They estimated a reduction by 10 orders of magnitude in the effective diffusivity of Li^+ after 100 cycles. Furthermore, experiments conducted by Moon et al.[254] on Si−graphite composite electrodes showed that excessive expansion of Si caused sharp capacity degradation of graphite after 200 cycles.

To quantitatively study the effect of porosity variation on electrochemical performance, one can refer to the literature on electrode calendaring, where the electrode is intentionally

https://doi.org/10.1021/acs.chemrev.2c00002
Chem. Rev. 2022, 122, 13043−13107

compressed by externally applied forces. This process is commonly carried out for commercial electrodes primarily to increase the energy density. For example, Schmidt et al.[255] evaluated the cyclic performance of NMC111 electrodes compacted at different pressures (i.e., varying porosities). Figure 15e,f shows cross section tomography images of NMC cathodes at the pristine state and compacted by 1 GPa, with 50% and 18% porosities, respectively. Upon cycling the electrodes with different porosities, it is observed that even at a low C-rate of C/20, the highly compacted electrode achieved a significantly lower capacity than the uncompacted electrode because of the limitation of Li^+ diffusion in the electrolyte, Figure 15g. This difference widens with increasing C-rate (except at 5C, where the capacity of all electrodes drops substantially). Interestingly, for C-rates up to 5C, the capacity density initially increases with a reduction of porosity. The authors attribute this improvement mainly to the reduction in electrode volume, until a threshold of porosity is reached beyond which the capacity density drops as the competing effect of limited access of the liquid electrolyte to the active materials overshadows the volume reduction.[256] The increased contact area between active particles and conductive matrix in the moderately compacted electrode is also thought to have a role in the improved performance by lowering the electrical resistance at the particle−matrix interface. External compaction is widely used in the industry to improve the specific capacity and can improve the rate performance of batteries, but excessive pressure will result in detrimental effects on the Li transport through the porous network. In addition, the high loading of active materials and insufficient open space to accommodate volume expansion have consequences on structural stability because of particle−particle impingement, as discussed in Section 2.2.1.

3.3. Mechanical Stress

In Section 2.2, we discussed how mismatched strains arising from diffusion and phase transformation generate stresses in the active materials. Here, we discuss how these stresses in turn regulate reaction and diffusion. Figure 16 compiles experiments that demonstrate different mechanisms of stress regulation. The first experiment consists of a mechanical energy harvester that operates under the thermodynamic principle of the stress contribution to the chemical potential.[257] The device, illustrated in Figure 16a, is a symmetric cell consisting of partially lithiated amorphous Si thin film (~Li_3Si) on both sides of an electrolyte-soaked separator. Bending the device creates an asymmetric stress where the inner film is under compression and the outer film is under tension. The potential difference between the electrode under compression and the electrode under tension drives Li^+ flux until the new equilibrium condition is satisfied. That is, until a concentration of $Li_{3.4}Si$ (point C′) is reached for the electrode in tension and $Li_{2.4}Si$ (point B′) for the electrode in compression (Figure 16b). At the same time, charge neutrality is maintained by the corresponding electron flux along the external electrical circuit enabling mechanical to electrical energy conversion (Figure 16c). The analysis presented in Figure 16b shows that the slope of the open circuit potential (OCP) curve dictates the composition sensitivity to stress. That is, a larger change in composition is expected for a given change in stress for a flatter OCP curve. This balance was discussed in detail by Sheldon et al.[258] Similar observations were made for the sodiation of black phosphorus nanosheets[259] and lithiation of vanadium pentoxide.[260]

In a stressed solid, the rate of diffusion is also affected by the stress contribution to the chemical potential, μ, which is given by $\mu = RT\ln(a) - \Omega\sigma_h$ where a is the activity, R is the gas constant, and T is the temperature. Note that this form assumes an isotropic solid and no network constraint.[263] Adopting linear kinetics, the flux is given by $j = -\frac{cD}{RT}\nabla\mu = \frac{cD}{RT}(RT\nabla\ln(a) - \Omega\nabla\sigma_h)$.[26] The first and second terms represent the chemical and mechanical driving forces, respectively. Numerous modeling studies employing two-way stress-diffusion coupling investigated the role of this interplay in electrodes of different materials and geometries.[116,264,265] For an intuitive understanding, consider the case of a free-standing particle undergoing Li insertion that, as a result, has its outer shell in compression and the core in tension. The stress gradient, in this case, promotes inward Li flux, helping homogenize the Li concentration.[266] A recent experiment on Si thin film observed a disruption in the self-similarity of the Li concentration profiles upon stress reversal that matches theoretical predictions using stress-coupled diffusion theory.[103]

While previous arguments dealt with driving forces, stress also affects the activation energy for diffusion. When a mobile species jumps from one site to another in a host, it creates a distortion of the lattice and work must be done during the jump against any elements of the stress field that resist this distortion. Hence, under hydrostatic stress, the diffusion coefficient is given by $D = D_0\exp\left(\frac{-Q_0 - \alpha\sigma_h\Omega}{k_BT}\right)$ where D_0 is the reference diffusivity, Q_0 is the activation energy at zero stress, α is a material-dependent prefactor,[24] k_B is the Boltzmann constant, and T is temperature.[267,268] One evidence of this effect in energy materials is shown Figure 16d. The Li diffusivity in vanadium pentoxide film changes significantly as a result of an externally applied in-plane strain.[260] Another example is the experiment presented in Figure 16e for Ge nanowire. The lithiation proceeds primarily along the surface because of the higher surface diffusivity. Without an externally applied stress, the lithiation proceeds at the same rate throughout the entire surface, whereas under applied bending (Figure 16e), lithiation propagates faster on the side under tension and slower on the side under compression.[261]

In summary, there are three different ways in which stress regulates diffusion: (i) boundary condition for equilibrium, where for a given chemical potential, the concentration for equilibrium is stress dependent; (ii) flux, where the driving force for flux depends on the stress gradient; and (iii) mobility, where the activation energy for diffusion depends on the stress value. The derivations and discussions for these relationships are available in the original works by Larché, Cahn, and Voorhees.[263,269]

Stress also regulates interfacial reaction rates. One such process is the rate of the redox reaction at the electrode−electrolyte interface. The ion flux i through the interface is a function of the overpotential $(E - E_0)$ and it must be equal to zero in the absence of an overpotential. E_0 is rest potential and E is potential drop across the interface. In the absense of stress, a commonly used function is the Butler−Volmer equation: $i = i_0\left\{\exp\left(\alpha\frac{F(E-E_0)}{RT}\right) - \exp\left(-(1-\alpha)\frac{F(E-E_0)}{RT}\right)\right\}$ where α is the charge transfer coefficient and i_0 is the exchange

https://doi.org/10.1021/acs.chemrev.2c00002
Chem. Rev. 2022, 122, 13043−13107

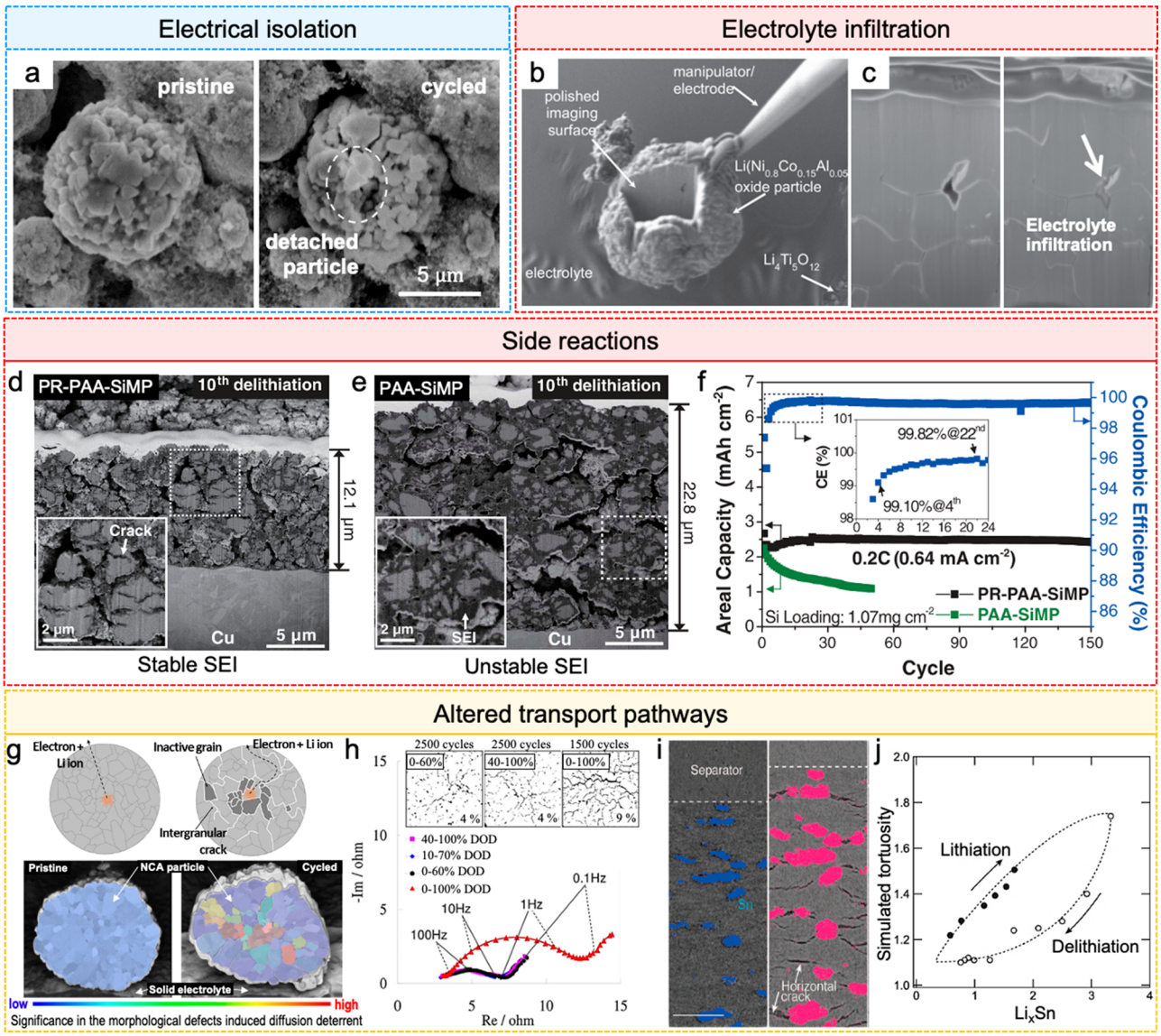

Figure 17. Effects of mechanical failure on electrochemical performance. (a) Electrical isolation of NMC primary particles detached after fracture. Reproduced from ref 112. Copyright 2018 Springer Nature. (b, c) Electrolyte infiltration into an NCA particle through intergranular cracks. Reproduced from ref 273. Copyright 2013 Wiley-VCH GmbH. (d) The stable Si electrode microstructure after 10 cycles using a highly elastic binder. (e) Excessive SEI growth and thickening after 10 cycles for another Si electrode using a normal binder. (f) Electrode with stable microstructure exhibits better capacity retention and good Coulombic efficiency. Reproduced from ref 171. Copyright 2017 AAAS. (g) Schematic illustrating the altered charge pathways and isolated grains as a result of the intergranular cracks. Reproduced from ref 274. Copyright 2019 American Chemical Society. (h) Relationship between impedance and microstructural degradation of NCA secondary particles. Reproduced from ref 275. Copyright 2014 Elsevier. (i) Cross-sectional image of pristine (left) and lithiated (right) all-solid-state Sn battery showing extensive cracking of the solid electrolyte and the (j) consequence on the ion transport tortuosity. Reproduced from ref 276. Copyright 2019 Wiley-VCH GmbH.

current.[270] Recall that the rest potential is a function of the stress. Bower et al.[271] thus proposed that the stress component of the rest potential be included in the Butler–Volmer equation. If E_0 is the stress-free rest potential, the ion flux across the stressed electrode surface and electrolyte is thus given by

$$i = i_0\left\{\exp\left(\alpha\frac{F(E - E_0 - \sigma_h\Omega)}{RT}\right) - \exp\left(-(1-\alpha)\frac{F(E - E_0 - \sigma_h\Omega)}{RT}\right)\right\}$$

This means that a tensile stress promotes ion insertion (reduces the free energy of the reduced state), and a compressive stress hinders it (increases the free energy of the reduced state). Modeling results for Si thin film electrodes including the stress-effect on charge transfer by Bower et al.[271] and Lu et al.[272] matched well experiments under various charging protocols.

The last mechanism is the stress effect on the reaction rate of phase-transforming materials. This effect was observed in an in situ TEM experiment of crystalline Si nanoparticles.[262] During lithiation, crystalline Si transforms into an amorphous phase, creating a sharp interface between reacted and unreacted phases (right side, Figure 16f). The reaction front

https://doi.org/10.1021/acs.chemrev.2c00002
Chem. Rev. 2022, 122, 13043−13107

slowed down during lithiation, which is not characteristic of a reaction-rate limited process (i.e., expected a constant interface velocity under constant potential). After ruling out other potential rate-controlling processes, the authors find that this slowdown is consistent with modeling predictions considering the stress buildup and its effect on the interfacial reaction-rate.[110,262]

3.4. Fracture

Active materials may fracture under the various chemo-mechanical loads ensuing from battery operation. The consequences of this mechanical failure on the electrochemical performance depend on various factors, and the long-term net result is generally negative. It is difficult to precisely isolate and experimentally validate the role of a single element when there are mutually dependent factors regulating electrochemical activity simultaneously and in interconnected ways. One common approach is to design control experiments in which cracking is minimized, and employ advanced imaging techniques to quantify morphological information, comparing against the performance of a system experiencing extensive cracking. Furthermore, numerical simulations are routinely used on reconstructed 3D models to develop a fundamental understanding of the regulating mechanisms. In the following, we show experimental evidence for the direct and indirect consequences of crack growth and refer to computational studies to rationalize results when applicable. Figure 17 groups crack-induced electrochemical regulation in three main types: (a) electrical isolation of active materials; (b−f) cracks exposure of fresh surfaces to the electrolyte; and (g−j) high-density cracks hampering ion and electron transport.

Figure 17a shows the microstructure of an NMC particle before and after cycling, where the secondary particle fractured and the debris became detached from the rest of the electrode.[112] Spanning cracks resulting in detachment may form through a self-feeding effect of chemomechanical instability in which a crack leads to more chemical activities at the crack site, resulting in further crack growth. For instance, when a surface crack opens up and is infiltrated by electrolytes, the mobile species concentration will be higher around the crack because of the direct access to the electrolyte and lead to preferential crack propagation.[277] Another case is when the tensile stress at the crack tip produces a phenomenon known as corrosive fracture.[278] In this process, the stress gradients around the crack drive the mobile species to concentrate at the crack tip leading to either crack arrest (by lowering the tensile stress through the chemical expansion associated with the mobile species) or unstable crack growth (by lowering the toughness at the crack tip).[278] Ultimately, electrical isolation of active materials is manifested in the battery performance as a capacity loss.[160]

In the cases where cracking does not separate active materials from the conductive network, there will still be meaningful consequences on battery performance. For example, cracks can regulate the rate capacity indirectly through their effect on the stress field. In crystalline Si nanoparticles, it has been shown that the stress field formed during lithiation retards the reaction front and, upon cracking, the built-up stresses are released, leading to an immediate observable increase in the reaction front velocity.[262] Also consider the case where structural degradation allows electrolyte infiltration into the particle; Figure 17b,c shows how the electrolyte can easily penetrate cracks into the interior of $LiNi_xCo_yAl_zO_2$ (NCA, $x + y + z = 1$) particles.[273] On one hand, the wet crack represents a shortcut for guest ions to reach the center of the particle through the electrolyte, rather than the slower alternative through the solid. This enhanced ion mobility could manifest as an improved rate capacity.[277] On the other hand, electrolyte exposure of fresh active surfaces outside the controlled conditions of the formation cycle is problematic because of the occurrence of side reactions. During the formation cycle (the final stage in the manufacturing process of batteries), passivation of the active material surface is carried out under a controlled temperature and C-rate to form a thin and stable SEI, followed by a degassing step to release gaseous decomposition products.[22] Fresh active surface exposure to the electrolyte outside these controlled conditions will lead to a range of harmful side reactions related to SEI growth (consumption of free Li, drying of the electrolyte, gas build-up, and impedance increase), as well as undesired reactions in the active materials (cation disorder, surface reconstruction, and metal dissolution).[279] In the Ni-rich NCA cathode, crack surfaces exposed to electrolyte react with unstable Ni^{4+}, forming a rocksalt impurity layer that increases the charge-transfer resistance.[280] Excessive cracking is now recognized as the underlying cause of the poor capacity retention and poor thermal stability of Ni-rich transition metal oxides.[280−282]

For active materials that undergo large volume expansion, the SEI layer fractures even when the active material itself is unharmed, as is the case for Si nanowires.[283] One example where volume change and cracking of the active materials contribute to SEI fracture and unstable growth was verified in Si microparticle electrodes via cross-sectional SEM imaging.[284] The SEI fracture exposes the fresh Si surface to the electrolyte and then causes the subsequent formation of the extra SEI. This cyclic fracture and formation of the SEI during battery cycling lead to the consumption of Li, drying of the electrolyte, increase of impedance, and eventually the premature failure of batteries. The electrode fabricated using a modified (highly elastic) binder that helps preserve structural integrity showed a minor thickness increase over cycles (Figure 17d), excellent capacity retention, and improved Coulombic efficiency (Figure 17f). In comparison, a sample using a less elastic binder (PAA-SiMP) formed a thick SEI layer and doubled in thickness after only 10 cycles (Figure 17e). The increase in impedance and free Li consumption associated with a thick SEI manifested as premature capacity loss (Figure 17f).

Electrode thickening because of structural degradation has also been linked to an "unwetting" problem in batteries where the porous network (initially wet) is drained from liquid electrolytes during cycling.[285] Deng et al.[285] showed through ultrasonic imaging that an NMC-graphite pouch cell cycled at 100% DOD (depth-of-discharge) underwent significant unwetting, leading to a capacity loss of roughly 30%, whereas a cell cycled at 30% DOD (same total cycling time of 2 years) maintained homogeneous electrolyte distribution and capacity loss of <10%. The authors suggested that the electrolyte draining was related to excessive swelling of the graphite anode by SEI thickening,[285] but research pinpointing exactly how the electrolyte is being consumed is still unfolding and will likely depend on the specific anode−cathode combination.[286,287] Recently, the same group ran computed tomography (CT) on an NMC622-graphite jellyroll and found the cathode to be responsible for the electrolyte drying. In this study, the thickness change happened largely at the cathode side, and it is

https://doi.org/10.1021/acs.chemrev.2c00002
Chem. Rev. 2022, 122, 13043−13107

hypothesized that this is caused by the extensive microcracking of NMC secondary particles. New empty spaces created by this thickness increase would cause the electrode to act as a sponge slurping the electrolyte out from other areas of the jellyroll.[287] We also note that it is common for pristine secondary particles of transition metal oxides to have large central voids.[178,288] Upon cracking, the electrolyte can access these pre-existing voids and potentially contribute to the drying problem without demanding a significant thickness change.

Cracks also represent a discontinuity in the solid ionic and electronic conduction volume, acting as physical barriers for charge transport. The schematic in the top panel of Figure 17g illustrates the difference in the charge transport path from the center to the outer surface of a pristine particle (left) versus a cracked particle (right) in a solid electrolyte (no electrolyte infiltration). To investigate this regulation for realistic crack morphologies, Besli et al.[274] calculated the diffusion length in 3D reconstructed models of pristine and cycled NCA particles in solid polymer batteries. The bottom Figure 17g shows a color-coded distribution of how transport to individual grains of pristine (left) and cycled (right) particles are distinctly affected by their morphology. Intuitively, the more interconnected the cracks, the greater their deterrent effect on transport. Note that regulation is different in traditional liquid electrolyte batteries where the Li diffusion length is decreased by the cracks because of electrolyte infiltration (direct access to electrolyte inside the interior of particles) while the electron transport length is instead increased (high-density cracks increase the tortuosity of the electron conduction path). This mismatch between the ionic and electronic transport paths is thought to contribute to known particle-level state-of-charge heterogeneity in these systems.[101]

Watanabe et al.[114,289] investigated the role of microcracks on cell impedance by varying the DOD of $LiAl_{0.10}Ni_{0.76}Co_{0.14}O_2$ cylindrical cells. The authors found that the structural disintegration of the particles was related to the overall width of the depth-of-discharge window (ΔDOD). The insets of Figure 17h show the binarized cross-sectional SEM images of NCA particles after 2500 cycles for 60% ΔDOD (left and middle insets) and after 1500 cycles for 100% ΔDOD (right inset). The 100% ΔDOD cell underwent the most structural degradation, which led to a larger impedance compared to the less damaged cell with a narrower ΔDOD (Figure 17h). Cells cycled through a wider charge window also experienced premature capacity fading (50% capacity loss after 1500 cycles) compared to those of narrower capacity windows (20% capacity loss after 2500 cycles). Note that this performance deterioration because of extended cracking likely stems from both altered charge transport lengths and undesirable reactions caused by electrolyte infiltration. For NCA, extensive cracking combined with electrolyte wetting leads to the formation of a NiO-like surface that is known to have poor electron and Li-ion conductivities.[114] In addition, the authors found that the structural damage only depended on the width of the operating window and not on the specific voltage value. That is, a similar performance was observed for 0−60% DOD and 40−100% DOD. This is not a general observation. For higher Ni content cathodes, mechanical degradation is amplified at higher voltages because of the H2 → H3 phase transition.[113] Hence, the ideal charging protocol to minimize mechanical degradation largely depends on the chemical composition and its corresponding characteristic lattice distortions.

It is also notable that for all-solid-state batteries, not only the active particle can crack but also the electrolyte itself (detailed discussion on the mechanical degradation modes of all-solid-state batteries in Section 2.4). Cracking can be particularly severe in cases where stiff, brittle solid electrolytes are paired with high-capacity active materials that undergo large volume changes. One study used synchrotron radiation X-ray tomography to map the morphological evolution of tin (Sn) particles embedded in amorphous LPS solid electrolytes.[276] Even though LPS is a relatively soft solid electrolyte with an elastic modulus of ∼18 GPa, it has low fracture toughness (∼0.2 MPa $m^{1/2}$, see the comparison in Table 1, Section 2.4.1), making it prone to cracking. Figure 17i shows the cross-sectional morphology of the electrode in a stack cell in unlithiated (left) and lithiated (right) states. The blue color indicates pure Sn, and the pink color indicates any alloyed phase (lithiated Sn). During the expansion of the Sn particle, many cracks can be observed parallel to the current collector. The authors speculate that the reason that particles expand primarily in the vertical direction could be a consequence of the cell construction, which has fixed side walls but allows thickness variation (only constrained by constant pressure on a flexible PMDS substrate). As a result, the cracks grow in the orientation perpendicular to Li-ion flux (from top to bottom), thus dramatically affecting the tortuosity of ion transport. That is, despite cracks representing less than 5% of the total electrode volume in the lithiated state, they have a larger effect on tortuosity than the particles themselves which represent 20% of the total volume. The evolution of the tortuosity factor calculated from the reconstructed images as a function of the Li content is shown in Figure 17j. One noticeable feature is that the horizontal cracks formed in the LPS during lithiation practically disappear upon delithiation, so the tortuosity is reversed to the original value. Ultimately, the physical barrier to charge transport created by an extended crack network will manifest as an increase in cell impedance and consequent power fade. This effect was also shown to be significant in LAGP electrolytes in a symmetric Li metal cell where the crack area growth was correlated to an increase in impedance of roughly two orders of magnitude.[213]

4. MODELING APPROACHES

Various modeling approaches, including atomistic modeling, mesoscale phase-field modeling, continuum mechanics modeling, and homogenization modeling, have been developed to capture the highly intertwined chemistry and mechanics in batteries at multiple length scales. The following subsections will cover the introduction of these modeling approaches and then their applications in battery research. It should be noted that different approaches have their own focus of interest that usually cannot cover the cross-scale features because of the trade-offs between computational cost and modeling details. It is always promising but challenging to develop modeling approaches that are efficient in time and computational cost while containing sufficient microstructural details.

4.1. Atomistic Modeling

The chemomechanical properties of battery materials are fundamentally dictated by their electronic structures and phase behaviors at the atomic level. The intricate structural dynamics at the ultrasmall length scale (Å ∼ nm) and ultrafine time scales (fs ∼ ns) challenge direct experimental observations. Powered by high-performance computing resources, atomistic

https://doi.org/10.1021/acs.chemrev.2c00002
Chem. Rev. 2022, 122, 13043−13107

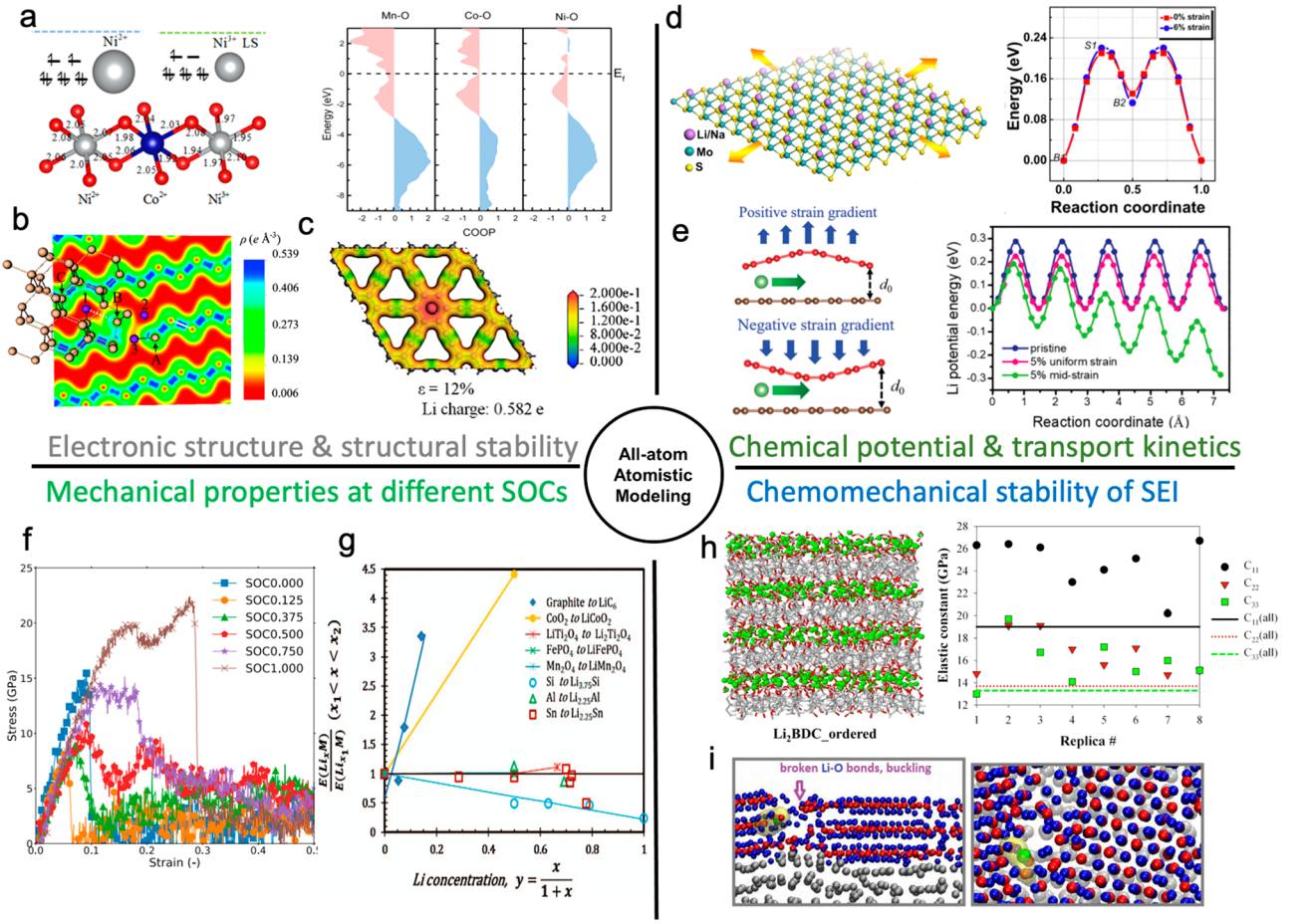

Figure 18. Atomistic modeling of chemomechanical behaviors of battery materials. (a) (left) Local view of the TM−O octahedral complexes. The degree of distortion of the octahedra indicates the ionic states of the TM elements. (right) Crystal orbital overlap population analyses of the TM−O pairs. Reproduced from ref 290. Copyright 2017 American Chemical Society. (b) Valence electron charge density distribution on a (110) plane of c-Si with four Li atoms. Reproduced from ref 291. Copyright 2011 American Chemical Society. (c) Electrostatic potentials for monolayer graphene with one adsorbed Li and under 12% strain. Reproduced from ref 292. Copyright 2018 American Chemical Society. (d) (left) Schematic of a Li/Na adsorbed MoS_2 sheet under a uniform tensile strain. (right) The adsorption energy of Li (square) and Na (circle) as a function of the tensile strain. Reproduced from ref 293. Copyright 2018 Springer Nature. (e) (left) Schematic configurations of Li diffusion inside the bilayer graphene under positive and negative strain gradient fields. (right) Energy profiles of Li along the diffusion path in different strain fields. Reproduced from ref 294. Copyright 2020 Royal Society of Chemistry. (f) Stress−strain response of $Li_xMn_2O_4$ cathode at different SOCs. Reproduced from ref 295. Copyright 2020 AIP Publishing. (g) The average values of Young's modulus in various electrode materials. Reproduced from ref 296. Copyright 2014 IOP Publishing. (left) A snapshot of the ordered phase of Li_2BDC. (right) Elastic constants obtained from the MD/MC modeling of the ordered Li_2EDC at 393 K. Reproduced from ref 297. Copyright 2017 American Chemical Society. (i) Side and top views of Li_2O films with grain boundaries and strained by ∼12%. Reproduced from ref 298. Copyright 2017 American Chemical Society.

modeling plays an increasingly important role in understanding the fundamental mechanisms of chemomechanics and providing insights into material design. Herein, we present a few representative cases of all-atom atomistic modeling in studying the chemomechanical behavior of battery materials.

The intrinsic structural stability of electrode materials can be informed by analyzing their electronic structures via atomistic modeling. The bonding environment, the degree of orbital overlapping, and the charge density distribution gauge the strength of atomic bonding and further indicate the inherent mechanical stability of electrodes. For example, Sun and Zhao investigated the electronic structure and valence states in NMC cathodes using the density functional theory (DFT) and genetic evolution algorithm.[299] Figure 18a (left panel) presents the chemical bonding of TM−O octahedral complexes in NMC, where the transition metal (TM) elements (Ni/Mn/Co) reside at the octahedral site surrounded by six O atoms. The oxidation state of the TM elements determines the Jahn−Teller effect as well as the TM−O bond length. Crystal orbital overlap population (COOP) analysis presented in Figure 18a (right panel) unveils the comparative TM−O interactions, wherein the positive values represent the bonding state, and the negative values show the antibonding interaction. The Jahn−Teller effect and orbital overlap population of TM−O pairs serve as indicators of the microscopic structural stability of NMC materials. Likewise, employing first-principle simulations, Zhao et al. elucidated the microscopic deformation mechanism of lithiated Si and underpinned the onset of plasticity induced by lithiation.[291] The reduction in strength of lithiated Si is attributed to the breaking of Si−Si bonds and the formation of weaker bonds of Li−S, which is associated with the variation of the valence electron charge density distribution on a (100) plane of Si upon lithiation (Figure 18b). Zhang et al. studied the effect of biaxial strains on the absorption and diffusion of Li on graphene anode.[300] The electrostatic potential map of Figure 18c reveals that more charges are

https://doi.org/10.1021/acs.chemrev.2c00002
Chem. Rev. 2022, 122, 13043−13107

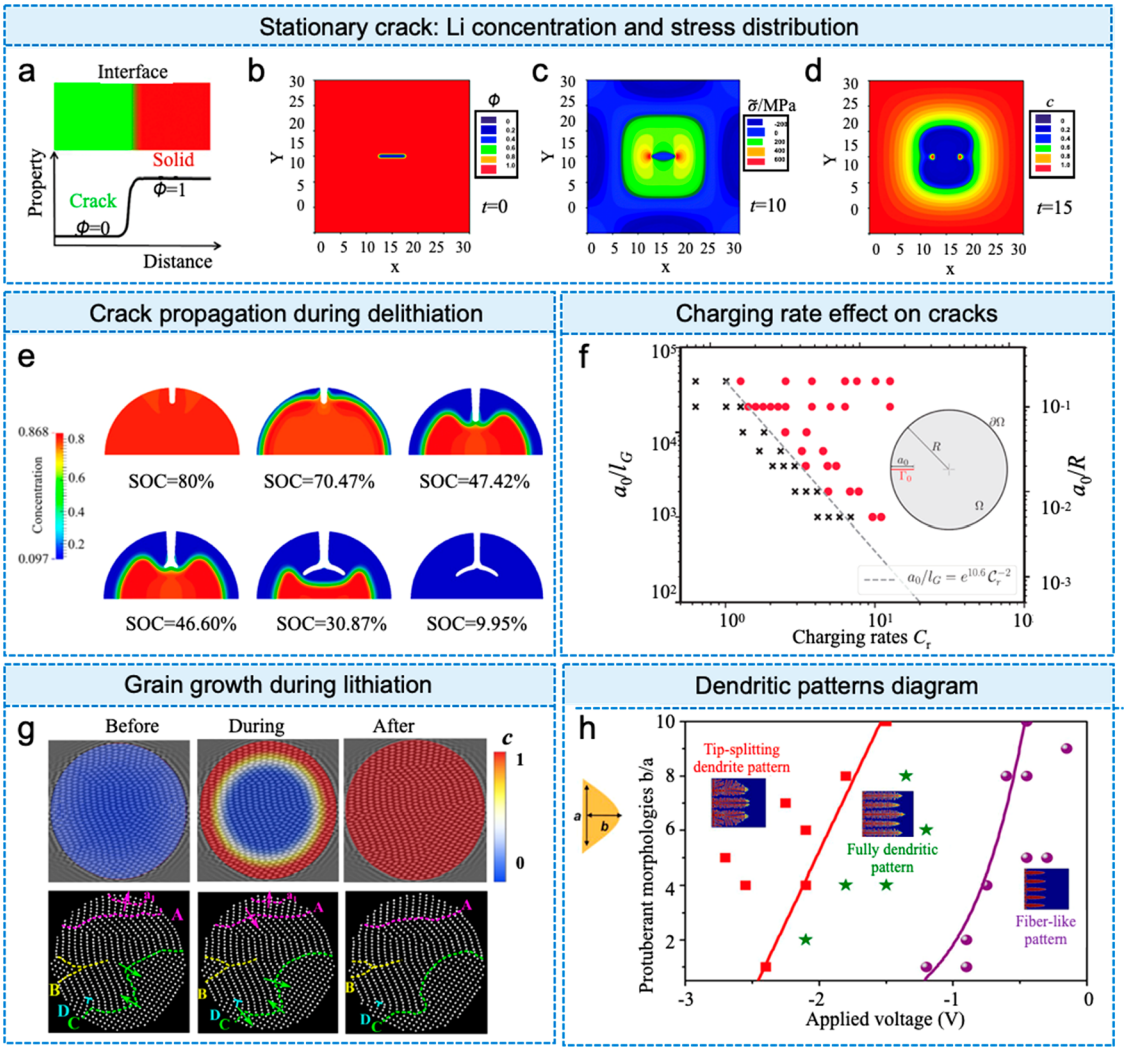

Figure 19. Phase-field method is applied in rechargeable batteries for chemomechanical coupling behaviors. (a) The diffuse interface model with continuously changed order parameter ϕ ($0 \le \phi \le 1$). (b) The crack at the center of the Si at $t = 0$, where t is a normalized and rescaled time. (c) Distribution of hydrostatic stress and stress concentrations appeared at crack tips at $t = 10$. (d) Distribution of Li concentration at $t = 15$, large Li fluxes toward the crack tips. Reproduced from ref 307. Copyright 2015 Royal Society of Chemistry. (e) Crack propagation during delithiation process in electrode particles. Phase segregation initiates the crack propagation at SOC = 70.47% and crack tip starts to branch out at SOC = 46.60%. Reproduced from ref 308. Copyright 2016 Elsevier (f). Crack activation diagram of charge rate C_r versus initial crack size a_0/l_G for cathodic particles. Circles show the activated cracks and crosses show the unactivated cracks; the black dash line is power-law distribution. Reproduced from ref 309. Copyright 2019 Elsevier. (g) Li-diffusion accelerates grain growth and grain boundary migration in the host-electrode $FePO_4$ during lithiation. Reproduced from ref 310. Copyright 2019 American Physical Society. (h) Diagram showing the effect of applied voltage and initial protuberant morphology on dendritic patterns in Li-metal. As the applied voltage increasing, fiber-like, fully dendritic, and tip-splitting dendritic patterns are divided by two fitted boundaries. Reproduced from ref 311. Copyright 2015 Elsevier.

transferred from Li to C with the increased strain, which corroborates that Li adsorption becomes more favorable on graphene under strain.

The atomistic modeling has been utilized to reveal the interplay among the strain, chemical potential, and transport kinetics in battery materials. For example, Hao et al. calculated the potential energy surface of Li diffusion on MoS_2 without and with 6% strain and determined the critical diffusion barrier along the minimum energy path.[301] Figure 18d demonstrates that, under 6% strain, Li follows the same migration path with a very similar diffusion barrier of 0.22 eV comparing to that of the unstrained states. It suggests that strain has a negligible effect on the fast diffusion behavior of Li on MoS_2. Meanwhile, Xu et al. argued that the strain gradient could induce a notable effect on the rate performance of batteries, as manifested by the considerable changes in Li diffusivity and conductivity.[302] As shown in Figure 18e, the variation of the diffusion barrier with the strain gradient is larger than that of a uniform strain, indicating that the strain gradient can be efficient in regulating the Li diffusion behavior.

The strong dependence of the mechanical properties of electrode materials on their state of charge has also been investigated using atomistic modeling. Using molecular dynamics simulations, Tyagi et al. studied the variation of mechanical properties of the $LiMn_2O_4$ cathode under different states of charge,[303] Figure 18f. It reveals that the material shows a more ductile behavior in the early stage of charging (higher SOCs), whereas the brittle behavior gradually emerges and dominates at smaller SOC values. Likewise, Qi et al. employed first-principle modeling to investigate the elastic

https://doi.org/10.1021/acs.chemrev.2c00002
Chem. Rev. 2022, 122, 13043−13107

properties of multiple electrode materials and their dependency on Li concentrations.[304] As shown in Figure 18g, different electrodes present distinct elastic behaviors with varying Li concentrations. Layered electrodes such as graphite and $LiCoO_2$ show dramatic changes in Young's modulus during lithiation, while a minimal change of modulus is observed for spinel and olivine structures (e.g., $LiMn_2O_4$ and $LiFePO_4$). For the alloying type anode such as amorphous Si, elastic modulus follows the linear rule of mixture of the two pure phases (Si and bulk Li) and exhibits substantial softening upon lithiation.

Atomic modeling has uncovered the crucial role of the mechanical stability of interphases such as SEI and GBs on battery performance. The intricate chemical compositions and complex ion kinetics in interphases demand thorough investigations at the molecular scale. Using a hybrid molecular dynamics and Monte Carlo simulation, Bedrov et al. studied the mechanical and transport properties of model SEIs comprising dilithium ethylene dicarbonate (Li_2EDC) and dilithium butylene dicarbonate (Li_2BDC).[305] Figure 18h shows the atomic configuration of the ordered Li_2EDC and its bulk/shear modulus calculated from the hybrid molecular dynamics and Monte Carlo (MD-MC) simulation. The two SEI models exhibit highly anisotropic mechanical properties in their ordered phase, with the shear modulus of Li_2BDC being systematically smaller than that of Li_2EDC. It suggests that the presence of Li_2BDC in the SEI can soften the interphase and reduce the ability to prevent dendrite growth. Leung et al. used static DFT simulations to examine Li metal surfaces covered with Li_2O and/or LiF thin films with grain boundaries.[306] Figure 18i demonstrates the buckling of the Li_2O thin film upon ~12% strain loading, accompanied by the multiple Li−O bond breaking and the formation of subnanometer-sized cracks. This indicates that incipient Li metal dendrites may nucleate at the defects of subnanometer size inside the crack of the Li_2O film.

4.2. Mesoscale Phase-Field Modeling

The phase-field method is a versatile computational approach to describe and predict the evolution of mesoscale microstructures and morphologies based on thermodynamics principles. Phase-field models have been widely used in the studies of rechargeable batteries. In this section, we introduce a few representative case studies on chemomechanical coupling in rechargeable batteries.

The phase-field model typically contains diffusive interfaces because of the difficulty of tracking the sharp interface. The order parameter ϕ, as the phase-field variable, is introduced to indicate the change of the phase property. The evolution of the order parameter reflects the phase transition without the need of tracking the interface. For example, cracks can be regarded as the diffuse interface, as shown in Figure 19a. The order parameter changes from 0 to 1, where $\phi = 1$ and $\phi = 0$ represent the intact and fully damaged regions, respectively. Also $0 < \phi < 1$ represents the transitional region, which is smooth across the interface according to a hyperbolic tangent function.[312] In general, the free energy of the system can also involve more field variables such as concentration, temperature, electromagnetic field, and others.

One particular application of phase-field modeling in battery research is to provide a powerful numerical approach to understand the dynamic evolution of cracks in electrode materials. For instance, Xie et al.[313] developed a phase-field model to study the deformation and stress evolution of Si nanowires during lithiation. Large local stress concentration and stress gradient can induce pervasive microcracks. Zuo and Zhao[307] used phase-field models to investigate the initial conditions of cracks in Si thin films and crack propagation. Li distribution and stresses coevolve near the stationary crack, as shown in Figure 19b−d. Furthermore, Zhao et al.[308] studied the dynamics of crack propagation and the effect of chemical reactions on fracture surfaces during delithiation of Si. Initially, Li concentration is homogeneous (SOC = 80%), and phase separation appeared at SOC = 70.47% because of the Li depletion in the outer regime. In the first two stages (Figure 19e), cracks propagated faster than the phase segregation because of the large tensile stresses at the crack tip. The mechanism of crack propagation in electrodes during (dis)-charging is critical to understand the structural stability of battery materials. Mesgarnejad and Karma[309] exploited the phase-field approach to quantify the relationship between crack propagation, flaw size, and charging rate. Figure 19f shows the phase diagram of crack activation in the space of the charge rate and the initial flaw size. In this study, it shows that the critical size of the pre-existing flaw for crack propagation follows a power law of the charging rate.

Another application of phase-field modeling in battery research is to study the diffusion-induced grain growth. During battery cycling, Li diffusion does not only induce volumetric strains, stresses, and crack propagation but also accelerates grain boundary migration in electrode materials. Generally, the grain size in polycrystals is affected by external fields such as temperature, stress,[314] electricity,[315] and magnetics.[316] In a polycrystalline electrode, cyclic insertion and extraction of Li induce inhomogeneous lattice strains and phase transformation.[317] Carter et al.[318] proposed that the internal strain fields drive grain boundary movement in the host electrode. Recently, Balakrishna et al.[319] developed a Cahn−Hilliard type phase-field model to investigate the interactions between Li intercalation and the structural evolution. They demonstrated the Li diffusion-induced grain-boundary migration in $FePO_4$ upon cycling, as shown in Figure 19g.

The most promising application of phase-field modeling is to simulate the Li dendrite growth in Li-metal batteries. The formation of Li dendrite is the major challenge in Li-metal batteries using liquid electrolytes.[320] Ely et al.[321] conducted a phase-field model to describe the growth kinetics of Li deposition. Liang et al.[322] presented a nonlinear phase-field model and took the Butler−Volmer reaction kinetics into account to simulate and predict the Li dendritic growth during the charging processes. In another exemplary study, Chen et al.[323] established a thermodynamically consistent phase-field model to investigate the dendritic patterns, Figure 19h. They found that Li dendritic morphology was a function of the applied voltage and the initial morphology features of the electrode surface. The phase diagram was proposed to guide the design of Li-metal batteries to avoid undesired dendritic growth.

4.3. Continuum Mechanics Modeling

The continuum mechanics modeling approach for a homogeneous domain is characterized by the balance laws (mass, energy, momentum, entropy) and constitutive relations that define material response under various loadings. The balance laws give rise to field equations defined at all points in a continuum domain at all times. The constitutive relations describe the distinct material behavior of each domain together

https://doi.org/10.1021/acs.chemrev.2c00002
Chem. Rev. 2022, 122, 13043−13107

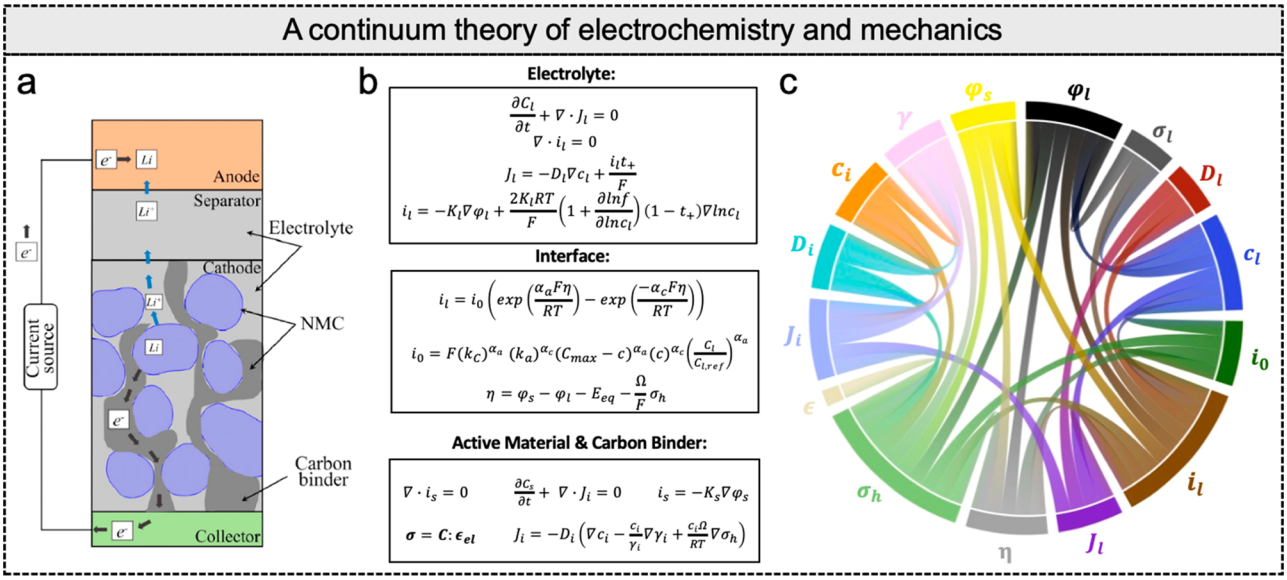

Figure 20. (a) Schematic of a half-cell composed of a NMC composite cathode and a Li metal anode. Reproduced from ref 62. Copyright 2019 Elsevier. (b) Set of equations for the continuum modeling of the coupled fields of electrochemistry and mechanics in a half cell. The coupling originates from the stress bias on the overpotential for the interfacial charge transfer and the diffusion potential for Li. (c) Connection network of the field variables in the equations in panel b to demonstrate the multiphysics nature of the continuum framework.

with the field equations. The solution aims to calculate the field variables at the region and time of interest. The Li concentration field (c) is one such field variable that defines the volumetric quantity of Li across the system. The multicomponent system is first segregated into homogeneous domains where the field variables vary in position and time. Figure 20a[62] demonstrates such a multicomponent system for a half cell model of a composite cathode. The active particle domains are dispersed within the cathode along with the carbon binder (another homogeneous domain) and electrolyte domain regions. Within a domain, the Li transport is governed by the mass conservation: $\partial c/\partial t + \nabla \cdot J = 0$, where J is the Li flux per unit area per unit time. The characteristics properties of the domain contribute to the driving force of the flux (J), e.g., within the electrolyte domain, the gradient of Li concentration and the electrolyte current-induced migration of Li-ion regulates the flux (J_l). In the active material domain, the mass balance law dictates the same field equation (Fick's law) for Li transport. However, its distinct physical properties require different constitutive relations than the electrolyte domain, and thus the driving force for the flux (J_i) has different contribution terms (Figure 20b).

The modeling of multiphysics problems is accomplished through the coupled governing equations. The expression for the electrolyte current (i_l) in Figure 20b is based on the multicomponent diffusion equation by Onsager–Maxwell–Stefan considering the equilibrium of all components' electric potential, chemical potential, and mechanical forces in a binary salt liquid electrolyte.[324] The electrolyte domain does not conduct any electrons. The potential in the electrolyte (φ_l) is thus measured in comparison to a reference electrode[325] of a given kind (e.g., Li reference electrode in the solution[326]) located at a fixed point in the solution. While the expression for electrolyte current (i_l) in a binary electrolyte consists of movement of both positive and negative ions, the flux (J_l) represents the movement of only positive ions (Li-ion in this case). Thus, both the electric potential (φ_l) and electrolyte concentration (c_l) variation determine the charge movement within the electrolyte. The carbon binder is a porous domain where the spatial electric potential difference (φ_s) drives the rate of electron transfer (i_s). The transport through the porous structure of homogeneous carbon binder and separator domains is modeled by considering tortuosity. The Bruggeman relation uses an effective geometric parameter to modify the intrinsic diffusivity and conductivity of the electrolyte within the carbon binder and separator domains.[327]

The Cauchy stress field ($\boldsymbol{\sigma}$) is governed by $\nabla \cdot \boldsymbol{\sigma} = 0$ with an assumption that mechanical equilibrium is achieved at a faster characteristic time scale than the electrochemical process. As Li-ions move in and out of the active material lattice, volumetric deformation is assumed to be separated into chemical, elastic, and plastic stretches.[328] The total deformation gradient $\mathbf{F}$ (second-order tensor that transforms line elements from reference configuration to the deformed configuration) is thus defined by multiplicative decomposition $\mathbf{F} = \mathbf{F}_c\mathbf{F}_e\mathbf{F}_p$. When the net volumetric change is zero between reference and deformed configuration, $\det(\mathbf{F}) = 1$. Considering elastic behavior ($\boldsymbol{\sigma} = \mathbf{C}:\boldsymbol{\varepsilon}_{el}$), small eigenstrain and small deformations, the change in diffusion potential[103,263] caused by the stress is $\Delta\Phi = -\sigma_h \Omega$, where Ω is the partial molar volume, σ_h is the hydrostatic stress defined as $\sigma_h = \mathrm{tr}(\sigma)/3$ (tr is the trace operator). Hence, the net flux within the particle (J_i, for species i is influenced by the gradients of Li concentration, activity, and hydrostatic stress. For large eigenstrains (induced by significant volumetric change), the stress-induced chemical potential change includes the Eshelby stress tensor terms.[329] Thus, within the active particle domain, stress and diffusion are coupled during lithiation and delithiation. The stress also affects the charge-transfer rate through modification of the overpotential term (η), as shown in Figure 20b. Because the reaction occurs at the interface of the active particle and the electrolyte, only the stress field at the interface contributes to the reaction rate. Figure 20c shows the connection between some variables based on the field equations listed in Figure 20b. The flow diagram shows the multiphysics nature of the

https://doi.org/10.1021/acs.chemrev.2c00002
Chem. Rev. 2022, 122, 13043−13107

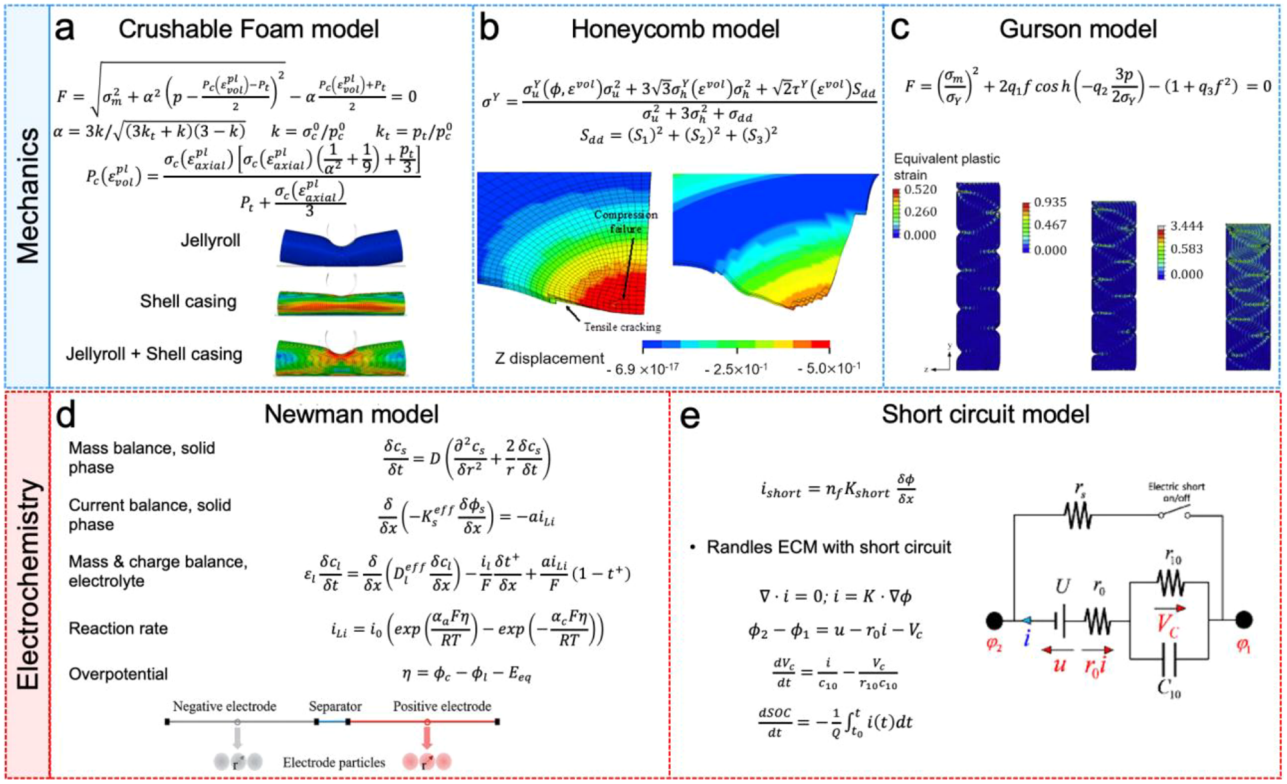

Figure 21. Homogenization theories for mechanics (a–c) and electrochemistry (d, e). (a) Crushable foam model flow rule. Reproduced from ref 345. Copyright 2015 Elsevier. (b) Honeycomb model yield stress. Reproduced from ref 346. Copyright 2017 Elsevier. (c) Gurson model flow rule. Reproduced from ref 347. Copyright 2013 Elsevier. (d) Newman electrochemical model and (e) short circuit models. Reproduced from refs 348 and 349. Copyright 2020 Elsevier.

continuum model where mass flow variables (D_i,J_i) and charge-transfer variables (η,i_i) relate to the mechanical variable (σ_h).

The most widely accepted continuum model on rechargeable batteries is the pseudo-2D (P2D) model, which consists of coupled nonlinear partial differential equations for the conservation of mass, charge, and force in three battery components: cathode, separator, and anode. The P2D model is efficient in computational cost because it does not present the details of microstructural features in batteries, such as the particle configuration, particle distribution, and tortuosity of ion transport. Rieger et al.[330] demonstrated the effectiveness of such a model by performing numerical calculations to model the thickness change of a commercial pouch cell during discharge. The effect of local deformation velocity of the solid domain generated by the diffusion of Li atoms on the local stress distribution was reported by Li et al.[331] By modifying the diffusion equation to account for local deformation velocity for spherical $LiMn_2O_4$ electrode particles, a more significant concentration gradient is generated near the electrode surface than the electrode's center.

Recently, researchers have tended to integrate the tomography reconstruction techniques into the continuum modeling to mimic the more realistic chemomechanical behaviors of batteries. Relying on advanced imaging techniques such as X-ray CT or FIB/SEM, the microstructure of battery components can be reconstructed with sufficient details and then imported into the numerical programs for simulation. For example, Rahani et al.[332] used 2D reconstructed microstructures to study the effect of the yield stress of binder on the average stress evolution within the graphite anode. Wu et al.[333] performed a 2D multiphysics computational study on a microstructure resolved model for the full cell comprising an anode, separator, and cathode. The rotation of realistic unsymmetrically shaped active particles because of cyclic volumetric changes induces shearing fracture at the binder interface. Mai et al.[334] developed a 3D particle-resolved model to capture the Li and stress distributions in the commercial $LiFePO_4$ electrodes with heterogeneous microstructures. They found that the active particles with an arbitrary shape experience an one order larger von Mises stress than the previously simplified spherical particles. Later, Malavé et al.[335] performed a numerical study on reconstructed $LiCoO_2$ active particles from FIB-SEM images. They found the uneven surface morphology of the active particles regulates the local stress distribution, where the local concave surfaces develop a field of high equivalent stress. Relying on a 3D reconstructed model from X-ray tomography, Hein et al.[336] demonstrated that inhomogeneous spatial distribution of the carbon binder in the electrode has consequences on the battery performance.

4.4. Homogenization of Battery Cell

Commercial rechargeable batteries are generally composed of an intricate assembly of multiple components. Multiple such components are stacked or rolled together to form a jellyroll, enclosed inside a shell casing or pouch, and then filled with a liquid electrolyte. The cell's response to an electrochemical or mechanical loading is determined by electrochemical, mechanical, and thermal interactions between individual components. Modeling attempts must therefore overcome not only the challenge of coupled multiphysics theory but also length scales ranging over at least 3 orders of magnitude. Predicting system behavior and possible catastrophic failure caused by electrical,

https://doi.org/10.1021/acs.chemrev.2c00002
Chem. Rev. 2022, 122, 13043–13107

thermal, or mechanical abuse has received significant attention in cell modeling. For example, when studying the response of batteries to mechanical abuse, researchers can employ the detailed modeling approaches mentioned in the previous section, where all the individual components of a single cell are modeled explicitly, including electrodes, current collectors, separators, shell casing, end-caps, and several other components.[337] These models are capable of predicting local deformation, buckling, and fracture within the jellyroll, which can help predict an internal short circuit under large external loads.[338−342] This capability, however, comes at the cost of significant computational time because of the large number of elements required to accurately discretize each thin component of the jellyroll and extensive experimental material parameter calibration for each of the separate components in the cell.

A less computationally expensive approach is the reduced detailed model, where some layers of the jellyroll are lumped as one to reduce the total number of layers.[343,344] This model can provide physically accurate deformation patterns but still requires material testing for each battery component. The final approach considers the jellyroll as a homogenized medium that allows greater freedom in finite element discretization and coarser mesh size, making it the most computationally efficient. Material parameter calibration is only required for the complete cell and not the individual components. It is important to select the correct constitutive model to accurately study the mechanical response of the homogenized battery material. The three most common constitutive models are (a) the crushable foam model, (b) the honeycomb model, and (c) the Gurson model.[337]

The crushable foam model (also known as Deshpande−Fleck model)[337,345,350] summarized in Figure 21a is by far the most used to model the mechanical response of homogenized battery cells. Though this model was initially developed for crushable metallic foams,[351] it is capable of accurately modeling the pressure dependence or tension-compression asymmetric response of the jellyroll in addition to the densification under compressive loading leading to an increasing hardening rate. Apart from densification[352] and tension-compression asymmetry,[353] different characteristic mechanical behaviors of battery cells have been studied, including (i) damage and fracture criteria to predict crack and shear band formation,[354] (ii) material anisotropy[352,355,356] and structural anisotropy,[342−344,357,358] (iii) SOC dependence,[359,360] and (iv) strain rate dependence.[360,361] While prior studies have included some of these effects separately in modeling attempts,[354,359,361] Li et al.[362] presented a comprehensive homogenized model combining all six of the aforementioned characteristics.

In addition to accurately modeling densification and pressure dependence, the built-in honeycomb model (Figure 21b) in LS-DYNA[363] is capable of modeling the structural anisotropic behavior of the jellyroll,[346] contingent on the definition of the hardening curves. Though the anisotropic model requires additional material parameter calibration and testing, it can produce better results in cases where the isotropic model fails.[364] Lastly, the Gurson model (Figure 21c)[337,347] is a physics-based model initially developed for porous metals, which has been implemented to model porous battery materials.[347,357,365] Crack nucleation and propagation can be predicted, but the applicability to battery modeling is limited as the results are unreliable beyond 10% porosity.[337]

The Newman electrochemical model[366,367] (Figure 21d) has a wide range of applications in the field of Li-ion batteries as it can accurately model the electrochemical reactions within the porous electrodes, mass transport in the electrolyte and the porous electrode, and electrical conduction. The different phases in the composite porous electrode, active material, inactive carbon-binder, and the electrolyte-soaked pore phases, are all treated as superimposed continua within the homogenized electrode and the active material is assumed to be composed of spherical particles. Alternatively, in large-scale simulations where the Newman model is not suitable, simpler equivalent circuit models (ECMs) such as the internal resistance model, Thevenin model, resistance-capacitance model, and Partnership for New Generation of Vehicles (PNGV) model can be implemented.[368,369] Both these approaches have been used to study internal short-circuiting among other applications. One such example is the lumped first-order Randles ECM as shown in Figure 21e.[348] Multiphysics models have been developed that couple either the Newman model or ECMs with thermal considerations to study internal short circuits and thermal runaway.[369,370] Furthermore, mechanical-electrochemical-thermal coupled multiphysics models have been used to study the impact of mechanical deformation on internal short circuits and battery performance under mechanical abuse.[370−374]

5. EXPERIMENTAL APPROACH

Widely used characterization tools such as the electron microscopes have enabled uncovering a range of rich chemomechanical interactions in electrode materials, including the formation of a high-density dislocation zone at the reaction front,[375] cavitation,[95] fracture,[100] anisotropic swelling and necking of nanowires,[376] and inhomogeneous reactions.[261,377] An immense effort has been put forth by researchers in the past decade in expanding experimental capabilities to (i) probe materials in realistic environments, (ii) acquire and interpret representative statistical information, (iii) improve resolution and elemental analysis sensitivity, and (iv) develop a comprehensive and timely mechanical property database. In the following, we review techniques that have recently undergone significant advances on these fronts. Comprehensive reviews on electron and optical microscopies are available elsewhere.[378−381]

5.1. Mechanical Characterization Techniques

Mechanical properties are a prerequisite for mechanics models and designing resilient structures. Suitable characterization techniques vary depending on the scale of interest. The electrode- and material-level properties are pertinent to understanding how to accommodate chemical strains inherent from battery operation, while the cell- or package-level mechanical response is most relevant for evaluating safety upon impact and puncture, or even to serve as structural members.[382] These two scales are discussed separately next.

5.1.1. Electrode Materials. Mechanical characterization of electrode materials is challenging for several reasons. For one, electrodes are typically composites, consisting of micrometer size metal- or ceramic-like particles embedded in a porous matrix of polymeric binders and carbon additives. These components have widely dissimilar properties that can vary by orders of magnitude,[64] making probing their individual phases both necessary and difficult. Furthermore, in situ properties may differ from ex situ ones because of the interaction with the

https://doi.org/10.1021/acs.chemrev.2c00002
Chem. Rev. 2022, 122, 13043−13107

Table 2. Mechanical Characterization Techniques Applied to Electrode/Electrolyte Materials[a]

tool	measurement	sample geometry	battery material
nanoindentation	elastic modulus, hardness	particle, composite, pellet, film	NMC,[64,384,393] LMO,[388,387,163,383] Li[25,389,395]
	creep exponent, strain-rate sensitivity	film, ribbon	Li,[25,389] Si[25,391]
	fracture toughness	pillar, particle, pellet, film	NMC,[154,384] LMO,[388,396] LCO[387]
	adhesion strength	composite	C composite[392]
nanoindentation (flat punch)	stress−strain curve	pillar	LCO,[394] Li[397]
	particle strength	particle	NMC[385]
wafer-curvature using multibeam optical stress sensor	biaxial stress	film,[140,141,386,398−400] composite[401,402]	S composite,[401] Si[138,386,399,403]/Si composite,[402] Sn,[398] Ge,[140,404] LCO, LMO,[400] C[405]
	fracture energy	film	Si,[406] Ge[404]
	biaxial modulus	film	Si[407]
	strain-rate sensitivity	film	Si[139]
uniaxial tension	stress−strain curve, creep exponent	bulk	Li[200,408]
	stress−strain curve	nanowire	Si[409]
digital image correlation	in-plane strain field	composite	graphite[410,411]

[a]Note: NMC = $LiNi_xMn_yCo_zO_2$, LCO = $LiCoO_2$, LMO = $LiMnO_2$

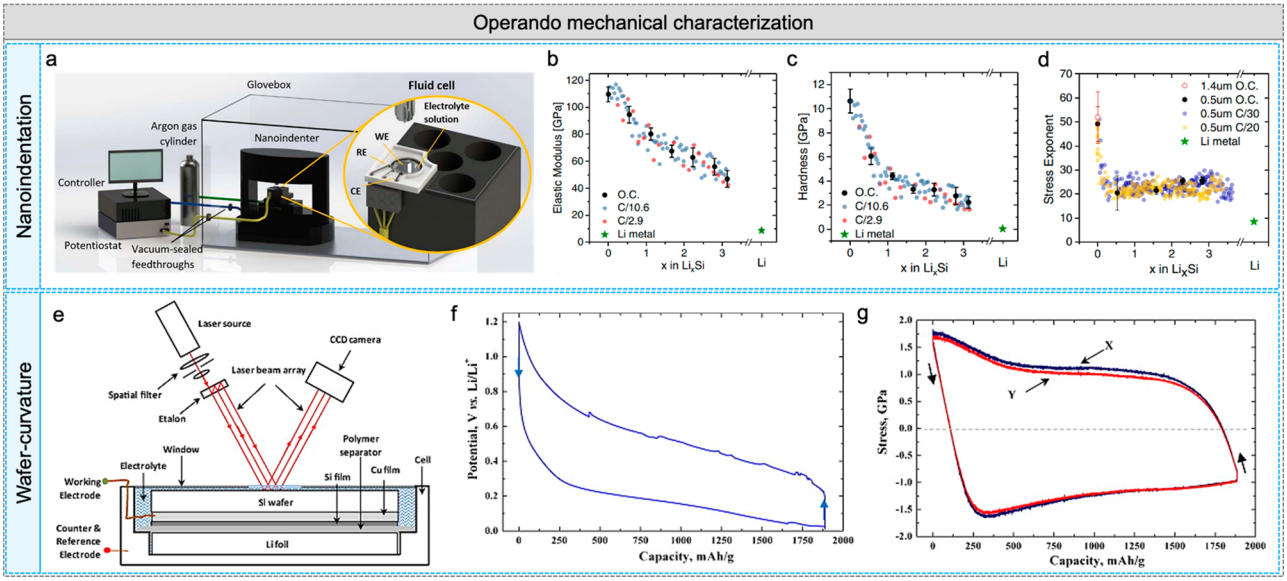

Figure 22. Mechanical characterization methods of electrode materials during electrochemical reactions. (a) Nanoindentation measurements of the (f) elastic modulus, (g) hardness, and (h) creep exponent of Si as a function of the Li content. Reproduced from ref 25. Copyright 2017 IOP Publishing. (e). Wafer-curvature measurement of Si thin film electrode and the corresponding (b) potential and (c) stress as a function of capacity. Reproduced from ref 138. Copyright 2010 Elsevier.

liquid electrolyte.[154,383] In addition to the high heterogeneity, small characteristic size, intricate microstructure, and electrolyte sensitivity, mechanical characterization is further complicated by the fact that the mechanical properties of active materials in particular are continuously evolving during the battery operation thanks to their dynamic composition and fatigue during cycles. For instance, Si is brittle in its pristine state but becomes ductile upon moderate Li insertion.[291] The fracture strength of transition metal oxide secondary particles is highly dependent on the state-of-charge and cycle number, as these two variables are linked with residual stresses and damage accumulation.[384,385] It is also possible that the mechanical response may differ in the equilibrium versus nonequilibrium thermodynamic states.[139,386] It is therefore desirable to integrate electrochemical and mechanical testing to perform measurements in situ and operando. These conditions require environmental control since reacted active materials and electrolytes generally cannot be exposed to the oxygen and moisture in the atmosphere. Hence, mechanical characterization of electrode materials is involved and often requires unconventional setups and revised mechanical models.

Table 2 surveys literature reports of characterization techniques applied to battery materials. Nanoindentation (also known as instrumented indentation) is the most used tool because of a combination of reliability (well-established technique), versatility (provides wide range of properties), and convenience (does not require complex sample geometry or intricate fixtures). Elastic modulus and hardness measurements using nanoindentation are standardized under the ISO14577 and ASTM E2546 and are widely used across different fields. The test consists of a rigid tip (usually diamond) pressing against a flat surface of the sample creating an indentation while tracking applied load and displacement. From these data and the knowledge of the precise (calibrated) shape of the tip

https://doi.org/10.1021/acs.chemrev.2c00002
Chem. Rev. 2022, 122, 13043−13107

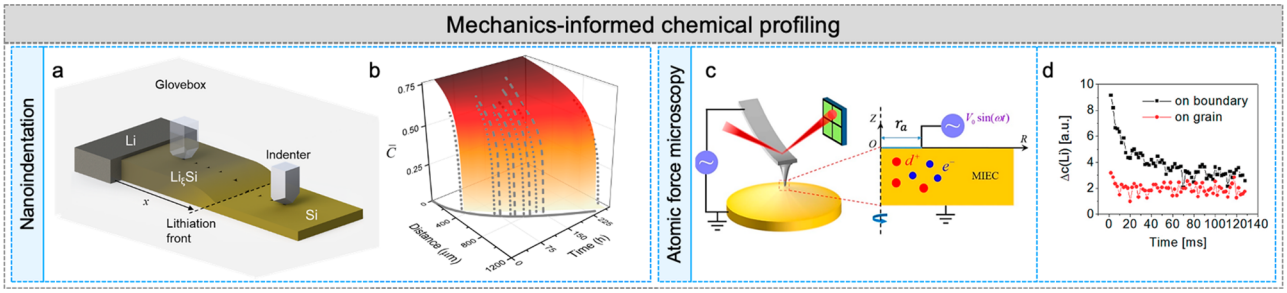

Figure 23. Examples of mechanics-informed chemical profiling. (a) A Si film probed via nanoindentation undergoing spontaneous lithiation. Reproduced from ref 103. Copyright 2020 Elsevier. (b) Spatiotemporal distribution of Li in the film obtained through the functional relationship between the mechanical properties and the chemical composition. (c) Schematic of electrochemical strain microscopy. Reproduced from ref 413. Copyright 2020 IOP Publishing. (d) Local volumetric change is used to infer the change in Li content upon application a voltage bias. Reproduced from ref 415. Copyright 2010 American Chemical Society.

geometry, the mechanical properties can be derived using well-established mechanics models. Measurements will correspond to the global properties of a composite material as long as the indentation depth is much greater than the characteristic size of the constituent phases. For example, Wang et al.[163] showed that the change in global modulus and hardness of a Si electrode (Si nanoparticles in a carbon black and polymer binder matrix) during (de)lithiation is dominated by the change in the porosity, which in turn is dictated by the volume change of the Si nanoparticles. Conversely, the intrinsic properties of individual material phases can be characterized if the indentation size is sufficiently small compared to the characteristic size of the phase and the stiffness mismatch between the different phases is not overwhelming.[64,387,388] Indentation creep exponent and strain-rate sensitivity may also be measured by defining an indentation strain rate and assuming a power law relationship with the applied stress.[25,389−391] Other methods using a sharp indenter tip to crack and scratch the sample have also been used to characterize fracture toughness[154,384,385] and adhesion strength,[392] respectively.

One advantage of nanoindentation compared to other techniques such as tensile testing is that hundreds of indents can be performed on a single sample, enabling high-throughput testing.[25,64,393] Figure 22a highlights a setup that enables *operando* nanoindentation. A nanoindenter installed inside a glovebox filled with inert gas holds a custom fluid cell that connects to an electrochemical station. An electrode in the center undergoes a sequence of indentations while the cell is being (dis)charged. Figure 22b,c shows the results of the experiment on a Si thin film half-cell. Each indentation gives one measurement of elastic modulus, hardness, and stress exponent at the corresponding specific capacity. Hence, the properties can be plotted as a function of Li content as shown in Figure 22b,c. Note that all the properties vary significantly throughout the operating range.

A variation of traditional nanoindentation uses a flat punch tip geometry to perform compression tests on nano- or micropillars. This test, often performed inside an electron microscope, gives the full uniaxial material response (stress−strain curve); however, the setup is significantly more involved. Using this approach, Feng et al.[394] found that the ultimate strength of $LiCoO_2$ pillars was uniform in the pristine state, but upon a single (de)lithiation cycle, the ultimate strength decreased significantly and varied widely. This variation indicates that the distribution of the defects responsible for the reduced strength is nonuniform. Flat punch compression tests were also applied to study the strength of the secondary particles (hierarchical structure) characteristic of the coprecipitation method.[385] The authors found that secondary particles are significantly fragilized during delithiation, and the strength is only partially recovered during lithiation.

The wafer-curvature technique is another widely used tool in the mechanical characterization of electrode materials.[138−141] It can probe the evolution of the biaxial stress in thin film electrodes during electrochemical reactions. Figure 22e illustrates the experiment: the film expansion is constrained by the substrate in the in-plane direction, creating biaxial stress that slightly curves the substrate.[138] With the known substrate properties and dimensions, the stress can be estimated. Figure 22f,g shows the electrochemical potential and stress as a function of specific capacity for a Si electrode. Initially, the compressive stress increases sharply with lithiation, and at ∼250 mAh/g, there is a distinct change in slope, marking the transition from elastic to plastic deformation regime (yield at ∼1.6 GPa). Further lithiation shows a gradual decrease in the flow stress. At ∼1900 mAh/g, the applied current is reversed, and delithiation starts. Consequently, the compressive stress initially decreases (elastic unloading) and then switches to tensile stress (elastic loading) before yields at ∼0.5 GPa. Using different charging protocols, Pharr et al. and Sethuraman et al. proposed methods of estimating the biaxial modulus,[407] fracture energy,[404,406] and strain rate strain-sensitivity[139] from water-curvature measurements. For example, charging the device at different C-rates is equivalent to varying the strain rate, thus determining the strain-rate sensitivity.[139]

There are a few literature reports on uniaxial tensile tests applied to energy materials (e.g., Li metal[200,408] and Si nanowire[409]). The major challenge lies in the characteristic size of active materials in batteries and the difficulties in preparing and gripping the sample. Similarly, single-edge-notched beam toughness measurements are suitable for materials of compatible characteristic size, such as solid electrolyte pellets.[412] In addition to mapping topography, advanced AFM-based techniques can probe elastic modulus but are usually applied to soft or ultrathin materials, such as SEI layers. A digital image correlation of electrodes coated with fluorescent silica nanoparticles to form the speckle pattern can be used to track the strain field during electrochemical reactions.[410,411]

It is noteworthy that mechanical characterization of some energy materials sometimes requires original assumptions (e.g., about homogeneity, isotropy, and absence of microstructural features) to be relaxed. For example, wafer curvature, originally

https://doi.org/10.1021/acs.chemrev.2c00002
Chem. Rev. 2022, 122, 13043−13107

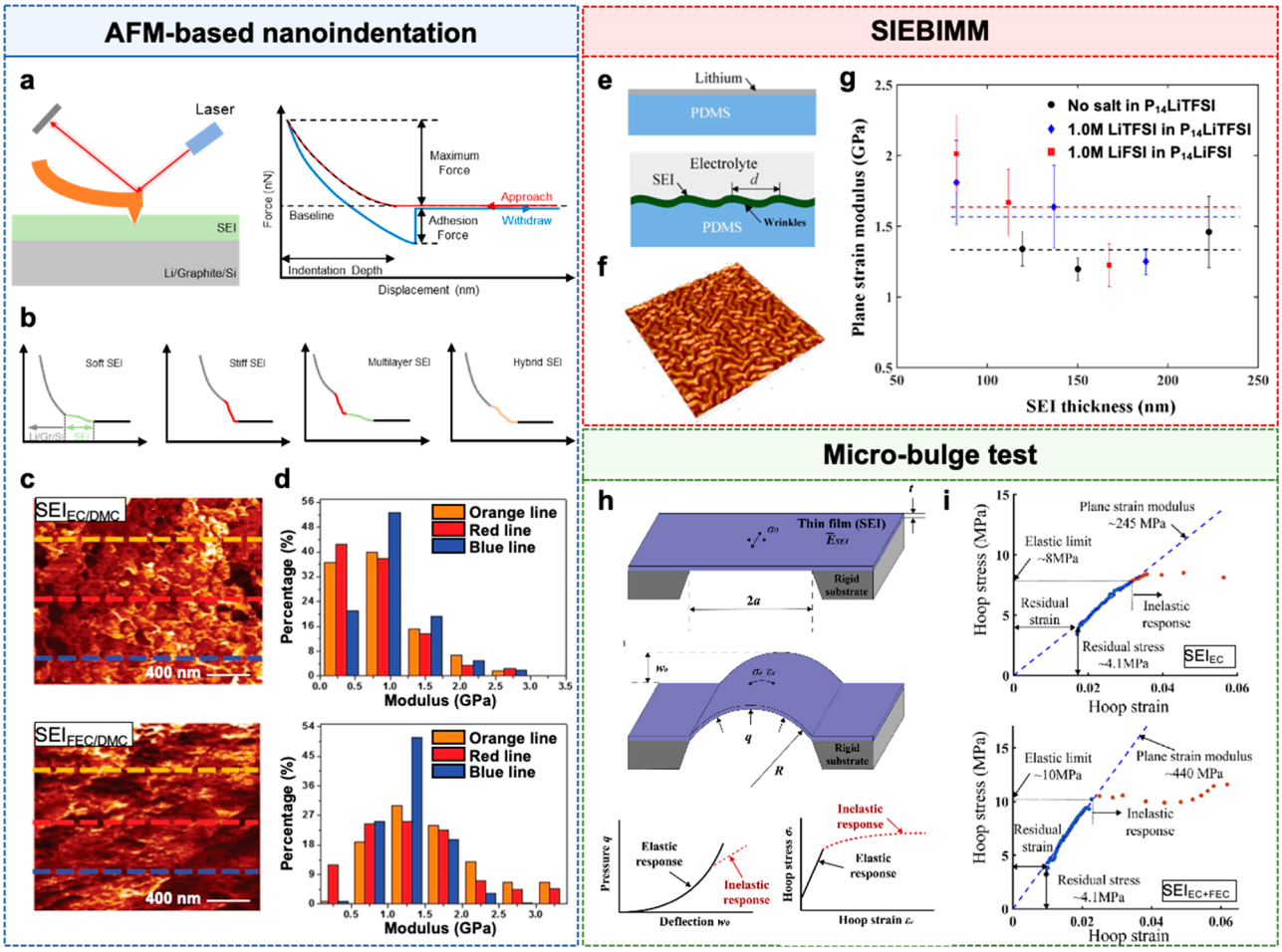

Figure 24. (a) Schematics of the AFM-based nanoindentation. The force−displacement curve is used to extract the mechanical properties of the sample. (b) Typical force−displacement curves of the SEI with different nanostructures. (c, d) Distributions of Young's modulus of SEI formed in different electrolytes. Reproduced from ref 145. Copyright 2018 Wiley-VCH GmbH. (e) Schematic of strain-induced elastic buckling instability for mechanical measurements. After contact with the electrolyte, the flat Li thin film on the PDMS substrate gets converted to a SEI, resulting in a state of compressive stress in the SEI and thus the SEI buckling. (f) AFM images of the surface topography for buckled SEI. Reproduced from ref 151. Copyright 2018 American Chemical Society. (g) Plane-strain modulus as a function of SEI thickness for the three electrolytes. (h) Schematic of microbulge test. (i) Hoop stress vs hoop strain of the SEI in different electrolytes, which gives the residual stress, elastic limit, plane strain modulus, and inelastic response. Reproduced from ref 424. Copyright 2020 Elsevier.

developed for homogeneous films, has been used in combination with X-ray diffraction (XRD) to understand the complex mechanical behaviors of sulfur cathodes, which include both sulfur particles, binders, carbon additives and pores.[401] This study revealed how the distinct solid-to-liquid and liquid-to-solid phase transformation characteristic of sulfur electrodes influence the average stress in the electrode. The stress estimation in this case does not correspond to the intrinsic flow stress of sulfur, but rather the combined global response of the ensemble and thus will highly depend on the packing density. Another example is the measurement of the fracture toughness of polycrystals and anisotropic particles using nanoindentation.[154] The crack patterns in these systems are often irregular, differing from the ideal half penny shape assumption, and the critical load is sensitive to the residual stresses introduced electrochemical cycling.[384] Such simplifications are necessary but imply that measurements do not represent intrinsic properties. Despite simplifications, these methods are still useful to understand the influence of the environment, chemical reactions, and damage accumulation on the chemomechanical behaviors. Current limitations emphasize the importance of ongoing research on uncertainty quantification, cross-validation using different techniques, and new methods to advance capabilities.

Lastly, we highlight how mechanical characterization has been adapted to probe elemental composition (Figure 23). Recall from Figure 22a−d that it is possible to fully characterize the relationship between mechanical properties (e.g., elastic modulus) and the composition using *operando* nanoindentation. Hence, given that this relationship is known and monotonic, it is possible to locally probe the Li concentration in an electrode by simply probing its mechanical properties. Vasconcelos et al.[103] introduced this method and used it to characterize the Li kinetics of amorphous Si. The experiment consisted of an array of nanoindentations performed on a Si film with nonuniform Li distribution (Figure 23a) at varying times. The corresponding concentration at each indent was determined from its functional relationship with mechanical properties, generating the spatiotemporal concentration map in Figure 23b. Another technique called electrochemical strain microscopy (ESM) uses the AFM tip displacement to map spatial variation in

https://doi.org/10.1021/acs.chemrev.2c00002
Chem. Rev. 2022, 122, 13043−13107

diffusion times. Figure 23c illustrates the experiment: a voltage bias applied to the cantilever drives ion redistribution underneath the tip, and the resulting cantilever deflection informs the change in concentration.[413,414]

5.1.2. Solid Electrolyte Interphase. The SEI, a passivation layer formed on the electrode surface from electrolyte decomposition, is essential for reactions in batteries and critically governs the battery stability. However, the composition−structure−property relationship of the SEI remains largely unknown so far, which hinders the improvement of battery performance through engineering better electrolytes or artificial SEIs. The major challenges come from the difficulties in probing the SEI with a thin thickness (∼10 nm), a complex substructure, and a highly air-sensitive nature. AFM-based nanoindentation offers the ability to conduct direct mechanical measurement at the nanoscale (nano-Newtons in force and nanometers in displacement), making it an ideal technique for the mechanical characterization of SEIs with small thicknesses and complex structures.[150,416] During a typical AFM-based nanoindentation test, the AFM probe is lowered toward the sample and pressed into the sample surface. The indentation force applied to the sample is estimated by the Hookean relationship using the calibrated cantilever stiffness and the recorded probe deflection (Figure 24a). The Young's modulus of the surface layer was determined by fitting the contact mechanics model to the obtained force−displacement curves.[417] The representative force−displacement curves for nanoindentations on different SEIs are illustrated in Figure 24b. Those characteristic features in the mechanical response of SEIs can be used to estimate their mechanical properties, chemical compositions, and influence on the electrochemical performance of batteries (Figure 24c,d).[145]

Because of the dynamic fracture and reformation, the SEI formed on a Si anode material is highly inhomogeneous in chemical composition and thickness ranging from tens to hundreds of nanometers. By tracing the mechanical response of the SEI at different indentation depths, Zheng et al. virtually reconstructed the multilayered structure of the SEI formed on a thin film Si anode with an EC-based electrolyte (1 M $LiPF_6$ in EC/DMC).[418] The dynamic coexistence of single-layered, double-layered, and multilayered structures with various Young's moduli and thickness has been observed and used to improve the SEI model on the Si anode material. A more detailed failure analysis of the bilayered SEI on the Si anode was recently performed by Guo et al. using in situ AFM.[134] They obtained an elastic modulus of ∼2.3 GPa for the outer SEI while a slightly higher modulus for the inner layer SEI.

Nanoindentation measurements on the native SEI formed on the Li metal are less explored because of the challenges of mechanical measurement of a thin SEI on the dendritic Li metal.[419,420] Instead, the mechanical stability of artificial SEIs on the Li metal anode, a protective layer purposely constructed to stabilize the Li plating/stripping, has been frequently studied.[419,421] As the artificial SEI is formed by controlled chemical/electrochemical reactions or thin-film fabrication techniques (e.g., atomic layer deposition, ALD), it has a well-defined composition and structure, and a smooth morphology that are more favorable for mechanical mapping. It is well acknowledged that a good artificial SEI should process high mechanical strength and serve as a physical barrier against dendrite nucleation and propagation during Li plating/stripping. The improvement of SEI mechanical strength can be achieved by embedding inorganic particles into an organic matrix. Liu et al. designed a composite artificial SEI layer composed of Cu_3N nanoparticles joined together by styrene butadiene rubber (SBR).[422] The packed inorganic phase with a high stiffness can act as a barrier to suppress Li dendrite propagation, while the polymeric phase with excellent fracture resistance can maintain the mechanical integrity of the SEI from the significant interface fluctuation during battery cycling. Nanoindentation measurements show that the elastic modulus of the composite SEI is around 0.8 GPa, in good agreement with the theoretical prediction that a modulus on the order of 1.0 GPa can suppress the nucleation and growth of Li dendrites. The mechanically robust SEI can also be constructed through controlled electrochemical/chemical reactions at the Li metal surface. Mao et al. proposed a general electrochemical approach to build the artificial SEI with alternating inorganic−organic-inorganic (I−O−I) multilayer structures.[421] This I−O−I SEI possesses excellent mechanical properties with both rigidity and elasticity. The middle organic layer (3.5 ± 0.9 GPa) mechanically behaves like a cushion layer to accommodate the interfacial fluctuation during Li plating/stripping while the stiff inorganic layer (168 ± 26 GPa) prevents the dendrite penetration into the organic layer. With these features, the I−O−I SEI can efficiently suppress dendrite growth and thus provide improved protection for the Li metal.

Although AFM nanoindentation offers a quantitative characterization of the mechanical properties of SEI, the elastic moduli fitted from the force microscopy usually show a large degree of scatters for an area of limited size. In addition, even for the same electrode and electrolyte system, statistical information on the SEI modulus from different reports can have considerable variations. The scatters and variations may be originated from several sources of uncertainties involved in the AFM nanoindentation. First, it is challenging to exclude the substrate effect when performing nanoindentation on the SEI with a typical thickness of tens to hundreds of nanometers. This substrate effect can become more dominant when measuring the mechanical properties of the thin SEI on the soft Li metal anode. Second, the surface roughness of native SEI can substantially alter the contact area between an AFM tip and SEI. Under this circumstance, fitting the force−displacement curves using the classic contact mechanics model that assumes perfect contact between the tip and sample can cause significant errors. Third, the different conditions adopted for preparing the fragile samples may cause variations in the measured results. For example, most ex-situ nanoindentation measurements require the rinsing and drying of samples before testing, which may alter the composition and structure of the SEI.[423] To eliminate these variations, Yoon et al. adopted the approach called strain-induced elastic buckling instability for mechanical measurements (SIEBIMM) to in situ measure the plane strain modulus of an SEI that results from reactions between a Li thin film and an ionic liquid electrolyte (Figure 24e−g).[151] Recently, the same group developed a new technique that combines AFM and a membrane-bulge configuration to accurately measure the stress−strain behavior of SEI including the onset of inelastic response (Figure 24e−h).[424] Figure 24 shows the hoop stress vs hoop strain of the SEI in different electrolytes, which gives the residual stress, elastic limit, plane strain modulus, and inelastic response. Other techniques such as electrochemical quartz crystal microbalance with dissipation monitoring (EQCM-D)[425] and

https://doi.org/10.1021/acs.chemrev.2c00002
Chem. Rev. 2022, 122, 13043−13107

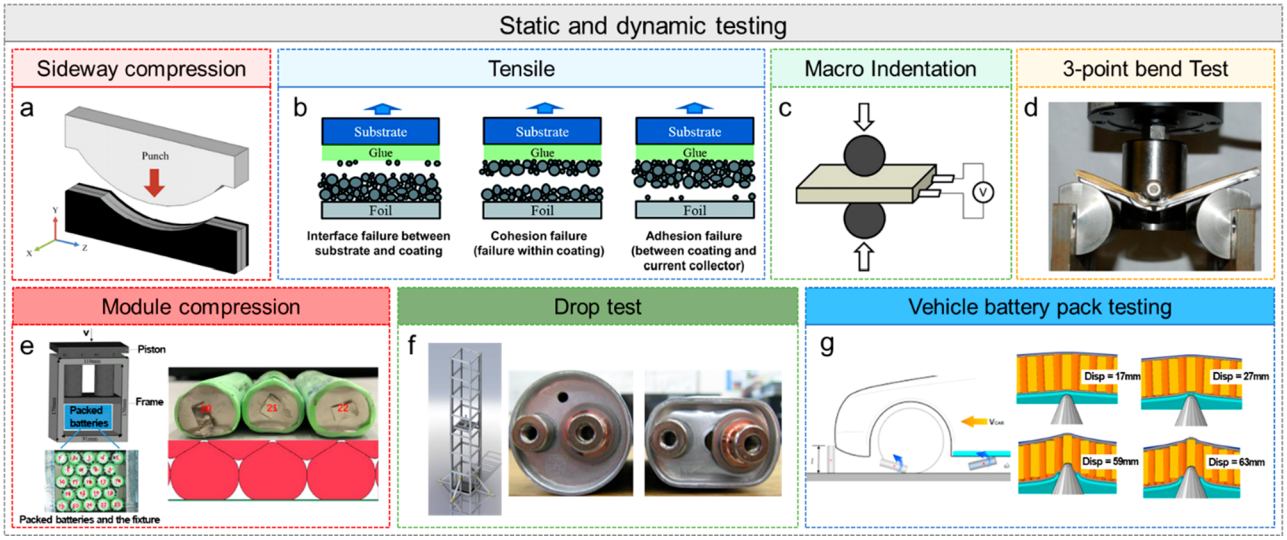

Figure 25. Schematic of (a) in-plane punch indentation on a Li-ion pouch cell. Reproduced from ref 426. Copyright 2015 Elsevier. (b) Tensile testing along the out-of-plane direction which shows three types of failure. Reproduced from ref 427. Copyright 2018 Royal Society of Chemistry. (c) Micro indentation using a spherical tip. Reproduced from ref 431. Copyright 2016 Elsevier. (d) Pouch cell under 3-point bending test. Reproduced from ref 434. Copyright 2012 Elsevier. (e) Quasi-static battery module compression test and the caused deformation of the battery packs. Reproduced from ref 436. Copyright 2020 Elsevier. (f) Dry cell drop test equipped with a high-speed camera to record the deformation. Reproduced from ref 437. Copyright 2014 Elsevier. (g) Simulated indentation process of a punching object into the battery pack of a vehicle. Reproduced from ref 350. Copyright 2014 Elsevier.

acoustic wave method[153] have also been utilized for determining the mechanical strength of native and artificial SEIs.

5.1.3. Cells and Battery Packs. Numerous characterization techniques are available to test the mechanical behavior of the battery cell and its components. On the basis of the desired property to be measured, test parameters can be varied: plane of loading, the magnitude of loading, quasi-static or impact loading, and battery component or module testing. The in-plane constrained compression test, as depicted in Figure 25a,[426] was used to study the buckling behavior of the pouch cells under uniform or nonuniform loading. In addition to studying the kink and shear band formation, in-plane compression tests are helpful in measuring critical bucking stresses and stress−strain relations.[357] Figure 25b illustrates the tensile test method for studying the electrodes under high shear leading.[427] By mounting the test specimen at different orientations relative to the tensile loading direction, the adhesion strength of the electrode can be measured accurately for a combined tensile/shear loading. The interfacial strength of the current collector and the electrode is often measured using the peeling test. From the results of 180° peeling tests, Guo et al.[428] studied the effects of aging and variation of the state of charge on the interfacial strength of graphite anode. The experimental results show a higher interfacial strength of charged electrode than the pristine electrode. In situ electrode bending tests are used to measure the effective mechanical behavior of electrodes during electrochemical cycling. Xie et al.[429] used in situ optical analysis to measure the bending deformation in the bilayer film electrodes to capture the nonlinear behavior of stress and modulus with the state of charge. To evaluate the local adhesion properties of an electrode, Son et al.[430] used a V-shaped microblade tool. As the tool cuts through the electrode at different depths, it measures the horizontal and vertical forces, directly measuring the adhesion strength.

Figure 25c[431] depicts the schematic of macro indentation tests using steel balls on the assembled cells. The indentation tests effectively perform controlled deformation, fragmentation/tearing of battery components, and short circuits induced by localized punching. Zhu et al.[432] studied the effect of different tip diameters on cells with various capacities using mechanical abuse loading. The inherent variation in the mechanical properties of the cell components and nonuniform strain conditions induced by indentation leads to the failure of the cell separator and thus causes short-circuiting. Dixon et al.[433] examined the effect of the presence of electrolytes on the outcomes of macro indentation tests. For the same indentation loads, the liquid electrolyte-filled pouch cells exhibit lower stress and displacement values than the dry cells. The location of indentation also plays an essential part in cell failure initiation. It is important to note that a single kind of test cannot provide information regarding various possible failures that can occur in the battery cell. For example, the presence or absence of the pouch casing around the cell does not significantly affect the results of macro indentation tests. However, the three-point bend tests (Figure 25d) show that the presence of even a thin pouch casing confines the cell from extreme buckling deformations.[434] Furthermore, instead of mechanical abuse loading, the application of small loading can also provide vital insights into the failure evolution during the operation of the battery cells. Goodman et al.[435] used three-point bend tests to apply low stresses on cells using three-point bend tests. Although the cycled cells show highly localized damage, any large-scale deformation or significant capacity loss did not occur.

When individual cells are stacked in a module, the load distribution can be nonuniform for each cell in the module. Hu et al.[436] studied the deformation of a cell module during crushing load, as depicted in Figure 25e. The impact loading generated row by row deformation in the module. The failure behavior of the cells in a module differs from that of an

https://doi.org/10.1021/acs.chemrev.2c00002
Chem. Rev. 2022, 122, 13043−13107

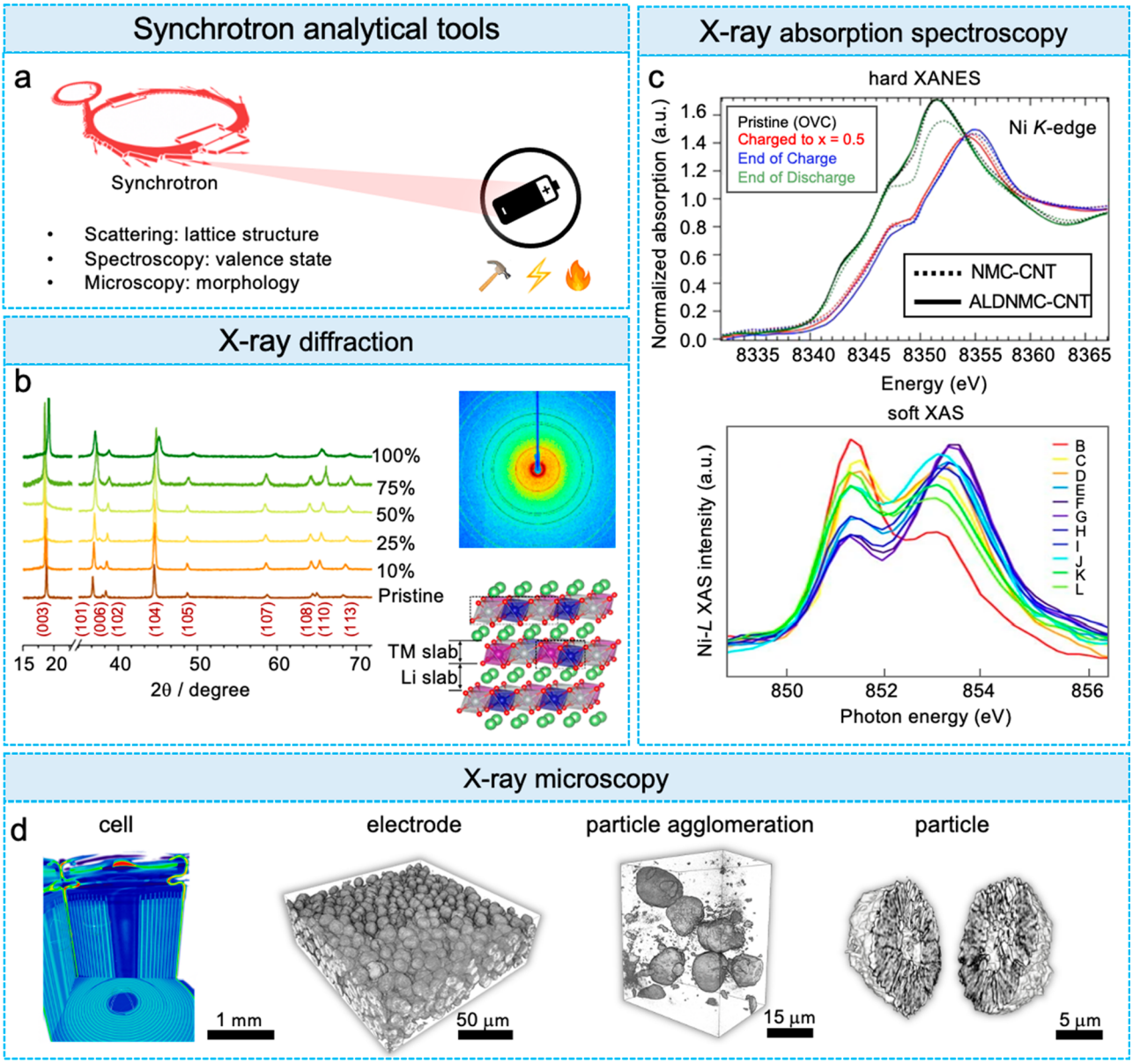

Figure 26. Synchrotron radiation (SR)-based experimental techniques for studying the structure, morphology, and chemical state of battery materials. (a) Schematic diagram of synchrotron-based battery study. (b) X-ray diffraction patterns of pristine and delithiated NMC622 powders, offering insights into the lattice distortion and transformation of the battery cathode at different SOCs. Reproduced from ref 465. Copyright 2020 American Chemical Society. (c) X-ray absorption spectroscopy over the Ni K-edge (top) and Ni L-edge (bottom) reveals different aspects of the redox reaction in the battery cathode. Reproduced from refs 453 and 455. Copyright 2015 American Chemical Society. Copyright 2013 Springer Nature. (d) Multiple length-scale X-ray tomographic imaging of battery from the cell scale to the particle level. Reproduced from ref 178. Copyright 2019 Wiley-VCH GmbH.

individual cell. Impact tests are thus necessary for ensuring the safety of batteries in a real-world application. Figure 25f[437] depicts the experimental setup where a cart carrying the weights drops on the stationary cylindrical Li-ion battery cells. The numerical FE study using homogenized models can efficiently simulate such experimental results for simple cell geometries. Kisters et al.[438] performed the impact test using a punch that hits the cell at various speeds. The force necessary to generate a short circuit with varying impact speed is different for elliptical cells (multilayer wounded cells) and for the stacked pouch cells. The dynamic behavior of constituting materials and the cell architecture significantly control the behavior under impact testing.

The effect of multiple impacts on the failure of prismatic Li-ion battery cells was studied by Chen et al.[439] using drop weight impact tests. As per anticipation, the low impact velocity is sustainable for multiple impacts, and the high impact velocity can lead to immediate failure of the battery cells on a single impact. Pan et al.[440] conducted an experimental and numerical study on pouch cells using a cylindrical punch to understand the difference between the failure induced by quasi-static and impact loading. The quasi-static case generates a more concentrated deformation and a smooth shearing fracture line. In contrast, the impact test case is characterized by powder residue and a rough shearing fracture line. From the drop impact tests, Jia et al.[441] measured the effect of the state of charge and loading rate on the failure of $LiCoO_2$ jellyroll

https://doi.org/10.1021/acs.chemrev.2c00002
Chem. Rev. 2022, 122, 13043−13107

battery cells. The increase in the state of charge is accompanied by increased structural stiffness of the battery, and a higher loading rate causes a more drastic fracture of electrodes within the battery. For locomotive usage, crash safety analysis of battery cells is essential. Because of the cost of infrastructure required to perform vehicle crash testing, the insights from impact tests of cell modules can help assess battery cell failure during a vehicle crash. Kukreja et al.[442] performed a numerical study of deformation in a battery pack during a frontal crash of the vehicle. The analysis shows that using collapsible metal tubes and arranging individual cylindrical cells in a bimodal packing distribution substantially reduces impact failure. Xia et al.[350] performed the numerical analysis of the failure because of ground debris of a battery pack situated on the vehicle's floor (Figure 25g). The various constraints of the vehicle design and the required design parameters of the cell and the module direct the best possible solution for the safety of the battery pack.

5.2. Synchrotron Techniques

5.2.1. X-ray Characterization. Synchrotron radiation (SR) is electromagnetic radiation emitted by charged particles moving at relativistic speed in a curved trajectory (see schematic illustration in Figure 26a).[443] The synchrotron facilities generate X-ray beams with high brilliance and flux over a broad electromagnetic spectrum, covering the range from far-infrared (wavelength ∼1000 nm) to hard X-ray (wavelength ∼0.01 nm).[23,444] Various SR-based X-ray techniques have been developed for a wide range of fundamental and/or applied research fields. Specific to the focus of this paper, the SR-based X-ray techniques can offer valuable insights into the batteries' structural and chemical characteristics over different time and length scales, which are key to the battery's functionality.[288,445,446] Depending on the experimental approach and on the type of the measured signals, SR-based X-ray techniques can be grouped into three different categories: XRD, X-ray absorption spectroscopy (XAS), and X-ray microscopy (XRM). These techniques harness different X-ray-to-matter interactions and offer valuable insights into the lattice configuration, the chemical/oxidation state, and multiscale/high-dimensional morphology. In this section, we will focus on the application of SR-based X-ray techniques in studying the chemomechanics of rechargeable batteries.[101,447]

5.2.1.1. X-ray Diffraction. XRD is a powerful tool to fingerprint the lattice structure of crystalline materials. It is often employed to characterize the lattice parameters, the preferred crystallographic orientation, and the microstructure, e.g., strain and grain size. These lattice-related material properties are very important to battery research. Depending on the sample form and on the configuration of the experimental setup, there are a few different types of XRD approaches, including X-ray single-crystal diffraction, X-ray powder diffraction, and X-ray Laue diffraction. Regardless of the formality, the fundamental aspect of the XRD is the same: incident X-rays are diffracted by the crystalline material preferentially in discrete directions that satisfy the Bragg condition. By analyzing the XRD patterns of battery materials under different conditions or at different electrochemical states, the atomic-scale structural evolution can be monitored. While XRD is broadly available through conventional laboratory XRD setups, the synchrotron-based XRD opens new scientific opportunities for battery research by enabling in situ and operando types of measurements with exceptional data quality and high temporal resolution. It has been demonstrated that the battery materials' lattice parameters and the phase transition phenomenon can be tracked by conducting synchrotron XRD measurements on working battery cells as the SOC is tuned electrochemically.[448] In addition to the electrochemical cycling, XRD is also compatible with various controls of sample environments, which can provide valuable insights into other aspects of the material property. Here we choose to discuss a study on the thermal stability of the NMC cathode at different SOCs as an example.

Thermal stability is one of the most important performance metrics concerning the safety of Li-ion batteries.[449] It is highly desirable, from both scientific and practical perspectives, to systemically understand the transformations of the battery electrode's structure and chemical state upon cycling under elevated temperature. This knowledge can critically inform the design of battery materials with superior thermal stability. Tian et al.[450] combined ex situ chemical delithiation and an in situ hot-stage XRD technique to study the phase transformation of a $LiNi_{0.6}Mn_{0.2}Co_{0.2}O_2$ (NMC-622) cathode at different SOCs upon exposure to high-temperature conditions. As shown in Figure 26b, the room-temperature XRD patterns of NMC-622 cathodes at the pristine state and at different delithiation levels exhibit good similarity, indicating that the lattice structure of these samples mostly retained the rhombohedral space group, $R\bar{3}m$, except for the 100% delithiated cathode. The peak broadening and shifting indicate a decrease of lattice parameters in the *c* direction. In contrast, under an elevated temperature, unwanted phase transformation occurs in the NMC-622 cathode, featuring a layered to spinel and/or rock-salt structural transition. The authors reported that the onset temperature for the phase transition is negatively correlated with the SOC. More specifically, in a 50% delithiated sample, the phase transition occurs at ∼300 °C; in a 70% delithiated sample, it occurs at ∼200 °C. The thermally driven phase transformation is accompanied by oxygen release from the cathode material in the form of oxygen gas, which poses a potential battery safety hazard. The synchrotron XRD technique has been broadly adopted in battery research. For a more comprehensive discussion of battery research using the synchrotron XRD technique, we refer to a review article by Bak et al.[451] Pair distribution function (PDF) is a notable development in the synchrotron XRD technique because it is capable of utilizing both the Bragg and the diffuse scattering signals. We refer to a recent review article by Zhu et al.[452] for an in-depth discussion of the PDF technique and its application in functional material research.

5.2.1.2. X-ray Absorption Spectroscopy. XAS has been broadly used for studying the local electronic structure, compositional, chemical, and structural characteristics of the sample. It can be applied to materials in gas, liquid, or solid forms. XAS measures the material's response to X-rays of different wavelengths and, thus, it greatly benefits from utilizing an intense and energy-tunable synchrotron source. A synchrotron XAS experiment is very versatile as it can be carried out in ex situ, in situ, and operando approaches, all of which are applicable to battery research. In a full XAS spectrum, there are two regions termed X-ray near edge structure (XANES) and extended X-ray absorption fine structure (EXAFS), respectively. The XANES region refers to the energy window from ∼50 eV below to ∼50 eV above

https://doi.org/10.1021/acs.chemrev.2c00002
Chem. Rev. 2022, 122, 13043−13107

the absorption edge. XANES is sensitive to the chemical state and is often used to quantify the valence state of the targeted element. In a battery cathode material, the lithiation/delithiation is often accompanied by the redox reactions of the transition metal cations. On one hand, XANES has become the go-to technique for tracking the electrochemical state of the battery electrode. EXAFS, on the other hand, covers a broader energy range, from the pre-edge region to 500−1000 eV above the edge. The EXAFS signal features a weak intensity oscillation that can be used to retrieve useful lattice structural information, including the bond length, coordination number, and the degree of local structural disordering. It is useful to note that, in this field, these terminologies, e.g., XANES and EXAFS, often refer to hard X-ray XAS experiments without specification.

As an example, here we discuss a study by Wise et al.,[453] in which the authors performed operando hard X-ray XANES experiments to study the effect of Al_2O_3 coating on a $LiNi_{0.4}Mn_{0.4}Co_{0.2}O_2$ (NMC442) battery cathode. The transition metal elements' oxidation states can be quantified by comparing the absorption edge energy and the shapes of XANES spectra. As shown in the top panel of Figure 26c, XANES spectra over the Ni K-edge were measured for the NMC442 cathodes with and without the Al_2O_3 coating through ALD. Upon battery charging, an obvious energy shift of the Ni K-edge XANES data is observed in both samples, indicating that the oxidation state of the Ni cation changes from Ni^{2+} to Ni^{3+} and finally to Ni^{4+}. The authors further compared the spectra of the bare and ALD-coated electrode samples at charged and discharged states. There is a shoulder peak at around 8347 eV that appears to be suppressed in the ALD-coated sample. This indicates that the ALD process has modified the local atomic environment around the Ni cation. Overall, the Ni K-edge XANES appears to be more reversible upon cycling for the ALD-coated electrode, echoing the improved electrochemical performance. The XANES data over Co and Mn edges were also collected, and the difference between bare and ALD-coated electrodes was relatively marginal. Combining the XANES measurements for Ni, Co, and Mn, the authors revealed that their ALD coating process selectively impacts the Ni cation's local environment and, therefore, promotes the cathode material's structural robustness against high-voltage cycling.

Compared to the hard XAS, XAS in the soft X-ray regime can offer a unique sensitivity with depth-dependent signal detection. In particular, there are three different modes for soft XAS signal detection: transmission, fluorescence yield (FY), and electron yield (EY). The transmission soft XAS probes the bulk information but is limited to very thin samples. The FY collects fluorescence photons from the sample and, therefore, can probe up to ∼100 nm (nm) underneath the surface. The EY signal is confined to the sample surface within a few nanometers' depth, providing an exceptional surface sensitivity. Integrating these modalities could provide a depth dependent soft XAS signal to evaluate the local chemistry at different depths. For example, the comparison of EY signal versus the FY signal in the NMC cathode has been used as key evidence for the surface reconstruction phenomenon, which is an important mechanism for the surface degradation in layered battery cathode.[454]

Here we briefly discuss a work by Liu et al.[455] that demonstrates an operando soft XAS on $Li(Co_{1/3}Ni_{1/3}Mn_{1/3})O_2$ cathodes in polymer electrolytes. As shown in the bottom panel of Figure 26c, the soft XAS spectra over the Ni L_3 edge clearly exhibit a twin-peak feature with competing intensity that evolves upon battery cycling. Quantification of the Ni's valence state is relatively easy in this case because one could simply calculate the ratio between the intensities of the two peaks. Although there are still significant technical challenges associated with the limited soft X-ray penetration, making it difficult to conduct soft XAS measurements in situ, it still attracts a strong interest from the battery community because of the fact that we can access not only the transition metal L-edges but also the edges for some other elements that could be important to the battery performance, e.g., the oxygen K-edge.

Finally, we highlight that, when energy resolving power is added to the detector side, soft X-ray emission spectroscopy (soft XES), and resonant inelastic X-ray scattering (RIXS) are facilitated. It has been demonstrated that RIXS over the oxygen K-edge has a unique advantage for fingerprinting the oxygen anionic redox activity,[456] which is being actively pursued by the battery community.[457]

5.2.1.3. X-ray Imaging. Since the discovery of X-rays at the end of the 19th century,[458] X-ray imaging, as a nondestructive technique for visualizing the sample's internal structure, has been widely applied. When implemented at the synchrotron, the strength of X-ray imaging techniques is further enhanced. Without going into too much detail, we divide synchrotron-based imaging methods into two categories, full-field imaging and scanning imaging, based on the experimental protocol. On the one hand, full-field imaging refers to imaging techniques that can obtain a 2D image of a sample in a single exposure. The scanning imaging technique,[244] on the other hand, utilizes a focused X-ray spot to scan the sample, building up a 2D image in a pixel-by-pixel raster scan. These two imaging modalities can both operate at different spatial resolutions. Advanced X-ray focusing optics plays an important role in determining the imaging resolution regardless of the data acquisition strategy. One exception is the coherence-base diffractive imaging approach, which takes coherent diffraction patterns as input and retrieves the real-space wavefront computationally. Therefore, coherent X-ray imaging methods are not limited by the X-ray optics and have the potential to achieve very high spatial resolution. All these imaging methods benefit from the high brilliance synchrotron radiation and have been applied to battery research.

We show, in Figure 26d, multiscale 3D X-ray tomographic imaging results on battery materials. The 18650-type cylindrical battery cell can be imaged using the micro-tomography technique. The cell-level structural features and defects can be visualized for understanding the degradation of the cell, e.g., internal soft short. Synchrotron microscopy with an ultrafast frame rate was also applied to imaging the thermal runaway process.[459] The composite cathode can be imaged using hard X-ray holotomography, which is sensitive to both the strong absorbing transition metal oxide particles and the carbon and binder matrix.[176,178] Secondary cathode particles and their agglomeration can be studied thoroughly using nanoresolution transmission X-ray microscopy,[101,460] featuring the battery's mesoscale chemomechanical evolution, which is being actively studied by the battery community.

In addition to reconstructing the sample's 3D structure, X-ray imaging can also offer compositional and chemical sensitivities when it is coupled with the spectroscopic scan. This approach is termed spectro-microscopy and has been quite successful in battery research.[461,462] In a full-field X-ray

https://doi.org/10.1021/acs.chemrev.2c00002
Chem. Rev. 2022, 122, 13043−13107

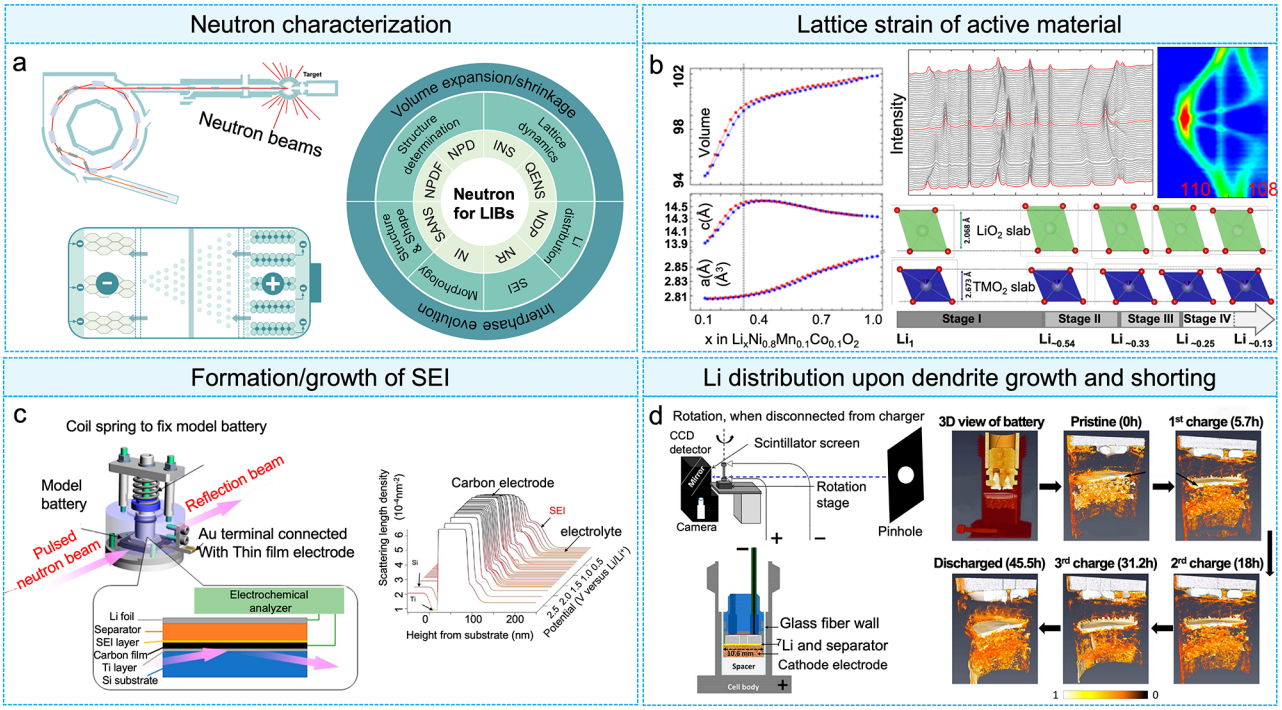

Figure 27. (a) Schematic of neutron diffraction and its applications in LIBs. Reproduced from ref 476. Copyright 1997 Birkbeck College. Schematic of a neutron source. (b) Neutron powder diffraction analysis of the structural evolution and the corresponding change in bond lengths in NMC811 when cycled between 2.8 and 4.6 V. Reproduced from ref 477. Copyright 2021 Royal Society of Chemistry. (c) Formation/growth of the SEI layer on graphite detected via the NR technique. Reproduced from ref 478. Copyright 2016 American Chemical Society. (d) 3D imaging of Li distribution within the cell under dendrite growth and following the electrical short. Reproduced from ref 479. Copyright 2019 American Chemical Society.

spectro-imaging experiment, a series of transmission X-ray images are collected as the incident X-ray energy is tuned across an absorption edge. The intensity of every image pixel changes as a function the energy, formulating a XANES spectrum that is specific to the localized region. Further analysis of the spatially resolved XANES spectra can reveal the local chemistry in 2D and 3D (when combined with tomography). This method is very popular in battery research. For example, Xu et al.[249] used the synchrotron spectro-microscopy to study the Ni valence distribution over two polycrystalline nickel-rich layered cathodes (NMC811) with a similar composition but different crystallographic arrangements: randomly oriented primary grains compared to radially oriented primary grains. They concluded that the gradient of Ni valence distribution could be modulated by the crystallographic arrangements, which is relevant to the tortuosity of the Li diffusion pathways in the particle.

Finally, we point out again that synchrotron imaging methods can offer multiple contrast mechanisms. We have elaborated on the absorption, compositional, and chemical contrasts above. And we would highlight the phase-contrast imaging approach, which is important for imaging weak-absorbing materials (such as low-Z materials, e.g., Li and carbon). Synchrotron phase-contrast imaging has demonstrated advantages in visualizing the battery's microstructure, in particular for imaging the carbon and binder matrix[176,178] and imaging Li dendrite growth.[463,464]

5.2.2. Neutron Characterization. Neutron research started since its discovery by Chadwick in 1932.[466] Unlike the photon−electron interactions in X-ray, neutrons, as charge-neutral subatomic particles, interact directly with atomic nuclei, and possess dominant penetration power. This leads to complementary characteristics with X-ray such as (1) good capability to distinguish adjacent transitional metals (Ni, Co, and Mn), (2) the capability of detecting light elements like oxygen and carbon that play important roles in LIBs, and (3) negligible damage to tested samples compared to that induced by high-energy X-rays.[467,468] Dedicated neutron sources mainly include research reactors and spallation sources. Figure 27a summarizes various neutron characterization techniques for LIBs, typically for examination of the structural evolution and morphology features. While the fundamental principles of each technique have been comprehensively reviewed in recent literature,[469−475] the following subsections briefly introduce a few modalities relevant to the chemomechanical research in LIBs.

5.2.2.1. Neutron Powder Diffraction. NPD follows the same principles as X-ray powder diffraction. Given its higher sensitivity of oxygen anions, NPD provides accurate measurement of lattice parameters, especially for electrochemical processes involving charge compensation of oxygen. In LIBs, it is typical that the anisotropic evolution of the lattice parameters in the layered electrodes (NMC and graphite) causes crack formation/propagation during lithiation/delithiation.[480] Recently, Liu et al.[481] systematically probed the lattice evolution in Ni-rich cathodes ($LiNi_{0.5}Mn_{0.3}Co_{0.2}O_2$, $LiNi_{0.6}Mn_{0.2}Co_{0.2}O_2$, $LiNi_{0.8}Mn_{0.1}Co_{0.1}O_2$, and $LiNi_{0.8}Co_{0.15}Al_{0.05}O_2$) within the voltage window of 2.8−4.6 V via in situ NPD. As shown in Figure 27b, during delithiation of NMC811, the lattice parameter in the *a*-direction follows a monotonic decrease from the initial value of ∼2.87 to ∼2.82 Å, while lattice *c* experiences an increase from ∼14.22 to ∼14.82

https://doi.org/10.1021/acs.chemrev.2c00002
Chem. Rev. 2022, 122, 13043−13107

Å and then a decrease to ∼14.2 Å, resulting in a volume change from ∼102 to ∼97.5 Å^3. This volume collapse is the key driving force for intergranular/intragranular cracks for NMC cathodes.[113] During the lithiation process, the lattice parameters in the *a*- and *c*-directions generally follow a reverse process but exhibit minor deviations from delithiation because of the irreversible Li loss upon the first cycling. Utilizing the same in situ NPD technique, Sørensen et al. studied the fatigue behavior of commercial 18 650 LIBs via probing the evolution of lattice parameters along different directions upon long-term cycling.[482]

5.2.2.2. Neutron Reflectometry. NR, as a novel technique particularly suitable for thin-film structures, emerged in the 1980s. Interested readers can refer to its principles in prior publications.[483,484] NR has the advantage of negligible damage to the samples and good penetration depth, facilitating its implementation in operando experiments. Nowadays, neutron reflectometry has been intensively utilized for LIBs for investigating the time evolution of the scattering length density−depth relation (with subnanometer resolution at ideal conditions) and inferred composition depth profile, formation/growth of the SEI layer, and volume expansion of Si anodes.[478,485−490] The detectable thickness ranges from nanometers to hundreds of nanometers.

Using the typical experimental setup for operando NR shown in Figure 27c, Kawaura et al.[478] probed the chemical components and the detailed growth profile of the SEI layer on a graphite anode during the charging process. The SEI shows an enhanced rate of growth in phase III (voltage below 0.6 V vs Li/Li$^+$) during Li intercalation into graphite.[491] Through isotopic labeling on DEC/EC, Rus et al. verified the two-layer structure of SEI formed on the thin-film tungsten electrode with a thickness of 2−3.5 nm for the inner SEI layer and 3−5 nm for the outer layer.[492] NR is also widely utilized to study the mechanical behavior of Si anodes. Combining operando NR with EIS, Ronneburg et al. studied the evolution of the surface structure of crystalline Si anodes. The degradation of the Coulombic efficiency was ascribed to the formation and the following dissolution of the SEI layer formed on Si, while the SEI layer of higher resistance was found to be formed during each discharge process.[489] Schmidt et al. probed the volume expansion of thin film amorphous Si via operando NR during potentiostatic intercalation of Li$^+$. A nonlinear relation between its volume change and the Li composition was found, and this behavior was attributed to the free volume created during the initial large charge current.[493]

5.2.2.3. Neutron Imaging. NI, also called neutron radiography, was first utilized in LIBs in the 1990s, following the initial experiments implemented by Kallmann and Kuhn in the 1930s.[494] The progress of the past few decades has made it a mature tool to provide 2D and 3D images for the internal structural evolution and spatial distributions of Li$^+$ within LIBs. The contrast mechanism for neutron imaging is mainly the intensity attenuation caused by compositional atoms during neutron beams penetrating the bulk samples that is complementary to X-ray.[495] Compared to X-ray-based imaging/tomography techniques, NI exhibits relatively lower temporal and spatial resolution, with the best spatial resolution about micrometers.[496−498] Nevertheless, the high absorption of neutrons for Li renders neutron imaging an indispensable tool in the study of LIBs, especially for Li dendrite formation/growth and spatial distribution of Li$^+$. Given the relatively higher neutron absorption of ^{6}Li over ^{7}Li, improved imaging contrast can be obtained via replacing ^{7}Li by ^{6}Li. Recently, Zhang et al. probed the spatial distribution of Li$^+$ within vanadium pentoxide (V_2O_5) coin cells via 3D neutron tomography.[499] The Li concentration profiles were successfully obtained at charged and discharged states and a higher Li$^+$ concentration gradient caused by higher charging rates was verified. 2D neutron imaging was utilized by Nie et al. in the study of thick sintered $Li_4Ti_5O_{12}$ || $LiCoO_2$ coin cells, and it was found that the $LiCoO_2$ cathode exhibited a smoother Li$^+$ distribution than the $Li_4Ti_5O_{12}$ anode.[500] Another example is shown in Figure 27d. With operando 2D neutron imaging and static 3D tomography techniques, Song et al.[479] studied the dendrite growth and the consequent internal shorting in a $LiMn_2O_4$ || Li metal half-cell. The large deformation of the $LiMn_2O_4$ cathode was also observed, which was attributed to the Joule heating generated by an internal short.[501] The dynamic redistribution of Li$^+$ after shorting was captured, and the competing depletion and growth of Li dendrite were proposed to account for the postshorting effects.

6. DATA-DRIVEN APPROACH

With tremendous efforts being devoted to improving the experimental techniques for studying the chemomechanics of batteries, experimental data grows at an unprecedented rate. For example, the synchrotron full-field X-ray spectro-microscopy technique generates millions of X-ray absorption spectra in just 10−15 min, which is over 6 orders of magnitude higher than a conventional X-ray spectroscopic experiment. While it is the technological developments that lead to such a high growth rate, the fundamental driving force for these developments is the complexity of our targeted scientific problems. Indeed, the chemomechanical behavior in batteries is highly complex, high dimensional, and multiscale in time and length. These characteristics require a high throughput experiment and big data approach. In many cases, it is not practical to perform manual data analysis. In practice, often only a subset of the experimental data can be analyzed carefully. This is ineffective and risky because important information can and most likely will be overlooked. A natural extension of the current research is to leverage the cutting-edge developments in the field of computational science.

Machine learning stands out as a promising approach and has been adopted by many researchers in the battery field spanning materials discovery, accelerated multiscale materials modeling, and microstructure characterization.[502] The machine learning approach consists of building models based on training data to make predictions or decisions without explicit programming. This is very applicable to battery research because a lot of the relevant data features cannot be explicitly described. For example, on the basis of the high-fidelity data from physics-based simulations, experiments, or both, machine learning methods are utilized to capture complex nonlinear and high-order relationships among a large number of variables. This approach accelerates the material discovery by accurately predicting target properties in new materials. Multiscale structural characterization with X-ray tomography also benefits from the advances of machine learning analysis techniques, which expands the development of predictive battery behavioral models.[503] These studies focus on the individual components of a battery sample, aiming at the improvement of battery performance from enhancing materials functionalities.

Machine learning has also demonstrated significant success at the system-level research and development, involving battery

https://doi.org/10.1021/acs.chemrev.2c00002
Chem. Rev. 2022, 122, 13043−13107

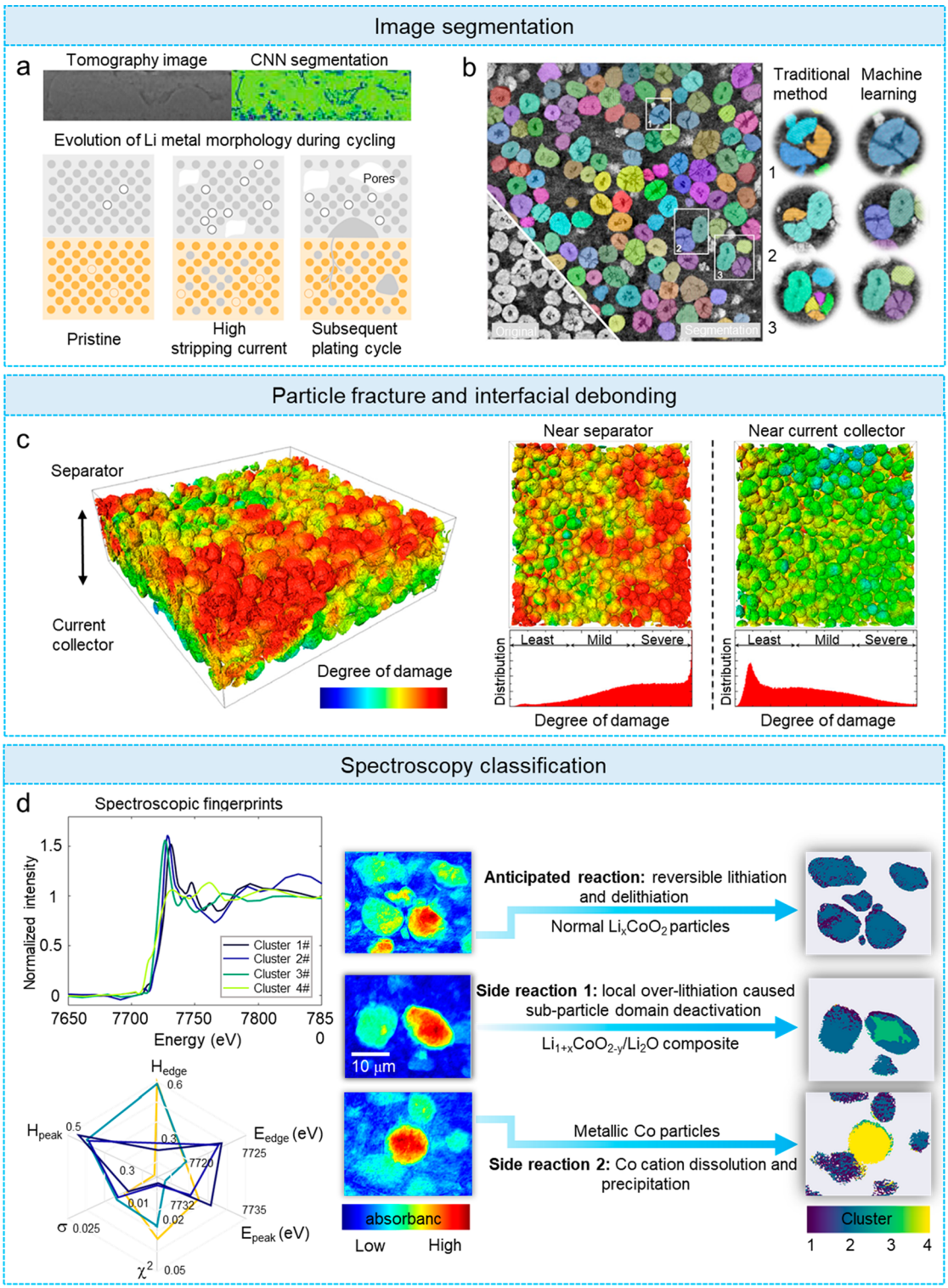

Figure 28. Machine learning-based image segmentation and clustering for battery research. (a) Tomographic image and the corresponding convolutional neural networks (CNNs) segmented image of a Li-metal anode. Reproduced from ref 506. Copyright 2020 American Chemical Society. Synchrotron imaging of pore formation in Li metal solid-state batteries aided by machine learning. (b) Comparison of conventional segmentation results and the machine-learning based segmentation results for NMC particles in a thick electrode. Reproduced from ref 176. Copyright 2020 Springer Nature. (c) 3D visualization of a heterogeneous damage profile in an aggressively cycled electrode. Reproduced from ref 62. Copyright 2019 Elsevier. (d) Unsupervised clustering analysis for identifying structural and chemical outliers in a spectromicroscopic study of $LiCoO_2$ pouch cell. Reproduced from ref 507. Copyright 2017 American Chemical Society.

engineering and manufacturing process, highlighting several exciting achievements in cell and pack design, state of health and state of charge estimation, and optimization of charging protocols.[504] A comprehensive review across the full range of battery research and development at multiple scales can be found in Lombardo et al.[505]

https://doi.org/10.1021/acs.chemrev.2c00002
Chem. Rev. 2022, 122, 13043−13107

Here we highlight a few case studies that feature the integration of synchrotron-based experimental techniques and machine learning methods for assessing the heterogeneous electrochemistry and mechanics in a composite electrode of lithium-ion batteries.

6.1. Defect Identification

Although many efforts have been devoted to optimizing the manufacturing process for the Li-ion battery electrodes and cells, structural defects are widely populated, negatively affecting the battery performance and causing both acute and chronic degradations. Therefore, it is important to monitor the electrode production process and to enable early detection of the electrode and cell defects. Image-based methods could be effective for this purpose. Because of the high-throughput nature of this task, it is highly desirable to conduct automatic defect detection in the imaging data using machine learning approaches. Badmos et al.[508] developed a convolutional neural network (CNN)-based method for detecting and classifying structural defects in cross section images of prismatic batteries for plug-in electric vehicles. The authors trained their network to automatically distinguish different types of structural defects, including layer deformation, metal particle contaminants, and nonuniform electrode coating. The demonstrated results show superior efficiency and accuracy, which is critical to this application scenario. It is important to note that the cell defects could have very different appearances in the images and, therefore, a machine learning approach without specifying the targeted morphological features is important to this application.

6.2. Tomography Image Segmentation

Although synchrotron tomography can offer 3D imaging data with good quality, the segmentation can still be challenging for features of low image contrast. Dixit et al.[506] used in situ synchrotron phase-contrast imaging to study the morphological evolution of Li metal in a Li-metal solid-state battery. Upon cycling, Li metal undergoes oxidation and migrates into the solid electrolyte in the form of Li cation, leaving an electron and a vacancy in the Li metal. Under a high stripping current, the vacancy accumulates because the Li^+ migration rate is faster than the vacancy replenishment rate (the Li metal self-diffusion rate). This effect could cause the formation of voids and pores in the Li-metal anode, which is indeed what the authors observed in their experiment (as shown in Figure 28a). However, because of the low contrast between Li metal and voids, conventional threshold-based image segmentation cannot provide an accurate image analysis and quantification. Therefore, the authors developed a convolutional neural network algorithm based on resnet34,[506] which trains a subset of the images from the same electrode. These training images were labeled using a conventional edge-detection-based method with manual validation and adjustment. They then utilized this model to segment the rest of the images automatically. The authors evaluated the efficiency and accuracy of their approach and showed that the segmentation of a single image takes only 0.3 s, and the reliability is over 80%. This segmentation process sets the basis for their further analysis, which suggests that the regions with low effective properties (e.g., transport and mechanical) are nuclei for the failure of Li-metal solid-state batteries.

In addition to handling image data with poor contrast, a machine learning approach has also been applied to identify and evaluate battery cathode particles with different degrees of chemomechanical breakdown. Jiang et al.[176] conducted synchrotron-based phase-contrast holotomography on a composite NMC cathode and visualized thousands of active cathode particles with high spatial resolution. Direct visual assessment of the tomogram can already reveal that these particles are highly heterogeneous. Depending on the local environment, these particles exhibit very different cracking patterns. Statistical analysis is highly desirable for understanding the charge and damage heterogeneity in this practical thick electrode. However, the identification of these particles in the tomographic data is nontrivial because many of the fragments detached from severely damaged particles could be mistakenly identified as individual particles (see illustration in Figure 28b), which complicates the statistical analysis. It requires some degree of "intelligence" to correctly associate these fragments as a particle. The authors developed a mask regional convolutional neural network (mask R-CNN) algorithm to fulfill this task (see illustration in Figure 28b). This method effectively reinforces an additional constraint on the segmentation process and enhances the overall quasi-spherical shape of the particles. Upon correctly identifying and labeling all the particles (regardless of their respective damage degree), the authors evaluated the detachment of the NMC particles from the carbon and binder matrix, which is an important mechanical degradation mechanism in the composite electrode. With more than 650 NMC particles identified and analyzed automatically, the authors concluded that the size-dependent particle detachment is statistically significant. As a follow-up to this work, Xu et al.[62] studied a synchrotron tomographic data set that contains more than 1000 active NMC particles. They observed a depth-dependent particle fracturing pattern (Figure 28c), which is attributed to a strong cell polarization effect upon the fast charging of the battery. This experimental observation is in good consistence with the finite elemental modeling results, highlighting the synergy between the cutting-edge experimental capabilities and the theoretical modeling. Moreover, the automatic identification of many particles in a real-world electrode not only can be utilized to study individual particles' behavior with statistical significance but also facilitated the investigation of particle-to-particle interactions, revealing a dynamic particle network evolution that governs the cathode degradation.[509]

6.3. Data Classification

In addition to image processing, machine learning methods are also used to handle other forms of large-scale experimental data in the study of chemomechanics in batteries. As mentioned, X-ray spectro-microscopy has successfully been applied to studying mesoscale structural and chemical characteristics in battery materials. It generates massive numbers of X-ray absorption spectra, fingerprinting the chemical heterogeneity either induced by aggressive or prolonged electrochemical cycling, or by purposely engineered synthesis procedures. With some prior knowledge of the material system, one could utilize standard spectra from known chemical species to fit the data. This approach is simple yet effective. The downside of this method is that we could potentially miss some unanticipated or unknown chemical features. Machine learning-based data classification and analysis have been adopted to tackle this issue and capture chemical outliers in the spectra.

Zhang et al.[507] employed the X-ray spectromicroscopy technique to image more than one hundred $LiCO_2$ particles in

https://doi.org/10.1021/acs.chemrev.2c00002
Chem. Rev. 2022, 122, 13043−13107

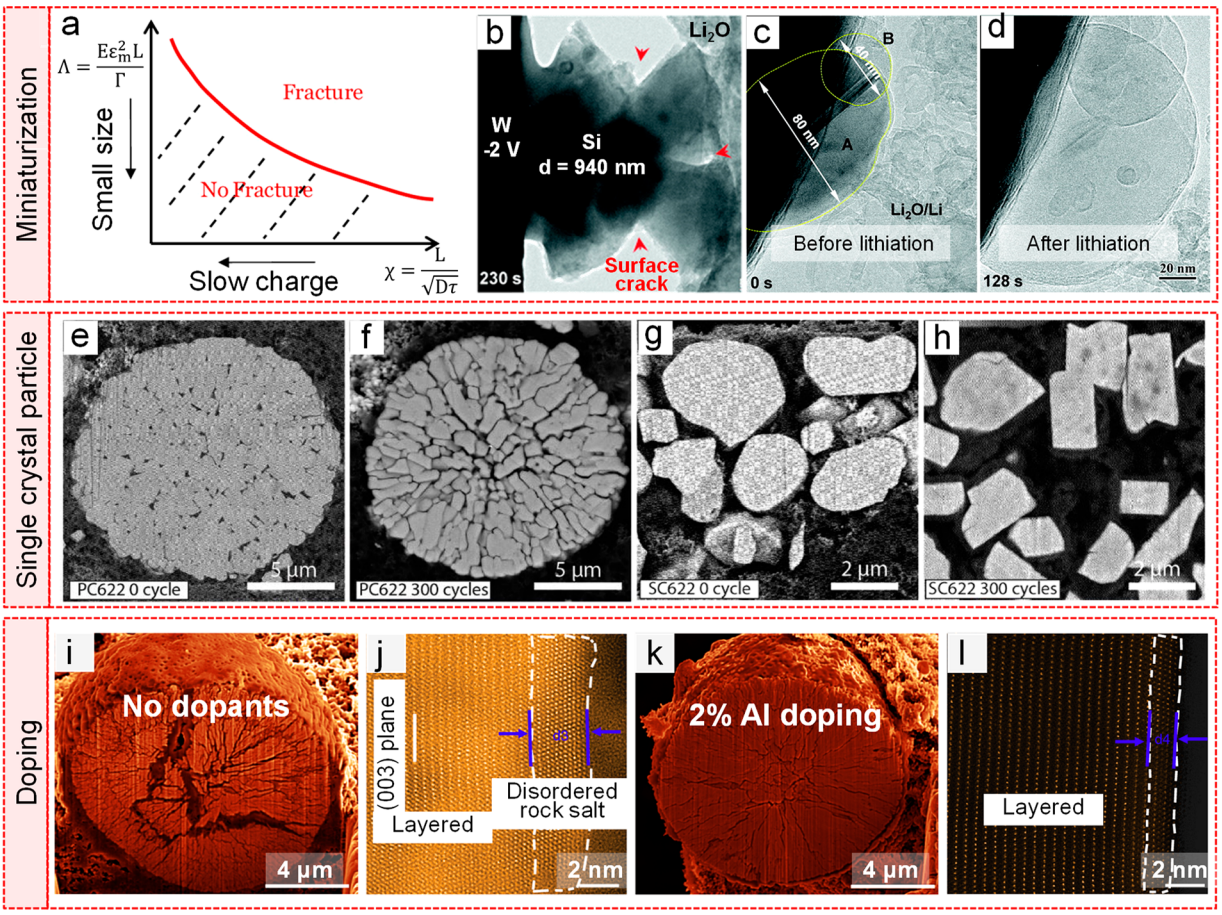

Figure 29. Particle miniaturization, single crystal design, and elemental doping strategies. (a) A theory for the effect of particle size and charging rate on the occurrence of fracture. Reproduced from ref 102. Copyright 2010 AIP Publishing. Si particles undergoing lithiation where (b) large particles crack and (c, d) small particles are crack-free. Reproduced from ref 516. Copyright 2012 American Chemical Society. Switch from (e, f) polycrystalline particles to (g, h) SC particles can mitigate detrimental intergranular crack formation. Cross section SEM images of polycrystalline $LiNi_{0.6}Mn_{0.2}Co_{0.2}O_2$ (PC622) underwent (e) 0 and (f) 300 cycles. Cross section SEM images of single-crystal $LiNi_{0.6}Mn_{0.2}Co_{0.2}O_2$ (SC622) underwent (g) 0 and (h) 300 cycles. Reproduced from ref 520. Copyright 2020 Elsevier. (i, j) Interfacial phase change causes crack formation. (k, l) Foreign elements doping can mitigate interfacial phase change induced cracking. Reproduced from ref 523. Copyright 2019 Springer Nature.

a $LiCoO_2$/Li battery pouch cell. This data set contains over ten million spatially resolved X-ray absorption spectra. While they could apply a conventional approach that uses standard spectra for linear combination fitting, which they did and reported in a different paper,[510] they developed a data-driven approach for capturing the important subsets of the spectra. They first extracted key spectroscopic features from all the spectra and then conducted unsupervised clustering analysis based on these features. As shown in Figure 28d, four different clusters of absorption spectra with distinct spectroscopic features were identified and were attributed to different reaction mechanisms. Most of the particles (over 98%) underwent anticipated delithiation/lithiation during the cycling process, with some degrees of chemical heterogeneity observed, featuring the mesoscale chemomechanical complexities. There are, however, a few particles with unexpected chemical profiles identified in this clustering analysis. More specifically, a metallic Co particle and a $Li_{1+x}CoO_{2-y}/Li_2O$ subparticle domain were found in the cell. The discovery of the Co metal particle was attributed to the decomposition and precipitation of the cathode electrode, while the subparticle domain of $Li_{1+x}CoO_{2-y}/Li_2O$ can be attributed to local excessive delithiation and deactivation.

7. SOLUTION STRATEGIES

Achieving high energy and power densities while maintaining good cycling stability is imperative for next-generation battery materials. Intensive research has been devoted to addressing and potentially eliminating chemomechanical degradation in batteries. This section will review different strategies to mitigate chemomechanical degradation, including a discussion of their efficacy and scalability. We categorize these solutions roughly into three groups: (1) improving mechanical robustness of materials, (2) accommodating strain/stress generation by surface or microstructural engineering, and (3) mitigating the destructive effects through crack self-healing or electrolyte modification.

7.1. Improving Mechanical Robustness of Materials

To address the chemomechanical degradation of battery materials, an intuitive approach is to improve the mechanical robustness of active materials. This method can reduce the probability of crack formation and propagation. We will review four strategies in this category.

7.1.1. Material Miniaturization. The repeating insertion and extraction of mobile ions cause breathing strains in electrodes, varying from a few percent to hundreds of percent in different material systems. The lattice strains can generate a

https://doi.org/10.1021/acs.chemrev.2c00002
Chem. Rev. 2022, 122, 13043−13107

stress field that may lead to particle cracking. Many studies found that material miniaturization can effectively avert electrode cracking. The underlying mechanism is well understood in Griffith fracture mechanics that pre-existing flaws cannot grow if the elastic energy released by crack formation is smaller than its fracture energy (Figure 29a).[102,511]

The miniaturization strategy has been successfully utilized in both cathode[512] and anode[513] materials. For example, the Si anode, with a specific capacity 10 times higher than the commercialized graphite anode, suffers from significant volume change, cracking, and pulverization.[514] Accordingly, researchers proposed a Si−C composite design, which can increase the energy density compared to the graphite anode while circumventing the significant volumetric swelling of a pure Si anode.[515] However, this approach is effective only for a very small percentage of Si in the composite and thus cannot deliver a substantial energy density. In recent years, Si nanoparticles have stood out as a potential solution to alleviate the severe mechanical degradation of Si anodes. Through in situ TEM experiments, Liu et al.[516] demonstrated that cracks initiate from the surface of large Si particles and lead to particle pulverization. Such crack formation is because of the tensile hoop stress at the particle surface (Figure 29b). Reducing the size of Si particles to less than 150 nm (Figure 29c,d) can significantly suppress particle cracking.

Particle miniaturization has the advantages of fast ion diffusion, good scalability, and low cost, potentially paving the path for the commercialization of Si anode materials. Yet, reducing particle size decreases packing density of battery electrodes, which causes inferior volumetric energy density. Moreover, nanoparticles tend to have a large specific surface area, which may induce a significant amount of destructive interfacial reactions. Therefore, Si nanoparticle anodes often need other processing, e.g., coating, to enable long cycling stability.

7.1.2. Single Crystal. Commercialized cathode materials are predominantly composed of polycrystalline particles with nanosized single grains as the building block. This design does not significantly decrease the tap density compared to large single crystals, but it can reduce the specific surface area than the use of nanosized single grains. Collectively, polycrystalline cathode materials deliver reasonably good performance in practical cells. However, upon ion insertion or extraction, the anisotropic volume change of the single grains induces stress mismatch at the grain boundaries, resulting in severe intergranular cracking (Figure 29e,f).

Recently, SC cathode materials have drawn extensive efforts because they can avoid intergranular cracking in their polycrystalline counterparts. Multiple studies have shed light on the syntheses of SC cathode materials, primarily based on an industry-relevant molten salt method.[517−521] It is found that SC cathode particles have much better mechanical robustness because of the elimination of grain boundaries. Moreover, compared to polycrystalline cathode particles,[78] SC particles have dramatically less lattice oxygen release—another critical reason for crack formation.[522] With the improved mechanical strength and lattice oxygen stability, the chemomechanical degradation in SC cathode particles is effectively mitigated, even after long cycles (Figure 29g,h).[520]

During electrode preparation, SC particles are less prone to cracking under high pressure. Therefore, the SC cathode typically has a high powder packing density (~3.8 g/cm^3). Nevertheless, it should be noted that SC particles also experience intragranular cracking at deep delithiated states (e.g., 4.7 V vs Li/Li$^+$), which cannot be addressed with the SC design. Lastly, the SC particles are usually about a few micrometers in size, causing a longer ion diffusion length and lower specific capacity than polycrystalline cathode materials, especially at high charging rates.

7.1.3. Doping. Intercalation chemistry has dominated the consumer electronics and electric vehicles market in the past few decades, mainly because of its good cycling performance, which originates from its highly reversible lattice upon ion extraction or insertion. It is, however, noted that the reversible lattice expansion and shrinkage could only exist under low state-of-charge conditions. For example, $LiCoO_2$, a dominating positive cathode material in consumer electronics, only has a reversible capacity of about 165 mAh/g ($Li_{1-x}CoO_2$, x = ~0.60),[524] although its theoretical capacity is 274 mAh/g. Extracting more Li from the lattice at a high voltage can cause detrimental phase transformations, leading to stress generation and chemomechanical degradation. Introducing foreign dopants into the lattice is a promising and effective method to ensure reversible lattice change. The underlying mechanisms are (1) dopants work as pillars to prevent lattice collapse[524,525] and (2) dopants work as fixed charge centers to suppress detrimental ion rearrangements and phase transformations.[524,526,527]

In addition to the change of bulk lattice parameters, undesired interfacial reactions between electrodes and liquid electrolytes can also induce irreversible phase transformations. The inherent lattice mismatch between various phases may cause cracks at the surface, which propagate to the bulk of electrode particles. An effective way to suppress the interfacial side reactions is to modify the liquid electrolyte composition, enabling a stable solid−electrolyte interface that protects the electrode materials.[528−530] Another strategy is to modify the composition of electrodes, either through coating or doping, to limit the detrimental phase transformations. Zou et al.[523] demonstrated that detrimental interfacial reactions could cause severe intergranular cracking in Ni-rich layered oxides (Figure 29i,j). With two percent Al doping, an Al-concentrated shell forms at the particle surface, effectively suppressing the interfacial reactions and alleviating particle cracking (Figure 29k,l).[523]

Design of electrode composition is one of the most prevailing methods to enhance the mechanical robustness of active materials, mainly because of its scalability and low cost. To date, doping has been widely used in commercial batteries to improve performance. Yet, it is worth pointing out that although dopants are designed to incorporate into the lattice, the low solubility of certain dopants can lead to their segregation in different regions.[244,531,532] Precise control of the dopant distribution at the mass production scale can be challenging, which may cause large variations in battery performance. Systematic studies are needed to understand the dopant distribution at various length scales and under different synthetic conditions.

7.2. Mitigating Destructive Effects

Although numerous strategies have been proposed to minimize the chemomechanical degradation of electrode materials, particle cracking and interfacial destruction are inevitable in many scenarios. Mitigating the destructive effects, therefore,

https://doi.org/10.1021/acs.chemrev.2c00002
Chem. Rev. 2022, 122, 13043−13107

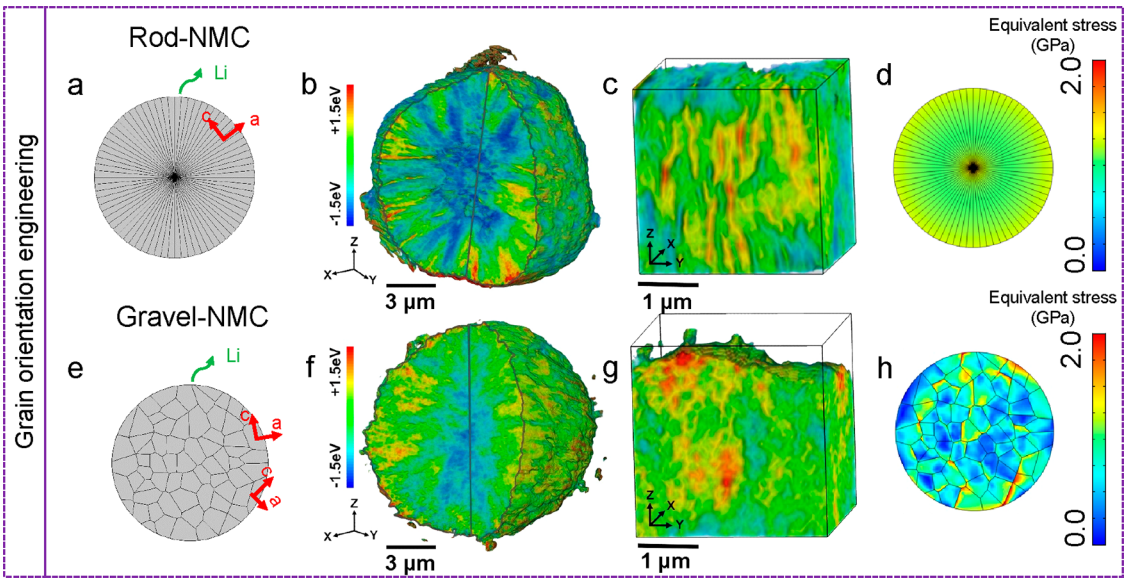

Figure 30. Grain orientation engineering mitigation strategies. Anisotropic strain induced stress mismatch can be mitigated through grain orientation engineering, where (a–d) the radially aligned single crystals produce less stress mismatch during redox reactions than (e–h) the randomly aligned single crystals. Schemes showing the (a) radially or (b) randomly aligned single crystals. State-of-charge distribution in (b, c) radially or (f, g) randomly aligned single crystals. Mechanical stress induced by delithiation reaction reactions in (d) radially or (h) randomly aligned single crystals. Reproduced from ref 249. Copyright 2020 Springer Nature.

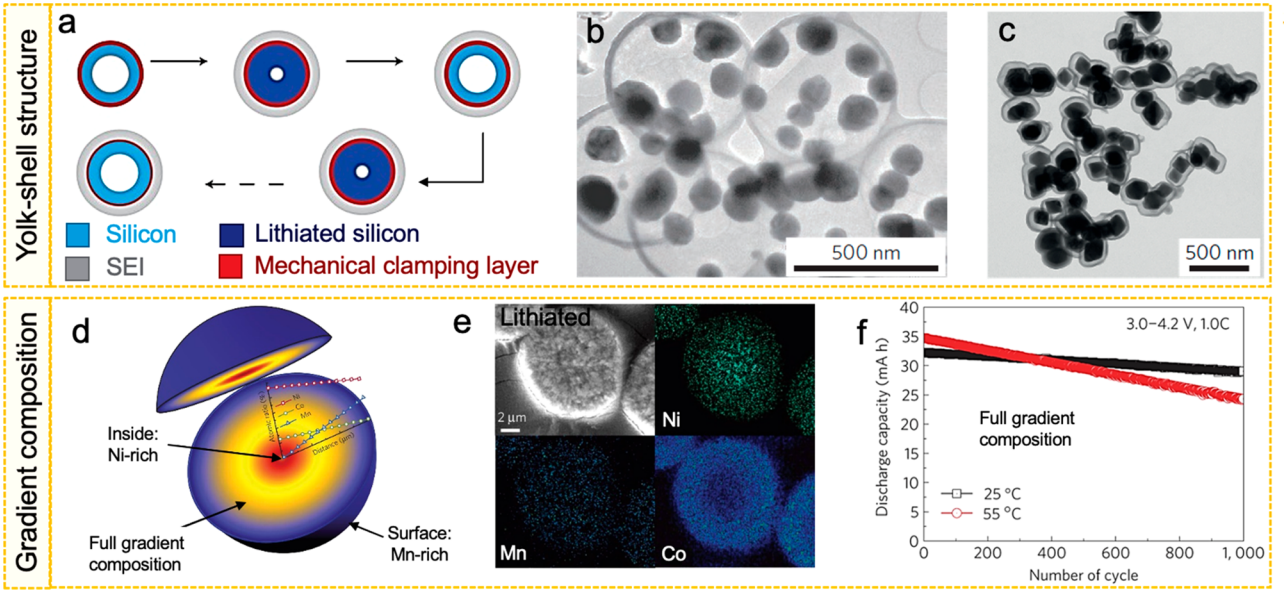

Figure 31. Surface engineering mitigation strategies. (a) Schematic figure showing that the mechanical clamping shell of a core–shell structure can limit the volume change of the interior. Reproduced from ref 540. Copyright 2008 Wiley-VCH GmbH. Examples of more core–shell structures: (b) Tin-nanoparticles and (c) iron oxide particles encapsulated in carbon spheres. Reproduced from refs 541 and 542. Copyright 2014 Wiley-VCH GmbH. Copyright 2018 Royal Society of Chemistry. (d) Scheme showing the composition gradient design, with decreasing Ni and increasing Mn-content from the particle center to the surface. (e) Elemental distribution shows the Ni-rich center and Mn-rich shell. (f) Electrochemical performance of the full gradient composition cathode at room and high temperatures. Reproduced from ref 543. Copyright 2012 Springer Nature.

plays an important role in the retention of electrochemical performance of batteries.

7.2.1. Grain Engineering. Recent studies have shown that redox reactions are largely heterogeneous at the particle level, often caused by the discontinuous electronic/ionic transport network by the random orientations of the building blocks, single grains.[533] Heterogeneous redox reactions may induce anisotropic volume changes of the single grains and breakdown of the grain boundaries.[30,101,113] Moreover, chemomechanical degradation causes poor contact between the single grains, further contributing to redox heterogeneity. This self-promoting effect plagues battery performance rapidly. To date, most research efforts focus on modifying the chemical composition, electronic structure, and crystal structure of active materials to mitigate chemomechanical degradations. Yet, grain orientation engineering, i.e. aligning single grains in a way that can relief the stress concentration, remains largely unexploited.

A few recent studies demonstrate that grain engineering can effectively suppress crack formation in cathode particles.[534−537]

https://doi.org/10.1021/acs.chemrev.2c00002
Chem. Rev. 2022, 122, 13043−13107

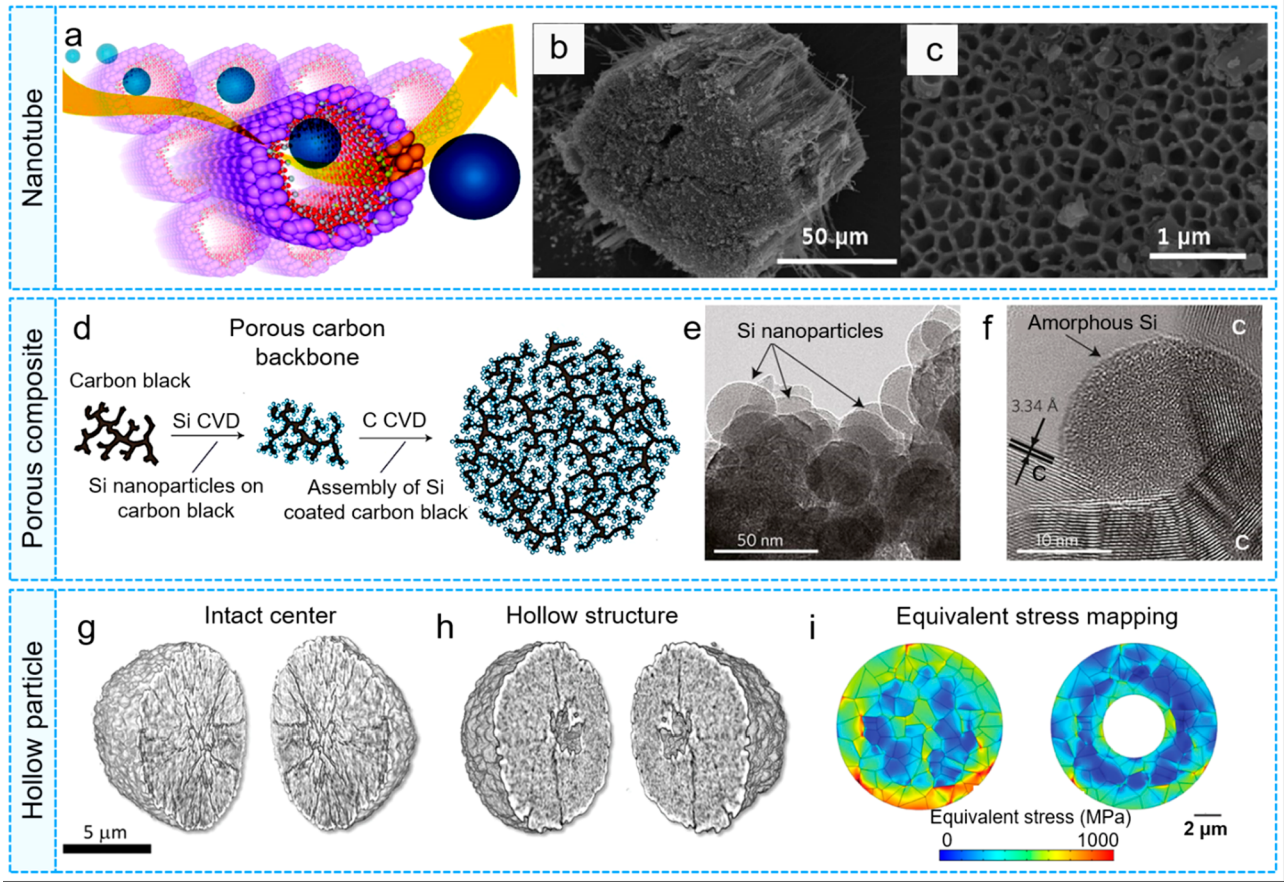

Figure 32. Accommodating strain/stress by microstructural engineering. (a) Schematic figure showing the tubular morphology design, which provides an extra free surface for stress relaxation and thus mitigating fracturing after long-term electrochemical cycling. (b, c) Examples of the hollow structure design. Reproduced from ref 545. Copyright 2009 American Chemical Society. (d) Scheme showing the porous Si−C composite design. (e, f) TEM images showing Si nanoparticles on the porous carbon backbone. Reproduced from ref 546. Copyright 2010 Springer Nature. (g, i) Hollow particle can accommodate the mechanical stress and mitigate mechanical degradation of NMC particles. Reproduced from ref 547. Copyright 2017 Royal Society of Chemistry.

Specifically, in Ni-rich layered oxide cathodes, Li ions can only migrate in the *ab* plane. By constructing radially aligned Li-ion diffusion channels within a spherical secondary particle, Li ions can move more easily upon charge or discharge (Figure 30a).[249] Such radially aligned grain orientations can guide the redox reactions, which essentially determines the charge distribution at the secondary particle level (Figure 30b,c). Moreover, radially aligned single grains lead to a uniform stress distribution (Figure 30d), which rationalizes the better mechanical integrity upon cycling. Conversely, most commercial cathode secondary particles are composed of single grains with random orientations. Therefore, Li-ion pathways are more likely to be tortuous (Figure 30e). Upon charging, discontinuous ion channels disturb Li-ion migration, leading to a heterogeneous charge distribution in the secondary particles (Figure 30f,g). Such heterogeneous charge distribution further increases the anisotropic mismatch strains of the single grains. As a result, cathode particles with random grain orientations tend to be more prone to crack formation.

Grain orientation engineering provides a large playground for enhancing the mechanical robustness of battery materials. This method is promising as the material syntheses are industry relevant. Yet, only a few grain orientations have been systematically investigated. Many other microstructures have not been explored.

7.2.2. Microstructural Engineering. Repetitive stress generation and detrimental electrode−electrolyte interfacial reactions ubiquitously occur in electrode materials and dramatically deteriorate battery performance. A core−shell microstructure can address these two issues simultaneously. The design is that by constructing a mechanical clamping shell, the mechanical stresses in the core region will not cause severe structural disintegration.[538] Moreover, the clamping shell is chemically stable against liquid electrolytes or other reactive chemicals.

Using the Si anode as an example, its poor cycling stability is attributed to the volume-change-induced cracking and severe solid−electrolyte interfacial reactions. As discussed in Section 7.1.1, the miniaturization strategy can effectively limit the cracking of Si nanoparticles,[516] which can achieve 80% capacity retention over a few hundred cycles.[539] This cycle life still cannot satisfy the needs of electric vehicles, which require batteries of thousands of stable cycles. A potential limiting factor might be the unstable solid−electrolyte interphase. Wu et al.[540] demonstrated that through a core−shell design with Si oxide as the shell and Si nanotube as the core (Figure 31a), the Si anode could deliver extremely stable long-term cycling performance, up to 6000 cycles, in the half-cell configuration. The ionically conductive and mechanically rigid Si oxide layer conducts ions while limiting the Si anode's outward expansion

https://doi.org/10.1021/acs.chemrev.2c00002
Chem. Rev. 2022, 122, 13043−13107

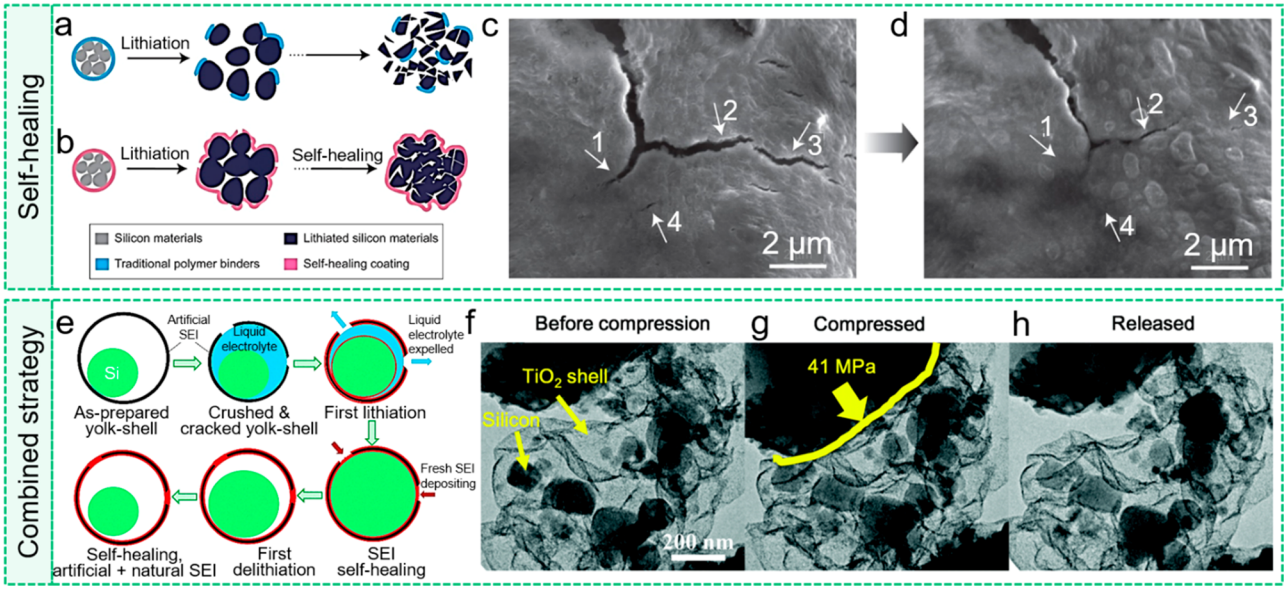

Figure 33. Self-healing of chemomechanical degradations. (a–d) Polymeric coating on battery materials can perform self-healing through the reassociation of hydrogen bonds. Reproduced from ref 549. Copyright 2013 Springer Nature. (e) Mitigating chemomechanical degradation through a combined strategy of self-healing and microstructure engineering. (f, g) In situ TEM indentation of TiO_2 shells, which shows superior mechanical robustness under mechanical pressing. Reproduced from ref 550. Copyright 2017 Royal Society of Chemistry.

and preventing the Si anode's direct contact with liquid electrolytes. This core–shell structure has also be used in other material designs, including tin oxide (Figure 31b)[541] or iron oxide (Figure 31c)[542] encapsulated by a carbon sphere. These studies prove that the mechanical clamping layer can accommodate the volume change of the active material during redox reactions to ensure prolonged cycling stability.

The fundamental principle for the core–shell design is that it has a mechanically and chemically stable shell, e.g., the stable Si oxide shell on top of the Si nanotubes. This material design has a potential drawback that the shell does not participate in the redox reaction, which may lead to inferior energy density. This issue is prominent in cathode materials, which usually have lower energy density than their anode counterparts. Therefore, a novel gradient composition design was developed to achieve good mechanical robustness while maintain high energy density. This gradient composition design was first demonstrated in Ni-rich NMC materials. It was known that increasing the Ni percentage in NMC materials can achieve higher energy density and reduce the usage of Co. Yet, Ni-rich NMC materials are prone to more detrimental interfacial reactions and a greater extent of anisotropic deformation. Decreasing the Ni content, i.e., designing Mn-rich NMC, can effectively improve NMC materials' mechanical and chemical stability. Such intrinsic difference between the Ni-rich versus Mn-rich NMC motivated the design of gradient composition distribution, with decreasing Ni and increasing Mn-content from the center to the surface within a cathode particle (Figure 31d,e). The gradient composition enables an extremely stable performance (90% capacity retention after 1000 cycles at 1C, Figure 31f).[543] It should be noted that the fine composition distribution requires precise control of the precursor synthesis, which may cause additional expenses than the traditional synthesis method.

Engineering the microstructure of electrodes by introducing voids is another effective method to accommodate mechanical deformation and internal stresses. The intentionally created voids can accommodate strain in a controlled manner. For example, Si nanotubes can accommodate the significant volume expansion upon a lithiation reaction (Figure 32a–c). It is demonstrated that although the thickness of the nanotube wall expanded from ~40 to ~300 nm after 200 cycles, no fracture or pulverization occurred. Such outstanding fracture resistance may originate from the large surface-to-volume ratio, benefiting from the nanotube design. Moreover, the internal voids can also facilitate the Li-ion transport between Si and liquid electrolytes because of the shorter diffusion path. Collectively, the Si nanotube design delivers stable performance under fast charging.

Along with Si nanotube design, porous Si–C composites provide an alternative strategy to accommodate stresses. The pre-existing pores in the Si nanoparticles can accommodate its large volume change and ensure fast ion diffusion, while the interconnecting C network facilitates electron conduction, stabilizes the solid–electrolyte interface, and enhances structural integrity. Such an approach requires precise control of the distribution of Si nanoparticles in an interconnecting C network. A bottom-up hierarchical Si–C composite synthesis method demonstrated that a two-step chemical vapor deposition (CVD) process (Figure 32d) could achieve this goal. TEM results show that Si nanoparticles are densely incorporated into the C network (Figure 32e,f). Properly engineered porous Si–C composites yield a high reversible capacity which is 5 times higher than the graphite anode.

Hollow structures can also help stress relaxation in cathode materials. Experiments revealed that grains near the core of NMC particles experience high stresses during cycling, leading to crack formation from the center of cathode particles.[544] Introducing voids into solid particles has two advantages. First, the hole region within the particle provides a buffer of mechanical deformation during battery cycling and avoids crack formation at the center. Second, the voids can decrease the ion diffusion length within the particles, reducing the state

https://doi.org/10.1021/acs.chemrev.2c00002
Chem. Rev. 2022, 122, 13043–13107

of charge heterogeneity and related stress damage in cathode particles.

Microstructural engineering has gained a tremendous amount of interest in the last few years, which enables a fundamental understanding of the microstructure−performance relation in batteries. These research efforts contributed to multiple commercially available advanced battery materials. It should be noted that although the voids can help stabilize the performance, they inevitably decrease the volumetric energy density of electrodes. A trade-off between the volumetric energy density and long-term cycling needs to be deliberated. Alternatively, other strategies, such as electrolyte modification to be discussed in the next section, may represent better solutions in practice.

7.2.3. Self-Healing. Nature often provides inspiration on remedying fracture of materials through a smart self-healing strategy. Recently, self-healing of electrode and electrolyte materials has gained increasing attention as it helps the durability and lifetime of batteries. In this regard, readers are referred to a review paper[548] to gain more insight into the research on self-healing electrolytes.

In a traditional Si anode, polymer binders are coated on the surface of Si particles. When Si particles experience a significant volume change upon charge and discharge reactions, the mechanical deformation may break the polymer binders and cause cracking and delamination of the Si particles (Figure 33a). Self-healing polymers with good stretchability and self-healing capability can potentially address mechanical degradation. In this design, self-healing polymers are coated on the surface of Si particles. Upon redox reactions, the large volume change of Si particles leads to fewer cracks in the self-healing polymers because of its good stretchability. More importantly, the cracks can be repaired spontaneously at room temperature through the formation of hydrogen bonding Figure 33b). It was demonstrated that while large cracks can still be observed at the polymer surface because of the significant deformation of Si particles (Figure 33c), small cracks are mostly healed after 5 h (Figure 33d). Self-healing provides a new dimension for mitigating the impact of chemomechanical degradation. Meanwhile, it is worth noting that the self-healing feature depends not only on the strength of various bonds but also on the phase segregation of the polymetric interfaces. To date, controlled phase segregation in battery cells represents a daunting challenge that requires more development before it can be utilized in commercial batteries.

The self-healing strategy was also introduced to stabilize the SEI. An artificial TiO_2 SEI on the surface of Si nanoparticles may have flaws, which allow the infiltration of liquid electrolytes. These flaws in the artificial SEI may seem catastrophic. However, during lithiation, Si particles undergo a large volume change, which can expel the liquid electrolyte out of the TiO_2 shell. More importantly, the newly formed SEI on the surface of Si particles can grow together with the TiO_2 shell. Because of the difference in the adhesion energy, the SEI formed on the Si particles will bind with the TiO_2 shell upon delithiation, which repairs the flaws on the artificial SEI (Figure 33e). Such a design strategy combines the advantages of the core−shell structure and the self-healing feature. The good mechanical robustness of the Si−TiO_2 core−shell structure is shown in Figure 33f−h, as attested by the good reversibility of the core−shell structure after mechanical compression.

8. OUTLOOK

Significant advances in battery technologies occurred in the last decades, leading to a dramatic energy density increase for energy storage. Despite these advances, breakthroughs in battery technologies are still urgently needed to ensure that battery performance meets the demands of the growing electric vehicle and grid storage markets. It has been increasingly evident that such breakthroughs are contingent on addressing the challenge at the interface between mechanics and chemistry. This review has highlighted the recent progress in understanding and regulating the chemomechanical processes in batteries. However, more research is necessary for this burgeoning field as several key challenges have yet to be addressed. We will outline those challenges in this section and hope to encourage and inspire solutions that pave the way to the eventual realization of mechanically and electrochemically resilient batteries.

How to Define and Evaluate the Mechanical Stability of Battery Materials

As the chemomechanical degradation of batteries is becoming the main bottleneck blocking their practical implementation, the mechanical reliability has been considered a predominant metric that needs to be carefully evaluated before new materials can be practically adopted. However, there is neither a clear definition of mechanical reliability of battery materials nor a well-accepted protocol for evaluating their mechanical reliability. Mechanical properties, including elastic modulus, hardness, and fracture toughness, have all been utilized in different contexts as parameters to represent the mechanical reliability of battery materials, which occasionally causes ambiguous results or even contradictory conclusions. Furthermore, quantifications on the mechanical properties by characterizations at different length scales, from the particle- to electrode-levels, sometimes show a significant variation, leading to the evaluation of mechanical reliability being inaccurate and thus of less practical importance. Therefore, a clear definition and standardized testing protocol for the mechanical reliability of battery materials need to be established in the future.

How to Quantify the Mechanical Degradation during Battery Cycling

Recently developed experimental techniques have revealed various types of mechanical degradation in batteries, but quantifying the degree of mechanical damage during battery operation is challenging. The advanced characterization techniques highlighted in Section 5.2 are either cost-intensive or require heavy data processing and analysis, limiting their in-house adoption in the battery industry. One approach to efficiently quantify the mechanical damage in batteries is to leverage cutting-edge development in data-driven modeling to implicitly correlate the degree of mechanical damage with the cycling conditions, such as the charging rate and cutoff window. On the basis of the insight extracted from the data-driven modeling, it becomes possible to further develop empirical models, similar to the widely used Paris' law for describing the fatigue crack growth under cyclic mechanical load, to predict the evolution of mechanical damage during battery operation. These simple models can be of practical importance for the battery industry.

https://doi.org/10.1021/acs.chemrev.2c00002
Chem. Rev. 2022, 122, 13043−13107

How to Correlate the Degree of Mechanical Degradation to the Battery Performance

Despite the extensive exploration in unraveling the impact of mechanical degradation on the electrochemical activities of batteries, the explicit relationship between different types of mechanical degradation (particle fracture, interfacial debonding, and structural failure) and the metrics of battery performance (power density, capacity retention, and Coulombic efficiency) remains unclear. Several reasons account for this ambiguity. First, not all types of mechanical degradation deteriorate battery performance. It necessitates further investigation to identify the types of mechanical degradation that significantly impact the battery performance. Second, different types of mechanical degradation are usually highly intertwined, making it challenging to quantify the impact of each type of damage separately. Under this circumstance, numerical simulation exhibits superior capability in quantifying the dependence of battery performance on different types of mechanical failure modes. Further development of numerical simulation should focus on improving efficiency either in time or in computational cost, particularly when dealing with the full cell modeling with sufficient microstructural details.

How to Develop Cycling Protocols to Improve the Electrochemical and Mechanical Reliability of Batteries

In terms of industrial adoption, it is attractive to develop cycling protocols that can realize fast charging and/or deep charging but eliminate the mechanical degradations in batteries. One pathway is to rationally design the cycling rate, cutoff voltage, and current profile (i.e., constant current−constant voltage, constant power−constant voltage, and pulse charging) based on the mechanistic understanding of the chemomechanics of batteries. It necessitates the previous two challenges to be well addressed, precisely quantifying the mechanical degradation and explicitly correlating the mechanical degradation to the battery performance. Another pathway is to leverage the state-of-the-art data-driven approach to optimize charging protocols. Such an approach can bypass the need for an explicit understanding of the highly intertwined chemomechanical interactions in batteries that govern their performance. However, the collection of data sets, for example, a data set containing batteries that have had varying levels of mechanical degradation intentionally induced by various cycling protocols, requires the continuous advancement of experimental techniques that can generate experimental data at an unprecedented rate.

How to Design and Manufacture Battery Materials with Improved Electrochemical and Mechanical Resilience

With the in-depth understanding of the intimate coupling between mechanics and electrochemistry in rechargeable batteries, a natural extension is to leverage this understanding to guide the design and manufacturing of battery materials with improved electrochemical and mechanical resilience. Two general strategies can be adopted. One is to increase the materials' resistance to mechanical degradation. Another is to reduce the driving force for the degradation. The former is expected to be achieved by modifying synthesis conditions to improve the fracture toughness of battery materials, including active materials, binders, and solid-state electrolytes, while the latter can be achieved by tuning the material microstructure or electrode architecture to mediate the mismatch strains. It should be noted that the electrochemical stability of battery materials might be altered when optimizing their mechanical reliability, opening an additional area that requires the optimization of battery design and manufacturing. Moreover, all the optimizations of materials synthesis or structural tuning need to consider the cost effectiveness and be in scale with the current battery manufacturing platform and fitting the battery supply chain.

Considering that chemomechanical degradation will continue to be a major concern in developing the next-generation batteries, the pursuit of more mechanically resilient battery materials will be a cornerstone to maintaining the continuous growth of battery technology and further developing the clean-energy economy. We hope that this paper helps the researchers in the mechanics, electrochemistry, and battery communities gain a comprehensive picture of the current progress in understanding the chemomechanics of rechargeable batteries and motivates further technological advancement in the near future.

AUTHOR INFORMATION

Corresponding Authors

Yijin Liu − *Stanford Synchrotron Radiation Lightsource, SLAC National Accelerator Laboratory, Menlo Park, California 94025, United States;* orcid.org/0000-0002-8417-2488; Email: liuyijin@slac.stanford.edu

Feng Lin − *Department of Chemistry, Virginia Tech, Blacksburg, Virginia 24061, United States;* orcid.org/0000-0002-3729-3148; Email: fenglin@vt.edu

Yi Cui − *Department of Materials Science and Engineering, Stanford University, Stanford, California 94305, United States;* orcid.org/0000-0002-6103-6352; Email: yicui@stanford.edu

Kejie Zhao − *School of Mechanical Engineering, Purdue University, West Lafayette, Indiana 47907, United States;* orcid.org/0000-0001-5030-7412; Email: kjzhao@purdue.edu

Authors

Luize Scalco de Vasconcelos − *School of Mechanical Engineering, Purdue University, West Lafayette, Indiana 47907, United States*

Rong Xu − *Department of Materials Science and Engineering, Stanford University, Stanford, California 94305, United States*

Zhengrui Xu − *Department of Chemistry, Virginia Tech, Blacksburg, Virginia 24061, United States;* orcid.org/0000-0002-6549-4713

Jin Zhang − *Stanford Synchrotron Radiation Lightsource, SLAC National Accelerator Laboratory, Menlo Park, California 94025, United States*

Nikhil Sharma − *School of Mechanical Engineering, Purdue University, West Lafayette, Indiana 47907, United States*

Sameep Rajubhai Shah − *School of Mechanical Engineering, Purdue University, West Lafayette, Indiana 47907, United States;* orcid.org/0000-0002-8561-4479

Jiaxiu Han − *School of Mechanical Engineering, Purdue University, West Lafayette, Indiana 47907, United States*

Xiaomei He − *School of Mechanical Engineering, Purdue University, West Lafayette, Indiana 47907, United States*

Xianyang Wu − *School of Mechanical Engineering, Purdue University, West Lafayette, Indiana 47907, United States*

Hong Sun − *School of Mechanical Engineering, Purdue University, West Lafayette, Indiana 47907, United States;* Present Address: H.S.: Lawrence Livermore National

https://doi.org/10.1021/acs.chemrev.2c00002
Chem. Rev. 2022, 122, 13043−13107

Laboratory, 7000 East Ave, Livermore, CA 94550; orcid.org/0000-0002-3586-7400
Shan Hu − *School of Mechanical Engineering, Purdue University, West Lafayette, Indiana 47907, United States*
Madison Perrin − *School of Mechanical Engineering, Purdue University, West Lafayette, Indiana 47907, United States*
Xiaokang Wang − *School of Mechanical Engineering, Purdue University, West Lafayette, Indiana 47907, United States*

Complete contact information is available at: https://pubs.acs.org/10.1021/acs.chemrev.2c00002

Author Contributions

⊥L.S.d.V. and R.X. contributed equally to this work.

Notes

The authors declare no competing financial interest.

Biographies

Dr. Luize Scalco de Vasconcelos received her Ph.D. from the School of Mechanical Engineering at Purdue University in 2020. During her doctorate, she designed experiments and computational models to explore how chemical reactions regulate mechanical properties and behaviors at small scales in Li-ion batteries. In 2021, she joined the University of Texas at Austin as a postdoctoral fellow where she works on manufacturing techniques and advanced materials for soft, biointegrated electronics.

Dr. Rong Xu is a postdoctoral scholar in the Department of Materials Science and Engineering at Stanford University. He received his Ph.D. from the School of Mechanical Engineering at Purdue University in 2019. His research lies at the intersection of mechanics, electrochemistry, and materials science, with interest in their applications in lithium-battery technologies. He conducted a series of studies using integrated experimental and numerical approaches to reveal the intimate coupling between mechanics and electrochemistry in lithium batteries and leverage this understanding to guide the material and structural design for state-of-the-art energy solutions.

Dr. Zhengrui Xu is currently a postdoctoral associate in Chemistry at Virginia Tech. He holds a Bachelor's degree in Renewable Energy Materials and Devices (2017) from the University of Electronic Science and Technology of China and a Ph.D. degree in Chemistry (2021) from Virginia Tech. He mainly investigates energy storage materials' multiscale chemical, structural, and redox properties through synchrotron spectroscopy, imaging, scattering methods, and electrochemical diagnosis.

Dr. Jin Zhang is currently an engineer at the Institute of High Energy Physics, Chinese Academy of Sciences (IHEP, CAS). She received her B.S. degree (2016) from Northwestern University, Xi'an, China, and Ph.D. degree (2021) from the IHEP, CAS. She was a visiting research scholar at the Stanford Synchrotron Radiation Lightsource (2019−2021). Her research interest is on the synchrotron X-ray imaging techniques and their applications to materials science.

Nikhil Sharma is currently a Ph.D. candidate in the School of Mechanical Engineering at Purdue University, working under Professor Kejie Zhao. He obtained his Bachelor's degree in Engineering from Punjab Engineering College, India, in 2015. His research is focused on experimental and computational techniques to understand the mechanics of electrochemical systems and the evolution of mechanical properties in rechargeable batteries.

Sameep Rajubhai Shah is a Ph.D. student in the School of Mechanical Engineering at Purdue University working with Professor Kejie Zhao. He obtained his Bachelor of Engineering (B.E.) degree from Visvesvaraya Technological University, India in 2017. His current research focuses on coupled electro-chemo-mechanical computational modeling of high-capacity composite electrodes for Li-ion batteries.

Jiaxiu Han received her Bachelor's degree in Energy and Power Engineering from Xi'an Jiaotong University, China in 2019. She is currently a Ph.D. student in the School of Mechanical Engineering at Purdue University, working under Professor Kejie Zhao's supervision. Her research primarily focuses on using finite element modeling to understand the fracture mechanism of Li-ion batteries.

Xiaomei He received her B.S. degree from Jilin University in 2014 and M.S. degree from Xi'an Jiaotong University in 2017. She is currently a Ph.D. candidate of Materials Science and Engineering at Xi'an Jiaotong University. Xiaomei was a visiting Ph.D. student at Purdue University from 2019 to 2021. Her research focuses on atomistic modelling for fundamental understanding of energy storage materials.

Dr. Xianyang Wu received his Bachelor's degree in Nuclear Engineering from Xi'an Jiaotong University, China in 2010, and his Ph.D. degree from the School of Mechanical Engineering at Purdue University in 2022 under the supervision of Professor Kejie Zhao. His research focuses on structural analysis and characterization of electrode materials for Li-ion batteries.

Dr. Hong Sun is currently a postdoctoral researcher at Lawrence Livermore National Laboratory. She obtained her Bachelor's degree in Materials Science from Xi'an Jiaotong University in 2015 and her Ph.D. degree in Mechanical Engineering from Purdue University in 2020. Her research focuses on atomistic modeling of energy materials and machine learning for materials design and discovery.

Dr. Shan Hu received her Ph.D. degree from Wuhan University of Technology in 2016. She was a visiting scholar at Purdue University from 2019 to 2021. Her research interest is on high-energy-density anode materials of lithium-ion batteries and mechanics and electrochemical performance of all-solid-state batteries.

Madison Perrin is a Master's student at Purdue University working under the supervision of Professor Kejie Zhao. She received her Bachelor's degree in Mechanical and Aeronautical Engineering from Clarkson University in 2017. Her current research focuses on mechanical degradation in electrochemical systems.

Xiaokang Wang received his Bachelor's degree in Engineering from Xi'an Jiaotong University, China in 2017. He is currently a Ph.D. candidate in the School of Mechanical Engineering at Purdue University, working under Professor Kejie Zhao's supervision. His research interest is on mechanics of organic mixed ionic-electronic conductors for mechanically reliable electrochemical devices.

Dr. Yijin Liu received his Ph.D. degree in Optics in 2009 through a joint education program at University of Science & Technology of China and Institute of High Energy Physics. He joined Stanford University as a postdoctoral scholar in 2009 and became an associate staff scientist at the SLAC National Accelerator Laboratory in 2012, a staff scientist in 2015, and a lead scientist in 2020. He is currently leading the Transmission X-ray Microscopy (TXM) program at Stanford Synchrotron Radiation Lightsource (SSRL). Liu has over 10 years of experience in developing state-of-the-art X-ray characterization techniques including multimodal and multiscale microscopy using both synchrotrons and compact laboratory X-ray sources. In addition to his expertise in X-ray techniques, Liu has broadly applied these methods for scientific research in renewable energy science, industry catalysis, oil production, and material under extreme conditions. In more recent years, Liu's research group focused on studying energy storage materials using synchrotron experimental

tools as well as the associated machine learning and data mining approaches.

Dr. Feng Lin is an associate professor of Chemistry at Virginia Tech. He holds a Bachelor's degree in Materials Science and Engineering from Tianjin University and a Ph.D. degree in Materials Science from Colorado School of Mines. Previously, he worked at QuantumScape, Lawrence Berkeley National Laboratory, and National Renewable Energy Laboratory. His research interests include energy storage, catalysis, and smart windows. His research covers the design and synthesis, processing, characterization, and applications of energy materials in electrochemical systems. To accelerate the materials discovery, his group develops an integral analytical program to study materials dynamics under operating conditions using synchrotron X-ray techniques. His awards and recognitions include ECS Battery Early Career Award, National Science Foundation CAREER Award, Energy Storage Materials Young Scientist Award, DOE SLAC Spicer Young Investigator, Ralph E. Powe Junior Faculty Enhancement Award, RCSA Scialog Fellow, and John C. Schug Faculty Research Award.

Dr. Yi Cui is a Fortinet Founders professor of Materials Science and Engineering and of Chemistry (by courtesy) at Stanford University. He obtained his B.S. from the University of Science and Technology of China in 1998 and Ph.D. from Harvard University in 2002. After that, he went to work as a Miller postdoctoral fellow at the University of California, Berkeley. He is a faculty member of Stanford Photon Science of SLAC and principal investigator at the Stanford Institute for Materials & Energy Sciences. He is a member of the National Academy of Sciences, and Fellow of the American Association for the Advancement of Science, Materials Research Society, Electrochemical Society, and the Royal Society of Chemistry. His research largely focused on the materials design for high-energy-density batteries, grid-scale storage, and the safety of batteries. His group also covers a diverse array of research topics, such as solar cells, two-dimensional materials, electrocatalysis, textile engineering, water technology, air filtration, soil cleanup, and bionano interface.

Dr. Kejie Zhao is an associate professor of Mechanical Engineering and B.F.S. Schaefer Scholar at Purdue University. He received his Ph.D. degree in Engineering Science in 2012 from Harvard University and worked as a postdoctoral associate at MIT in 2012−2014. His group at Purdue focuses on the chemomechanics of electrochemically active materials using experimentation and multiscale modeling approaches. He is a recipient of the NSF CAREER Award, EML Young Investigator Award, 3M Nontenured Faculty Award, EnSM Young Scientist Award, and James W. Dally Young Investigator Award from the Society for Experimental Mechanics.

ACKNOWLEDGMENTS

K.Z. and his research group at Purdue University acknowledge the support by the National Science Foundation under Grants DMR-1832707 and CMMI-1726392. Y.C. and R.X. at Stanford University acknowledge the support by the Assistant Secretary for Energy Efficiency and Renewable Energy, Office of Vehicle Technologies of the U.S. Department of Energy under the Battery Materials Research program and the Battery500 Consortium program. F.L. and Z.X. are supported by the National Science Foundation under Grant No. DMR-1832613. Y.L. and J.Z. acknowledge the use of the Stanford Synchrotron Radiation Lightsource, SLAC National Accelerator Laboratory, supported by the U.S. Department of Energy, Office of Science, Office of Basic Energy Sciences under Contract No. DE-AC02-76SF00515.

REFERENCES

(1) Oersted, H. C. Experiments on the Effect of a Current of Electricity on the Magnetic Needle. *Annals Philos.* **1820**, *16*, 273−277.
(2) Elliot, R. The History of Electromagnetics as Hertz Would Have Known It. *IEEE Antennas Propag. Soc. Newsl.* **1988**, *30* (3), 5.
(3) Winter, M.; Barnett, B.; Xu, K. Before Li Ion Batteries. *Chem. Rev.* **2018**, *118* (23), 11433−11456.
(4) Alotto, P.; Guarnieri, M.; Moro, F. Redox Flow Batteries for the Storage of Renewable Energy: A Review. *Renewable and Sustainable Energy Reviews* **2014**, *29*, 325−335.
(5) Gyuk, I.; Johnson, M.; Vetrano, J.; Lynn, K.; Parks, W.; Handa, R.; Kannberg, L. D.; Hearne, S.; Waldrip, K.; Braccio, R. Grid Energy Storage; U.S. Department of Energy, 2013.
(6) Cabana, J.; Monconduit, L.; Larcher, D.; Palacín, M. R. Beyond Intercalation-Based Li-Ion Batteries: The State of the Art and Challenges of Electrode Materials Reacting through Conversion Reactions. *Adv. Mater.* **2010**, *22* (35), 170−192.
(7) Ray, T. R.; Choi, J.; Bandodkar, A. J.; Krishnan, S.; Gutruf, P.; Tian, L.; Ghaffari, R.; Rogers, J. A. Bio-Integrated Wearable Systems: A Comprehensive Review. *Chem. Rev.* **2019**, *119* (8), 5461−5533.
(8) Kwade, A.; Haselrieder, W.; Leithoff, R.; Modlinger, A.; Dietrich, F.; Droeder, K. Current Status and Challenges for Automotive Battery Production Technologies. *Nature Energy* **2018**, *3* (4), 290−300.
(9) Yan, P.; Zheng, J.; Gu, M.; Xiao, J.; Zhang, J. G.; Wang, C. M. Intragranular Cracking as a Critical Barrier for High-Voltage Usage of Layer-Structured Cathode for Lithium-Ion Batteries. *Nat. Commun.* **2017**, *8*, 1−9.
(10) McDowell, M. T.; Quintero Cortes, F. J.; Thenuwara, A. C.; Lewis, J. A. Toward High-Capacity Battery Anode Materials: Chemistry and Mechanics Intertwined. *Chem. Mater.* **2020**, *32*, 8755−8771.
(11) Mims, C. The Battery Boost We've Been Waiting for Is Only a Few Years out. *Wall Street Journal*, March 18, 2018, pp 1−5.
(12) Larcher, D.; Tarascon, J. M. Towards Greener and More Sustainable Batteries for Electrical Energy Storage. *Nat. Chem.* **2015**, *7* (1), 19−29.
(13) Lai, J.; Zhang, J.; Li, Z.; Xiao, Y.; Hua, W.; Wu, Z.; Chen, Y.; Zhong, Y.; Xiang, W.; Guo, X. Structural Elucidation of the Degradation Mechanism of Nickel-Rich Layered Cathodes during High-Voltage Cycling. *Chem. Commun.* **2020**, *56* (36), 4886−4889.
(14) Walter, M.; Kovalenko, M. V.; Kravchyk, K. V. Challenges and Benefits of Post-Lithium-Ion Batteries. *New J. Chem.* **2020**, *44* (5), 1677−1683.
(15) Sharma, S. S.; Manthiram, A. Towards More Environmentally and Socially Responsible Batteries. *Energy Environ. Sci.* **2020**, *13* (11), 4087−4097.
(16) Fu, K. K.; Cheng, J.; Li, T.; Hu, L. Flexible Batteries: From Mechanics to Devices. *ACS Energy Lett.* **2016**, *1*, 1065.
(17) Martirosyan, N.; Kalani, M. Y. S. Epidermal Electronics. *World Neurosurgery.* **2011**, *76*, 485−486.
(18) Snyder, J. F.; O'Brien, D. J.; Baechle, D. M.; Mattson, D. E.; Wetzel, E. D. Structural Composite Capacitors, Supercapacitors, and Batteries for U.S. Army Applications. *Proceedings of the ASME Conference on Smart Materials, Adaptive Structures and Intelligent Systems, SMASIS2008* **2009**, *1*, 1−8.
(19) Jin, T.; Ma, Y.; Xiong, Z.; Fan, X.; Luo, Y.; Hui, Z.; Chen, X.; Yang, Y. Bioinspired, Tree-Root-Like Interfacial Designs for Structural Batteries with Enhanced Mechanical Properties. *Adv. Energy Mater.* **2021**, *11* (25), 2100997.
(20) Huang, W.; Wang, P.; Liao, X.; Chen, Y.; Borovilas, J.; Jin, T.; Li, A.; Cheng, Q.; Zhang, Y.; Zhai, H.; Chitu, A.; Shan, Z.; Yang, Y. Mechanically-Robust Structural Lithium-Sulfur Battery with High Energy Density. *Energy Storage Materials* **2020**, *33*, 416−422.
(21) Winter, M.; Brodd, R. J. What Are Batteries, Fuel Cells, and Supercapacitors? *Chem. Rev.* **2004**, *104* (10), 4245−4269.
(22) Palacín, M. R.; De Guibert, A. Batteries: Why Do Batteries Fail? *Science* **2016**, *351* (6273). DOI: 10.1126/science.1253292.
(23) Lin, F.; Liu, Y.; Yu, X.; Cheng, L.; Singer, A.; Shpyrko, O. G.; Xin, H. L.; Tamura, N.; Tian, C.; Weng, T. C.; Yang, X. Q.; Meng, Y.

https://doi.org/10.1021/acs.chemrev.2c00002
Chem. Rev. 2022, 122, 13043−13107

S.; Nordlund, D.; Yang, W.; Doeff, M. M. Synchrotron X-Ray Analytical Techniques for Studying Materials Electrochemistry in Rechargeable Batteries. *Chem. Rev.* **2017**, *117* (21), 13123−13186.
(24) Mehrer, H. The Effect of Pressure on Diffusion. *Defect and Diffusion Forum* **1996**, *129*−*130*, 57−74.
(25) de Vasconcelos, L. S.; Xu, R.; Zhao, K. Operando Nanoindentation: A New Platform to Measure the Mechanical Properties of Electrodes during Electrochemical Reactions. *J. Electrochem. Soc.* **2017**, *164* (14), A3840−A3847.
(26) Balluffi, R. W.; Allen, S. M.; Carter, W. C. *Kinetics Mater.* **2005**. DOI: 10.1002/0471749311.
(27) Cammarata, R. C. Generalized Thermodynamics of Surfaces with Applications to Small Solid Systems. *Solid State Physics* **2009**, *61*, 1−75.
(28) Ryu, J. H.; Kim, J. W.; Sung, Y. E.; Oh, S. M. Failure Modes of Silicon Powder Negative Electrode in Lithium Secondary Batteries. *Electrochem. Solid-State Lett.* **2004**, *7* (10), A306.
(29) Wang, C.; John Appleby, A.; Little, F. E. Electrochemical Study on Nano-Sn, $Li_{4.4}Sn$ and $AlSi_{0.1}$ Powders Used as Secondary Lithium Battery Anodes. *J. Power Sources* **2001**, *93* (1−2), 174−185.
(30) Li, Y.; Yan, K.; Lee, H. W.; Lu, Z.; Liu, N.; Cui, Y. Growth of Conformal Graphene Cages on Micrometre-Sized Silicon Particles as Stable Battery Anodes. *Nat. Energy* **2016**, *1* (2), 15029 DOI: 10.1038/nenergy.2015.29.
(31) Jin, Y.; Li, S.; Kushima, A.; Zheng, X.; Sun, Y.; Xie, J.; Sun, J.; Xue, W.; Zhou, G.; Wu, J.; Shi, F.; Zhang, R.; Zhu, Z.; So, K.; Cui, Y.; Li, J. Self-Healing SEI Enables Full-Cell Cycling of a Silicon-Majority Anode with a Coulombic Efficiency Exceeding 99.9%. *Energy Environ. Sci.* **2017**, *10* (2), 580−592.
(32) Wang, A.; Tang, S.; Kong, D.; Liu, S.; Chiou, K.; Zhi, L.; Huang, J.; Xia, Y. Y.; Luo, J. Bending-Tolerant Anodes for Lithium-Metal Batteries. *Adv. Mater.* **2018**, *30* (1), 1−7.
(33) Liu, Y.; Zhou, G.; Liu, K.; Cui, Y. Design of Complex Nanomaterials for Energy Storage: Past Success and Future Opportunity. *Acc. Chem. Res.* **2017**, *50* (12), 2895−2905.
(34) Liu, B.; Zhang, J.-G.; Xu, W. Advancing Lithium Metal Batteries. *Joule* **2018**, *2* (5), 833−845.
(35) Lin, D.; Liu, Y.; Cui, Y. Reviving the Lithium Metal Anode for High-Energy Batteries. *Nat. Nanotechnol.* **2017**, *12* (3), 194−206.
(36) Sun, F.; Gao, R.; Zhou, D.; Osenberg, M.; Dong, K.; Kardjilov, N.; Hilger, A.; Markötter, H.; Bieker, P. M.; Liu, X.; Manke, I. Revealing Hidden Facts of Li Anode in Cycled Lithium-Oxygen Batteries through X-Ray and Neutron Tomography. *ACS Energy Letters* **2019**, *4* (1), 306−316.
(37) Cheng, X. B.; Zhang, R.; Zhao, C. Z.; Zhang, Q. Toward Safe Lithium Metal Anode in Rechargeable Batteries: A Review. *Chem. Rev.* **2017**, *117* (15), 10403−10473.
(38) Zhao, Q.; Stalin, S.; Zhao, C. Z.; Archer, L. A. Designing Solid-State Electrolytes for Safe, Energy-Dense Batteries. *Nature Reviews Materials* **2020**, *5*, 229−252.
(39) Morimoto, H.; Awano, H.; Terashima, J.; Shindo, Y.; Nakanishi, S.; Ito, N.; Ishikawa, K.; Tobishima, S. Preparation of Lithium Ion Conducting Solid Electrolyte of NASICON-Type $Li_{1+x}Al_xTi_{2-x}(PO_4)_3$ (X= 0.3) Obtained by Using the Mechanochemical Method and Its Application as Surface Modification Materials. *J. Power Sources* **2013**, *240*, 636−643.
(40) Safanama, D.; Sharma, N.; Rao, R. P.; Brand, H. E. A.; Adams, S. Structural Evolution of NASICON-Type $Li_{1+x}Al_xGe_{2-x}(PO_4)_3$ Using in Situ Synchrotron X-Ray Powder Diffraction. *Journal of Materials Chemistry A* **2016**, *4* (20), 7718−7726.
(41) Murugan, R.; Thangadurai, V.; Weppner, W. Fast Lithium Ion Conduction in Garnet-Type $Li_7La_3Zr_2O_{12}$. *Angewandte Chemie - International Edition* **2007**, *46* (41), 7778−7781.
(42) Kamaya, N.; Homma, K.; Yamakawa, Y.; Hirayama, M.; Kanno, R.; Yonemura, M.; Kamiyama, T.; Kato, Y.; Hama, S.; Kawamoto, K.; Mitsui, A. A Lithium Superionic Conductor. *Nat. Mater.* **2011**, *10* (9), 682−686.
(43) Tang, Y.; Zhang, L.; Chen, J.; Sun, H.; Yang, T.; Liu, Q.; Huang, Q.; Zhu, T.; Huang, J. Electro-Chemo-Mechanics of Lithium in Solid State Lithium Metal Batteries. *Energy Environ. Sci.* **2021**, *14* (2), 602−642.
(44) Lewis, J. A.; Tippens, J.; Cortes, F. J. Q.; McDowell, M. T. Chemo-Mechanical Challenges in Solid-State Batteries. *Trends in Chemistry* **2019**, *1* (9), 845−857.
(45) Wang, D.; Zhu, C.; Fu, Y.; Sun, X.; Yang, Y. Interfaces in Garnet-Based All-Solid-State Lithium Batteries. *Adv. Energy Mater.* **2020**, *10* (39), 2001318.
(46) Bucci, G.; Swamy, T.; Chiang, Y. M.; Carter, W. C. Modeling of Internal Mechanical Failure of All-Solid-State Batteries during Electrochemical Cycling, and Implications for Battery Design. *Journal of Materials Chemistry A* **2017**, *5* (36), 19422−19430.
(47) Kasemchainan, J.; Zekoll, S.; Spencer Jolly, D.; Ning, Z.; Hartley, G. O.; Marrow, J.; Bruce, P. G. Critical Stripping Current Leads to Dendrite Formation on Plating in Lithium Anode Solid Electrolyte Cells. *Nat. Mater.* **2019**, *18* (10), 1105−1111.
(48) Wang, D.; Sun, Q.; Luo, J.; Liang, J.; Sun, Y.; Li, R.; Adair, K.; Zhang, L.; Yang, R.; Lu, S.; Huang, H.; Sun, X. Mitigating the Interfacial Degradation in Cathodes for High-Performance Oxide-Based Solid-State Lithium Batteries. *ACS Appl. Mater. Interfaces* **2019**, *11* (5), 4954−4961.
(49) Krauskopf, T.; Dippel, R.; Hartmann, H.; Peppler, K.; Mogwitz, B.; Richter, F. H.; Zeier, W. G.; Janek, J. Lithium-Metal Growth Kinetics on LLZO Garnet-Type Solid Electrolytes. *Joule* **2019**, *3* (8), 2030−2049.
(50) Cheng, E. J.; Sharafi, A.; Sakamoto, J. Intergranular Li Metal Propagation through Polycrystalline $Li_{6.25}Al_{0.25}La_3Zr_2O_{12}$ Ceramic Electrolyte. *Electrochim. Acta* **2017**, *223*, 85−91.
(51) Nayak, P. K.; Yang, L.; Brehm, W.; Adelhelm, P. From Lithium-Ion to Sodium-Ion Batteries: Advantages, Challenges, and Surprises. *Angew. Chem., Int. Ed.* **2018**, *57* (1), 102−120.
(52) Chayambuka, K.; Mulder, G.; Danilov, D. L.; Notten, P. H. L. From Li-Ion Batteries toward Na-Ion Chemistries: Challenges and Opportunities. *Adv. Energy Mater.* **2020**, *10* (38), 2001310.
(53) Xu, C.; Chen, Y.; Shi, S.; Li, J.; Kang, F.; Su, D. Secondary Batteries with Multivalent Ions for Energy Storage. *Sci. Rep.* **2015**, *5*, 1−8.
(54) Aurbach, D.; McCloskey, B. D.; Nazar, L. F.; Bruce, P. G. Advances in Understanding Mechanisms Underpinning Lithium-Air Batteries. *Nature Energy* **2016**, *1* (9), 1−11.
(55) Le, H. T. T.; Ngo, D. T.; Ho, V. C.; Cao, G.; Park, C. N.; Park, C. J. Insights into Degradation of Metallic Lithium Electrodes Protected by a Bilayer Solid Electrolyte Based on Aluminium Substituted Lithium Lanthanum Titanate in Lithium-Air Batteries. *Journal of Materials Chemistry A* **2016**, *4* (28), 11124−11138.
(56) Zhao, C.; Lu, Y.; Chen, L.; Hu, Y.-S. Ni-Based Cathode Materials for Na-Ion Batteries. *Nano Research* **2019**, *12* (9), 2018−2030.
(57) Yuan, D.; Liang, X.; Wu, L.; Cao, Y.; Ai, X.; Feng, J.; Yang, H. A Honeycomb-Layered $Na_3Ni_2SbO_6$: A High-Rate and Cycle-Stable Cathode for Sodium-Ion Batteries. *Advanced materials* **2014**, *26* (36), 6301−6306.
(58) Munoz-Marquez, M. A.; Saurel, D.; Gomez-Camer, J. L.; Casas-Cabanas, M.; Castillo-Martinez, E.; Rojo, T. Na-Ion Batteries for Large Scale Applications: A Review on Anode Materials and Solid Electrolyte Interphase Formation. *Adv. Energy Mater.* **2017**, *7* (20), 1700463.
(59) Hou, H.; Qiu, X.; Wei, W.; Zhang, Y.; Ji, X. Carbon Anode Materials for Advanced Sodium-Ion Batteries. *Adv. Energy Mater.* **2017**, *7* (24), 1602898.
(60) Usui, H.; Domi, Y.; Yamagami, R.; Sakaguchi, H. Degradation Mechanism of Tin Phosphide as Na-Ion Battery Negative Electrode. *Green Energy and Environment* **2019**, *4* (2), 121−126.
(61) Han, M. H.; Gonzalo, E.; Singh, G.; Rojo, T. A Comprehensive Review of Sodium Layered Oxides: Powerful Cathodes for Na-Ion Batteries. *Energy Environ. Sci.* **2015**, *8* (1), 81−102.
(62) Xu, R.; Yang, Y.; Yin, F.; Liu, P.; Cloetens, P.; Liu, Y.; Lin, F.; Zhao, K. Heterogeneous Damage in Li-Ion Batteries: Experimental

Analysis and Theoretical Modeling. *Journal of the Mechanics and Physics of Solids* **2019**, *129*, 160−183.
(63) Nguyen, C. C.; Yoon, T.; Seo, D. M.; Guduru, P.; Lucht, B. L. Systematic Investigation of Binders for Silicon Anodes: Interactions of Binder with Silicon Particles and Electrolytes and Effects of Binders on Solid Electrolyte Interphase Formation. *ACS Appl. Mater. Interfaces* **2016**, *8* (19), 12211−12220.
(64) Vasconcelos, L. S. de; Xu, R.; Li, J.; Zhao, K. Grid Indentation Analysis of Mechanical Properties of Composite Electrodes in Li-Ion Batteries. *Extreme Mech Lett.* **2016**, *9*, 495−502.
(65) Ely, D. R.; Jana, A.; García, R. E. Phase Field Kinetics of Lithium Electrodeposits. *J. Power Sources* **2014**, *272*, 581−594.
(66) Kumar, R.; Tokranov, A.; Sheldon, B. W.; Xiao, X.; Huang, Z.; Li, C.; Mueller, T. In Situ and Operando Investigations of Failure Mechanisms of the Solid Electrolyte Interphase on Silicon Electrodes. *ACS Energy Letters* **2016**, *1* (4), 689−697.
(67) Pietsch, P.; Westhoff, D.; Feinauer, J.; Eller, J.; Marone, F.; Stampanoni, M.; Schmidt, V.; Wood, V. Quantifying Microstructural Dynamics and Electrochemical Activity of Graphite and Silicon-Graphite Lithium Ion Battery Anodes. *Nat. Commun.* **2016**, *7*, 12909.
(68) Zheng, J.; Ye, Y.; Liu, T.; Xiao, Y.; Wang, C.; Wang, F.; Pan, F. Ni/Li Disordering in Layered Transition Metal Oxide: Electrochemical Impact, Origin, and Control. *Acc. Chem. Res.* **2019**, *52* (8), 2201−2209.
(69) Cheng, J. H.; Pan, C. J.; Nithya, C.; Thirunakaran, R.; Gopukumar, S.; Chen, C. H.; Lee, J. F.; Chen, J. M.; Sivashanmugam, A.; Hwang, B. J. Effect of Mg Doping on the Local Structure of $LiMg_yCo_{1-y}O_2$ Cathode Material Investigated by X-Ray Absorption Spectroscopy. *J. Power Sources* **2014**, *252*, 292−297.
(70) Yang, Z.; Mu, L.; Hou, D.; Rahman, M. M.; Xu, Z.; Liu, J.; Nordlund, D.; Sun, C.-J. J.; Xiao, X.; Lin, F. Probing Dopant Redistribution, Phase Propagation, and Local Chemical Changes in the Synthesis of Layered Oxide Battery Cathodes. *Adv. Energy Mater.* **2021**, *11* (1), 2002719.
(71) Li, Q.; Yao, Z.; Lee, E.; Xu, Y.; Thackeray, M. M.; Wolverton, C.; Dravid, V. P.; Wu, J. Dynamic Imaging of Crystalline Defects in Lithium-Manganese Oxide Electrodes during Electrochemical Activation to High Voltage. *Nat. Commun.* **2019**, *10* (1), 1−7.
(72) Li, S.; Yao, Z.; Zheng, J.; Fu, M.; Cen, J.; Hwang, S.; Jin, H.; Orlov, A.; Gu, L.; Wang, S.; Chen, Z.; Su, D. Direct Observation of Defect-Aided Structural Evolution in a Nickel-Rich Layered Cathode. *Angew. Chem.* **2020**, *132* (49), 22276−22283.
(73) Moriwake, H.; Kuwabara, A.; Fisher, C. A. J.; Huang, R.; Hitosugi, T.; Ikuhara, Y. H. Y.; Oki, H.; Ikuhara, Y. H. Y. First-Principles Calculations of Lithium-Ion Migration at a Coherent Grain Boundary in a Cathode Material, $LiCoO_2$. *Adv. Mater.* **2013**, *25* (4), 618−622.
(74) Park, H.; Mesnier, A.; Lee, S.; Jarvis, K.; Manthiram, A.; Warner, J. H. Intrinsic Li Distribution in Layered Transition-Metal Oxides Using Low-Dose Scanning Transmission Electron Microscopy and Spectroscopy. *Chem. Mater.* **2021**, *33* (12), 4638−4650.
(75) Chu, M.; Huang, Z.; Zhang, T.; Wang, R.; Shao, T.; Wang, C.; Zhu, W.; He, L.; Chen, J.; Zhao, W.; Xiao, Y. Enhancing the Electrochemical Performance and Structural Stability of Ni-Rich Layered Cathode Materials via Dual-Site Doping. *ACS Appl. Mater. Interfaces* **2021**, *13* (17), 19950−19958.
(76) Zheng, J.; Ye, Y.; Liu, T.; Xiao, Y.; Wang, C.; Wang, F.; Pan, F. Ni/Li Disordering in Layered Transition Metal Oxide: Electrochemical Impact, Origin, and Control. *Acc. Chem. Res.* **2019**, *52* (8), 2201−2209.
(77) Sun, C.; Liao, X.; Xia, F.; Zhao, Y.; Zhang, L.; Mu, S.; Shi, S.; Li, Y.; Peng, H.; Van Tendeloo, G.; Zhao, K.; Wu, J. High-Voltage Cycling Induced Thermal Vulnerability in $LiCoO_2$ Cathode: Cation Loss and Oxygen Release Driven by Oxygen Vacancy Migration. *ACS Nano* **2020**, *14* (5), 6181−6190.
(78) Mu, L.; Lin, R.; Xu, R.; Han, L.; Xia, S.; Sokaras, D.; Steiner, J.; Weng, T.-C.; Nordlund, D.; Doeff, M. M.; Liu, Y.; Zhao, K.; Xin, H. L.; Lin, F. Oxygen Release Induced Chemomechanical Breakdown of Layered Cathode Materials. *Nano Lett.* **2018**, *18* (5), 3241−3249.
(79) Lee, S.; Jin, W.; Kim, S. H.; Joo, S. H.; Nam, G.; Oh, P.; Kim, Y.-K.; Kwak, S. K.; Cho, J. Oxygen Vacancy Diffusion and Condensation in Lithium-Ion Battery Cathode Materials. *Angew. Chem.* **2019**, *131* (31), 10588−10595.
(80) Fell, C. R.; Qian, D.; Carroll, K. J.; Chi, M.; Jones, J. L.; Meng, Y. S. Correlation Between Oxygen Vacancy, Microstrain, and Cation Distribution in Lithium-Excess Layered Oxides During the First Electrochemical Cycle. *Chem. Mater.* **2013**, *25* (9), 1621−1629.
(81) Hong, Y. S.; Huang, X.; Wei, C.; Wang, J.; Zhang, J. N.; Yan, H.; Chu, Y. S.; Pianetta, P.; Xiao, R.; Yu, X.; Liu, Y.; Li, H. Hierarchical Defect Engineering for $LiCoO_2$ through Low-Solubility Trace Element Doping. *Chem.* **2020**, *6*, 2759−2769.
(82) Ulvestad, U.; Singer, A.; Clark, J. N.; Cho, H. M.; Kim, J. W.; Harder, R.; Maser, J.; Meng, Y. S.; Shpyrko, O. G. Topological Defect Dynamics in Operando Battery Nanoparticles. *Science* **2015**, *348* (6241), 1344−1347.
(83) Singer, A.; Zhang, M.; Hy, S.; Cela, D.; Fang, C.; Wynn, T. A.; Qiu, B.; Xia, Y.; Liu, Z.; Ulvestad, A.; Hua, N.; Wingert, J.; Liu, H.; Sprung, M.; Zozulya, A. V.; Maxey, E.; Harder, R.; Meng, Y. S.; Shpyrko, O. G. Nucleation of Dislocations and Their Dynamics in Layered Oxide Cathode Materials during Battery Charging. *Nature Energy* **2018**, *3* (8), 641−647.
(84) Yan, P.; Zheng, J.; Chen, T.; Luo, L.; Jiang, Y.; Wang, K.; Sui, M.; Zhang, J.-G.; Zhang, S.; Wang, C. Coupling of Electrochemically Triggered Thermal and Mechanical Effects to Aggravate Failure in a Layered Cathode. *Nat. Commun.* **2018**, *9* (1), 2437.
(85) Zhang, H.; Omenya, F.; Yan, P.; Luo, L.; Whittingham, M. S.; Wang, C.; Zhou, G. Rock-Salt Growth-Induced (003) Cracking in a Layered Positive Electrode for Li-Ion Batteries. *ACS Energy Letters* **2017**, *2* (11), 2607−2615.
(86) Van Der Ven, A.; Marianetti, C.; Morgan, D.; Ceder, G. Phase Transformations and Volume Changes in Spinel $Li_xMn_2O_4$. *Solid State Ionics* **2000**, *135* (1−4), 21−32.
(87) McCalla, E.; Abakumov, A. M.; Saubanère, M.; Foix, D.; Berg, E. J.; Rousse, G.; Doublet, M.-L.; Gonbeau, D.; Novák, P.; Van Tendeloo, G.; Dominko, R.; Tarascon, J.-M. Visualization of O-O Peroxo-like Dimers in High-Capacity Layered Oxides for Li-Ion Batteries. *Science* **2015**, *350* (6267), 1516−1521.
(88) Yu, D. Y. W.; Yanagida, K.; Kato, Y.; Nakamura, H. Electrochemical Activities in Li_2MnO_3. *J. Electrochem. Soc.* **2009**, *156* (6), A417.
(89) Li, S.; Yao, Z.; Zheng, J.; Fu, M.; Cen, J.; Hwang, S.; Jin, H.; Orlov, A.; Gu, L.; Wang, S.; Chen, Z.; Su, D. Direct Observation of Defect-Aided Structural Evolution in a Nickel-Rich Layered Cathode. *Angew. Chem.* **2020**, *132* (49), 22276−22283.
(90) Moriwake, H.; Kuwabara, A.; Fisher, C. A. J.; Huang, R.; Hitosugi, T.; Ikuhara, Y. H. Y.; Oki, H.; Ikuhara, Y. H. Y. First-Principles Calculations of Lithium-Ion Migration at a Coherent Grain Boundary in a Cathode Material, $LiCoO_2$. *Adv. Mater.* **2013**, *25* (4), 618−622.
(91) Sun, G.; Sui, T.; Song, B.; Zheng, H.; Lu, L.; Korsunsky, A. M. On the Fragmentation of Active Material Secondary Particles in Lithium Ion Battery Cathodes Induced by Charge Cycling. *Extreme Mech Lett.* **2016**, *9* (March), 449−458.
(92) He, X.; Sun, H.; Ding, X.; Zhao, K. Grain Boundaries and Their Impact on Li Kinetics in Layered-Oxide Cathodes for Li-Ion Batteries. *J. Phys. Chem. C* **2021**, *125* (19), 10284−10294.
(93) Bai, Y.; Zhao, K.; Liu, Y.; Stein, P.; Xu, B. X. A Chemo-Mechanical Grain Boundary Model and Its Application to Understand the Damage of Li-Ion Battery Materials. *Scripta Materialia* **2020**, *183*, 45−49.
(94) Hong, Y. S.; Huang, X.; Wei, C.; Wang, J.; Zhang, J. N.; Yan, H.; Chu, Y. S.; Pianetta, P.; Xiao, R.; Yu, X.; Liu, Y.; Li, H. Hierarchical Defect Engineering for $LiCoO_2$ through Low-Solubility Trace Element Doping. *Chem.* **2020**, *6*, 2759−2769.
(95) Liu, X. H.; Huang, S.; Picraux, S. T.; Li, J.; Zhu, T.; Huang, J. Y. Reversible Nanopore Formation in Ge Nanowires during Lithiation-Delithiation Cycling: An in Situ Transmission Electron Microscopy Study. *Nano Lett.* **2011**, *11* (9), 3991−3997.

https://doi.org/10.1021/acs.chemrev.2c00002
Chem. Rev. 2022, 122, 13043−13107

(96) Zhou, X.; Li, T.; Cui, Y.; Meyerson, M. L.; Mullins, C. B.; Liu, Y.; Zhu, L. In Situ Focused Ion Beam-Scanning Electron Microscope Study of Crack and Nanopore Formation in Germanium Particle during (De)Lithiation. *ACS Applied Energy Materials* **2019**, *2* (4), 2441−2446.
(97) Li, Q.; Du, P.; Yuan, Y.; Yao, W.; Ma, Z.; Guo, B.; Lyu, Y.; Wang, P.; Wang, H.; Nie, A.; Shahbazian-Yassar, R.; Lu, J. Real-Time TEM Study of Nanopore Evolution in Battery Materials and Their Suppression for Enhanced Cycling Performance. *Nano Lett.* **2019**, *19* (5), 3074−3082.
(98) He, Y.; Jiang, L.; Chen, T.; Xu, Y.; Jia, H.; Yi, R.; Xue, D.; Song, M.; Genc, A.; Bouchet-Marquis, C.; Pullan, L.; Tessner, T.; Yoo, J.; Li, X.; Zhang, J. G.; Zhang, S.; Wang, C. Progressive Growth of the Solid-Electrolyte Interphase towards the Si Anode Interior Causes Capacity Fading. *Nat. Nanotechnol.* **2021**, *16* (10), 1113−1120.
(99) McDowell, M. T.; Lee, S. W.; Harris, J. T.; Korgel, B. A.; Wang, C.; Nix, W. D.; Cui, Y. In Situ TEM of Two-Phase Lithiation of Amorphous Silicon Nanospheres. *Nano Lett.* **2013**, *13* (2), 758−764.
(100) Liu, X. H.; Zhong, L.; Huang, S.; Mao, S. X.; Zhu, T.; Huang, J. Y. Size-Dependent Fracture of Silicon Nanoparticles during Lithiation. *ACS Nano* **2012**, *6* (2), 1522−1531.
(101) Xia, S.; Mu, L.; Xu, Z.; Wang, J.; Wei, C.; Liu, L.; Pianetta, P.; Zhao, K.; Yu, X.; Lin, F.; Liu, Y. Chemomechanical Interplay of Layered Cathode Materials Undergoing Fast Charging in Lithium Batteries. *Nano Energy* **2018**, *53*, 753−762.
(102) Zhao, K.; Pharr, M.; Vlassak, J. J.; Suo, Z. Fracture of Electrodes in Lithium-Ion Batteries Caused by Fast Charging. *J. Appl. Phys.* **2010**, *108* (7), 1−7.
(103) de Vasconcelos, L. S.; Xu, R.; Zhao, K. Quantitative Spatiotemporal Li Profiling Using Nanoindentation. *Journal of the Mechanics and Physics of Solids* **2020**, *144*, 104102.
(104) Liu, X. H.; Wang, J. W.; Huang, S.; Fan, F.; Huang, X.; Liu, Y.; Krylyuk, S.; Yoo, J.; Dayeh, S. A.; Davydov, A. V.; Mao, S. X.; Picraux, S. T.; Zhang, S.; Li, J.; Zhu, T.; Huang, J. Y. In Situ Atomic-Scale Imaging of Electrochemical Lithiation in Silicon. *Nat. Nanotechnol.* **2012**, *7* (11), 749−756.
(105) Bohn, E.; Eckl, T.; Kamlah, M.; Mcmeeking, R. A Model for Lithium Diffusion and Stress Generation in an Intercalation Storage Particle with Phase Change. *J. Electrochem. Soc.* **2013**, *160* (10), A1638.
(106) Lee, S. W.; Lee, H. W.; Ryu, I.; Nix, W. D.; Gao, H.; Cui, Y. Kinetics and Fracture Resistance of Lithiated Silicon Nanostructure Pairs Controlled by Their Mechanical Interaction. *Nat. Commun.* **2015**, *6*, 7533 DOI: 10.1038/ncomms8533.
(107) Liu, X. H.; Wang, J. W.; Huang, S.; Fan, F.; Huang, X.; Liu, Y.; Krylyuk, S.; Yoo, J.; Dayeh, S. A.; Davydov, A. V.; Mao, S. X.; Picraux, S. T.; Zhang, S.; Li, J.; Zhu, T.; Huang, J. Y. In Situ Atomic-Scale Imaging of Electrochemical Lithiation in Silicon. *Nat. Nanotechnol.* **2012**, *7* (11), 749−756.
(108) Deng, H. D.; Zhao, H.; Jin, N.; Hughes, L.; Savitzky, B. H.; Ophus, C.; Fraggedakis, D.; Borbély, A.; Yu, Y. S.; Lomeli, E. G.; Yan, R.; Liu, J.; Shapiro, D. A.; Cai, W.; Bazant, M. Z.; Minor, A. M.; Chueh, W. C. Correlative Image Learning of Chemo-Mechanics in Phase-Transforming Solids. *Nat. Mater.* **2022**, *21* (5), 547−554.
(109) Hu, Y.; Zhao, X.; Suo, Z. Averting Cracks Caused by Insertion Reaction In Lithium-Ion Batteries. *J. Mater. Res.* **2010**, *25* (6), 1007−1010.
(110) Zhao, K.; Pharr, M.; Wan, Q.; Wang, W. L.; Kaxiras, E.; Vlassak, J. J.; Suo, Z. Concurrent Reaction and Plasticity during Initial Lithiation of Crystalline Silicon in Lithium-Ion Batteries. *J. Electrochem. Soc.* **2012**, *159* (3), A238−A243.
(111) Lim, J. M.; Hwang, T.; Kim, D.; Park, M. S.; Cho, K.; Cho, M. Intrinsic Origins of Crack Generation in Ni-Rich $LiNi_{0.8}Co_{0.1}Mn_{0.1}O_2$ Layered Oxide Cathode Material. *Sci. Rep.* **2017**, *7* (1), 1−10.
(112) Xu, R.; de Vasconcelos, L. S.; Shi, J.; Li, J.; Zhao, K. Disintegration of Meatball Electrodes for $LiNi_xMn_yCo_zO_2$ Cathode Materials. *Experimental Mechanics* **2018**, *58* (4), 549−559.
(113) Ryu, H. H.; Park, K. J.; Yoon, C. S.; Sun, Y. K. Capacity Fading of Ni-Rich $Li[Ni_xCo_yMn_{1-x-y}]O_2$ ($0.6 \leq x \leq 0.95$) Cathodes for High-Energy-Density Lithium-Ion Batteries: Bulk or Surface Degradation? *Chem. Mater.* **2018**, *30* (3), 1155−1163.
(114) Watanabe, S.; Kinoshita, M.; Hosokawa, T.; Morigaki, K.; Nakura, K. Capacity Fade of $LiAl_yNi_{1-x-y}Co_xO_2$ Cathode for Lithium-Ion Batteries during Accelerated Calendar and Cycle Life Tests (Surface Analysis of $LiAl_yNi_{1-x-y}Co_xO_2$ Cathode Af. *J. Power Sources* **2014**, *258*, 210−217.
(115) Xu, R.; Zhao, K. Mechanical Interactions Regulated Kinetics and Morphology of Composite Electrodes in Li-Ion Batteries. *Extreme Mech Lett.* **2016**, *8*, 13−21.
(116) Xu, R.; Scalco De Vasconcelos, L.; Zhao, K. Computational Analysis of Chemomechanical Behaviors of Composite Electrodes in Li-Ion Batteries. *J. Mater. Res.* **2016**, *31* (18), 2715−2727.
(117) Ali, Y.; Iqbal, N.; Lee, S. Inhomogeneous Stress Development at the Multiparticle Electrode of Lithium-Ion Batteries. *Int. J. Energy Res.* **2021**, *45*, 14788.
(118) Bard, A. J.; Abruna, H. D.; Chidsey, C. E.; Faulkner, L. R.; Feldberg, S. W.; Itaya, K.; Majda, M.; Melroy, O.; Murray, R. W. The Electrode/Electrolyte Interface-a Status Report. *J. Phys. Chem.* **1993**, *97* (28), 7147−7173.
(119) Winter, M. The Solid Electrolyte Interphase - The Most Important and the Least Understood Solid Electrolyte in Rechargeable Li Batteries. *Zeitschrift für Physikalische Chemie* **2009**, *223* (10−11), 1395−1406.
(120) Dey, A. N.; Sullivan, B. P. The Electrochemical Decomposition of Propylene Carbonate on Graphite. *J. Electrochem. Soc.* **1970**, *117* (2), 222.
(121) Xu, K. Electrolytes and Interphases in Li-Ion Batteries and Beyond. *Chem. Rev.* **2014**, *114* (23), 11503−11618.
(122) Aurbach, D.; Markovsky, B.; Levi, M. D.; Levi, E.; Schechter, A.; Moshkovich, M.; Cohen, Y. New Insights into the Interactions between Electrode Materials and Electrolyte Solutions for Advanced Nonaqueous Batteries. *J. Power Sources* **1999**, *81*−*82*, 95−111.
(123) Wang, A.; Kadam, S.; Li, H.; Shi, S.; Qi, Y. Review on Modeling of the Anode Solid Electrolyte Interphase (SEI) for Lithium-Ion Batteries. *npj Computational Materials* **2018**, *4* (1), 15.
(124) Peled, E. The Electrochemical Behavior of Alkali and Alkaline Earth Metals in Nonaqueous Battery Systems—The Solid Electrolyte Interphase Model. *J. Electrochem. Soc.* **1979**, *126* (12), 2047−2051.
(125) Peled, E.; Menkin, S. Review—SEI: Past, Present and Future. *J. Electrochem. Soc.* **2017**, *164* (7), A1703−A1719.
(126) Peled, E.; Golodnitsky, D.; Ardel, G. Advanced Model for Solid Electrolyte Interphase Electrodes in Liquid and Polymer Electrolytes. *J. Electrochem. Soc.* **1997**, *144* (8), L208−L210.
(127) Aurbach, D.; Daroux, M. L.; Faguy, P. W.; Yeager, E. Identification of Surface Films Formed on Lithium in Propylene Carbonate Solutions. *J. Electrochem. Soc.* **1987**, *134* (7), 1611−1620.
(128) Aurbach, D.; Moshkovich, M.; Cohen, Y.; Schechter, A. The Study of Surface Film Formation on Noble-Metal Electrodes in Alkyl Carbonates/Li Salt Solutions, Using Simultaneous in Situ AFM, EQCM, FTIR, and EIS. *Langmuir* **1999**, *15* (8), 2947−2960.
(129) Li, Y.; Huang, W.; Li, Y.; Pei, A.; Boyle, D. T.; Cui, Y. Correlating Structure and Function of Battery Interphases at Atomic Resolution Using Cryoelectron Microscopy. *Joule* **2018**, *2* (10), 2167−2177.
(130) Shen, C.; Wang, S.; Jin, Y.; Han, W. Q. In Situ AFM Imaging of Solid Electrolyte Interfaces on HOPG with Ethylene Carbonate and Fluoroethylene Carbonate-Based Electrolytes. *ACS Appl. Mater. Interfaces* **2015**, *7* (45), 25441−25447.
(131) Li, Y.; Li, Y.; Pei, A.; Yan, K.; Sun, Y.; Wu, C.-L.; Joubert, L.-M.; Chin, R.; Koh, A. L.; Yu, Y.; Perrino, J.; Butz, B.; Chu, S.; Cui, Y. Atomic Structure of Sensitive Battery Materials and Interfaces Revealed by Cryo-Electron Microscopy. *Science* **2017**, *358* (6362), 506−510.
(132) Peled, E.; Bar Tow, D.; Merson, A.; Gladkich, A.; Burstein, L.; Golodnitsky, D. Composition, Depth Profiles and Lateral Distribution of Materials in the SEI Built on HOPG-TOF SIMS and XPS Studies. *J. Power Sources* **2001**, *97*−*98*, 52−57.

(133) Heine, J.; Hilbig, P.; Qi, X.; Niehoff, P.; Winter, M.; Bieker, P. Fluoroethylene Carbonate as Electrolyte Additive in Tetraethylene Glycol Dimethyl Ether Based Electrolytes for Application in Lithium Ion and Lithium Metal Batteries. *J. Electrochem. Soc.* **2015**, *162* (6), A1094−A1101.
(134) Guo, K.; Kumar, R.; Xiao, X.; Sheldon, B. W.; Gao, H. Failure Progression in the Solid Electrolyte Interphase (SEI) on Silicon Electrodes. *Nano Energy* **2020**, *68*, 104257.
(135) Xu, W.; Wang, J.; Ding, F.; Chen, X.; Nasybulin, E.; Zhang, Y.; Zhang, J. G. Lithium Metal Anodes for Rechargeable Batteries. *Energy Environ. Sci.* **2014**, *7* (2), 513−537.
(136) Zhao, K.; Cui, Y. Understanding the Role of Mechanics in Energy Materials: A Perspective. *Extreme Mech Lett.* **2016**, *9*, 347−352.
(137) Wachtler, M.; Besenhard, J. O.; Winter, M. Tin and Tin-Based Intermetallics as New Anode Materials for Lithium-Ion Cells. *J. Power Sources* **2001**, *94* (2), 189−193.
(138) Sethuraman, V. A.; Chon, M. J.; Shimshak, M.; Srinivasan, V.; Guduru, P. R. In Situ Measurements of Stress Evolution in Silicon Thin Films during Electrochemical Lithiation and Delithiation. *J. Power Sources* **2010**, *195* (15), 5062−5066.
(139) Pharr, M.; Suo, Z.; Vlassak, J. J. Variation of Stress with Charging Rate Due to Strain-Rate Sensitivity of Silicon Electrodes of Li-Ion Batteries. *J. Power Sources* **2014**, *270*, 569−575.
(140) Nadimpalli, S. P. V.; Tripuraneni, R.; Sethuraman, V. A. Real-Time Stress Measurements in Germanium Thin Film Electrodes during Electrochemical Lithiation/Delithiation Cycling. *J. Electrochem. Soc.* **2015**, *162* (14), A2840−A2846.
(141) Pyun, S. Il; Go, J. Y.; Jang, T. S. An Investigation of Intercalation-Induced Stresses Generated during Lithium Transport through $Li_{1-\delta}CoO_2$ Film Electrode Using a Laser Beam Deflection Method. *Electrochim. Acta* **2004**, *49* (25), 4477−4486.
(142) Tikekar, M. D.; Choudhury, S.; Tu, Z.; Archer, L. A. Design Principles for Electrolytes and Interfaces for Stable Lithium-Metal Batteries. *Nat. Energy* **2016**, *1* (9), 16114 DOI: 10.1038/nenergy.2016.114.
(143) Kushima, A.; So, K. P.; Su, C.; Bai, P.; Kuriyama, N.; Maebashi, T.; Fujiwara, Y.; Bazant, M. Z.; Li, J. Liquid Cell Transmission Electron Microscopy Observation of Lithium Metal Growth and Dissolution: Root Growth, Dead Lithium and Lithium Flotsams. *Nano Energy* **2017**, *32* (November 2016), 271−279.
(144) Ghassemi, H.; Au, M.; Chen, N.; Heiden, P. A.; Yassar, R. S. Real-Time Observation of Lithium Fibers Growth inside a Nanoscale Lithium-Ion Battery. *Appl. Phys. Lett.* **2011**, *99* (12), 123113.
(145) Shen, C.; Hu, G.; Cheong, L.-Z.; Huang, S.; Zhang, J.-G.; Wang, D. Direct Observation of the Growth of Lithium Dendrites on Graphite Anodes by Operando EC-AFM. *Small Methods* **2018**, *2* (2), 1700298.
(146) Yamada, Y.; Wang, J.; Ko, S.; Watanabe, E.; Yamada, A. Advances and Issues in Developing Salt-Concentrated Battery Electrolytes. *Nature Energy* **2019**, *4* (4), 269−280.
(147) Wang, H.; Huang, W.; Yu, Z.; Huang, W.; Xu, R.; Zhang, Z.; Bao, Z.; Cui, Y. Efficient Lithium Metal Cycling over a Wide Range of Pressures from an Anion-Derived Solid-Electrolyte Interphase Framework. *ACS Energy Letters* **2021**, *6* (2), 816−825.
(148) Chen, J.; Fan, X.; Li, Q.; Yang, H.; Khoshi, M. R.; Xu, Y.; Hwang, S.; Chen, L.; Ji, X.; Yang, C.; He, H.; Wang, C.; Garfunkel, E.; Su, D.; Borodin, O.; Wang, C. Electrolyte Design for LiF-Rich Solid-Electrolyte Interfaces to Enable High-Performance Microsized Alloy Anodes for Batteries. *Nat. Energy* **2020**, *5*, 386−397.
(149) Zhao, W.; Song, W.; Cheong, L.-Z.; Wang, D.; Li, H.; Besenbacher, F.; Huang, F.; Shen, C. Beyond Imaging: Applications of Atomic Force Microscopy for the Study of Lithium-Ion Batteries. *Ultramicroscopy* **2019**, *204*, 34−48.
(150) Wang, S.; Liu, Q.; Zhao, C.; Lv, F.; Qin, X.; Du, H.; Kang, F.; Li, B. Advances in Understanding Materials for Rechargeable Lithium Batteries by Atomic Force Microscopy. *Energy & Environmental Materials* **2018**, *1* (1), 28−40.
(151) Yoon, I.; Jurng, S.; Abraham, D. P.; Lucht, B. L.; Guduru, P. R. In Situ Measurement of the Plane-Strain Modulus of the Solid Electrolyte Interphase on Lithium-Metal Anodes in Ionic Liquid Electrolytes. *Nano Lett.* **2018**, *18* (9), 5752−5759.
(152) Zhang, Q.; Xiao, X.; Cheng, Y.-T.; Verbrugge, M. W. A Non-Destructive Method for Measuring the Mechanical Properties of Ultrathin Films Prepared by Atomic Layer Deposition. *Appl. Phys. Lett.* **2014**, *105* (6), 61901.
(153) Zhang, Q.; Xiao, X.; Zhou, W.; Cheng, Y.; Verbrugge, M. W. Toward High Cycle Efficiency of Silicon-Based Negative Electrodes by Designing the Solid Electrolyte Interphase. *Adv. Energy Mater.* **2015**, *5* (5), 1401398.
(154) de Vasconcelos, L. S.; Sharma, N.; Xu, R.; Zhao, K. In-Situ Nanoindentation Measurement of Local Mechanical Behavior of a Li-Ion Battery Cathode in Liquid Electrolyte. *Experimental Mechanics* **2019**, *59* (3), 337−347.
(155) Magasinski, A.; Zdyrko, B.; Kovalenko, I.; Hertzberg, B.; Burtovyy, R.; Huebner, C. F.; Fuller, T. F.; Luzinov, I.; Yushin, G. Toward Efficient Binders for Li-Ion Battery Si-Based Anodes: Polyacrylic Acid. *ACS Appl. Mater. Interfaces* **2010**, *2* (11), 3004−3010.
(156) Amanieu, H.-Y.; Rosato, D.; Sebastiani, M.; Massimi, F.; Lupascu, D. C. Mechanical Property Measurements of Heterogeneous Materials by Selective Nanoindentation: Application to $LiMn_2O_4$ Cathode. *Materials Science and Engineering: A* **2014**, *593*, 92−102.
(157) Cheng, E. J.; Taylor, N. J.; Wolfenstine, J.; Sakamoto, J. Elastic Properties of Lithium Cobalt Oxide (LiCoO 2). *Journal of Asian Ceramic Societies* **2017**, *5* (2), 113−117.
(158) Wang, H.; Nadimpalli, S. P. V.; Shenoy, V. B. Inelastic Shape Changes of Silicon Particles and Stress Evolution at Binder/Particle Interface in a Composite Electrode during Lithiation/Delithiation Cycling. *Extreme Mech Lett.* **2016**, *9*, 430−438.
(159) Iqbal, N.; Ali, Y.; Lee, S. Chemo-Mechanical Response of Composite Electrode Systems with Multiple Binder Connections. *Electrochim. Acta* **2020**, *364*, 137312.
(160) Müller, S.; Pietsch, P.; Brandt, B. E.; Baade, P.; De Andrade, V.; De Carlo, F.; Wood, V. Quantification and Modeling of Mechanical Degradation in Lithium-Ion Batteries Based on Nanoscale Imaging. *Nat. Commun.* **2018**, *9* (1), 1−8.
(161) Iqbal, N.; Lee, S. Mechanical Failure Analysis of Graphite Anode Particles with PVDF Binders in Li-Ion Batteries. *J. Electrochem. Soc.* **2018**, *165* (9), A1961−A1970.
(162) Lee, S.; Park, J.; Yang, J.; Lu, W. Molecular Dynamics Simulations of the Traction-Separation Response at the Interface between PVDF Binder and Graphite in the Electrode of Li-Ion Batteries. *J. Electrochem. Soc.* **2014**, *161* (9), A1218−A1223.
(163) Wang, Y.; Zhang, Q.; Li, D.; Hu, J.; Xu, J.; Dang, D.; Xiao, X.; Cheng, Y. T. Mechanical Property Evolution of Silicon Composite Electrodes Studied by Environmental Nanoindentation. *Adv. Energy Mater.* **2018**, *8* (10), 1−8.
(164) Tariq, F.; Yufit, V.; Eastwood, D. S.; Merla, Y.; Biton, M.; Wu, B.; Chen, Z.; Freedman, K.; Offer, G.; Peled, E.; Lee, P. D.; Golodnitsky, D.; Brandon, N. In-Operando X-Ray Tomography Study of Lithiation Induced Delamination of Si Based Anodes for Lithium-Ion Batteries. *ECS Electrochem. Lett.* **2014**, *3* (7), A76−A78.
(165) Guo, Z.; Liu, C.; Lu, B.; Feng, J. Theoretical and Experimental Study on the Interfacial Adhesive Properties of Graphite Electrodes in Different Charging and Aging States. *Carbon N Y* **2019**, *150*, 32−42.
(166) Jaiser, S.; Kumberg, J.; Klaver, J.; Urai, J. L.; Schabel, W.; Schmatz, J.; Scharfer, P. Microstructure Formation of Lithium-Ion Battery Electrodes during Drying - An Ex-Situ Study Using Cryogenic Broad Ion Beam Slope-Cutting and Scanning Electron Microscopy (Cryo-BIB-SEM). *J. Power Sources* **2017**, *345*, 97−107.
(167) Baunach, M.; Jaiser, S.; Schmelzle, S.; Nirschl, H.; Scharfer, P.; Schabel, W. Delamination Behavior of Lithium-Ion Battery Anodes: Influence of Drying Temperature during Electrode Processing. *Drying Technology* **2016**, *34* (4), 462−473.
(168) Jeon, H.; Cho, I.; Jo, H.; Kim, K.; Ryou, M. H.; Lee, Y. M. Highly Rough Copper Current Collector: Improving Adhesion

Property between a Silicon Electrode and Current Collector for Flexible Lithium-Ion Batteries. *RSC Adv.* **2017**, *7* (57), 35681−35686.
(169) Dai, C.; Wang, Z.; Liu, K.; Zhu, X.; Liao, X.; Chen, X.; Pan, Y. Effects of Cycle Times and C-Rate on Mechanical Properties of Copper Foil and Adhesive Strength of Electrodes in Commercial LiCoO 2 LIBs. *Eng. Failure Anal.* **2019**, *101* (September 2018), 193−205.
(170) Jäckel, N.; Dargel, V.; Shpigel, N.; Sigalov, S.; Levi, M. D.; Daikhin, L.; Aurbach, D.; Presser, V. In Situ Multi-Length Scale Approach to Understand the Mechanics of Soft and Rigid Binder in Composite Lithium Ion Battery Electrodes. *J. Power Sources* **2017**, *371* (August), 162−166.
(171) Choi, S.; Kwon, T.-w.; Coskun, A.; Choi, J. W. Highly Elastic Binders Integrating Polyrotaxanes for Silicon Microparticle Anodes in Lithium Ion Batteries. *Science* **2017**, *357* (6348), 279−283.
(172) Li, Y.; Meyer, S.; Lim, J.; Lee, S. C.; Gent, W. E.; Marchesini, S.; Krishnan, H.; Tyliszczak, T.; Shapiro, D.; Kilcoyne, A. L. D.; Chueh, W. C. Effects of Particle Size, Electronic Connectivity, and Incoherent Nanoscale Domains on the Sequence of Lithiation in LiFePO4 Porous Electrodes. *Adv. Mater.* **2015**, *27* (42), 6591−6597.
(173) Nagai, H.; Morita, M.; Satoh, K. Development of the Li-Ion Battery Cell for Hybrid Vehicle; SAE Technical Paper 2016-01-1207; SAE, 2016. DOI: 10.4271/2016-01-1207.
(174) Ebner, M.; Chung, D. W.; García, R. E.; Wood, V. Tortuosity Anisotropy in Lithium-Ion Battery Electrodes. *Adv. Energy Mater.* **2014**, *4* (5), 1301278.
(175) Müller, M.; Pfaffmann, L.; Jaiser, S.; Baunach, M.; Trouillet, V.; Scheiba, F.; Scharfer, P.; Schabel, W.; Bauer, W. Investigation of Binder Distribution in Graphite Anodes for Lithium-Ion Batteries. *J. Power Sources* **2017**, *340*, 1−5.
(176) Jiang, Z.; Li, J.; Yang, Y.; Mu, L.; Wei, C.; Yu, X.; Pianetta, P.; Zhao, K.; Cloetens, P.; Lin, F.; Liu, Y. Machine-Learning-Revealed Statistics of the Particle-Carbon/Binder Detachment in Lithium-Ion Battery Cathodes. *Nat. Commun.* **2020**, *11* (1), 2310.
(177) Park, K. Y.; Park, J. W.; Seong, W. M.; Yoon, K.; Hwang, T. H.; Ko, K. H.; Han, J. H.; Jaedong, Y.; Kang, K. Understanding Capacity Fading Mechanism of Thick Electrodes for Lithium-Ion Rechargeable Batteries. *J. Power Sources* **2020**, *468*, 228369.
(178) Yang, Y.; Xu, R.; Zhang, K.; Lee, S.; Mu, L.; Liu, P.; Waters, C. K.; Spence, S.; Xu, Z.; Wei, C.; Kautz, D. J.; Yuan, Q.; Dong, Y.; Yu, Y.; Xiao, X.; Lee, H.; Pianetta, P.; Cloetens, P.; Lee, J.; Zhao, K.; Lin, F.; Liu, Y. Quantification of Heterogeneous Degradation in Li-ion Batteries. *Adv. Energy Mater.* **2019**, *9* (25), 1900674.
(179) Hawley, W. B.; Li, J. Electrode Manufacturing for Lithium-Ion Batteries—Analysis of Current and next Generation Processing. *Journal of Energy Storage* **2019**, *25* (July), 100862.
(180) Bauer, W.; Nötzel, D. Rheological Properties and Stability of NMP Based Cathode Slurries for Lithium Ion Batteries. *Ceram. Int.* **2014**, *40* (3), 4591−4598.
(181) Zielke, L.; Sun, F.; Markötter, H.; Hilger, A.; Moroni, R.; Zengerle, R.; Thiele, S.; Banhart, J.; Manke, I. Synchrotron X-Ray Tomographic Study of a Silicon Electrode Before and After Discharge and the Effect of Cavities on Particle Fracturing. *ChemElectroChem.* **2016**, *3* (7), 1170−1177.
(182) Bockholt, H.; Indrikova, M.; Netz, A.; Golks, F.; Kwade, A. The Interaction of Consecutive Process Steps in the Manufacturing of Lithium-Ion Battery Electrodes with Regard to Structural and Electrochemical Properties. *J. Power Sources* **2016**, *325*, 140−151.
(183) Sangrós Giménez, C.; Finke, B.; Schilde, C.; Froböse, L.; Kwade, A. Numerical Simulation of the Behavior of Lithium-Ion Battery Electrodes during the Calendaring Process via the Discrete Element Method. *Powder Technol.* **2019**, *349*, 1−11.
(184) Roberts, S. A.; Brunini, V. E.; Long, K. N.; Grillet, A. M. A Framework for Three-Dimensional Mesoscale Modeling of Anisotropic Swelling and Mechanical Deformation in Lithium-Ion Electrodes. *J. Electrochem. Soc.* **2014**, *161* (11), F3052−F3059.
(185) Chen, Z.; Danilov, D. L.; Eichel, R.; Notten, P. H. L. Electrochemistry Communications On the Reaction Rate Distribution in Porous Electrodes. *Electrochem. Commun.* **2020**, *121* (September), 106865.
(186) Kim, H.; Oh, S. K.; Lee, J.; Doo, S. W.; Kim, Y.; Lee, K. T. Electrochimica Acta Failure Mode of Thick Cathodes for Li-Ion Batteries: Variation of State-of-Charge along the Electrode Thickness Direction. *Electrochim. Acta* **2021**, *370*, 137743.
(187) Yari, S.; Hamed, H.; D'Haen, J.; Van Bael, M. K.; Renner, F. U.; Hardy, A.; Safari, M. Constructive versus Destructive Heterogeneity in Porous Electrodes of Lithium-Ion Batteries. *ACS Applied Energy Materials* **2020**, *3* (12), 11820−11829.
(188) Bachman, J. C.; Muy, S.; Grimaud, A.; Chang, H. H.; Pour, N.; Lux, S. F.; Paschos, O.; Maglia, F.; Lupart, S.; Lamp, P.; Giordano, L.; Shao-Horn, Y. Inorganic Solid-State Electrolytes for Lithium Batteries: Mechanisms and Properties Governing Ion Conduction. *Chem. Rev.* **2016**, *116* (1), 140−162.
(189) Kerman, K.; Luntz, A.; Viswanathan, V.; Chiang, Y.-M.; Chen, Z. Review—Practical Challenges Hindering the Development of Solid State Li Ion Batteries. *J. Electrochem. Soc.* **2017**, *164* (7), A1731−A1744.
(190) Liu, H.; Cheng, X. B.; Huang, J. Q.; Yuan, H.; Lu, Y.; Yan, C.; Zhu, G. L.; Xu, R.; Zhao, C. Z.; Hou, L. P.; He, C.; Kaskel, S.; Zhang, Q. Controlling Dendrite Growth in Solid-State Electrolytes. *ACS Energy Letters* **2020**, *5* (3), 833−843.
(191) Wang, Z. Q.; Wu, M. S.; Liu, G.; Lei, X. L.; Xu, B.; Ouyang, C. Y. Elastic Properties of New Solid State Electrolyte Material $Li_{10}GeP_2S_{12}$: A Study from First-Principles Calculations. *Int. J. Electrochem. Sci.* **2014**, *9* (2), 562−568.
(192) Herbert, E. G.; Tenhaeff, W. E.; Dudney, N. J.; Pharr, G. M. Mechanical Characterization of LiPON Films Using Nanoindentation. *Thin Solid Films* **2011**, *520* (1), 413−418.
(193) Zekoll, S. Tuning the Properties of Ceramic Solid Electrolytes for Lithium Batteries. Thesis; University of Oxford, 2018.
(194) Athanasiou, C. E.; Jin, M. Y.; Ramirez, C.; Padture, N. P.; Sheldon, B. W. High-Toughness Inorganic Solid Electrolytes via the Use of Reduced Graphene Oxide. *Matter* **2020**, *3* (1), 212−229.
(195) Kim, Y.; Jo, H.; Allen, J. L.; Choe, H.; Wolfenstine, J.; Sakamoto, J. The Effect of Relative Density on the Mechanical Properties of Hot-Pressed Cubic $Li_7La_3Zr_2O_{12}$. *J. Am. Ceram. Soc.* **2016**, *99* (4), 1367−1374.
(196) Wang, A.-N.; Nonemacher, J. F.; Yan, G.; Finsterbusch, M.; Malzbender, J.; Krüger, M. Mechanical Properties of the Solid Electrolyte Al-Substituted $Li_7La_3Zr_2O_{12}$ (LLZO) by Utilizing Micro-Pillar Indentation Splitting Test. *J. Eur. Ceram Soc.* **2018**, *38* (9), 3201−3209.
(197) Yu, S.; Schmidt, R. D.; Garcia-Mendez, R.; Herbert, E.; Dudney, N. J.; Wolfenstine, J. B.; Sakamoto, J.; Siegel, D. J. Elastic Properties of the Solid Electrolyte $Li_7La_3Zr_2O_{12}$ (LLZO). *Chem. Mater.* **2016**, *28* (1), 197−206.
(198) Guo, H.; Su, J.; Zha, W.; Xiu, T.; Song, Z.; Badding, M. E.; Jin, J.; Wen, Z. Achieving High Critical Current Density in Ta-Doped $Li_7La_3Zr_2O_{12}$/MgO Composite Electrolytes. *J. Alloys Compd.* **2021**, *856*, 157222.
(199) Cho, Y. H.; Wolfenstine, J.; Rangasamy, E.; Kim, H.; Choe, H.; Sakamoto, J. Mechanical Properties of the Solid Li-Ion Conducting Electrolyte: $Li_{0.33}La_{0.57}TiO_3$. *J. Mater. Sci.* **2012**, *47* (16), 5970−5977.
(200) LePage, W. S.; Chen, Y.; Kazyak, E.; Chen, K.-H.; Sanchez, A. J.; Poli, A.; Arruda, E. M.; Thouless, M. D.; Dasgupta, N. P. Lithium Mechanics: Roles of Strain Rate and Temperature and Implications for Lithium Metal Batteries. *J. Electrochem. Soc.* **2019**, *166* (2), A89−A97.
(201) Fincher, C. D.; Ojeda, D.; Zhang, Y.; Pharr, G. M.; Pharr, M. Mechanical Properties of Metallic Lithium: From Nano to Bulk Scales. *Acta Mater.* **2020**, *186*, 215−222.
(202) He, Y.; Ren, X.; Xu, Y.; Engelhard, M. H.; Li, X.; Xiao, J.; Liu, J.; Zhang, J. G.; Xu, W.; Wang, C. Origin of Lithium Whisker Formation and Growth under Stress. *Nat. Nanotechnol.* **2019**, *14* (11), 1042−1047.

(203) Zhang, L.; Yang, T.; Du, C.; Liu, Q.; Tang, Y.; Zhao, J.; Wang, B.; Chen, T.; Sun, Y.; Jia, P.; Li, H.; Geng, L.; Chen, J.; Ye, H.; Wang, Z.; Li, Y.; Sun, H.; Li, X.; Dai, Q.; Tang, Y.; Peng, Q.; Shen, T.; Zhang, S.; Zhu, T.; Huang, J. Lithium Whisker Growth and Stress Generation in an in Situ Atomic Force Microscope-Environmental Transmission Electron Microscope Set-Up. *Nat. Nanotechnol.* **2020**, *15* (2), 94−98.
(204) Stallard, J. C.; Wheatcroft, L.; Booth, S. G.; Boston, R.; Corr, S. A.; De Volder, M. F. L.; Inkson, B. J.; Fleck, N. A. Mechanical Properties of Cathode Materials for Lithium-Ion Batteries. *Joule* **2022**, *6* (5), 984−1007.
(205) Porz, L.; Swamy, T.; Sheldon, B. W.; Rettenwander, D.; Frömling, T.; Thaman, H. L.; Berendts, S.; Uecker, R.; Carter, W. C.; Chiang, Y. M. Mechanism of Lithium Metal Penetration through Inorganic Solid Electrolytes. *Adv. Energy Mater.* **2017**, *7* (20), 1701003.
(206) Hull, D.; Rosenberg, H. M. The Deformation of Lithium, Sodium and Potassium at Low Temperatures: Tensile and Resistivity Experiments. *Philos. Mag.* **1959**, *4* (39), 303−315.
(207) Gorgas, I.; Herke, P.; Schoeck, G. The Plastic Behaviour of Lithium Single Crystals. *Phys. Status Solidi* **1981**, *67* (2), 617−623.
(208) Pichl, W.; Krystian, M. The Flow Stress of High Purity Alkali Metals. *Phys. Status Solidi* **1997**, *160* (2), 373−383.
(209) Schultz, R. P. *Lithium: Measurement of Young's Modulus and Yield Strength*; FERMILAB-TM-2191; Fermi National Accelerator Laboratory: Batavia, IL, 2002. DOI: 10.2172/804180.
(210) Masias, A.; Felten, N.; Garcia-Mendez, R.; Wolfenstine, J.; Sakamoto, J. Elastic, Plastic, and Creep Mechanical Properties of Lithium Metal. *J. Mater. Sci.* **2019**, *54* (3), 2585−2600.
(211) Uchic, M. D.; Dimiduk, D. M.; Florando, J. N.; Nix, W. D. J. Sample Dimensions Influence Strength and Crystal Plasticity. *Science* **2004**, *305* (5686), 986−989.
(212) Zhu, J.; Zhao, J.; Xiang, Y.; Lin, M.; Wang, H.; Zheng, B.; He, H.; Wu, Q.; Huang, J. Y.; Yang, Y. Chemomechanical Failure Mechanism Study in NASICON-Type Li1.3Al0.3Ti1.7(PO4)3Solid-State Lithium Batteries. *Chem. Mater.* **2020**, *32* (12), 4998−5008.
(213) Tippens, J.; Miers, J. C.; Afshar, A.; Lewis, J. A.; Cortes, F. J. Q.; Qiao, H.; Marchese, T. S.; Di Leo, C. V.; Saldana, C.; McDowell, M. T. Visualizing Chemomechanical Degradation of a Solid-State Battery Electrolyte. *ACS Energy Letters* **2019**, *4* (6), 1475−1483.
(214) Lewis, J. A.; Cortes, F. J. Q.; Boebinger, M. G.; Tippens, J.; Marchese, T. S.; Kondekar, N.; Liu, X.; Chi, M.; McDowell, M. T. Interphase Morphology between a Solid-State Electrolyte and Lithium Controls Cell Failure. *ACS Energy Letters* **2019**, *4* (2), 591−599.
(215) Wang, M. J.; Choudhury, R.; Sakamoto, J. Characterizing the Li-Solid-Electrolyte Interface Dynamics as a Function of Stack Pressure and Current Density. *Joule* **2019**, *3* (9), 2165−2178.
(216) Swamy, T.; Park, R.; Sheldon, B. W.; Rettenwander, D.; Porz, L.; Berendts, S.; Uecker, R.; Carter, W. C.; Chiang, Y.-M. Lithium Metal Penetration Induced by Electrodeposition through Solid Electrolytes: Example in Single-Crystal $Li_7La_3Zr_2O_{12}$ Garnet. *J. Electrochem. Soc.* **2018**, *165* (16), A3648−A3655.
(217) Ning, Z.; Jolly, D. S.; Li, G.; De Meyere, R.; Pu, S. D.; Chen, Y.; Kasemchainan, J.; Ihli, J.; Gong, C.; Liu, B.; Melvin, D. L. R.; Bonnin, A.; Magdysyuk, O.; Adamson, P.; Hartley, G. O.; Monroe, C. W.; Marrow, T. J.; Bruce, P. G. Visualizing Plating-Induced Cracking in Lithium-Anode Solid-Electrolyte Cells. *Nat. Mater.* **2021**, *20*, 1121−1129.
(218) Xiao, Y.; Wang, Y.; Bo, S.-H.; Kim, J. C.; Miara, L. J.; Ceder, G. Understanding Interface Stability in Solid-State Batteries. *Nature Reviews Materials* **2020**, *5* (2), 105−126.
(219) Xu, R.; Liu, F.; Ye, Y.; Chen, H.; Yang, R. R.; Ma, Y.; Huang, W.; Wan, J.; Cui, Y. A Morphologically Stable Li/Electrolyte Interface for All-Solid-State Batteries Enabled by 3D-Micropatterned Garnet. *Adv. Mater.* **2021**, *33* (49), 2104009.
(220) Gao, X.; Liu, B.; Hu, B.; Ning, Z.; Jolly, D. S.; Zhang, S.; Perera, J.; Bu, J.; Liu, J.; Doerrer, C.; Darnbrough, E.; Armstrong, D.; Grant, P. S.; Bruce, P. G. Solid-State Lithium Battery Cathodes Operating at Low Pressures. *Joule* **2022**, *6* (3), 636−646.
(221) Klinsmann, M.; Hildebrand, F. E.; Ganser, M.; McMeeking, R. M. Dendritic Cracking in Solid Electrolytes Driven by Lithium Insertion. *J. Power Sources* **2019**, *442*, 227226.
(222) Li, Y.; Chen, X.; Dolocan, A.; Cui, Z.; Xin, S.; Xue, L.; Xu, H.; Park, K.; Goodenough, J. B. Garnet Electrolyte with an Ultralow Interfacial Resistance for Li-Metal Batteries. *J. Am. Chem. Soc.* **2018**, *140* (20), 6448−6455.
(223) Sharafi, A.; Kazyak, E.; Davis, A. L.; Yu, S.; Thompson, T.; Siegel, D. J.; Dasgupta, N. P.; Sakamoto, J. Surface Chemistry Mechanism of Ultra-Low Interfacial Resistance in the Solid-State Electrolyte $Li_7La_3Zr_2O_{12}$. *Chem. Mater.* **2017**, *29* (18), 7961−7968.
(224) Monroe, C.; Newman, J. The Impact of Elastic Deformation on Deposition Kinetics at Lithium/Polymer Interfaces. *J. Electrochem. Soc.* **2005**, *152* (2), A396.
(225) Liu, X.; Garcia-Mendez, R.; Lupini, A. R.; Cheng, Y.; Hood, Z. D.; Han, F.; Sharafi, A.; Idrobo, J. C.; Dudney, N. J.; Wang, C.; Ma, C.; Sakamoto, J.; Chi, M. Local Electronic Structure Variation Resulting in Li "filament" Formation within Solid Electrolytes. *Nat. Mater.* **2021**, *20*, 1485−1490.
(226) Sharafi, A.; Haslam, C. G.; Kerns, R. D.; Wolfenstine, J.; Sakamoto, J. Controlling and Correlating the Effect of Grain Size with the Mechanical and Electrochemical Properties of $Li_7La_3Zr_2O_{12}$ Solid-State Electrolyte. *Journal of Materials Chemistry A* **2017**, *5* (40), 21491−21504.
(227) Yu, S.; Siegel, D. J. Grain Boundary Softening: A Potential Mechanism for Lithium Metal Penetration through Stiff Solid Electrolytes. *ACS Appl. Mater. Interfaces* **2018**, *10* (44), 38151−38158.
(228) Aguesse, F.; Manalastas, W.; Buannic, L.; Lopez Del Amo, J. M.; Singh, G.; Llordes, A.; Kilner, J. Investigating the Dendritic Growth during Full Cell Cycling of Garnet Electrolyte in Direct Contact with Li Metal. *ACS Appl. Mater. Interfaces* **2017**, *9* (4), 3808−3816.
(229) Griffith, A. A. Containing Papers of a Mathematical or Physical Character.- VI. The Phenomena of Rupture and Flow in Solids. *Phil. Trans. Royal Soc. A* **1921**, *221* (582−593), 163−198.
(230) David, I. N.; Thompson, T.; Wolfenstine, J.; Allen, J. L.; Sakamoto, J. Microstructure and Li-Ion Conductivity of Hot-Pressed Cubic $Li_7La_3Zr_2O_{12}$. *J. Am. Ceram. Soc.* **2015**, *98* (4), 1209−1214.
(231) Raj, R.; Wolfenstine, J. Current Limit Diagrams for Dendrite Formation in Solid-State Electrolytes for Li-Ion Batteries. *J. Power Sources* **2017**, *343*, 119−126.
(232) Chen, Y.-T.; Jena, A.; Pang, W. K.; Peterson, V. K.; Sheu, H.-S.; Chang, H.; Liu, R.-S. Voltammetric Enhancement of Li-Ion Conduction in Al-Doped $Li_{7-x}La_3Zr_2O_{12}$ Solid Electrolyte. *J. Phys. Chem. C* **2017**, *121* (29), 15565−15573.
(233) Pesci, F. M.; Brugge, R. H.; Hekselman, A. K. O.; Cavallaro, A.; Chater, R. J.; Aguadero, A. Elucidating the Role of Dopants in the Critical Current Density for Dendrite Formation in Garnet Electrolytes. *Journal of Materials Chemistry A* **2018**, *6* (40), 19817−19827.
(234) Han, F.; Westover, A. S.; Yue, J.; Fan, X.; Wang, F.; Chi, M.; Leonard, D. N.; Dudney, N. J.; Wang, H.; Wang, C. High Electronic Conductivity as the Origin of Lithium Dendrite Formation within Solid Electrolytes. *Nature Energy* **2019**, *4* (3), 187−196.
(235) Lewis, J. A.; Cortes, F. J. Q.; Liu, Y.; Miers, J. C.; Verma, A.; Vishnugopi, B. S.; Tippens, J.; Prakash, D.; Marchese, T. S.; Han, S. Y.; Lee, C.; Shetty, P. P.; Lee, H. W.; Shevchenko, P.; de Carlo, F.; Saldana, C.; Mukherjee, P. P.; McDowell, M. T. Linking Void and Interphase Evolution to Electrochemistry in Solid-State Batteries Using Operando X-Ray Tomography. *Nat. Mater.* **2021**, *20* (4), 503−510.
(236) Banerjee, A.; Wang, X.; Fang, C.; Wu, E. A.; Meng, Y. S. Interfaces and Interphases in All-Solid-State Batteries with Inorganic Solid Electrolytes. *Chem. Rev.* **2020**, *120* (14), 6878−6933.
(237) Koerver, R.; Aygün, I.; Leichtweiß, T.; Dietrich, C.; Zhang, W.; Binder, J. O.; Hartmann, P.; Zeier, W. G.; Janek, J. Capacity Fade in Solid-State Batteries: Interphase Formation and Chemomechanical Processes in Nickel-Rich Layered Oxide Cathodes and Lithium

Thiophosphate Solid Electrolytes. *Chem. Mater.* **2017**, *29* (13), 5574−5582.
(238) Liu, H.; Choe, M.-J.; Enrique, R. A.; Orvañanos, B.; Zhou, L.; Liu, T.; Thornton, K.; Grey, C. P. Effects of Antisite Defects on Li Diffusion in $LiFePO_4$ Revealed by Li Isotope Exchange. *J. Phys. Chem. C* **2017**, *121* (22), 12025−12036.
(239) Zhang, B.; Xu, Y.; Wang, J.; Ma, X.; Hou, W. Suppressing Fe-Li, Ni-Li Antisite Defects in $LiFePO_4$ and $LiNi_{1/3}Co_{1/3}Mn_{1/3}O_2$ by Optimized Synthesis Methods. *ACS Applied Energy Materials* **2020**, *3* (6), 5893−5901.
(240) Chung, S.-Y.; Choi, S.-Y.; Yamamoto, T.; Ikuhara, Y. Orientation-Dependent Arrangement of Antisite Defects in Lithium Iron(II) Phosphate Crystals. *Angew. Chem.* **2009**, *121* (3), 551−554.
(241) Chung, S.-Y.; Choi, S.-Y.; Yamamoto, T.; Ikuhara, Y. Orientation-Dependent Arrangement of Antisite Defects in Lithium Iron(II) Phosphate Crystals. *Angew. Chem.* **2009**, *121* (3), 551−554.
(242) Kang, K.; Meng, Y. S.; Bréger, J.; Grey, C. P.; Ceder, G. Electrodes with High Power and High Capacity for Rechargeable Lithium Batteries. *Science* **2006**, *311* (5763), 977−980.
(243) Lee, S.; Jin, W.; Kim, S. H.; Joo, S. H.; Nam, G.; Oh, P.; Kim, Y.-K.; Kwak, S. K.; Cho, J. Oxygen Vacancy Diffusion and Condensation in Lithium-Ion Battery Cathode Materials. *Angew. Chem.* **2019**, *131* (31), 10588−10595.
(244) Zhang, J.-N.; Li, Q.; Ouyang, C.; Yu, X.; Ge, M.; Huang, X.; Hu, E.; Ma, C.; Li, S.; Xiao, R.; Yang, W.; Chu, Y.; Liu, Y.; Yu, H.; Yang, X.-Q.; Huang, X.; Chen, L.; Li, H. Trace Doping of Multiple Elements Enables Stable Battery Cycling of $LiCoO_2$ at 4.6 V. *Nature Energy* **2019**, *4* (7), 594−603.
(245) Zhang, J.-N.; Li, Q.; Ouyang, C.; Yu, X.; Ge, M.; Huang, X.; Hu, E.; Ma, C.; Li, S.; Xiao, R.; Yang, W.; Chu, Y.; Liu, Y.; Yu, H.; Yang, X.-Q.; Huang, X.; Chen, L.; Li, H. Trace Doping of Multiple Elements Enables Stable Battery Cycling of $LiCoO_2$ at 4.6 V. *Nature Energy* **2019**, *4* (7), 594−603.
(246) Zhang, H.; Omenya, F.; Yan, P.; Luo, L.; Whittingham, M. S.; Wang, C.; Zhou, G. Rock-Salt Growth-Induced (003) Cracking in a Layered Positive Electrode for Li-Ion Batteries. *ACS Energy Letters* **2017**, *2* (11), 2607−2615.
(247) Gent, W. E.; Li, Y.; Ahn, S.; Lim, J.; Liu, Y.; Wise, A. M.; Gopal, C. B.; Mueller, D. N.; Davis, R.; Weker, J. N.; Park, J. H.; Doo, S. K.; Chueh, W. C. Persistent State-of-Charge Heterogeneity in Relaxed, Partially Charged $Li_{1-x}Ni_{1/3}Co_{1/3}Mn_{1/3}O_2$ Secondary Particles. *Adv. Mater.* **2016**, *28*, 6631−6638.
(248) Xu, Z.; Jiang, Z.; Kuai, C.; Xu, R.; Qin, C.; Zhang, Y.; Rahman, M. M.; Wei, C.; Nordlund, D.; Sun, C. J. C.-J. C.-J.; Xiao, X.; Du, X.-W. W.; Zhao, K.; Yan, P.; Liu, Y.; Lin, F. Charge Distribution Guided by Grain Crystallographic Orientations in Polycrystalline Battery Materials. *Nat. Commun.* **2020**, *11* (1), 83.
(249) Xu, Z.; Jiang, Z.; Kuai, C.; Xu, R.; Qin, C.; Zhang, Y.; Rahman, M. M.; Wei, C.; Nordlund, D.; Sun, C. J. C.-J. C.-J.; Xiao, X.; Du, X.-W. W.; Zhao, K.; Yan, P.; Liu, Y.; Lin, F. Charge Distribution Guided by Grain Crystallographic Orientations in Polycrystalline Battery Materials. *Nat. Commun.* **2020**, *11* (1), 83.
(250) Xu, Z.; Hou, D.; Kautz, D. J.; Liu, W.; Xu, R.; Xiao, X.; Lin, F. Charging Reactions Promoted by Geometrically Necessary Dislocations in Battery Materials Revealed by In Situ Single-Particle Synchrotron Measurements. *Adv. Mater.* **2020**, *32* (37), 2003417.
(251) Bai, Y.; Zhao, K.; Liu, Y.; Stein, P.; Xu, B. X. A Chemo-Mechanical Grain Boundary Model and Its Application to Understand the Damage of Li-Ion Battery Materials. *Scripta Materialia* **2020**, *183*, 45−49.
(252) Gent, W. E.; Li, Y.; Ahn, S.; Lim, J.; Liu, Y.; Wise, A. M.; Gopal, C. B.; Mueller, D. N.; Davis, R.; Weker, J. N.; Park, J. H.; Doo, S. K.; Chueh, W. C. Persistent State-of-Charge Heterogeneity in Relaxed, Partially Charged $Li_{1-x}Ni_{1/3}Co_{1/3}Mn_{1/3}O_2$ Secondary Particles. *Adv. Mater.* **2016**, *28*, 6631−6638.
(253) Radvanyi, E.; Porcher, W.; De Vito, E.; Montani, A.; Franger, S.; Jouanneau Si Larbi, S. Failure Mechanisms of Nano-Silicon Anodes upon Cycling: An Electrode Porosity Evolution Model. *Phys. Chem. Chem. Phys.* **2014**, *16* (32), 17142−17153.
(254) Moon, J.; Lee, H. C.; Jung, H.; Wakita, S.; Cho, S.; Yoon, J.; Lee, J.; Ueda, A.; Choi, B.; Lee, S.; Ito, K.; Kubo, Y.; Lim, A. C.; Seo, J. G.; Yoo, J.; Lee, S.; Ham, Y.; Baek, W.; Ryu, Y. G.; Han, I. T. Interplay between Electrochemical Reactions and Mechanical Responses in Silicon-Graphite Anodes and Its Impact on Degradation. *Nat. Commun.* **2021**, *12* (1), 2714 DOI: 10.1038/s41467-021-22662-7.
(255) Schmidt, D.; Kamlah, M.; Knoblauch, V. Highly Densified NCM-Cathodes for High Energy Li-Ion Batteries: Microstructural Evolution during Densification and Its Influence on the Performance of the Electrodes. *Journal of Energy Storage* **2018**, *17*, 213−223.
(256) Schmidt, D.; Kamlah, M.; Knoblauch, V. Highly Densified NCM-Cathodes for High Energy Li-Ion Batteries: Microstructural Evolution during Densification and Its Influence on the Performance of the Electrodes. *Journal of Energy Storage* **2018**, *17*, 213−223.
(257) Kim, S.; Choi, S. J.; Zhao, K.; Yang, H.; Gobbi, G.; Zhang, S.; Li, J. Electrochemically Driven Mechanical Energy Harvesting. *Nat. Commun.* **2016**, *7*, 10146.
(258) Sheldon, B. W.; Soni, S. K.; Xiao, X.; Qi, Y. Stress Contributions to Solution Thermodynamics in Li-Si Alloys. *Electrochem. Solid-State Lett.* **2012**, *15* (1), A9.
(259) Muralidharan, N.; Li, M.; Carter, R. E.; Galioto, N.; Pint, C. L. Ultralow Frequency Electrochemical-Mechanical Strain Energy Harvester Using 2D Black Phosphorus Nanosheets. *ACS Energy Letters* **2017**, *2* (8), 1797−1803.
(260) Muralidharan, N.; Brock, C. N.; Cohn, A. P.; Schauben, D.; Carter, R. E.; Oakes, L.; Walker, D. G.; Pint, C. L. Tunable Mechanochemistry of Lithium Battery Electrodes. *ACS Nano* **2017**, *11* (6), 6243−6251.
(261) Gu, M.; Yang, H.; Perea, D. E.; Zhang, J. G.; Zhang, S.; Wang, C. M. Bending-Induced Symmetry Breaking of Lithiation in Germanium Nanowires. *Nano Lett.* **2014**, *14* (8), 4622−4627.
(262) McDowell, M. T.; Ryu, I.; Lee, S. W.; Wang, C.; Nix, W. D.; Cui, Y. Studying the Kinetics of Crystalline Silicon Nanoparticle Lithiation with in Situ Transmission Electron Microscopy. *Adv. Mater.* **2012**, *24* (45), 6034−6041.
(263) Larché, F. C.; Cahn, J. W. The Interactions of Composition and Stress in Crystalline Solids. *Journal of Research of the National Bureau of Standards (United States)* **1984**, *89* (6), 467−500.
(264) Haftbaradaran, H.; Song, J.; Curtin, W. A.; Gao, H. Continuum and Atomistic Models of Strongly Coupled Diffusion, Stress, and Solute Concentration. *J. Power Sources* **2011**, *196* (1), 361−370.
(265) Di Leo, C. V.; Rejovitzky, E.; Anand, L. Diffusion-Deformation Theory for Amorphous Silicon Anodes: The Role of Plastic Deformation on Electrochemical Performance. *International Journal of Solids and Structures* **2015**, *67*−*68*, 283−296.
(266) Xu, R.; Zhao, K. Electrochemomechanics of Electrodes in Li-Ion Batteries: A Review. *Journal of Electrochemical Energy Conversion and Storage* **2016**, *13* (3), 030803.
(267) Ding, B.; Wu, H.; Xu, Z.; Li, X.; Gao, H. Stress Effects on Lithiation in Silicon. *Nano Energy* **2017**, *38*, 486−493.
(268) Pan, J.; Zhang, Q.; Li, J.; Beck, M. J.; Xiao, X.; Cheng, Y.-T. Effects of Stress on Lithium Transport in Amorphous Silicon Electrodes for Lithium-Ion Batteries. *Nano Energy* **2015**, *13*, 192−199.
(269) Larché, F. C.; Voorhees, P. W. Diffusion and Stresses: Basic Thermodynamics. *Defect and Diffusion Forum* **1996**, *129*−*130*, 31−36.
(270) Butler, J. Studies in Heterogeneous Equilibria. Part III. A Kinetic Theory of Reversible Oxidation Potentials at Inert Electrodes. *Trans. Faraday Soc.* **1924**, *19*, 734−739.
(271) Bower, A. F.; Guduru, P. R.; Sethuraman, V. A. A Finite Strain Model of Stress, Diffusion, Plastic Flow, and Electrochemical Reactions in a Lithium-Ion Half-Cell. *Journal of the Mechanics and Physics of Solids* **2011**, *59* (4), 804−828.
(272) Lu, B.; Song, Y.; Zhang, Q.; Pan, J.; Cheng, Y.-T.; Zhang, J. Voltage Hysteresis of Lithium Ion Batteries Caused by Mechanical Stress. *Phys. Chem. Chem. Phys.* **2016**, *18*, 4721.

(273) Miller, D. J.; Proff, C.; Wen, J. G.; Abraham, D. P.; Bareño, J. Observation of Microstructural Evolution in Li Battery Cathode Oxide Particles by in Situ Electron Microscopy. *Adv. Energy Mater.* **2013**, *3* (8), 1098−1103.
(274) Besli, M. M.; Xia, S.; Kuppan, S.; Huang, Y.; Metzger, M.; Shukla, A. K.; Schneider, G.; Hellstrom, S.; Christensen, J.; Doeff, M. M.; Liu, Y. Mesoscale Chemomechanical Interplay of the $LiNi_{0.8}Co_{0.15}Al_{0.05}O_2$ Cathode in Solid-State Polymer Batteries. *Chem. Mater.* **2019**, *31* (2), 491−501.
(275) Watanabe, S.; Kinoshita, M.; Hosokawa, T.; Morigaki, K.; Nakura, K. Capacity Fading of $LiAl_yNi_{1-x-y}Co_xO_2$ Cathode for Lithium-Ion Batteries during Accelerated Calendar and Cycle Life Tests (Effect of Depth of Discharge in Charge-Discharge Cycling on the Suppression of the Micro-c. *J. Power Sources* **2014**, *260*, 50−56.
(276) Wu, X.; Billaud, J.; Jerjen, I.; Marone, F.; Ishihara, Y.; Adachi, M.; Adachi, Y.; Villevieille, C.; Kato, Y. Operando Visualization of Morphological Dynamics in All-Solid-State Batteries. *Adv. Energy Mater.* **2019**, *9* (34), 1901547.
(277) Kotak, N.; Barai, P.; Verma, A.; Mistry, A.; Mukherjee, P. P. Electrochemistry-Mechanics Coupling in Intercalation Electrodes. *J. Electrochem. Soc.* **2018**, *165* (5), A1064−A1083.
(278) Xu, R.; Zhao, K. Corrosive Fracture of Electrodes in Li-Ion Batteries. *Journal of the Mechanics and Physics of Solids* **2018**, *121*, 258−280.
(279) Jiang, M.; Danilov, D. L.; Eichel, R.-A.; Notten, P. H. L. A Review of Degradation Mechanisms and Recent Achievements for Ni-Rich Cathode-Based Li-Ion Batteries. *Adv. Energy Mater.* **2021**, *11*, 2103005.
(280) Nam, G. W.; Park, N. Y.; Park, K. J.; Yang, J.; Liu, J.; Yoon, C. S.; Sun, Y. K. Capacity Fading of Ni-Rich NCA Cathodes: Effect of Microcracking Extent. *ACS Energy Letters* **2019**, *4* (12), 2995−3001.
(281) Yin, S.; Deng, W.; Chen, J.; Gao, X.; Zou, G.; Hou, H.; Ji, X. Fundamental and Solutions of Microcrack in Ni-Rich Layered Oxide Cathode Materials of Lithium-Ion Batteries. *Nano Energy* **2021**, *83* (February), 105854.
(282) Sun, Y. K. High-Capacity Layered Cathodes for Next-Generation Electric Vehicles. *ACS Energy Letters* **2019**, *4* (5), 1042−1044.
(283) Wu, H.; Chan, G.; Choi, J. W.; Ryu, I.; Yao, Y.; McDowell, M. T.; Lee, S. W.; Jackson, A.; Yang, Y.; Hu, L.; Cui, Y. Stable Cycling of Double-Walled Silicon Nanotube Battery Anodes through Solid-Electrolyte Interphase Control. *Nat. Nanotechnol.* **2012**, *7* (5), 310−315.
(284) Choi, S.; Kwon, T.-w.; Coskun, A.; Choi, J. W. Highly Elastic Binders Integrating Polyrotaxanes for Silicon Microparticle Anodes in Lithium Ion Batteries. *Science* **2017**, *357* (6348), 279−283.
(285) Deng, Z.; Huang, Z.; Shen, Y.; Huang, Y.; Ding, H.; Luscombe, A.; Johnson, M.; Harlow, J. E.; Gauthier, R.; Dahn, J. R. Ultrasonic Scanning to Observe Wetting and "Unwetting" in Li-Ion Pouch Cells. *Joule* **2020**, *4* (9), 2017−2029.
(286) Louli, A. J.; Eldesoky, A.; Weber, R.; Genovese, M.; Coon, M.; deGooyer, J.; Deng, Z.; White, R. T.; Lee, J.; Rodgers, T.; Petibon, R.; Hy, S.; Cheng, S. J. H.; Dahn, J. R. Diagnosing and Correcting Anode-Free Cell Failure via Electrolyte and Morphological Analysis. *Nature Energy* **2020**, *5* (9), 693−702.
(287) Gauthier, R. Understanding and Preventing Lifetime Failure in Lithium-Ion Batteries. Thesis, Dalhouse University, 2021.
(288) Ebner, M.; Geldmacher, F.; Marone, F.; Stampanoni, M.; Wood, V. X-Ray Tomography of Porous, Transition Metal Oxide Based Lithium Ion Battery Electrodes. *Adv. Energy Mater.* **2013**, *3* (7), 845−850.
(289) Watanabe, S.; Kinoshita, M.; Hosokawa, T.; Morigaki, K.; Nakura, K. Capacity Fading of $LiAl_yNi_{1-x-y}Co_xO_2$ Cathode for Lithium-Ion Batteries during Accelerated Calendar and Cycle Life Tests (Effect of Depth of Discharge in Charge-Discharge Cycling on the Suppression of the Micro-c. *J. Power Sources* **2014**, *260*, 50−56.
(290) Sun, H.; Zhao, K. Electronic Structure and Comparative Properties of $LiNi_xMn_yCo_zO_2$ Cathode Materials. *J. Phys. Chem. C* **2017**, *121* (11), 6002−6010.
(291) Zhao, K.; Wang, W. L.; Gregoire, J.; Pharr, M.; Suo, Z.; Vlassak, J. J.; Kaxiras, E. Lithium-Assisted Plastic Deformation of Silicon Electrodes in Lithium-Ion Batteries: A First-Principles Theoretical Study. *Nano Lett.* **2011**, *11*, 2962−2967.
(292) Zhang, Q.; Tang, C.; Zhu, W.; Cheng, C. Strain-Enhanced Li Storage and Diffusion on the Graphyne as the Anode Material in the Li-Ion Battery. *J. Phys. Chem. C* **2018**, *122* (40), 22838−22848.
(293) Hao, J.; Zheng, J.; Ling, F.; Chen, Y.; Jing, H.; Zhou, T.; Fang, L.; Zhou, M. Strain-Engineered Two-Dimensional MoS_2 as Anode Material for Performance Enhancement of Li/Na-Ion Batteries. *Sci. Rep* **2018**, *8* (1), 1−9.
(294) Xu, G.; Hao, F.; Weng, M.; Hong, J.; Pan, F.; Fang, D. Strong Influence of Strain Gradient on Lithium Diffusion: Flexo-Diffusion Effect. *Nanoscale* **2020**, *12* (28), 15175−15184.
(295) Tyagi, R.; Srinivasan, S. Molecular Dynamics Modeling of Lithium Ion Intercalation Induced Change in the Mechanical Properties of $Li_xMn_2O_4$. *J. Chem. Phys.* **2020**, *153* (16), 164712.
(296) Qi, Y.; Hector Jr, L. G.; James, C.; Kim, K. J. Lithium Concentration Dependent Elastic Properties of Battery Electrode Materials from First Principles Calculations. *J. Electrochem. Soc.* **2014**, *161* (11), F3010.
(297) Bedrov, D.; Borodin, O.; Hooper, J. B. Li^+ Transport and Mechanical Properties of Model Solid Electrolyte Interphases (SEI): Insight from Atomistic Molecular Dynamics Simulations. *J. Phys. Chem. C* **2017**, *121* (30), 16098−16109.
(298) Leung, K.; Jungjohann, K. L. Spatial Heterogeneities and Onset of Passivation Breakdown at Lithium Anode Interfaces. *J. Phys. Chem. C* **2017**, *121* (37), 20188−20196.
(299) Sun, H.; Zhao, K. Electronic Structure and Comparative Properties of $LiNi_xMn_yCo_zO_2$ Cathode Materials. *J. Phys. Chem. C* **2017**, *121* (11), 6002−6010.
(300) Zhang, Q.; Tang, C.; Zhu, W.; Cheng, C. Strain-Enhanced Li Storage and Diffusion on the Graphyne as the Anode Material in the Li-Ion Battery. *J. Phys. Chem. C* **2018**, *122* (40), 22838−22848.
(301) Hao, J.; Zheng, J.; Ling, F.; Chen, Y.; Jing, H.; Zhou, T.; Fang, L.; Zhou, M. Strain-Engineered Two-Dimensional MoS_2 as Anode Material for Performance Enhancement of Li/Na-Ion Batteries. *Sci. Rep* **2018**, *8* (1), 1−9.
(302) Xu, G.; Hao, F.; Weng, M.; Hong, J.; Pan, F.; Fang, D. Strong Influence of Strain Gradient on Lithium Diffusion: Flexo-Diffusion Effect. *Nanoscale* **2020**, *12* (28), 15175−15184.
(303) Tyagi, R.; Srinivasan, S. Molecular Dynamics Modeling of Lithium Ion Intercalation Induced Change in the Mechanical Properties of $Li_xMn_2O_4$. *J. Chem. Phys.* **2020**, *153* (16), 164712.
(304) Qi, Y.; Hector Jr, L. G.; James, C.; Kim, K. J. Lithium Concentration Dependent Elastic Properties of Battery Electrode Materials from First Principles Calculations. *J. Electrochem. Soc.* **2014**, *161* (11), F3010.
(305) Bedrov, D.; Borodin, O.; Hooper, J. B. Li^+ Transport and Mechanical Properties of Model Solid Electrolyte Interphases (SEI): Insight from Atomistic Molecular Dynamics Simulations. *J. Phys. Chem. C* **2017**, *121* (30), 16098−16109.
(306) Leung, K.; Jungjohann, K. L. Spatial Heterogeneities and Onset of Passivation Breakdown at Lithium Anode Interfaces. *J. Phys. Chem. C* **2017**, *121* (37), 20188−20196.
(307) Zuo, P.; Zhao, Y.-P. A Phase Field Model Coupling Lithium Diffusion and Stress Evolution with Crack Propagation and Application in Lithium Ion Batteries. *Phys. Chem. Chem. Phys.* **2015**, *17* (1), 287−297.
(308) Zhao, Y.; Xu, B.-X.; Stein, P.; Gross, D. Phase-Field Study of Electrochemical Reactions at Exterior and Interior Interfaces in Li-Ion Battery Electrode Particles. *Comput. Methods Appl. Mech Eng.* **2016**, *312*, 428−446.
(309) Mesgarnejad, A.; Karma, A. Phase Field Modeling of Chemomechanical Fracture of Intercalation Electrodes: Role of Charging Rate and Dimensionality. *Journal of the Mechanics and Physics of Solids* **2019**, *132*, 103696.
(310) Balakrishna, A. R.; Chiang, Y.-M.; Carter, W. C. Phase-Field Model for Diffusion-Induced Grain Boundary Migration: An

https://doi.org/10.1021/acs.chemrev.2c00002
Chem. Rev. 2022, 122, 13043−13107

Application to Battery Electrodes. *Physical Review Materials* **2019**, *3* (6), 65404.
(311) Chen, L.; Zhang, H. W.; Liang, L. Y.; Liu, Z.; Qi, Y.; Lu, P.; Chen, J.; Chen, L.-Q. Modulation of Dendritic Patterns during Electrodeposition: A Nonlinear Phase-Field Model. *J. Power Sources* **2015**, *300*, 376−385.
(312) Zuo, P.; Zhao, Y.-P. A Phase Field Model Coupling Lithium Diffusion and Stress Evolution with Crack Propagation and Application in Lithium Ion Batteries. *Phys. Chem. Chem. Phys.* **2015**, *17* (1), 287−297.
(313) Xie, Y.; Qiu, M.; Gao, X.; Guan, D.; Yuan, C. Phase Field Modeling of Silicon Nanowire Based Lithium Ion Battery Composite Electrode. *Electrochim. Acta* **2015**, *186*, 542−551.
(314) Zhang, Y.; Tucker, G. J.; Trelewicz, J. R. Stress-Assisted Grain Growth in Nanocrystalline Metals: Grain Boundary Mediated Mechanisms and Stabilization through Alloying. *Acta Mater.* **2017**, *131*, 39−47.
(315) Rheinheimer, W.; Parras, J. P.; Preusker, J.; De Souza, R. A.; Hoffmann, M. J. Grain Growth in Strontium Titanate in Electric Fields: The Impact of Space-charge on the Grain-boundary Mobility. *J. Am. Ceram. Soc.* **2019**, *102* (6), 3779−3790.
(316) Sheikh-Ali, A. D.; Molodov, D. A.; Garmestani, H. Boundary Migration in Zn Bicrystal Induced by a High Magnetic Field. *Appl. Phys. Lett.* **2003**, *82* (18), 3005−3007.
(317) Yuan, Y.; Nie, A.; Odegard, G. M.; Xu, R.; Zhou, D.; Santhanagopalan, S.; He, K.; Asayesh-Ardakani, H.; Meng, D. D.; Klie, R. F.; Johnson, C.; Lu, J.; Shahbazian-Yassar, R. Asynchronous Crystal Cell Expansion during Lithiation of K^+-Stabilized α-MnO_2. *Nano Lett.* **2015**, *15* (5), 2998−3007.
(318) Carter, W. C.; Handwerker, C. A. Morphology of Grain Growth in Response to Diffusion Induced Elastic Stresses: Cubic Systems. *Acta metallurgica et materialia* **1993**, *41* (5), 1633−1642.
(319) Balakrishna, A. R.; Chiang, Y.-M.; Carter, W. C. Phase-Field Model for Diffusion-Induced Grain Boundary Migration: An Application to Battery Electrodes. *Physical Review Materials* **2019**, *3* (6), 65404.
(320) Goodenough, J. B.; Kim, Y. Challenges for Rechargeable Li Batteries. *Chemistry of materials* **2010**, *22* (3), 587−603.
(321) Ely, D. R.; Jana, A.; García, R. E. Phase Field Kinetics of Lithium Electrodeposits. *J. Power Sources* **2014**, *272*, 581−594.
(322) Liang, L.; Chen, L.-Q. Nonlinear Phase Field Model for Electrodeposition in Electrochemical Systems. *Appl. Phys. Lett.* **2014**, *105* (26), 263903.
(323) Chen, L.; Zhang, H. W.; Liang, L. Y.; Liu, Z.; Qi, Y.; Lu, P.; Chen, J.; Chen, L.-Q. Modulation of Dendritic Patterns during Electrodeposition: A Nonlinear Phase-Field Model. *J. Power Sources* **2015**, *300*, 376−385.
(324) Bird, R. B.; Stewart, W. E.; Lightfoot, E. N. *Transport Phenomena*, Revised 2nd ed.; John Wiley & Sons, Inc: New York, 2006; p 780.
(325) Bizeray, A. M.; Howey, D. A.; Monroe, C. W. Resolving a Discrepancy in Diffusion Potentials, with a Case Study for Li-Ion Batteries. *J. Electrochem. Soc.* **2016**, *163* (8), E223−E229.
(326) Ma, Y.; Doyle, M.; Fuller, T. F.; Doeff, M. M.; De Jonghe, L. C.; Newman, J. The Measurement of a Complete Set of Transport Properties for a Concentrated Solid Polymer Electrolyte Solution. *J. Electrochem. Soc.* **1995**, *142* (6), 1859−1868.
(327) Thorat, I. V.; Stephenson, D. E.; Zacharias, N. A.; Zaghib, K.; Harb, J. N.; Wheeler, D. R. Quantifying Tortuosity in Porous Li-Ion Battery Materials. *J. Power Sources* **2009**, *188* (2), 592−600.
(328) Zhao, K.; Pharr, M.; Cai, S.; Vlassak, J. J.; Suo, Z. Large Plastic Deformation in High-Capacity Lithium-Ion Batteries Caused by Charge and Discharge. *J. Am. Ceram. Soc.* **2011**, *94* (SUPPL. 1), 226−235.
(329) Wan, T. H.; Ciucci, F. Continuum Level Transport and Electro-Chemo-Mechanics Coupling—Solid Oxide Fuel Cells and Lithium Ion Batteries. In *Electro-Chemo-Mechanics of Solids*; Bishop, S. R., Perry, N. H., Marrocchelli, D., Sheldon, B. W., Eds.; Springer International Publishing: Cham, 2017; pp 161−189. DOI: 10.1007/978-3-319-51407-9_7.
(330) Rieger, B.; Erhard, S. V.; Rumpf, K.; Jossen, A. A New Method to Model the Thickness Change of a Commercial Pouch Cell during Discharge. *J. Electrochem. Soc.* **2016**, *163* (8), A1566−A1575.
(331) Li, Y.; Zhang, K.; Zheng, B.; Yang, F. Effect of Local Deformation on the Coupling between Diffusion and Stress in Lithium-Ion Battery. *International Journal of Solids and Structures* **2016**, *87*, 81−89.
(332) Rahani, E. K.; Shenoy, V. B. Role of Plastic Deformation of Binder on Stress Evolution during Charging and Discharging in Lithium-Ion Battery Negative Electrodes. *J. Electrochem. Soc.* **2013**, *160* (8), A1153−A1162.
(333) Wu, W.; Xiao, X.; Wang, M.; Huang, X. A Microstructural Resolved Model for the Stress Analysis of Lithium-Ion Batteries. *J. Electrochem. Soc.* **2014**, *161* (5), A803−A813.
(334) Mai, W.; Yang, M.; Soghrati, S. A Particle-Resolved 3D Finite Element Model to Study the Effect of Cathode Microstructure on the Behavior of Lithium Ion Batteries. *Electrochim. Acta* **2019**, *294*, 192−209.
(335) Malavé, V.; Berger, J. R.; Zhu, H.; Kee, R. J. A Computational Model of the Mechanical Behavior within Reconstructed Li_xCoO_2 Li-Ion Battery Cathode Particles. *Electrochim. Acta* **2014**, *130*, 707−717.
(336) Hein, S.; Danner, T.; Westhoff, D.; Prifling, B.; Scurtu, R.; Kremer, L.; Hoffmann, A.; Hilger, A.; Osenberg, M.; Manke, I.; Wohlfahrt-Mehrens, M.; Schmidt, V.; Latz, A. Influence of Conductive Additives and Binder on the Impedance of Lithium-Ion Battery Electrodes: Effect of Morphology. *J. Electrochem. Soc.* **2020**, *167* (1), 013546.
(337) Zhu, J.; Wierzbicki, T.; Li, W. A Review of Safety-Focused Mechanical Modeling of Commercial Lithium-Ion Batteries. *J. Power Sources* **2018**, *378* (December 2017), 153−168.
(338) Sahraei, E.; Campbell, J.; Wierzbicki, T. Modeling and Short Circuit Detection of 18650 Li-Ion Cells under Mechanical Abuse Conditions. *J. Power Sources* **2012**, *220*, 360−372.
(339) Wang, L.; Yin, S.; Xu, J. A Detailed Computational Model for Cylindrical Lithium-Ion Batteries under Mechanical Loading: From Cell Deformation to Short-Circuit Onset. *J. Power Sources* **2019**, *413* (November 2018), 284−292.
(340) Zhu, J.; Zhang, X.; Sahraei, E.; Wierzbicki, T. Deformation and Failure Mechanisms of 18650 Battery Cells under Axial Compression. *J. Power Sources* **2016**, *336*, 332−340.
(341) Sheikh, M.; Elmarakbi, A.; Elkady, M. Thermal Runaway Detection of Cylindrical 18650 Lithium-Ion Battery under Quasi-Static Loading Conditions. *J. Power Sources* **2017**, *370* (October), 61−70.
(342) Zhu, J.; Li, W.; Wierzbicki, T.; Xia, Y.; Harding, J. Deformation and Failure of Lithium-Ion Batteries Treated as a Discrete Layered Structure. *International Journal of Plasticity* **2019**, *121* (May), 293−311.
(343) Zhu, J.; Koch, M. M.; Lian, J.; Li, W.; Wierzbicki, T. Mechanical Deformation of Lithium-Ion Pouch Cells under In-Plane Loads—Part I: Experimental Investigation. *J. Electrochem. Soc.* **2020**, *167* (9), 090533.
(344) Lian, J.; Koch, M.; Li, W.; Wierzbicki, T.; Zhu, J. Mechanical Deformation of Lithium-Ion Pouch Cells under in-Plane Loads—Part II: Computational Modeling. *J. Electrochem. Soc.* **2020**, *167* (9), 090556.
(345) Zhang, X.; Wierzbicki, T. Characterization of Plasticity and Fracture of Shell Casing of Lithium-Ion Cylindrical Battery. *J. Power Sources* **2015**, *280*, 47−56.
(346) Zhang, C.; Xu, J.; Cao, L.; Wu, Z.; Santhanagopalan, S. Constitutive Behavior and Progressive Mechanical Failure of Electrodes in Lithium-Ion Batteries. *J. Power Sources* **2017**, *357*, 126−137.
(347) Ali, M. Y.; Lai, W. J.; Pan, J. Computational Models for Simulations of Lithium-Ion Battery Cells under Constrained Compression Tests. *J. Power Sources* **2013**, *242*, 325−340.
(348) Lee, D. C.; Kim, C. W. Two-Way Nonlinear Mechanical-Electrochemical-Thermal Coupled Analysis Method to Predict

Thermal Runaway of Lithium-Ion Battery Cells Caused by Quasi-Static Indentation. *J. Power Sources* **2020**, *475* (August), 228678.
(349) Xu, J.; Wu, Y.; Yin, S. Investigation of Effects of Design Parameters on the Internal Short-Circuit in Cylindrical Lithium-Ion Batteries. *RSC Adv.* **2017**, *7* (24), 14360−14371.
(350) Xia, Y.; Wierzbicki, T.; Sahraei, E.; Zhang, X. Damage of Cells and Battery Packs Due to Ground Impact. *J. Power Sources* **2014**, *267*, 78−97.
(351) Deshpande, V. S.; Fleck, N. A. Isotropic Constitutive Models for Metallic Foams. *Journal of the Mechanics and Physics of Solids* **2000**, *48* (6), 1253−1283.
(352) Zhu, J.; Li, W.; Xia, Y.; Sahraei, E. Testing and Modeling the Mechanical Properties of the Granular Materials of Graphite Anode. *J. Electrochem. Soc.* **2018**, *165* (5), A1160−A1168.
(353) Wierzbicki, T.; Sahraei, E. Homogenized Mechanical Properties for the Jellyroll of Cylindrical Lithium-Ion Cells. *J. Power Sources* **2013**, *241*, 467−476.
(354) Lian, J.; Wierzbicki, T.; Zhu, J.; Li, W. Prediction of Shear Crack Formation of Lithium-Ion Batteries under Rod Indentation: Comparison of Seven Failure Criteria. *Engineering Fracture Mechanics* **2019**, *217* (April), 106520.
(355) Zhang, X.; Sahraei, E.; Wang, K. Deformation and Failure Characteristics of Four Types of Lithium-Ion Battery Separators. *J. Power Sources* **2016**, *327*, 693−701.
(356) Bonatti, C.; Mohr, D. Anisotropic Viscoplasticity and Fracture of Fine Grained Metallic Aluminum Foil Used in Li-Ion Batteries. *Mater. Sci. Eng. A* **2016**, *654*, 329−343.
(357) Lai, W. J.; Ali, M. Y.; Pan, J. Mechanical Behavior of Representative Volume Elements of Lithium-Ion Battery Cells under Compressive Loading Conditions. *J. Power Sources* **2014**, *245*, 609−623.
(358) Lai, W. J.; Ali, M. Y.; Pan, J. Mechanical Behavior of Representative Volume Elements of Lithium-Ion Battery Modules under Various Loading Conditions. *J. Power Sources* **2014**, *248*, 789−808.
(359) Li, W.; Xia, Y.; Zhu, J.; Luo, H. State-of-Charge Dependence of Mechanical Response of Lithium-Ion Batteries: A Result of Internal Stress. *J. Electrochem. Soc.* **2018**, *165* (7), A1537−A1546.
(360) Xu, J.; Liu, B.; Wang, X.; Hu, D. Computational Model of 18650 Lithium-Ion Battery with Coupled Strain Rate and SOC Dependencies. *Applied Energy* **2016**, *172*, 180−189.
(361) Zhu, J.; Luo, H.; Li, W.; Gao, T.; Xia, Y.; Wierzbicki, T. Mechanism of Strengthening of Battery Resistance under Dynamic Loading. *International Journal of Impact Engineering* **2019**, *131* (May), 78−84.
(362) Li, W.; Zhu, J. A Large Deformation and Fracture Model of Lithium-Ion Battery Cells Treated as a Homogenized Medium. *J. Electrochem. Soc.* **2020**, *167* (12), 120504.
(363) *LS-DYNA Theory Manual Material Models Material Model 126*; Livermore Software Technology Corporation, 1991.
(364) Sahraei, E.; Kahn, M.; Meier, J.; Wierzbicki, T. Modelling of Cracks Developed in Lithium-Ion Cells under Mechanical Loading. *RSC Adv.* **2015**, *5* (98), 80369−80380.
(365) Khosrownejad, S. M.; Curtin, W. A. Crack Growth and Fracture Toughness of Amorphous Li-Si Anodes: Mechanisms and Role of Charging/Discharging Studied by Atomistic Simulations. *Journal of the Mechanics and Physics of Solids* **2017**, *107*, 542−559.
(366) Doyle, M.; Fuller, T. F.; Newman, J. Modeling of Galvanostatic Charge and Discharge of the Lithium/Polymer/Insertion Cell. *J. Electrochem. Soc.* **1993**, *140* (6), 1526−1533.
(367) Fuller, T. F.; Doyle, M.; Newman, J. Simulation and Optimization of the Dual Lithium Ion Insertion Cell. *J. Electrochem. Soc.* **1994**, *141* (1), 1−10.
(368) Wang, Q.; Jiang, B.; Li, B.; Yan, Y. A Critical Review of Thermal Management Models and Solutions of Lithium-Ion Batteries for the Development of Pure Electric Vehicles. *Renewable and Sustainable Energy Reviews* **2016**, *64*, 106−128.
(369) Lai, X.; Jin, C.; Yi, W.; Han, X.; Feng, X.; Zheng, Y.; Ouyang, M. Mechanism, Modeling, Detection, and Prevention of the Internal Short Circuit in Lithium-Ion Batteries: Recent Advances and Perspectives. *Energy Storage Materials* **2021**, *35* (October2020), 470−499.
(370) Deng, J.; Bae, C.; Marcicki, J.; Masias, A.; Miller, T. Safety Modelling and Testing of Lithium-Ion Batteries in Electrified Vehicles. *Nature Energy* **2018**, *3* (4), 261−266.
(371) Liu, B.; Yin, S.; Xu, J. Integrated Computation Model of Lithium-Ion Battery Subject to Nail Penetration. *Applied Energy* **2016**, *183*, 278−289.
(372) Yuan, C.; Gao, X.; Wong, H. K.; Feng, B.; Xu, J. A Multiphysics Computational Framework for Cylindrical Battery Behavior upon Mechanical Loading Based on LS-DYNA. *J. Electrochem. Soc.* **2019**, *166* (6), A1160−A1169.
(373) Marcicki, J.; Zhu, M.; Bartlett, A.; Yang, X. G.; Chen, Y.; Miller, T.; L'Eplattenier, P.; Caldichoury, I. A Simulation Framework for Battery Cell Impact Safety Modeling Using LS-DYNA. *J. Electrochem. Soc.* **2017**, *164* (1), A6440−A6448.
(374) Li, H.; Liu, B.; Zhou, D.; Zhang, C. Coupled Mechanical-Electrochemical-Thermal Study on the Short-Circuit Mechanism of Lithium-Ion Batteries under Mechanical Abuse. *J. Electrochem. Soc.* **2020**, *167* (12), 120501.
(375) Huang, J. Y.; Zhong, L.; Wang, C. M.; Sullivan, J. P.; Xu, W.; Zhang, L. Q.; Mao, S. X.; Hudak, N. S.; Liu, X. H.; Subramanian, A.; Fan, H.; Qi, L.; Kushima, A.; Li, J. In Situ Observation of the Electrochemical Lithiation of a Single SnO_2 Nanowire Electrode. *Science* **2010**, *330* (6010), 1515−1520.
(376) Liu, X. H.; Zheng, H.; Zhong, L.; Huang, S.; Karki, K.; Zhang, L. Q.; Liu, Y.; Kushima, A.; Liang, W. T.; Wang, J. W.; Cho, J. H.; Epstein, E.; Dayeh, S. A.; Picraux, S. T.; Zhu, T.; Li, J.; Sullivan, J. P.; Cumings, J.; Wang, C.; Mao, S. X.; Ye, Z. Z.; Zhang, S.; Huang, J. Y. Anisotropic Swelling and Fracture of Silicon Nanowires during Lithiation. *Nano Lett.* **2011**, *11* (8), 3312−3318.
(377) He, K.; Xin, H. L.; Zhao, K.; Yu, X.; Nordlund, D.; Weng, T. C.; Li, J.; Jiang, Y.; Cadigan, C. A.; Richards, R. M.; Doeff, M. M.; Yang, X. Q.; Stach, E. A.; Li, J.; Lin, F.; Su, D. Transitions from Near-Surface to Interior Redox upon Lithiation in Conversion Electrode Materials. *Nano Lett.* **2015**, *15* (2), 1437−1444.
(378) Lu, J.; Wu, T.; Amine, K. State-of-the-Art Characterization Techniques for Advanced Lithium-Ion Batteries. *NATURE ENERGY* **2017**, *2*, 17011.
(379) Li, Y.; Cheng, X.; Zhang, Y.; Zhao, K. Recent Advance in Understanding the Electro-Chemo-Mechanical Behavior of Lithium-Ion Batteries by Electron Microscopy. *Mater. Today Nano.* **2019**, *7*, 100040.
(380) Chen, B.; Zhang, H.; Xuan, J.; Offer, G. J.; Wang, H. Seeing Is Believing: In Situ/Operando Optical Microscopy for Probing Electrochemical Energy Systems. *Adv. Mater. Technol.* **2020**, *5* (10), 2000555.
(381) Liu, X. H.; Huang, J. Y. In Situ TEM Electrochemistry of Anode Materials in Lithium Ion Batteries. *Energy Environ. Sci.* **2011**, *4* (10), 3844−3860.
(382) Asp, L. E.; Bouton, K.; Carlstedt, D.; Duan, S.; Harnden, R.; Johannisson, W.; Johansen, M.; Johansson, M. K. G.; Lindbergh, G.; Liu, F.; Peuvot, K.; Schneider, L. M.; Xu, J.; Zenkert, D. A Structural Battery and Its Multifunctional Performance. *Advanced Energy and Sustainability Research* **2021**, *2* (3), 2000093.
(383) Wang, Y.; Dang, D.; Li, D.; Hu, J.; Cheng, Y. T. Influence of Polymeric Binders on Mechanical Properties and Microstructure Evolution of Silicon Composite Electrodes during Electrochemical Cycling. *J. Power Sources* **2019**, *425*, 170−178.
(384) Xu, R.; Sun, H.; de Vasconcelos, L. S.; Zhao, K. Mechanical and Structural Degradation of $LiNi_xMn_yCo_zO_2$ Cathode in Li-Ion Batteries: An Experimental Study. *J. Electrochem. Soc.* **2017**, *164* (13), A3333−A3341.
(385) Dang, D.; Wang, Y.; Cheng, Y.-T. Communication—Fracture Behavior of Single $LiNi_{0.33}Mn_{0.33}Co_{0.33}O_2$ Particles Studied by Flat Punch Indentation. *J. Electrochem. Soc.* **2019**, *166* (13), A2749−A2751.

https://doi.org/10.1021/acs.chemrev.2c00002
Chem. Rev. 2022, 122, 13043−13107

(386) Zhao, K.; Tritsaris, G. A.; Pharr, M.; Wang, W. L.; Okeke, O.; Suo, Z.; Vlassak, J. J.; Kaxiras, E. Reactive Flow in Silicon Electrodes Assisted by the Insertion of Lithium. *Nano Lett.* **2012**, *12* (8), 4397−4403.
(387) Qu, M.; Woodford, W. H.; Maloney, J. M.; Carter, W. C.; Chiang, Y. M.; Van Vliet, K. J. Nanomechanical Quantification of Elastic, Plastic, and Fracture Properties of $LiCoO_2$. *Adv. Energy Mater.* **2012**, *2* (8), 940−944.
(388) Mughal, M. Z.; Moscatelli, R.; Amanieu, H. Y.; Sebastiani, M. Effect of Lithiation on Micro-Scale Fracture Toughness of $Li_xMn_2O_4$ Cathode. *Scripta Materialia* **2016**, *116*, 62−66.
(389) Wang, Y.; Cheng, Y. T. A Nanoindentation Study of the Viscoplastic Behavior of Pure Lithium. *Scripta Materialia* **2017**, *130*, 191−195.
(390) Herbert, E. G.; Dudney, N. J.; Rochow, M.; Thole, V.; Hackney, S. A. On the Mechanisms of Stress Relaxation and Intensification at the Lithium/Solid-State Electrolyte Interface. *J. Mater. Res.* **2019**, *34* (21), 3593−3616.
(391) Berla, L. A.; Lee, S. W.; Cui, Y.; Nix, W. D. Mechanical Behavior of Electrochemically Lithiated Silicon. *J. Power Sources* **2015**, *273*, 41−51.
(392) Chen, J.; Liu, J.; Qi, Y.; Sun, T.; Li, X. Unveiling the Roles of Binder in the Mechanical Integrity of Electrodes for Lithium-Ion Batteries. *J. Electrochem. Soc.* **2013**, *160* (9), A1502−A1509.
(393) Kim, D.; Shim, H. C.; Yun, T. G.; Hyun, S.; Han, S. M. High Throughput Combinatorial Analysis of Mechanical and Electrochemical Properties of $Li[Ni_xCo_yMn_z]O_2$ Cathode. *Extreme Mech Lett.* **2016**, *9*, 439−448.
(394) Feng, L.; Lu, X.; Zhao, T.; Dillon, S. The Effect of Electrochemical Cycling on the Strength of $LiCoO_2$. *J. Am. Ceram. Soc.* **2019**, *102* (1), 372−381.
(395) Herbert, E. G.; Hackney, S. A.; Dudney, N. J.; Sudharshan Phani, P. Nanoindentation of High-Purity Vapor Deposited Lithium Films: The Elastic Modulus. *J. Mater. Res.* **2018**, *33* (10), 1335−1346.
(396) Mughal, M. Z.; Amanieu, H.-Y.; Moscatelli, R.; Sebastiani, M. A Comparison of Microscale Techniques for Determining Fracture Toughness of $LiMn_2O_4$ Particles. *Materials* **2017**, *10* (4), 403.
(397) Xu, C.; Ahmad, Z.; Aryanfar, A.; Viswanathan, V.; Greer, J. R. Enhanced Strength and Temperature Dependence of Mechanical Properties of Li at Small Scales and Its Implications for Li Metal Anodes. *Proc. Natl. Acad. Sci. U. S. A.* **2017**, *114* (1), 57−61.
(398) Chen, C.-H.; Chason, E.; Guduru, P. R. Measurements of the Phase and Stress Evolution during Initial Lithiation of Sn Electrodes. *J. Electrochem. Soc.* **2017**, *164* (4), A574−A579.
(399) Bucci, G.; Nadimpalli, S. P. V.; Sethuraman, V. A.; Bower, A. F.; Guduru, P. R. Measurement and Modeling of the Mechanical and Electrochemical Response of Amorphous Si Thin Film Electrodes during Cyclic Lithiation. *Journal of the Mechanics and Physics of Solids* **2014**, *62*, 276−294.
(400) Sheth, J.; Karan, N. K.; Abraham, D. P.; Nguyen, C. C.; Lucht, B. L.; Sheldon, B. W.; Guduru, P. R. In Situ Stress Evolution in $Li_{1+x}Mn_2O_4$ Thin Films during Electrochemical Cycling in Li-Ion Cells. *J. Electrochem. Soc.* **2016**, *163* (13), A2524−A2530.
(401) Zhang, Y.; Luo, Y.; Fincher, C.; McProuty, S.; Swenson, G.; Banerjee, S.; Pharr, M. In-Situ Measurements of Stress Evolution in Composite Sulfur Cathodes. *Energy Storage Materials* **2019**, *16* (October 2018), 491−497.
(402) Li, D.; Wang, Y.; Hu, J.; Lu, B.; Cheng, Y. T.; Zhang, J. In Situ Measurement of Mechanical Property and Stress Evolution in a Composite Silicon Electrode. *J. Power Sources* **2017**, *366*, 80−85.
(403) Nadimpalli, S. P. V.; Sethuraman, V. A.; Bucci, G.; Srinivasan, V.; Bower, A. F.; Guduru, P. R. On Plastic Deformation and Fracture in Si Films during Electrochemical Lithiation/Delithiation Cycling. *J. Electrochem. Soc.* **2013**, *160* (10), A1885−A1893.
(404) Pharr, M.; Choi, Y. S.; Lee, D.; Oh, K. H.; Vlassak, J. J. Measurements of Stress and Fracture in Germanium Electrodes of Lithium-Ion Batteries during Electrochemical Lithiation and Delithiation. *J. Power Sources* **2016**, *304*, 164−169.
(405) Xie, H.; Song, H.; Guo, J.-g.; Kang, Y.; Yang, W.; Zhang, Q. In Situ Measurement of Rate-Dependent Strain/Stress Evolution and Mechanism Exploration in Graphene Electrodes during Electrochemical Process. *Carbon* **2019**, *144*, 342−350.
(406) Pharr, M.; Suo, Z.; Vlassak, J. J. Measurements of the Fracture Energy of Lithiated Silicon Electrodes of Li-Ion Batteries. *Nano Lett.* **2013**, *13* (11), 5570−5577.
(407) Sethuraman, V. A.; Chon, M. J.; Shimshak, M.; Van Winkle, N.; Guduru, P. R. In Situ Measurement of Biaxial Modulus of Si Anode for Li-Ion Batteries. *Electrochem. Commun.* **2010**, *12* (11), 1614−1617.
(408) Tariq, S.; Ammigan, K.; Hurh, P.; Schultz, R.; Liu, P.; Shang, J. Li Material Testing - Fermilab Antiproton Source Litihum Collection Lens. In *Proceedings of the 2003 Particle Accelerator Conference*; IEEE, 2003; Vol. 3, pp 1452−1454. DOI: 10.1109/PAC.2003.1288558.
(409) Kushima, A.; Huang, J. Y.; Li, J. Quantitative Fracture Strength and Plasticity Measurements of Lithiated Silicon Nanowires by in Situ TEM Tensile Experiments. *ACS Nano* **2012**, *6* (11), 9425−9432.
(410) Jones, E. M. C.; Silberstein, M. N.; White, S. R.; Sottos, N. R. In Situ Measurements of Strains in Composite Battery Electrodes during Electrochemical Cycling. *Experimental Mechanics* **2014**, *54* (6), 971−985.
(411) Xie, H. M.; Yang, W.; Kang, Y. L.; Zhang, Q.; Han, B.; Qiu, W. In-Situ Strain Field Measurement and Mechano-Electro-Chemical Analysis of Graphite Electrodes Via Fluorescence Digital Image Correlation. *Experimental Mechanics* **2021**, *61* (8), 1249−1260.
(412) Fu, Z.; Zhang, L.; Gritton, J. E.; Godbey, G.; Hamann, T.; Gong, Y.; McOwen, D.; Wachsman, E. Probing the Mechanical Properties of a Doped $Li_7La_3Zr_2O_{12}$ Garnet Thin Electrolyte for Solid-State Batteries. *ACS Appl. Mater. Interfaces* **2020**, *12* (22), 24693−24700.
(413) Zhang, G.; Liu, W.; Chen, J.; Shen, S. Nonlinear Electro-chemomechanical Modelling of Electrochemical Strain Microscopy Imaging. *Nanotechnology* **2020**, *31* (31), 315704.
(414) Balke, N.; Jesse, S.; Morozovska, A. N.; Eliseev, E.; Chung, D. W.; Kim, Y.; Adamczyk, L.; García, R. E.; Dudney, N.; Kalinin, S. V. Nanoscale Mapping of Ion Diffusion in a Lithium-Ion Battery Cathode. *Nat. Nanotechnol.* **2010**, *5* (10), 749−754.
(415) Balke, N.; Jesse, S.; Kim, Y.; Adamczyk, L.; Tselev, A.; Ivanov, I. N.; Dudney, N. J.; Kalinin, S. V. Real Space Mapping of Li-Ion Transport in Amorphous Si Anodes with Nanometer Resolution. *Nano Lett.* **2010**, *10* (9), 3420−3425.
(416) Clifford, C. A.; Seah, M. P. Quantification Issues in the Identification of Nanoscale Regions of Homopolymers Using Modulus Measurement via AFM Nanoindentation. *Appl. Surf. Sci.* **2005**, *252* (5), 1915−1933.
(417) Butt, H.-J.; Cappella, B.; Kappl, M. Force Measurements with the Atomic Force Microscope: Technique, Interpretation and Applications. *Surf. Sci. Rep.* **2005**, *59* (1−6), 1−152.
(418) Zheng, J.; Zheng, H.; Wang, R.; Ben, L.; Lu, W.; Chen, L.; Chen, L.; Li, H. 3D Visualization of Inhomogeneous Multi-Layered Structure and Young's Modulus of the Solid Electrolyte Interphase (SEI) on Silicon Anodes for Lithium Ion Batteries. *Phys. Chem. Chem. Phys.* **2014**, *16* (26), 13229−13238.
(419) Wang, W.-W.; Gu, Y.; Yan, H.; Li, S.; He, J.-W.; Xu, H.-Y.; Wu, Q.-H.; Yan, J.-W.; Mao, B.-W. Evaluating Solid-Electrolyte Interphases for Lithium and Lithium-Free Anodes from Nano-indentation Features. *Chem.* **2020**, *6* (10), 2728−2745.
(420) Wang, M.; Huai, L.; Hu, G.; Yang, S.; Ren, F.; Wang, S.; Zhang, Z.; Chen, Z.; Peng, Z.; Shen, C.; Wang, D. Effect of LiFSI Concentrations To Form Thickness- and Modulus-Controlled SEI Layers on Lithium Metal Anodes. *J. Phys. Chem. C* **2018**, *122* (18), 9825−9834.
(421) Gu, Y.; Wang, W. W.; Li, Y. J.; Wu, Q. H.; Tang, S.; Yan, J. W.; Zheng, M. S.; Wu, D. Y.; Fan, C. H.; Hu, W. Q.; Chen, Z. B.; Fang, Y.; Zhang, Q. H.; Dong, Q. F.; Mao, B. W. Designable Ultra-Smooth Ultra-Thin Solid-Electrolyte Interphases of Three Alkali Metal Anodes. *Nat. Commun.* **2018**, *9* (1), 1339.

(422) Liu, Y.; Lin, D.; Yuen, P. Y.; Liu, K.; Xie, J.; Dauskardt, R. H.; Cui, Y. An Artificial Solid Electrolyte Interphase with High Li-Ion Conductivity, Mechanical Strength, and Flexibility for Stable Lithium Metal Anodes. *Adv. Mater.* **2017**, *29* (10), 1605531.
(423) Zhang, Z.; Li, Y.; Xu, R.; Zhou, W.; Li, Y.; Oyakhire, S. T.; Wu, Y.; Xu, J.; Wang, H.; Yu, Z.; Boyle, D. T.; Huang, W.; Ye, Y.; Chen, H.; Wan, J.; Bao, Z.; Chiu, W.; Cui, Y. Capturing the Swelling of Solid-Electrolyte Interphase in Lithium Metal Batteries. *Science* **2022**, *375* (6576), 66−70.
(424) Yoon, I.; Jurng, S.; Abraham, D. P.; Lucht, B. L.; Guduru, P. R. Measurement of Mechanical and Fracture Properties of Solid Electrolyte Interphase on Lithium Metal Anodes in Lithium Ion Batteries. *Energy Storage Materials* **2020**, *25*, 296−304.
(425) Shpigel, N.; Levi, M. D.; Sigalov, S.; Daikhin, L.; Aurbach, D. In Situ Real-Time Mechanical and Morphological Characterization of Electrodes for Electrochemical Energy Storage and Conversion by Electrochemical Quartz Crystal Microbalance with Dissipation Monitoring. *Acc. Chem. Res.* **2018**, *51* (1), 69−79.
(426) Ali, M. Y.; Lai, W. J.; Pan, J. Computational Models for Simulation of a Lithium-Ion Battery Module Specimen under Punch Indentation. *J. Power Sources* **2015**, *273*, 448−459.
(427) Luo, H.; Zhu, J.; Sahraei, E.; Xia, Y. Adhesion Strength of the Cathode in Lithium-Ion Batteries under Combined Tension/Shear Loadings. *RSC Adv.* **2018**, *8* (8), 3996−4005.
(428) Guo, Z.; Liu, C.; Lu, B.; Feng, J. Theoretical and Experimental Study on the Interfacial Adhesive Properties of Graphite Electrodes in Different Charging and Aging States. *Carbon N Y* **2019**, *150*, 32−42.
(429) Xie, H.; Kang, Y.; Song, H.; Guo, J.; Zhang, Q. In Situ Method for Stress Measurements in Film-Substrate Electrodes during Electrochemical Processes: Key Role of Softening and Stiffening. *Acta Mechanica Sinica/Lixue Xuebao* **2020**, *36* (6), 1319−1335.
(430) Son, B.; Ryou, M. H.; Choi, J.; Lee, T.; Yu, H. K.; Kim, J. H.; Lee, Y. M. Measurement and Analysis of Adhesion Property of Lithium-Ion Battery Electrodes with SAICAS. *ACS Appl. Mater. Interfaces* **2014**, *6* (1), 526−531.
(431) Wang, H.; Simunovic, S.; Maleki, H.; Howard, J. N.; Hallmark, J. A. Internal Configuration of Prismatic Lithium-Ion Cells at the Onset of Mechanically Induced Short Circuit. *J. Power Sources* **2016**, *306*, 424−430.
(432) Zhu, X.; Wang, H.; Wang, X.; Gao, Y.; Allu, S.; Cakmak, E.; Wang, Z. Internal Short Circuit and Failure Mechanisms of Lithium-Ion Pouch Cells under Mechanical Indentation Abuse Conditions: An Experimental Study. *J. Power Sources* **2020**, *455* (February), 227939.
(433) Dixon, B.; Mason, A.; Sahraei, E. Effects of Electrolyte, Loading Rate and Location of Indentation on Mechanical Integrity of Li-Ion Pouch Cells. *J. Power Sources* **2018**, *396* (May), 412−420.
(434) Sahraei, E.; Hill, R.; Wierzbicki, T. Calibration and Finite Element Simulation of Pouch Lithium-Ion Batteries for Mechanical Integrity. *J. Power Sources* **2012**, *201*, 307−321.
(435) Goodman, J. K. S.; Miller, J. T.; Kreuzer, S.; Forman, J.; Wi, S.; Choi, J.; Oh, B.; White, K. Lithium-Ion Cell Response to Mechanical Abuse: Three-Point Bend. *Journal of Energy Storage* **2020**, *28* (July 2019), 101244.
(436) Hu, L. L.; Zhang, Z. W.; Zhou, M. Z.; Zhang, H. J. International Journal of Impact Engineering Crushing Behaviors and Failure of Packed Batteries. *International Journal of Impact Engineering* **2020**, *143* (January), 103618.
(437) Avdeev, I.; Gilaki, M. Structural Analysis and Experimental Characterization of Cylindrical Lithium-Ion Battery Cells Subject to Lateral Impact. *J. Power Sources* **2014**, *271*, 382−391.
(438) Kisters, T.; Sahraei, E.; Wierzbicki, T. Dynamic Impact Tests on Lithium-Ion Cells. *International Journal of Impact Engineering* **2017**, *108*, 205−216.
(439) Chen, X.; Yuan, Q.; Wang, T.; Ji, H.; Ji, Y.; Li, L.; Liu, Y. Experimental Study on the Dynamic Behavior of Prismatic Lithium-Ion Battery upon Repeated Impact. *Eng. Failure Anal.* **2020**, *115* (June), 104667.
(440) Pan, Z.; Li, W.; Xia, Y. Experiments and 3D Detailed Modeling for a Pouch Battery Cell under Impact Loading. *J. Energy Storage* **2020**, *27* (September 2019), 101016.
(441) Jia, Y.; Yin, S.; Liu, B.; Zhao, H.; Yu, H.; Li, J.; Xu, J. Unlocking the Coupling Mechanical-Electrochemical Behavior of Lithium-Ion Battery upon Dynamic Mechanical Loading. *Energy* **2019**, *166*, 951−960.
(442) Kukreja, J.; Nguyen, T.; Siegmund, T.; Chen, W.; Tsutsui, W.; Balakrishnan, K.; Liao, H.; Parab, N. Crash Analysis of a Conceptual Electric Vehicle with a Damage Tolerant Battery Pack. *Extreme Mech. Lett.* **2016**, *9*, 371−378.
(443) Attwood, D.; Sakdinawat, A. *X-Rays and Extreme Ultraviolet Radiation: Principles and Applications*, 2nd ed.; Cambridge University Press: Cambridge, 2017. DOI: 10.1017/CBO9781107477629.
(444) Kunz, C. Synchrotron Radiation: Third Generation Sources. *J. Phys. Condens. Matter* **2001**, *13* (34), 7499−7510.
(445) McBreen, J. The Application of Synchrotron Techniques to the Study of Lithium-Ion Batteries. *J. Solid State Electrochem.* **2009**, *13* (7), 1051−1061.
(446) Nelson, J.; Misra, S.; Yang, Y.; Jackson, A.; Liu, Y.; Wang, H.; Dai, H.; Andrews, J. C.; Cui, Y.; Toney, M. F. In Operando X-Ray Diffraction and Transmission X-Ray Microscopy of Lithium Sulfur Batteries. *J. Am. Chem. Soc.* **2012**, *134* (14), 6337−6343.
(447) Xu, Y.; Hu, E.; Yang, F.; Corbett, J.; Sun, Z.; Lyu, Y.; Yu, X.; Liu, Y.; Yang, X.-Q.; Li, H. Structural Integrity—Searching the Key Factor to Suppress the Voltage Fade of Li-Rich Layered Cathode Materials through 3D X-Ray Imaging and Spectroscopy Techniques. *Nano Energy* **2016**, *28*, 164−171.
(448) Muhammad, S.; Kim, H.; Kim, Y.; Kim, D.; Song, J. H.; Yoon, J.; Park, J.-H.; Ahn, S.-J.; Kang, S.-H.; Thackeray, M. M.; Yoon, W.-S. Evidence of Reversible Oxygen Participation in Anomalously High Capacity Li- and Mn-Rich Cathodes for Li-Ion Batteries. *Nano Energy* **2016**, *21*, 172−184.
(449) Wang, Q.; Ping, P.; Zhao, X.; Chu, G.; Sun, J.; Chen, C. Thermal Runaway Caused Fire and Explosion of Lithium Ion Battery. *Journal of Power Sources.* **2012**, *208*, 210−224.
(450) Tian, C.; Xu, Y.; Kan, W. H.; Sokaras, D.; Nordlund, D.; Shen, H.; Chen, K.; Liu, Y.; Doeff, M. Distinct Surface and Bulk Thermal Behaviors of $LiNi_{0.6}Mn_{0.2}Co_{0.2}O_2$ Cathode Materials as a Function of State of Charge. *ACS Appl. Mater. Interfaces* **2020**, *12* (10), 11643−11656.
(451) Bak, S.-M.; Shadike, Z.; Lin, R.; Yu, X.; Yang, X.-Q. In Situ/Operando Synchrotron-Based X-Ray Techniques for Lithium-Ion Battery Research. *NPG Asia Materials.* **2018**, *10*, 563−580.
(452) Zhu, H.; Huang, Y.; Ren, J.; Zhang, B.; Ke, Y.; Jen, A. K. -Y.; Zhang, Q.; Wang, X.; Liu, Q. Bridging Structural Inhomogeneity to Functionality: Pair Distribution Function Methods for Functional Materials Development. *Advanced Science.* **2021**, *8*, 2003534.
(453) Wise, A. M.; Ban, C.; Weker, J. N.; Misra, S.; Cavanagh, A. S.; Wu, Z.; Li, Z.; Whittingham, M. S.; Xu, K.; George, S. M.; Toney, M. F. Effect of Al_2O_3 Coating on Stabilizing $LiNi_{0.4}Mn_{0.4}Co_{0.2}O_2$ Cathodes. *Chem. Mater.* **2015**, *27* (17), 6146−6154.
(454) Lin, F.; Markus, I. M.; Nordlund, D.; Weng, T.-C.; Asta, M. D.; Xin, H. L.; Doeff, M. M. Surface Reconstruction and Chemical Evolution of Stoichiometric Layered Cathode Materials for Lithium-Ion Batteries. *Nat. Commun.* **2014**, *5*, 3529.
(455) Liu, X.; Wang, D.; Liu, G.; Srinivasan, V.; Liu, Z.; Hussain, Z.; Yang, W. Distinct Charge Dynamics in Battery Electrodes Revealed by in Situ and Operando Soft X-Ray Spectroscopy. *Nat. Commun.* **2013**, *4* (May), 1−8.
(456) Li, S.; Lee, S.-J.; Wang, X.; Yang, W.; Huang, H.; Swetz, D. S.; Doriese, W. B.; O'Neil, G. C.; Ullom, J. N.; Titus, C. J.; Irwin, K. D.; Lee, H.-K.; Nordlund, D.; Pianetta, P.; Yu, C.; Qiu, J.; Yu, X.; Yang, X.-Q.; Hu, E.; Lee, J.-S.; Liu, Y. Surface-to-Bulk Redox Coupling through Thermally Driven Li Redistribution in Li- and Mn-Rich Layered Cathode Materials. *J. Am. Chem. Soc.* **2019**, *141* (30), 12079−12086.
(457) Rahman, M. M.; Lin, F. Oxygen Redox Chemistry in Rechargeable Li-Ion and Na-Ion Batteries. *Matter.* **2021**, *4*, 490−527.

(458) Frankel, R. I. Centennial of Rontgen's Discovery of X-rays. *West. J. Med.* **1996**, *164* (6), 497−501.
(459) Finegan, D. P.; Scheel, M.; Robinson, J. B.; Tjaden, B.; Hunt, I.; Mason, T. J.; Millichamp, J.; Di Michiel, M.; Offer, G. J.; Hinds, G.; Brett, D. J. L.; Shearing, P. R. In-Operando High-Speed Tomography of Lithium-Ion Batteries during Thermal Runaway. *Nat. Commun.* **2015**, *6* (1), 6924.
(460) Zhang, J.; Wang, Q.; Li, S.; Jiang, Z.; Tan, S.; Wang, X.; Zhang, K.; Yuan, Q.; Lee, S.-J.; Titus, C. J.; Irwin, K. D.; Nordlund, D.; Lee, J.-S.; Pianetta, P.; Yu, X.; Xiao, X.; Yang, X.-Q.; Hu, E.; Liu, Y. Depth-Dependent Valence Stratification Driven by Oxygen Redox in Lithium-Rich Layered Oxide. *Nat. Commun.* **2020**, *11* (1), 6342.
(461) Yu, Y.-S.; Farmand, M.; Kim, C.; Liu, Y.; Grey, C. P.; Strobridge, F. C.; Tyliszczak, T.; Celestre, R.; Denes, P.; Joseph, J.; Krishnan, H.; Maia, F. R. N. C.; Kilcoyne, A. L. D.; Marchesini, S.; Leite, T. P. C.; Warwick, T.; Padmore, H.; Cabana, J.; Shapiro, D. A. Three-Dimensional Localization of Nanoscale Battery Reactions Using Soft X-Ray Tomography. *Nat. Commun.* **2018**, *9* (1), 921.
(462) Wei, C.; Xia, S.; Huang, H.; Mao, Y.; Pianetta, P.; Liu, Y. Mesoscale Battery Science: The Behavior of Electrode Particles Caught on a Multispectral X-Ray Camera. *Acc. Chem. Res.* **2018**, *51* (10), 2484−2492.
(463) Frenck, L.; Sethi, G. K.; Maslyn, J. A.; Balsara, N. P. Factors That Control the Formation of Dendrites and Other Morphologies on Lithium Metal Anodes. *Fron. Energy Res.* **2019**, *7*. DOI: 10.3389/fenrg.2019.00115.
(464) Maslyn, J. A.; Loo, W. S.; McEntush, K. D.; Oh, H. J.; Harry, K. J.; Parkinson, D. Y.; Balsara, N. P. Growth of Lithium Dendrites and Globules through a Solid Block Copolymer Electrolyte as a Function of Current Density. *J. Phys. Chem. C* **2018**, *122* (47), 26797−26804.
(465) Tian, C.; Xu, Y.; Kan, W. H.; Sokaras, D.; Nordlund, D.; Shen, H.; Chen, K.; Liu, Y.; Doeff, M. Distinct Surface and Bulk Thermal Behaviors of $LiNi_{0.6}Mn_{0.2}Co_{0.2}O_2$ Cathode Materials as a Function of State of Charge. *ACS Appl. Mater. Interfaces* **2020**, *12* (10), 11643−11656.
(466) Chadwick, J. The Existence of a Neutron. *Proceedings of the Royal Society London Series A, Containing Papers of a Mathematical and Physical Character* **1932**, *136* (830), 692−708.
(467) Lim, C.; Kang, H.; De Andrade, V.; De Carlo, F.; Zhu, L. Hard X-Ray-Induced Damage on Carbon-Binder Matrix for in Situ Synchrotron Transmission X-Ray Microscopy Tomography of Li-Ion Batteries. *Journal of Synchrotron Radiation* **2017**, *24* (3), 695−698.
(468) Young, B. T.; Heskett, D. R.; Woicik, J. C.; Lucht, B. L. X-Ray-Induced Changes to Passivation Layers of Lithium-Ion Battery Electrodes. *J. Spect.* **2018**, *2018*, 1075902.
(469) Wang, H.; Downing, R. G.; Dura, J. A.; Hussey, D. S. In Situ Neutron Techniques for Studying Lithium Ion Batteries. In *Polymers for Energy Storage and Delivery: Polyelectrolytes for Batteries and Fuel Cells*; ACS Symposium Series; American Chemical Society, 2012; Vol. *1096*, pp 6−91. DOI: 10.1021/bk-2012-1096.ch006.
(470) Balagurov, A. M.; Bobrikov, I. A.; Samoylova, N. Y.; Drozhzhin, O. A.; Antipov, E. V. Neutron Scattering for Analysis of Processes in Lithium-Ion Batteries. *Russ. Chem. Rev.* **2014**, *83* (12), 1120−1134.
(471) Ren, Y.; Zuo, X. Synchrotron X-Ray and Neutron Diffraction, Total Scattering, and Small-Angle Scattering Techniques for Rechargeable Battery Research. *Small Methods* **2018**, *2* (8), 1800064.
(472) Kardjilov, N.; Manke, I.; Woracek, R.; Hilger, A.; Banhart, J. Advances in Neutron Imaging. *Mater. Today* **2018**, *21* (6), 652−672.
(473) Goonetilleke, D.; Sharma, N. In Situ Neutron Powder Diffraction Studies. *Physical Sciences Reviews* **2021**, *6* (3), 20180155.
(474) Wang, X.; Tan, S.; Yang, X.-Q.; Hu, E. Pair Distribution Function Analysis: Fundamentals and Application to Battery Materials. *Chin. Phys. B* **2020**, *29* (2), 28802.
(475) Zhao, E.; Zhang, Z.-G.; Li, X.; He, L.; Yu, X.; Li, H.; Wang, F. Neutron-Based Characterization Techniques for Lithium-Ion Battery Research. *Chin. Phys. B* **2020**, *29* (1), 18201.
(476) Attfield, M.; Barnes, P.; Cockcroft, J. K.; Driessen, H. *Advanced Certificate in Powder Diffraction on the Web*; **1997**.
(477) Liu, J.; Du, Z.; Wang, X.; Tan, S.; Wu, X.; Geng, L.; Song, B.; Chien, P.-H.; Everett, S. M.; Hu, E. Anionic Redox Induced Anomalous Structural Transition in Ni-Rich Cathodes. *Energy Environ. Sci.* **2021**, *14*, 6441−6454.
(478) Kawaura, H.; Harada, M.; Kondo, Y.; Kondo, H.; Suganuma, Y.; Takahashi, N.; Sugiyama, J.; Seno, Y.; Yamada, N. L. Operando Measurement of Solid Electrolyte Interphase Formation at Working Electrode of Li-Ion Battery by Time-Slicing Neutron Reflectometry. *ACS Appl. Mater. Interfaces* **2016**, *8* (15), 9540−9544.
(479) Song, B.; Dhiman, I.; Carothers, J. C.; Veith, G. M.; Liu, J.; Bilheux, H. Z.; Huq, A. Dynamic Lithium Distribution upon Dendrite Growth and Shorting Revealed by Operando Neutron Imaging. *ACS Energy Letters* **2019**, *4*, 2402−2408.
(480) Rieger, B.; Schlueter, S.; Erhard, S. V.; Jossen, A. Strain Propagation in Lithium-Ion Batteries from the Crystal Structure to the Electrode Level. *J. Electrochem. Soc.* **2016**, *163* (8), A1595.
(481) Liu, J.; Du, Z.; Wang, X.; Tan, S.; Wu, X.; Geng, L.; Song, B.; Chien, P.-H.; Everett, S. M.; Hu, E. Anionic Redox Induced Anomalous Structural Transition in Ni-Rich Cathodes. *Energy Environ. Sci.* **2021**, *14*, 6441−6454.
(482) Sørensen, D. R.; Heere, M.; Zhu, J.; Darma, M. S. D.; Zimnik, S. M.; Mühlbauer, M. J.; Mereacre, L.; Baran, V.; Senyshyn, A.; Knapp, M.; Ehrenberg, H. Fatigue in High-Energy Commercial Li Batteries While Cycling at Standard Conditions: An In Situ Neutron Powder Diffraction Study. *ACS Applied Energy Materials* **2020**, *3* (7), 6611−6622.
(483) Baibich, M. N.; Broto, J. M.; Fert, A.; Van Dau, F. N.; Petroff, F.; Etienne, P.; Creuzet, G.; Friederich, A.; Chazelas, J. Giant Magnetoresistance of (001)Fe/(001)Cr Magnetic Superlattices. *Phys. Rev. Lett.* **1988**, *61* (21), 2472−2475.
(484) Daillant, J.; Gibaud, A. *X-Ray and Neutron Reflectivity: Principles and Applications*; Lecture Notes in Physics Monographs; Springer, 2008; Vol. *770*.
(485) Steinhauer, M.; Stich, M.; Kurniawan, M.; Seidlhofer, B.-K.; Trapp, M.; Bund, A.; Wagner, N.; Friedrich, K. A. In Situ Studies of Solid Electrolyte Interphase (SEI) Formation on Crystalline Carbon Surfaces by Neutron Reflectometry and Atomic Force Microscopy. *ACS Appl. Mater. Interfaces* **2017**, *9* (41), 35794−35801.
(486) Kawaura, H.; Harada, M.; Kondo, Y.; Mizutani, M.; Takahashi, N.; Yamada, N. L. Operando Time-Slicing Neutron Reflectometry Measurements of Solid Electrolyte Interphase Formation on Amorphous Carbon Surfaces of a Li-Ion Battery. *Bull. Chem. Soc. Jpn.* **2020**, *93* (7), 854−861.
(487) Veith, G. M.; Browning, K. L.; Doucet, M.; Browning, J. F. Solid Electrolyte Interphase Architecture Determined through In Situ Neutron Scattering. *J. Electrochem. Soc.* **2021**, *168* (6), 060523.
(488) Rus, E. D.; Dura, J. A. In Situ Neutron Reflectometry Study of Solid Electrolyte Interface (SEI) Formation on Tungsten Thin-Film Electrodes. *ACS Appl. Mater. Interfaces* **2019**, *11* (50), 47553−47563.
(489) Ronneburg, A.; Trapp, M.; Cubitt, R.; Silvi, L.; Cap, S.; Ballauff, M.; Risse, S. Surface Structure Inhibited Lithiation of Crystalline Silicon Probed with Operando Neutron Reflectivity. *Energy Storage Materials* **2019**, *18*, 182−189.
(490) Schmidt, H.; Jerliu, B.; Hüger, E.; Stahn, J. Volume Expansion of Amorphous Silicon Electrodes during Potentiostatic Lithiation of Li-Ion Batteries. *Electrochem. Commun.* **2020**, *115*, 106738.
(491) Kawaura, H.; Harada, M.; Kondo, Y.; Kondo, H.; Suganuma, Y.; Takahashi, N.; Sugiyama, J.; Seno, Y.; Yamada, N. L. Operando Measurement of Solid Electrolyte Interphase Formation at Working Electrode of Li-Ion Battery by Time-Slicing Neutron Reflectometry. *ACS Appl. Mater. Interfaces* **2016**, *8* (15), 9540−9544.
(492) Rus, E. D.; Dura, J. A. In Situ Neutron Reflectometry Study of Solid Electrolyte Interface (SEI) Formation on Tungsten Thin-Film Electrodes. *ACS Appl. Mater. Interfaces* **2019**, *11* (50), 47553−47563.
(493) Schmidt, H.; Jerliu, B.; Hüger, E.; Stahn, J. Volume Expansion of Amorphous Silicon Electrodes during Potentiostatic Lithiation of Li-Ion Batteries. *Electrochem. Commun.* **2020**, *115*, 106738.

(494) Kamata, M.; Esaka, T.; Kodama, N.; Fujine, S.; Yoneda, K.; Kanda, K. Application of Neutron Radiography to Visualize the Motion of Lithium Ions in Lithium-Ion Conducting Materials. *J. Electrochem. Soc.* **1996**, *143* (6), 1866−1870.
(495) Banhart, J.; Borbély, A.; Dzieciol, K.; Garcia-Moreno, F.; Manke, I.; Kardjilov, N.; Kaysser-Pyzalla, A. R.; Strobl, M.; Treimer, W. X-Ray and Neutron Imaging - Complementary Techniques for Materials Science and Engineering. *International Journal of Materials Research* **2010**, *101* (9), 1069−1079.
(496) Trtik, P.; Lehmann, E. H. Progress in High-Resolution Neutron Imaging at the Paul Scherrer Institut - The Neutron Microscope Project. *J. Phys.: Conf. Ser.* **2016**, *746*, 012004.
(497) Morgano, M.; Trtik, P.; Meyer, M.; Lehmann, E. H.; Hovind, J.; Strobl, M. Unlocking High Spatial Resolution in Neutron Imaging through an Add-on Fibre Optics Taper. *Opt. Express* **2018**, *26* (2), 1809−1816.
(498) Kaestner, A. P.; Hartmann, S.; Kühne, G.; Frei, G.; Grünzweig, C.; Josic, L.; Schmid, F.; Lehmann, E. H. The ICON Beamline - A Facility for Cold Neutron Imaging at SINQ. *Nuclear Instruments and Methods in Physics Research Section A: Accelerators, Spectrometers, Detectors and Associated Equipment* **2011**, *659* (1), 387−393.
(499) Zhang, Y.; Chandran, K. S. R.; Bilheux, H. Z. Imaging of the Li Spatial Distribution within V_2O_5 Cathode in a Coin Cell by Neutron Computed Tomography. *J. Power Sources* **2018**, *376*, 125−130.
(500) Nie, Z.; McCormack, P.; Bilheux, H. Z.; Bilheux, J. C.; Robinson, J. P.; Nanda, J.; Koenig, G. M. Probing Lithiation and Delithiation of Thick Sintered Lithium-Ion Battery Electrodes with Neutron Imaging. *J. Power Sources* **2019**, *419*, 127−136.
(501) Song, B.; Dhiman, I.; Carothers, J. C.; Veith, G. M.; Liu, J.; Bilheux, H. Z.; Huq, A. Dynamic Lithium Distribution upon Dendrite Growth and Shorting Revealed by Operando Neutron Imaging. *ACS Energy Letters* **2019**, *4*, 2402−2408.
(502) Xu, H.; Zhu, J.; Finegan, D. P.; Zhao, H.; Lu, X.; Li, W.; Hoffman, N.; Bertei, A.; Shearing, P.; Bazant, M. Z. Guiding the Design of Heterogeneous Electrode Microstructures for Li-Ion Batteries: Microscopic Imaging, Predictive Modeling, and Machine Learning. *Adv. Energy Mater.* **2021**, *11* (19), 2003908.
(503) Scharf, J.; Chouchane, M.; Finegan, D. P.; Lu, B.; Redquest, C.; Kim, M.; Yao, W.; Franco, A. A.; Gostovic, D.; Liu, Z.; Riccio, M.; Zelenka, F.; Doux, J.-M.; Meng, Y. S. Bridging Nano- and Microscale X-Ray Tomography for Battery Research by Leveraging Artificial Intelligence. *Nat. Nanotechnol.* **2022**, *17*, 446−459.
(504) Attia, P. M.; Grover, A.; Jin, N.; Severson, K. A.; Markov, T. M.; Liao, Y. H.; Chen, M. H.; Cheong, B.; Perkins, N.; Yang, Z.; Herring, P. K.; Aykol, M.; Harris, S. J.; Braatz, R. D.; Ermon, S.; Chueh, W. C. Closed-Loop Optimization of Fast-Charging Protocols for Batteries with Machine Learning. *Nature* **2020**, *578* (7795), 397−402.
(505) Lombardo, T.; Duquesnoy, M.; El-Bouysidy, H.; Årén, F.; Gallo-Bueno, A.; Jørgensen, P. B.; Bhowmik, A.; Demortière, A.; Ayerbe, E.; Alcaide, F.; Reynaud, M.; Carrasco, J.; Grimaud, A.; Zhang, C.; Vegge, T.; Johansson, P.; Franco, A. A. Artificial Intelligence Applied to Battery Research: Hype or Reality? *Chem. Rev.* **2021**, *122* (12), 10899−10969, DOI: 10.1021/acs.chemrev.1c00108.
(506) Dixit, M. B.; Verma, A.; Zaman, W.; Zhong, X.; Kenesei, P.; Park, J. S.; Almer, J.; Mukherjee, P. P.; Hatzell, K. B. Synchrotron Imaging of Pore Formation in Li Metal Solid-State Batteries Aided by Machine Learning. *ACS Applied Energy Materials* **2020**, *3* (10), 9534−9542.
(507) Zhang, K.; Ren, F.; Wang, X.; Hu, E.; Xu, Y.; Yang, X.-Q.; Li, H.; Chen, L.; Pianetta, P.; Mehta, A.; Yu, X.; Liu, Y. Finding a Needle in the Haystack: Identification of Functionally Important Minority Phases in an Operating Battery. *Nano Lett.* **2017**, *17* (12), 7782−7788.
(508) Badmos, O.; Kopp, A.; Bernthaler, T.; Schneider, G. Image-Based Defect Detection in Lithium-Ion Battery Electrode Using Convolutional Neural Networks. *Journal of Intelligent Manufacturing* **2020**, *31* (4), 885−897.
(509) Li, J.; Sharma, N.; Jiang, Z.; Yang, Y.; Monaco, F.; Xu, Z.; Hou, D.; Ratner, D.; Pianetta, P.; Cloetens, P.; Lin, F.; Zhao, K.; Liu, Y. Dynamics of Particle Network in Composite Battery Cathodes. *Science* **2022**, *376* (6592), 517−521.
(510) Xu, Y.; Hu, E.; Zhang, K.; Wang, X.; Borzenets, V.; Sun, Z.; Pianetta, P.; Yu, X.; Liu, Y.; Yang, X. Q.; Li, H. In Situ Visualization of State-of-Charge Heterogeneity within a $LiCoO_2$ Particle That Evolves upon Cycling at Different Rates. *ACS Energy Letters* **2017**, *2* (5), 1240−1245.
(511) Hu, Y.; Zhao, X.; Suo, Z. Averting Cracks Caused by Insertion Reaction in Lithium-Ion Batteries. *J. Mater. Res.* **2010**, *25* (6), 1007−1010.
(512) Jo, M.; Hong, Y.-S.; Choo, J.; Cho, J. Effect of $LiCoO_2$ Cathode Nanoparticle Size on High Rate Performance for Li-Ion Batteries. *J. Electrochem. Soc.* **2009**, *156* (6), A430.
(513) Liu, X. H.; Zhong, L.; Huang, S.; Mao, S. X.; Zhu, T.; Huang, J. Y. Size-Dependent Fracture of Silicon Nanoparticles During Lithiation. *ACS Nano* **2012**, *6* (2), 1522−1531.
(514) Boukamp, B. A.; Lesh, G. C.; Huggins, R. A. All-Solid Lithium Electrodes with Mixed-Conductor Matrix. *J. Electrochem. Soc.* **1981**, *128* (4), 725.
(515) Yi, R.; Dai, F.; Gordin, M. L.; Chen, S.; Wang, D. Micro-Sized Si-C Composite with Interconnected Nanoscale Building Blocks as High-Performance Anodes for Practical Application in Lithium-Ion Batteries. *Adv. Energy Mater.* **2013**, *3* (3), 295−300.
(516) Liu, X. H.; Zhong, L.; Huang, S.; Mao, S. X.; Zhu, T.; Huang, J. Y. Size-Dependent Fracture of Silicon Nanoparticles During Lithiation. *ACS Nano* **2012**, *6* (2), 1522−1531.
(517) Li, J.; Cameron, A. R.; Li, H.; Glazier, S.; Xiong, D.; Chatzidakis, M.; Allen, J.; Botton, G. A.; Dahn, J. R. Comparison of Single Crystal and Polycrystalline $LiNi_{0.5}Mn_{0.3}Co_{0.2}O_2$ Positive Electrode Materials for High Voltage Li-Ion Cells. *J. Electrochem. Soc.* **2017**, *164* (7), A1534−A1544.
(518) Li, H.; Li, J.; Ma, X.; Dahn, J. R. Synthesis of Single Crystal $LiNi_{0.6}Mn_{0.2}Co_{0.2}O_2$ with Enhanced Electrochemical Performance for Lithium Ion Batteries. *J. Electrochem. Soc.* **2018**, *165* (5), A1038−A1045.
(519) Li, H.; Li, J.; Zaker, N.; Zhang, N.; Botton, G. A.; Dahn, J. R. Synthesis of Single Crystal $LiNi_{0.88}Co_{0.09}Al_{0.03}O_2$ with a Two-Step Lithiation Method. *J. Electrochem. Soc.* **2019**, *166* (10), A1956.
(520) Qian, G.; Zhang, Y.; Li, L.; Zhang, R.; Xu, J.; Cheng, Z.; Xie, S.; Wang, H.; Rao, Q.; He, Y.; Shen, Y.; Chen, L.; Tang, M.; Ma, Z. F. Single-Crystal Nickel-Rich Layered-Oxide Battery Cathode Materials: Synthesis, Electrochemistry, and Intra-Granular Fracture. *Energy Storage Materials* **2020**, *27*, 140−149.
(521) Fan, X.; Hu, G.; Zhang, B.; Ou, X.; Zhang, J.; Zhao, W.; Jia, H.; Zou, L.; Li, P.; Yang, Y. Crack-Free Single-Crystalline Ni-Rich Layered NCM Cathode Enable Superior Cycling Performance of Lithium-Ion Batteries. *Nano Energy* **2020**, *70*, 104450.
(522) Li, J.; Cameron, A. R.; Li, H.; Glazier, S.; Xiong, D.; Chatzidakis, M.; Allen, J.; Botton, G. A.; Dahn, J. R. Comparison of Single Crystal and Polycrystalline $LiNi_{0.5}Mn_{0.3}Co_{0.2}O_2$ Positive Electrode Materials for High Voltage Li-Ion Cells. *J. Electrochem. Soc.* **2017**, *164* (7), A1534−A1544.
(523) Zou, L.; Li, J.; Liu, Z.; Wang, G.; Manthiram, A.; Wang, C. Lattice Doping Regulated Interfacial Reactions in Cathode for Enhanced Cycling Stability. *Nat. Commun.* **2019**, *10* (1), 1−11.
(524) Liu, Q.; Su, X.; Lei, D.; Qin, Y.; Wen, J.; Guo, F.; Wu, Y. A.; Rong, Y.; Kou, R.; Xiao, X.; Aguesse, F.; Bareño, J.; Ren, Y.; Lu, W.; Li, Y. Approaching the Capacity Limit of Lithium Cobalt Oxide in Lithium Ion Batteries via Lanthanum and Aluminium Doping. *Nature Energy* **2018**, *3* (11), 936−943.
(525) Xie, Q.; Li, W.; Manthiram, A. A Mg-Doped High-Nickel Layered Oxide Cathode Enabling Safer, High-Energy-Density Li-Ion Batteries. *Chem. Mater.* **2019**, *31* (3), 938−946.
(526) Li, Q.; Li, G.; Fu, C.; Luo, D.; Fan, J.; Li, L. K+-Doped $Li_{1.2}Mn_{0.54}Co_{0.13}Ni_{0.13}O_2$: A Novel Cathode Material with an Enhanced Cycling Stability for Lithium-Ion Batteries. *ACS Appl. Mater. Interfaces* **2014**, *6* (13), 10330−10341.

(527) Yoon, C. S.; Kim, U.-H.; Park, G.-T.; Kim, S. J.; Kim, K.-H.; Kim, J.; Sun, Y.-K. Self-Passivation of a $LiNiO_2$ Cathode for a Lithium-Ion Battery through Zr Doping. *ACS Energy Letters* **2018**, *3* (7), 1634−1639.
(528) Kim, H.; Kim, M. G.; Jeong, H. Y.; Nam, H.; Cho, J. A New Coating Method for Alleviating Surface Degradation of $LiNi_{0.6}Co_{0.2}Mn_{0.2}O_2$ Cathode Material: Nanoscale Surface Treatment of Primary Particles. *Nano Lett.* **2015**, *15* (3), 2111−2119.
(529) Liu, W.; Li, X.; Xiong, D.; Hao, Y.; Li, J.; Kou, H.; Yan, B.; Li, D.; Lu, S.; Koo, A.; Adair, K.; Sun, X. Significantly Improving Cycling Performance of Cathodes in Lithium Ion Batteries: The Effect of Al_2O_3 and $LiAlO_2$ Coatings on $LiNi_{0.6}Co_{0.2}Mn_{0.2}O_2$. *Nano Energy* **2018**, *44*, 111−120.
(530) Hu, X.; Qiang, W.; Huang, B. Surface Layer Design of Cathode Materials Based on Mechanical Stability towards Long Cycle Life for Lithium Secondary Batteries. *Energy Storage Materials* **2017**, *8*, 141−146.
(531) Yang, Z.; Mu, L.; Hou, D.; Rahman, M. M.; Xu, Z.; Liu, J.; Nordlund, D.; Sun, C.-J. J.; Xiao, X.; Lin, F. Probing Dopant Redistribution, Phase Propagation, and Local Chemical Changes in the Synthesis of Layered Oxide Battery Cathodes. *Adv. Energy Mater.* **2021**, *11* (1), 2002719.
(532) Yoon, C. S.; Kim, U.-H.; Park, G.-T.; Kim, S. J.; Kim, K.-H.; Kim, J.; Sun, Y.-K. Self-Passivation of a $LiNiO_2$ Cathode for a Lithium-Ion Battery through Zr Doping. *ACS Energy Letters* **2018**, *3* (7), 1634−1639.
(533) Zhang, Y.; Yang, Z.; Tian, C. Probing and Quantifying Cathode Charge Heterogeneity in Li Ion Batteries. *Journal of Materials Chemistry A* **2019**, *7* (41), 23628−23661.
(534) Xu, X.; Huo, H.; Jian, J.; Wang, L.; Zhu, H.; Xu, S.; He, X.; Yin, G.; Du, C.; Sun, X. Radially Oriented Single-Crystal Primary Nanosheets Enable Ultrahigh Rate and Cycling Properties of $LiNi_{0.8}Co_{0.1}Mn_{0.1}O_2$ Cathode Material for Lithium-Ion Batteries. *Adv. Energy Mater.* **2019**, *9* (15), 1803963.
(535) Yoon, C. S.; Park, K. J.; Kim, U. H.; Kang, K. H.; Ryu, H. H.; Sun, Y. K. High-Energy Ni-Rich $Li[Ni_xCo_yMn_{1-x-y}]O_2$ Cathodes via Compositional Partitioning for Next-Generation Electric Vehicles. *Chem. Mater.* **2017**, *29* (24), 10436−10445.
(536) Kim, U. H.; Ryu, H. H.; Kim, J. H.; Mücke, R.; Kaghazchi, P.; Yoon, C. S.; Sun, Y. K. Microstructure-Controlled Ni-Rich Cathode Material by Microscale Compositional Partition for Next-Generation Electric Vehicles. *Adv. Energy Mater.* **2019**, *9* (15), 1803902.
(537) Kim, U.-H.; Park, G.-T.; Son, B.-K.; Nam, G. W.; Liu, J.; Kuo, L.-Y.; Kaghazchi, P.; Yoon, C. S.; Sun, Y.-K. Heuristic Solution for Achieving Long-Term Cycle Stability for Ni-Rich Layered Cathodes at Full Depth of Discharge. *Nature Energy* **2020**, *5* (11), 860−869.
(538) Liu, N.; Wu, H.; McDowell, M. T.; Yao, Y.; Wang, C.; Cui, Y. A Yolk-Shell Design for Stabilized and Scalable Li-Ion Battery Alloy Anodes. *Nano Lett.* **2012**, *12* (6), 3315−3321.
(539) Magasinski, A.; Dixon, P.; Hertzberg, B.; Kvit, A.; Ayala, J.; Yushin, G. High-Performance Lithium-Ion Anodes Using a Hierarchical Bottom-up Approach. *Nat. Mater.* **2010**, *9* (4), 353−358.
(540) Wu, H.; Chan, G.; Choi, J. W.; Ryu, I.; Yao, Y.; McDowell, M. T.; Lee, S. W.; Jackson, A.; Yang, Y.; Hu, L.; Cui, Y. Stable Cycling of Double-Walled Silicon Nanotube Battery Anodes through Solid-Electrolyte Interphase Control. *Nat. Nanotechnol.* **2012**, *7* (5), 310−315.
(541) Zhang, W.-M.; Hu, J.-S.; Guo, Y.-G.; Zheng, S.-F.; Zhong, L.-S.; Song, W.-G.; Wan, L.-J. Tin-Nanoparticles Encapsulated in Elastic Hollow Carbon Spheres for High-Performance Anode Material in Lithium-Ion Batteries. *Adv. Mater.* **2008**, *20* (6), 1160−1165.
(542) Zhang, H.; Zhou, L.; Noonan, O.; Martin, D. J.; Whittaker, A. K.; Yu, C. Tailoring the Void Size of Iron Oxide@Carbon Yolk-Shell Structure for Optimized Lithium Storage. *Adv. Funct. Mater.* **2014**, *24* (27), 4337−4342.
(543) Sun, Y. K.; Chen, Z.; Noh, H. J.; Lee, D. J.; Jung, H. G.; Ren, Y.; Wang, S.; Yoon, C. S.; Myung, S. T.; Amine, K. Nanostructured High-Energy Cathode Materials for Advanced Lithium Batteries. *Nat. Mater.* **2012**, *11* (11), 942−947.
(544) Mao, Y.; Wang, X.; Xia, S.; Zhang, K.; Wei, C.; Bak, S.; Shadike, Z.; Liu, X.; Yang, Y.; Xu, R.; Pianetta, P.; Ermon, S.; Stavitski, E.; Zhao, K.; Xu, Z.; Lin, F.; Yang, X.; Hu, E.; Liu, Y. High-Voltage Charging-Induced Strain, Heterogeneity, and Micro-Cracks in Secondary Particles of a Nickel-Rich Layered Cathode Material. *Adv. Funct. Mater.* **2019**, *29* (18), 1900247.
(545) Park, M.-H.; Kim, M. G.; Joo, J.; Kim, K.; Kim, J.; Ahn, S.; Cui, Y.; Cho, J. Silicon Nanotube Battery Anodes. *Nano Lett.* **2009**, *9* (11), 3844−3847.
(546) Magasinski, A.; Dixon, P.; Hertzberg, B.; Kvit, A.; Ayala, J.; Yushin, G. High-Performance Lithium-Ion Anodes Using a Hierarchical Bottom-up Approach. *Nat. Mater.* **2010**, *9* (4), 353−358.
(547) Mao, Y.; Wang, X.; Xia, S.; Zhang, K.; Wei, C.; Bak, S.; Shadike, Z.; Liu, X.; Yang, Y.; Xu, R.; Pianetta, P.; Ermon, S.; Stavitski, E.; Zhao, K.; Xu, Z.; Lin, F.; Yang, X.; Hu, E.; Liu, Y. High-Voltage Charging-Induced Strain, Heterogeneity, and Micro-Cracks in Secondary Particles of a Nickel-Rich Layered Cathode Material. *Adv. Funct. Mater.* **2019**, *29* (18), 1900247.
(548) Ezeigwe, E. R.; Dong, L.; Manjunatha, R.; Tan, M.; Yan, W.; Zhang, J. A Review of Self-Healing Electrode and Electrolyte Materials and Their Mitigating Degradation of Lithium Batteries. *Nano Energy* **2021**, *84*, 105907.
(549) Wang, C.; Wu, H.; Chen, Z.; McDowell, M. T.; Cui, Y.; Bao, Z. Self-Healing Chemistry Enables the Stable Operation of Silicon Microparticle Anodes for High-Energy Lithium-Ion Batteries. *Nat. Chem.* **2013**, *5* (12), 1042−1048.
(550) Jin, Y.; Li, S.; Kushima, A.; Zheng, X.; Sun, Y.; Xie, J.; Sun, J.; Xue, W.; Zhou, G.; Wu, J.; Shi, F.; Zhang, R.; Zhu, Z.; So, K.; Cui, Y.; Li, J. Self-Healing SEI Enables Full-Cell Cycling of a Silicon-Majority Anode with a Coulombic Efficiency Exceeding 99.9%. *Energy Environ. Sci.* **2017**, *10* (2), 580−592.

https://doi.org/10.1021/acs.chemrev.2c00002
Chem. Rev. 2022, 122, 13043−13107